Repurposing legacy iron and steel slag: a resource potential

Robin Xiaofang Hilderman
MSc, BA

Submitted in fulfilment of the requirements for the
Degree of Master's by Research in Geology

School of Geographical and Earth Sciences
College of Science & Engineering
University of Glasgow

Abstract

The reuse of legacy iron and steel wastes presents opportunities for resource recovery and atmospheric carbon dioxide (CO_2) storage. Limited documentation of these anthropogenically derived rocks and the natural environmental processes altering slag deposits resulting in ecotoxic metal leaching pose challenges to repurposing. Increasing interest in integrating Circular Economic (CE) approaches into waste management requires a comprehensive understanding of the materials and developing innovative methods to resolve characterisation complexities. In this study, the opportunities for legacy slag are explored using the two Carnforth Iron Work deposits in Warton, South Lancashire, England that are located on the Morecambe Bay coast and ~ 435 meters (m) inland. The mineralogy and trace metal content are quantified and identified using a data-driven unsupervised learning approach from the inland deposit (A), and the lithification mechanisms and mineralogic features are identified from the coastal deposit (B).

From the inland setting deposit A, 23 sections spanning five stratigraphic horizons were analysed for microstructural compositional variation using scanning electron microscopy-energy dispersive X-ray spectrometry spectrometry (SEM-EDS). These large and highly-dimensional datasets were quantified using a semi-automated approach leveraging nonnegative matrix factorisation (NMF) and Hierarchical Density-Based Spatial Clustering of Applications with Noise (HDBSCAN), the regions were segmented into mineral phases and the trace metal constitutes were quantified. The variable mineralogy and metal content between horizons reflects contemporaneous iron and steel production and possibly early iron pig production. While this approach is not fully automated, the automated dimensional reduction and clustering is a turnkey operation for processing numerous large datasets. Applying the approach on specific phases (iterative phase classification (IPC)) drove the analysis that confirmed and revealed both the microstructures and trace Ba, Fe, and Mn from the model outliers and more statistically representative phases.

At the coastal deposit B, X-Ray Diffraction (XRD) and EDS analysis of the slag and thermogravimetric analysis (TGA) of the cream-coloured material covering the slag shows lithification on the top surface and seaward side above the mean high-water mark (MHWM) is the result of carbonate mineralisation. This is driven by water and leached calcium from weathering slag minerals (i.e., gehlenite, åkermanite, pseudowollastonite) reacting with ingassed and hydroxylated atmospheric CO_2, forming calcite with slightly to strongly depleted $\delta^{13}C$ values (-6.4 ‰ to -22.7 ‰) following partial dissolved inorganic carbonate (DIC) equilibrium. Calcium-silicate-hydrate (CSH), a component in cement, precipitated and was responsible for lithifying the deposit where more frequent and abundant seawater washing prevents subsequent slag mineral dissolution and carbonate precipitation.

The trace Ba, Fe, and Mn quantified at deposit A and the carbonate and CSH precipitation identified at deposit B are evidence that legacy iron and steel slag deposits can be sources of critical raw materials (CRM) and are prone to lithification in coastal settings. The iterative approach utilising machine learning provides a tool for locating hidden and non-majority component regions, enhancing microstructural analysis. This lithification can draw down atmospheric CO_2 and the CSH precipitation could help to slow the release of toxic metals, reducing the environmental contamination risk of repurposing legacy slag for

‘hard’ protection and coastal defence. Considering how the environment affects industrial waste deposit evolution can elucidate the most appropriate and safest slag repurposing option between CRM recovery, atmospheric CO_2 storage, and coastal defence.

Table of Contents

List of Tables

List of Figures

List of Accompanying material

Acknowledgement

The author would like to acknowledge and express the greatest appreciation towards Joshua Einsle and John MacDonald for providing support during this research, interpretive guidance, insightful comments, and edits to improve this thesis. The following are thanked for helping with the TGA, XRD, and stable O and C isotope data collection at the University of Glasgow: Connor Brolly, Andrew Monaghan, Charlotte Slaymark, Liene Spruženice, and Claire Wilson. Chapter 3 of this research was funded by NERC Exploring the Frontiers award NE/X009718/1 to JMM.

Author's Declaration

The author declares that this thesis was composed by themselves, that the work contained herein is my own except where explicitly stated otherwise in the text, and that this work has not been submitted for any other degree or professional qualification. Chapter 3 has been approved for publication in the journal *Sedimentologika*.

The author declares that they have no known competing financial interests or personal relationships that could have appeared to influence the work reported in this paper.

List of Abbreviations

BF	Blast furnaces
BSE	Backscatter Electron
BOF	Basic oxygen furnaces
CCS	Carbon capture and storage
CO_2	Carbon dioxide
CRM	Critical raw material
CSH	Calcium-silicate-hydrate
DIC	Dissolved inorganic carbon
EAF	Electric arc furnaces
EDS	Energy dispersive X-r9ay spectrometry
FA	Factor analysis
GEMS	Geoanalytical Electron and Microscopy and Spectroscopy
GLOSH	Global-Local Outlier Scores from Hierarchies
HDBSCAN	Hierarchical Density-Based Spatial Clustering of Application with Noise
IPC	Iterative phase classification
ICA	Independent component analysis
ICP-AES	Inductively coupled plasma-atomic emission spectrometry
IPCC	Intergovernmental Panel on Climate Change
LA-ICP-MS	Laser ablation inductively coupled plasma mass spectrometry
LF	Ladle furnaces
MHWM	Mean high-water mark
MLA	Mineral Liberation Analysis
NMF	Nonnegative matrix factorisation
P/B ZAF	Peak-to-Background Zero-Absorption-Florescence
PCA	Principal Component Analysis
PGM	Platinum group metals
QEMSCAN	Quantitative Evaluation of Materials by Scanning Electron Microscopy
REE	Rare earth elements
SEM	Scanning electron microscopy
SEM-AM	Scanning electron microscopy-based automated mineralogy
TGA	Thermogravimetric analysis
TGA-DTG	Thermogravimetric analysis-derivative thermogravimetry
TIMA-X	Tescan Integrated Mineral Analyzer
UK	United Kingdom
US	United States
WDS	Wave-Dispersive X-ray spectrometry
XRD	X-ray Diffraction
XRF	X-ray Fluorescence

1. Chapter 1: Introduction

The by-products of iron and steel making present a range of opportunities that can help facilitate the green energy transition to meet net-zero goals. Slags are formed from reactions between gangue minerals, fluxes, and other possible reactants smelting in the furnace feed (Piatak & Ettler, 2021), representing the undesirable waste product from ore processing (Peng et al., 2017). Historically, slags have been reused in the construction industry (i.e., aggregates) but increasing interest to utilise these by-products may help in achieving energy transition targets (Piatak & Ettler, 2021; Riley et al., 2020) and contributing to Circular Economy (CE). This is demonstrated by the shift of slag-related research focusing on metal recovery (i.e., Gomes et al., 2016; Habib et al., 2020; Mayes et al., 2022; Naden, 2013; Piatak et al., 2004; Riley et al., 2020) and carbon capture and storage (CCS) (Bobicki et al., 2012; Doucet, 2010; Gomes et al., 2016; Huijgen et al., 2005; MacDonald, Khudhur, et al., 2023; Mayes et al., 2022; Naden, 2013; Piatak et al., 2004; Renforth, 2019; Riley et al., 2020; Sanna et al., 2012) from alkaline waste. Besides ensuring CE aspects of development, processing, and recycling yield economic benefits, these sustainable approaches must become commonplace in future industrial processes and waste management (Martins & Castro, 2020). Minimising and closing energy and material loops through long-lasting design, reuse, and recycling will be crucial for meeting net-zero goals (Geissdoerfer et al., 2017).

Reaching the Paris Agreement goals will require quadrupling the mineral requirements for clean energy technologies by 2040, and global net-zero by 2050 will require six times more mineral inputs in 2040 than in 2021 (IEA, 2021). Furthermore, increasing estimated quantities of iron and steelmaking slag from between 295 and 354 megatonne (Mt) and 169 to 254 Mt in 2017 (van Oss, 2014) to 299.4 to 354 Mt and 172 to 263 Mt in 2022 (USGS, 2023), respectively, indicate industrial waste management must be able to handle these increasing volumes of material.

1.1 Metallurgical overview

The two major slag groups are ferrous, generated from iron and steel production, and non-ferrous, generated from the recovery of base metals (e.g., Cu, Ni, Pb, Zn), which can be classified by the specific furnace used for metal extraction. Fe-slag is produced from blast furnaces (BF) (Chiang & Pan, 2017), whereas steel slags are by-products of combining molten iron from BFs, scrap steel, and alloys, from using either electric arc furnaces (EAF), basic oxygen furnaces (BOF), or ladle furnaces (LF) to make specific steel grades (Bobicki et al., 2012; Bonenfant et al., 2008; Brandt, 1985; De Windt et al., 2011; Piatak et al., 2015; Proctor et al., 2000; Wang et al., 2010). Further BF slag classification is based on the cooling method: air-cooled BF slag, granulated water-quenched BF slag, pelletised (air- and water-cooled) BF slag, and expanded or foamed air-, water-, or steam-cooled BF slag (Tripathy et al., 2020; Zhang et al., 2020).

1.1.1 Ferrous slag

Ferrous slag generated during iron recovery and steelmaking varies depending on the type of furnace used, the cooling method (Piatak et al., 2015) in addition to the starting material

(Proctor et al., 2000). Blast furnace slag is the by-product of pig iron production where iron ore, iron scraps, fluxes (i.e., lime, limestone and/or dolomite) and coke as fuel, react with excess oxygen to reduce the ore to molten iron (Chiang & Pan, 2017; Piatak et al., 2021). The liquid iron will either be cased into pig iron or used for steelmaking in an EAF, BOF and LF, resulting in steel slag as the by-product (Chiang & Pan, 2017; Habib et al., 2020). The various rates and methods used to solidify molten iron slag affect the slag properties, influencing future commercial use and recovery potential (Lewis, 1982; Piatak et al., 2021; Tripathy et al., 2020). While variations between iron and steel slag refining aim to remove remaining S, gases or impurities, and adjust C content, both slags may be used for similar purposes as the same cooling processes result in comparable properties (van Oss, 2013).

Reporting of ferrous slag composition and mineralogy is often generalised, challenging efficient critical raw material (CRM) recovery method development. Additionally, elements such as rare earth elements (REE) and platinum group metals (PGM) included in CRM lists are rarely if ever reported in slags (Piatak et al., 2021), despite REE abundances reaching up to 420 mg kg^{-1} in steel slag (Douglas et al., 2012; Piatak et al., 2019; Wendling et al., 2010; Wendling et al., 2013) and up to 440 mg kg^{-1} in BF slags (Cravotta, 2005; Piatak et al., 2019; Wendling et al., 2013).

1.2 Bulk chemistry

1.2.1 Iron/ BF slag

Ferrous slag composition dominantly comprises CaO (12.1 to 36.9 weight (wt)%) and SiO_2 (33.2 to 34.2 wt%). BF iron slag predating the twentieth century dominates the SiO_2–rich end (>70 wt%) of the FeO–SiO_2–CaO ternary diagram in Piatak et al. (2021) and may contain significant amounts of FeO as the result of ineffective iron recovery compared to that of modern BF slags. Fluxes added to improve metal recovery, olivine-bearing rocks, and quartzite or quartz sand generally source the Ca, Mg, and Si in slag. Gangue minerals in the iron ore and coke tend to source the Si, Al, and S. Pre-1900 BF slags have on average less than half the concentration of Ca (12.1 wt% CaO) compared to that in modern BF slags (36.9 wt% CaO). However, SiO_2 concentrations are similar for both iron slags (34.2 wt% SiO_2 for modern and 33.2 wt% SiO_2 for pre-1900) (Piatak et al., 2021). While iron slag contains significantly more Al (7.7 to 12.5 wt% Al) and slightly more Mg (6.2 to 8.2 wt% Mg) compared to that in steel slag (5.3 wt% Al and 6.3 wt% Mg), both iron and steel slag can have high concentrations of the trace elements Cr (9.1 to 328 mg kg^{-1}: iron slag; 1988 mg kg^{-1} steel slag) and Mn (0.7 to 0.8 wt%: iron slag; 4.9 wt%: steel slag) (Piatak et al., 2021).

1.2.2 Steel slag

Similar to modern BF slag, steel slag is dominated by CaO (45 to 60 wt%) and equal or less FeO is usually found followed by SiO_2 (10 to 15 wt%) reflecting the common use of limestone as a flux (Motz & Geiseler, 2001; Piatak et al., 2015, 2021; Xuequan et al., 1999). Abundant Al_2O_3 (5.3 wt%), MgO (6.3 wt%), and MnO (4.9 wt%) can also be found in steel slag with the latter generally being the highest (Piatak et al., 2021). Free lime can reach 12wt% and CaO as lime or dolomitic lime can exceed 35 wt% (Yildirim & Prezzi, 2011), as the results of fluxed rich in Ca and Mg added to the furnace to optimise slag

formation (Piatak et al., 2021). At legacy steelmaking sites, slag piles may be a combination of both BF and steel slags (Piatak et al., 2021).

1.3 Mineralogy and petrography

1.3.1 Iron slag

Although the mineralogy and textures of iron slag can vary widely, minerals from the melilite group are the most commonly reported and often abundant regardless of the time of production and the cooling method (Piatak et al., 2021). Spinel-, olivine-, pyroxene-, melilite-group, and glasses are found in pre-1900 BF slag in addition to silicate-rich, feldspar, garnet, oxide, and carbonate which are from fluxes (Piatak et al., 2015, 2021). The solid solution of wüstite (FeO) is typically observed since BF slags have a high Fe oxide content (Yildirim & Prezzi, 2011). Native metals such as Cu, Fe and Pb and intermetallic compounds are common and may contain trace elements (i.e., Ag, As, Au, Co, Cd Ni, Sn, Sb: Piatak et al., 2015a). Both crystalline or glass-like textures occur in slag and depend on the composition and cooling method. For example, when quenched molten slag is cooled with high volume, high-pressure sprays of water, crystallization is prevented, and sand-sized amorphous vitrified fragments are generated. Amorphous phases are reported from both pre-1900 and modern BF slag (Butler, 1977; Piatak et al., 2021; Scott et al., 1986). Carbonates are found in both modern and weathered/legacy ferrous slag as calcite, dolomite, aragonite, and vaterite (Piatak et al., 2021). Notably, CaO and SiO_2 content in BOF slag increases with the decrease in particle size, whereas the Fe_2O_3 fraction decreases significantly (Pan et al., 2015; Zhang et al., 2011).

1.3.2 Steel slag

The common mineral phases in steel slags including larnite (Ca_2SiO_4), tricalcium silicate (Ca_3SiO_5), and Ca-oxide (CaO, free lime), reflect the higher CaO content compared to that of Fe slags (Piatak et al., 2015). Merwinite, olivine, β-C_2S ($2CaO{\cdot}SiO_2$), α-C_2S, C_4AF ($4CaO{\cdot}Al_2O_3{\cdot}FeO_3$), C_2F ($2CaO{\cdot}Fe_2O_3$), MgO, FeO, and C_3S($3CaO{\cdot}SiO_2$), the RO phase (solid solution of CaO-FeO-MnO-MgO) (Qian et al., 2002; Qian et al., 2002; Shen et al., 2004), trace varieties of sulfides, intermediate compounds, pure metals, and calcite are also observed (Piatak et al., 2015). The lower silica content (21.1 wt%: steel slag; 33.2 to 34.2 wt%: iron slag: Piatak et al. (2021)) tends to prevent steel slag from vitrifying even when cooled rapidly (Yildirim & Prezzi, 2011), though if quenched, Ca silicate glass would form (Piatak et al., 2015).

1.4 Process evolution

Variations in the physical textures, chemical composition, and mineralogy of the hundreds of millions of tonnes of slag produced annually can be correlated to the starting material, furnace used, and cooling method (Piatak et al., 2015; Piatak & Ettler, 2021; Proctor et al., 2000). Thus, the major developments during the second half of the 19th century, especially in steel production should be evident in the slags and tailings (Lundén & Paulsson, 2009). For example, the development of the Bessemer process revolutionised the mass production of cheap steel in the United States (US) and Europe as the phosphorus in the pig iron could

be removed when chemically basic material was combined (Jones, 1920; Spoerl, 2004). However, with subsequent technological advances, the open hearth process allowed for scrap metal recycling and larger steel batch production than possible with the Bessemer process and ultimately dominated by the 20th century. After 1960 the basic oxygen process gained popularity to produce steel from Fe ore, and the EAF in the production of steel from scrap (Spoerl, 2004). While the continuous improvement in metallurgy processes has decreased the material quality of current industrial waste generated (Hudson-Edwards, 2016), the incomplete recovery of target metals and partitioning of by-product elements into slag during smelting may yield a promising source of CRM preserved at historical deposits (Piatak & Ettler, 2021; Riley et al., 2020).

1.5 Resource recovery

As the energy sector is set to lead mineral consumption, increasing, and diversifying the supply must be an immediate focus for mineral security (IEA, 2021). Recycling alone will not make up for the discrepancy in total reserves expected to contribute to the renewable energy scenarios in the Intergovernmental Panel on Climate Change (IPCC) Fifth Assessment Report (IPCC, 2014). The growing interest and research on slags, especially at legacy deposits, is contributing to the limited fundamental knowledge and demonstrating their potential as a source for CRM recovery (Habib et al., 2020). The historical metallurgical processes from the 1900th to 2000th centuries were likely less efficient than those of today and did not target the metals that are urgently needed for low-carbon technologies.

Critical metals, defined as of high economic importance and with high supply risk are found intrinsically in enriched rock bodies in ‘companion’ with more abundant major meals that have similar chemical and physical properties. However, supply risk from lower bulk concentrations combined with sparse ore reserve reporting on the smaller market (e.g., Se, Co) and more economically challenging (e.g., Cd, In, Ga, Ge, Hf) metals limits our understanding of critical metal abundances (Hagelüken, 2012; Mudd et al., 2017). Furthermore, reported usage ranges from tens to thousands of tonnes per year, with no globally accepted list, compromising renewable energy scenarios (Grandell et al., 2016; Gunn, 2014). The British Geological Survey include 26 candidate materials on the UK Critical Mineral List 2021 (Fig. 1) and will be used for the purpose of this study as the material focus is UK-based.

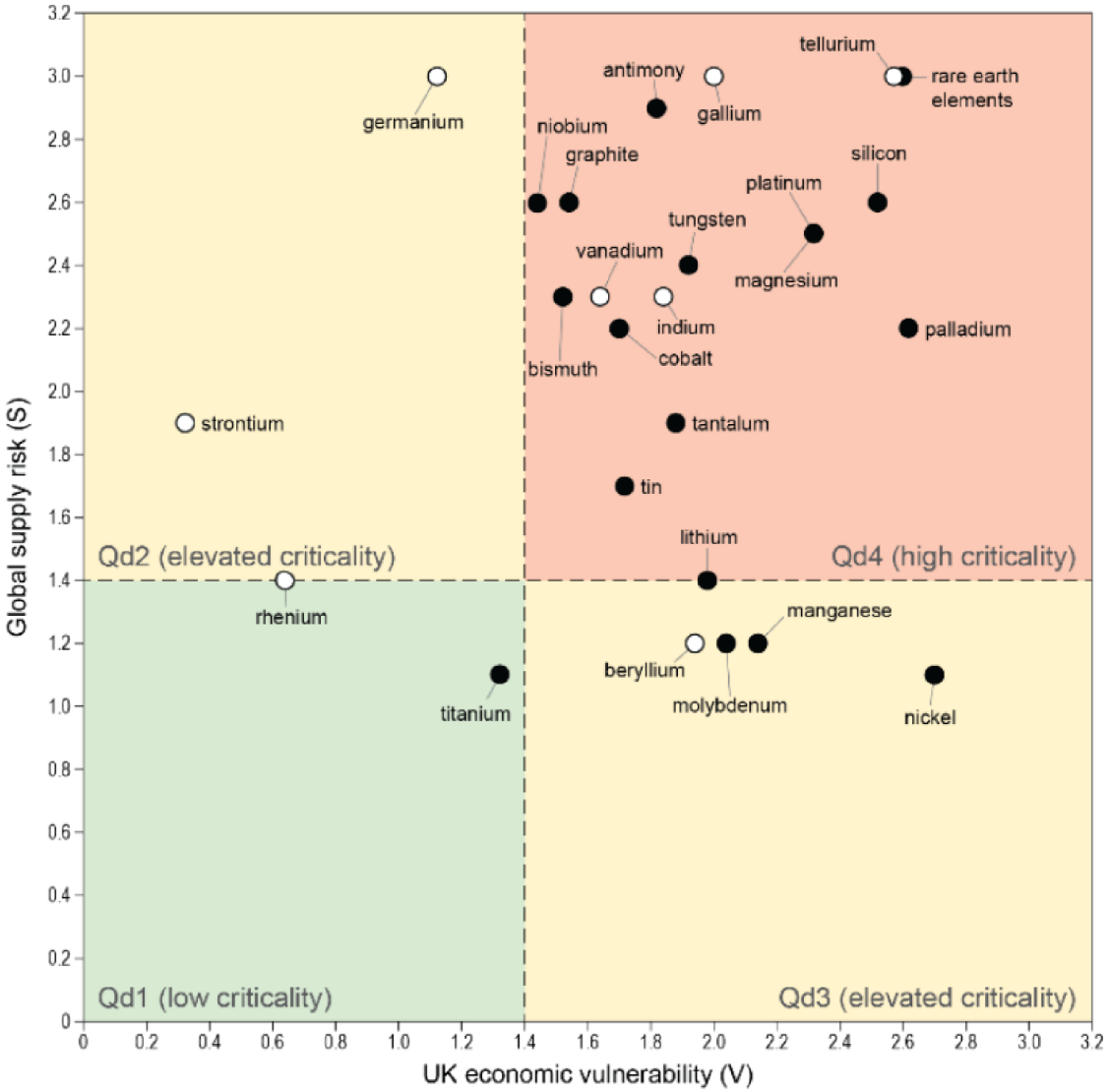

Figure 1. Assessment of 26 candidate materials potentially critical to the UK. The horizontal axis of the criticality matrix reflects the economic vulnerability of the UK. From Lusty et al. (2021).

There needs to be an immediate paradigm shift regarding Earth's finite resources and a focus on the material processing (Hofmann et al., 2018). Stegen (2015) dispels the common misconception that China is the only country with substantial REE deposits and draws attention to China's near-monopoly on the processing capacity and supply chain for converting the elements into products (Humphries, 2013). The geographical concentration of production and processing on mineral supply risk is further exacerbated by geopolitical disruption, such as China's export ban on REEs and Indonesia's ban on nickel ore export (Reuter, 2016).

More reserves of critical metals will need to be identified to meet the increasing demand for low-carbon technologies. Chukwuma et al. (2021) estimate between 490 and 640 million tonnes of slag may have been generated in the UK since 1875 alone. Together with the estimated over 190 million tonnes of legacy iron and steel slag at current and former iron and steel workings (Riley et al., 2020), the UK could improve the resilience of their critical metal supply chains As such, critical metal exploration should expand to existing mines to identify new prospects through comprehensive characterisation of the geologic source (Rabe et al., 2017). Without adequate metal resources and reserves, renewable

energy scenarios will be unachievable and greenhouse gas emissions will continue at distressing rates. It is now essential to improve CRM production, recycling (Grilli et al., 2017; Popov et al., 2021; Rizzo et al., 2020), and let CE potentially help drive the management and development of potentially innovative low-carbon solutions.

1.6 Carbon capture and storage

The carbon storage potential of slags is an increasingly promising opportunity. The drawdown and mineralisation of atmospheric CO_2 by legacy waste can contribute to the reduction of greenhouse gases. Riley et al. (2020) estimates a cumulative CO_2 capture potential of 57 to 138 Mt from the potential stockpiles of legacy iron and steel slag spanning the UK. From 10 legacy iron and steel slag sites in South Wales, (Chukwuma et al. (2021) estimate a CO_2 uptake potential of up to 17 Mt CO_2 by direct carbonation and up to 25 Mt CO_2 through enhanced weathering, yielding a total carbonation potential between 0 to 77 % of total carbonation potential. However, the limitation of carbonation reactions and management challenges for resource recovery will impact achieving these carbon uptake estimates. Carbonate precipitation is impacted by numerous factors including the source and frequency of water interaction (MacDonald et al., 2023a; Mayes et al., 2018; Wilson et al., 2009), mineralogy (Pullin et al., 2019), kinetic limitation (Khudhur et al., 2022; Mayes et al., 2018), and CO_2 supply (Renforth, 2019). With over one-third of legacy slag sites located in close proximity to designated conservation areas, and others near redeveloped for housing and urban cover, multifarious characterisation that informs resource recovery should be a priority (Riley et al., 2020).

1.7 Research objectives

This research aims to provide multifarious characterisation of legacy iron and steel slag to inform this industrial waste's valorisation and opportunity potential. CRM extraction is one of the many opportunities offered by legacy slag. However, likely physical and chemical changes through time could have implications for slag reuse. Before resource recovery methods can be developed, a thorough understanding of the processes altering deposits is needed to identify extraction challenges. Using the inland (A) and coastal (B) legacy slag deposits at Warton in South Lancashire, England as the case study sites, the research objectives are addressed over two studies. Chapters 2 and 3 detail the first and second studies, respectively. The first study demonstrates a novel workflow that informs environmentally sensitive metal recovery methods by helping correlate the chemical compositions associated with metallurgical processing methods to those identified in slag deposit A. The data-driven microstructural approach that leverages unsupervised machine learning reveals chemical and spatial associations that are quantified to determine the slag mineralogy and metal content. The observed lithification of slag deposit B that cemented originally loose pieces of slag together that could challenge metal extraction is explored in the second study. The mechanisms lithifying the slag deposit are identified to understand how legacy slag changed over time, to identify opportunities for atmospheric CO_2 storage and coastal defence, and to identify the challenges to slag reuse. Together, the results from this study provide new insights into the microstructural identification capabilities of machine learning for CRM recovery and characterise the lithification mechanisms that have implications for CCS.

2. Chapter 2: Uncovering the Mineralogy and Metal Concentrations in Metal Processing Wastes: A data-driven microstructural approach

2.1 Introduction

Legacy industrial waste presents the opportunity for CRM recovery and to understand how the resource potential changes through time. Although recent exploration has increased reserves of many energy transition metals, ore quality has declined as high-quality deposits and the higher-quality part of previously explored deposits are being exhausted (IEA, 2021). Growing climate risk and water stress are exposing the vulnerability of mining assets. Natural disasters are the third most frequent cause of mineral supply disruption, and the increased frequency and severity must motivate a focus on developing innovative metal recovery methods that are not resource-intensive and contribute to CE (Hatayama & Tahara, 2018; IEA, 2021).

The increasing discussions concerning CE in Europe have inevitably involved the metallurgy and mineral industries (Saikia et al., 2008; Spooren et al., 2020). Popov et al. (2021) urge securing the supply chain by developing own mining and recycling as a primary solution for addressing the CRM security problem. Given the declining quality of ore grade for many materials (Hudson-Edwards, 2016), leveraging the relative stratigraphy in legacy slag deposits reflecting metallurgical processing methods and their possible evolution over time (Humphris & Carey, 2016) could help focus resource recovery efforts. However, as demonstrated in Chapter 1, slags are extremely heterogeneous at multiple length scales with their metal content reflecting the ore mineralogy provided by the sulphides (Montour, 1994), the less reactive oxide and silicate minerals, the glass phases (Parsons et al., 2001), and/or the steel scrap (Piatak et al., 2015). Thus, quantification methods used to identify CRM from these industrial wastes must be able to handle the complex material and identify trace metal concentrations (< 0.01 wt%).

Scanning electron microscope (SEM) based characterisation by energy dispersive X-ray spectroscopy (EDS) is a widely used microanalytical technique to obtain elemental mapping (Goldstein et al., 2017). Microstructural analyses using EDS data is a core technique of characterisation as each measurement comprises all the characteristic X-ray peaks for the specified photon energy range (Newbury & Ritchie, 2015). However, commercial automatic peak identification procedures have been shown to fail at labelling ‘problem regions’ and misidentify coincidence peaks as minor or trace element peaks, despite proper calibration and reasonable input rates (Newbury, 2005, 2009). This is especially concerning with the increasing use of EDS data for critical material identification. It is evident from the increasing instances of elemental misidentification that minor and trace constitutes that have low counts per pixel and signals just above background are key challenges to these automatic peak identification algorithms (Newbury, 2005, 2007, 2009).

Similar signal characterisation and identification challenges to transmission electron microscope (TEM) of regions with variable phases occurring at different depths in the beam path (Jany et al., 2017) resulting in mixed signals (Rossouw et al., 2015) also affect

EDS data. While the interaction volume depth used for EDS mapping is roughly 1 μm (micron) (Tominaga et al., 2021), overlapping peaks from trace concentrations of small features that are spatially sparsely distributed in the dataset can contribute to mis- and incomplete identification. However, as datasets grow in size and complexity, using multivariate statical analysis (MSA) during processing is shown to reveal the most relevant information from microscopy and diffraction methods. MSA applications range from reducing data dimensionality (Duran et al., 2023; Georget et al., 2022; Martineau et al., 2019), isolating 'latent' variables (Keenan, 2009), unmixing signals from nanostructures (Jany et al., 2017), and enhancing the efficiency and accuracy of phase identification (Teng & Gauvin, 2020) to producing mineral phase distribution maps (Rossouw et al., 2015). Applying machine learning to geologic characterisation may allow for faster and more accurate pattern extraction (Rizzo et al., 2020) with reduced overall human intervention.

Many scanning electron-based automated mineralogy (SEM-AM) software packages (i.e., Mineral Liberation Analysis (MLA), Quantitative Evaluation of Material by Scanning Electron Microscopy (QEMSCAN), Tescan Integrated Mineral Analyzer (TIMA-X)) developed to characterise ore and mineral processing products (Schulz et al., 2020) are largely supervised machine learning methods that compare spectra to a labelled reference. While these techniques are promising, for novel applications, including artificial materials such as slags given the versatility for resolving chemical zonation, phase relationships, intra-particle details, full particle size, and geometries (Schulz et al., 2020), they require the user to know or assume what the phases present are. This presents the opportunity for significantly misfitting data as anthropogenic minerals lack robust databases. Furthermore, the element and mineral spectral maps produced by SEM-AM are semi-quantitative, limiting their utility for metal abundance estimations. Thus, characterisation methods that are developed for CRM recovery from anthropogenic material must be capable of handling these challenges and producing quantitative mineral maps. In this study, the capabilities of using a data-driven unsupervised machine learning approach were explored to identify the mineral phases, possible trace metal concentrations, and relative stratigraphy from a legacy slag deposit, aimed at informing resource potential and environmentally sensitive recovery methods.

2.2 Materials and methods

2.2.1 Site location

Remnants of the iron and steel produced by Carnforth Iron Works in South Lancashire, England are evident as slag banks on the southern edge of the Warton Saltmarsh and as a slag heap approximately 435 m inland. The iron works opened in 1864 producing solely haematite (Bessemer) iron pig, but at peak production, five blast furnaces and two Bessemer converters (established 1871: LCC (2006)) ran for steelmaking (Harris, 1960; Riden & Owen, 1995; Taylor, 2013). The steel plant closed in 1890 and was demolished by 1898 (LCC, 2006). However, iron works continued by the renamed Carnforth Hematite Iron Company Ltd using two blast furnaces from 1889 until closure in 1929 (LCC, 2006; Riden & Owen, 1995). The slag heap (Fig. 2) is underlaid by a raised tidal flat comprising clay, silt and glaciofluvial deposits of sand and gravel, and overlies the Urswick Limestone Formation (Taylor, 2013).

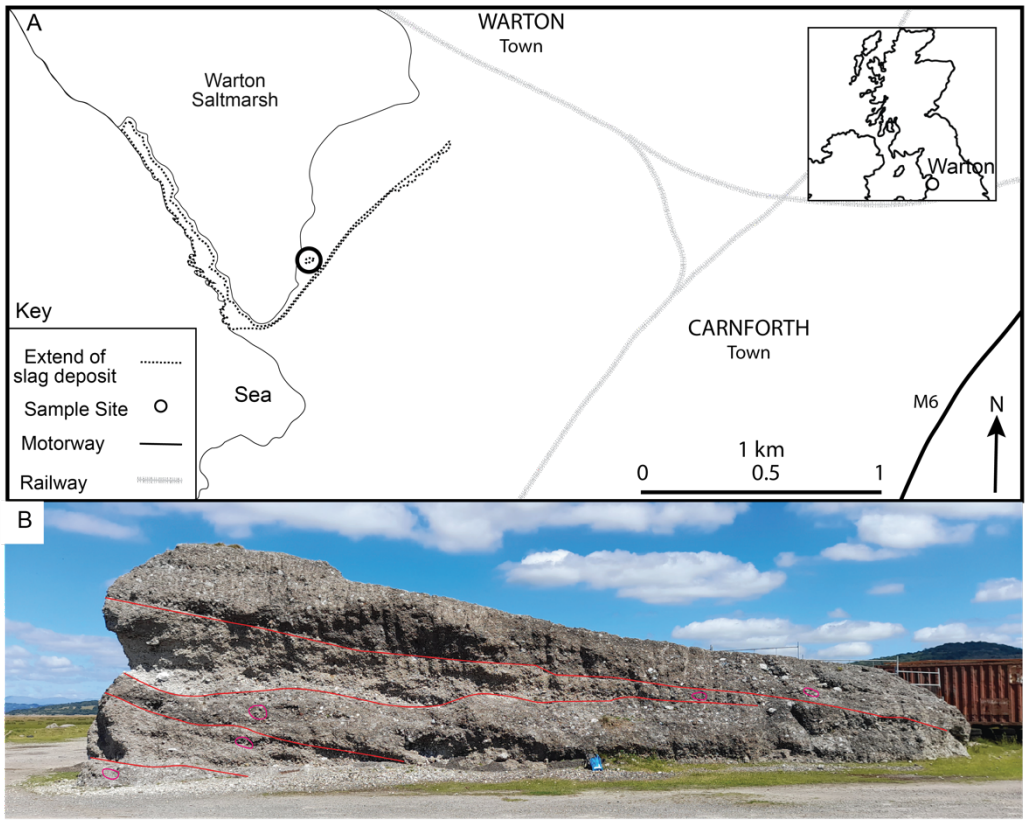

Figure 2. A) Location of sampling site in South Lancashire, England. B) Field photograph showing the inland slag deposit with the stratigraphic horizons and sampling locations outlined; 0.3 m blue tote bag for scale.

2.2.2 Optical microscopy and SEM-EDS data acquisition

Slag samples from the surface of the inland heap were collected across five vertical stratigraphic heights (Fig. 2B) from distinct layers. Stitched optical microscopy images of polished thin sections using a Zeiss Axio Imager M2 at 10x magnification in plain polarised reflected light informed SEM-EDS analysis (Fig. S1 to S5). Backscatter Electron (BSE) imaging and EDS chemical mapping were performed on the polished thin sections with a ~20 nm conductive carbon layer using a Zeiss Sigma variable pressure field-emission-gun SEM (VP-FEG SEM) equipped with a BSE detector and an Oxford Instruments Ultimax 170 mm^2 EDS detector at the Geoanalytical Electron and Microscopy and Spectroscopy (GEMS) facility at the School of Geographical and Earth Sciences, University of Glasgow. Twenty-three regions were identified from petrographic analysis to represent the range of microstructures and textures in the five stratigraphic horizons (W24, W25, W26, W27, W28). The various textures include slag clast matrix with and without pores, reaction rims occurring with (TM) and without (T) metal grains, and metal-dominated microstructures (M). The EDS maps collected from the twenty-three regions were analysed with Oxford Instrument AZtec ® 4.3 and AZtec ® Flex software. When multiple data tiles were acquired for a single region they were stitched and montaged into a single file.

It has been shown that high-count EDS spectra (five million or more counts per pixels (cpp)) can be used to match Wavelength-dispersive X-ray spectroscopy (WDS) measurements even with severe peak interference for major and minor constituents (Ritchie et al., 2012). However, achieving higher cpp it is at the expense of reduced spectral resolution, impacting the spectral data quality. Therefore, the SEM and EDS settings used for data collection (Table 1) aimed at collecting at least 800 cpp, limiting

possible surface damage and drift by the instrument, and completion within a reasonable time. An accelerating voltage of 20 keV, aperture size of 60 and 120 micrometre (μm), dwell time between 25 to 30 μs, process time of 3, frame count of 100, and working distance of 8.0, and 8.1 millimetre (mm) were used to collect the EDS data spanning 2048 energy channels.

Table 1. SEM and EDS settings used for data collection.

Sample		SEM settings			
Stratigraphic horizon	Region	Accelerating voltage (keV)	Aperture size (μm)	Dwell time (μs)	Energy channels
W28	T1	20	120	30	2048
	M1	20	120	30	2048
	T2M2	20	120	30	2048
	T3M3	20	120	30	2048
W27	T1M1	20	120	30	2048
	T2M2	20	120	30	2048
	M3	20	120	30	2048
	M4	20	120	30	2048
W26	T1	20	60	25	2048
	T3	20	60	25	2048
	T4	20	60	25	2048
	T5M2	20	60	25	2048
	T6.1	20	60	25	2048
	T6.2M3	20	60	25	2048
	M4	20	60	25	2048
W25	T1	20	120	30	2048
	M1	20	120	30	2048
	M2	20	120	30	2048
W24	T1	20	60	25	2048
	T2	20	60	25	2048
	M1	20	60	25	2048
	T3M2	20	60	25	2048
	T4	20	60	25	2048

Sample		SEM settings			
Stratigraphic horizon	Region	Process Time	Frame count	Working distance (mm)	Magnification
W28	T1	3	100	8.1	700
	M1	3	100	8.1	700
	T2M2	3	100	8.1	700
	T3M3	3	100	8.1	700
W27	T1M1	3	100	8.1	700
	T2M2	3	100	8.1	700
	M3	3	100	8.1	700
	M4	3	100	8.1	700
W26	T1	3	100	8	700
	T3	3	100	8	700
	T4	3	100	8	700
	T5M2	3	100	8	700
	T6.1	3	100	8	600
	T6.2M3	3	100	8	600
	M4	3	100	8	600
W25	T1	3	100	8.1	700
	M1	3	100	8.1	700
	M2	3	100	8.1	700
W24	T1	3	100	8	700
	T2	3	100	8	700
	M1	3	100	8	650
	T3M2	3	100	8	700
	T4	3	100	8	700

Sample		EDS Map					
Stratigraphic horizon	Region	File size (byte)	Resolution width (pix)	Resolution height (pix)	Width (μm)	Height (μm)	Total count
W28	T1	186	512	384	416	312	$2.3x10^8$
	M1	186	512	384	416	312	$3.3x10^8$
	T2M2	186	587	785	792	591	$4.2x10^8$
	T3M3	186	512	384	416	312	$2x10^8$
W27	T1M1	186	972	729	790	592	$8.9x10^8$
	T2M2	186	972	729	790	592	$9.8x10^8$
	M3	186	584	631	785	587	$4.5x10^8$
	M4	186	512	384	416	312	$3.2x10^8$
W26	T1	186	512	384	416	312	$2x10^8$
	T3	186	512	384	416	312	$1.7x10^8$
	T4	186	512	384	416	312	$1.6x10^8$
	T5M2	186	512	384	416	312	$1.2x10^8$
	T6.1	186	981	720	797	585	$5.2x10^8$
	T6.2M3	186	512	384	485	364	$1.4x10^8$
	M4	186	512	384	485	364	$1.7x10^8$
W25	T1	186	512	384	416	312	$2.8x10^8$
	M1	186	511	729	415	592	$4.6x10^8$
	M2	186	397	1068	423	868	$6.3x10^8$
W24	T1	186	512	384	416	312	$2x10^8$
	T2	186	960	725	786	589	$4.8x10^8$
	M1	186	929	1059	851	929	$4.9x10^8$
	T3M2	186	512	384	416	312	$1.4x10^8$
	T4	186	1873	386	1520	314	$4.x10^8$

Sample		EDS Map	EDS Image				
Stratigraphic horizon	Region	Counts per pixel	Resolution width (pix)	Resolution height (pix)	Area (pix)	Pixel size (µm)	Width (µm)
W28	T1	1162	1024	768	786432	0.406	416
	M1	1676	1024	768	786432	0.406	416
	T2M2	922	1950	1454	2835300	0.406	792
	T3M3	1036	1024	768	786432	0.406	416
W27	T1M1	1253	1945	1459	2837755	0.406	790
	T2M2	1387	1945	1459	2837755	0.406	790
	M3	1222	1932	1444	2789808	0.406	785
	M4	1644	1024	768	786432	0.406	416
W26	T1	1007	1024	768	786432	0.406	416
	T3	869	1024	768	786432	0.8125	416
	T4	839	1024	768	786432	0.8125	416
	T5M2	635	512	384	196608	0.8125	416
	T6.1	751	1962	1440	2825280	0.406	797
	T6.2M3	697	512	384	196608	0.94792	485
	M4	844	512	384	196608	0.947	485
W25	T1	1427	1024	768	786432	0.406	416
	M1	1230	1024	1459	1494016	0.406	416
	M2	1479	1043	2136	2227848	0.406	423
W24	T1	1030	512	384	196608	0.8125	416
	T2	691	1934	1450	2804300	0.406	786
	M1	499	2125	1944	4131000	0.4375	851
	T3M2	713	512	384	196608	0.8125	416
	T4	810	773	3747	2896431	0.406	1520

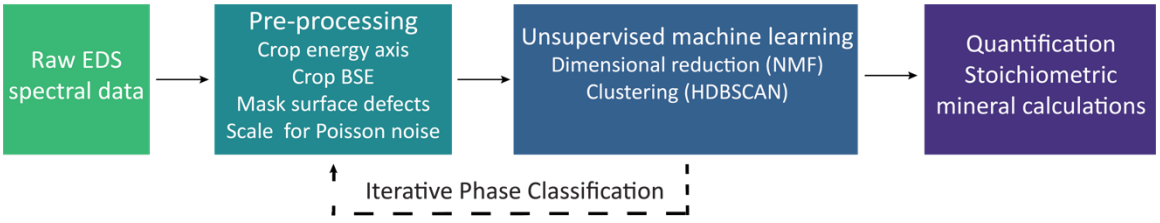

Figure 3. Analytical approach workflow. EDS spectral data is collected and pre-processed. The dimensionality of the data is reduced and the resulting components are clustered. The outliers or segmented regions may be isolated and the full approach reiterated.

2.2.3 Pre-processing

The energy axis of the raw EDS maps must be calibrated and any potential edge artefacts removed. For visualisation purposes, cropping and reshaping the BSE images to the same x and y dimensions as the calibrated EDS maps improve the interpretability of cluster phase maps when underlain. EDS does not obey Gaussian statistics as the quality of a spectral peak is a function of the dwell time on a single pixel. Instead, EDS data obey Poisson statistics where variation results from counting errors. To account for these errors, a Poisson noise scaling was applied (Keenan & Kotula, 2004). The porous nature of slag is accounted for by creating a pore space mask that excludes these regions that provide no mineralogic or elemental information of the sample. The pore space mask was created by

manually thresholding the corresponding BSE image of a given sample (Khudhur et al., 2024).

2.2.4 Dimensional reduction

Each energy channel of the X-ray spectra represents a single experimental dimension. With over 1000 dimensions per measurement, each EDS map becomes a dense collection of measurements. To simplify this problem, a variety of dimensional reduction tools are explored, including Principal Component Analysis (PCA), Non-negative matrix factorisation (NMF), and Factor Analysis (FA). The quality and interpretability of these algorithms were investigated on the W24 and W26 samples. The dimensional reduction step reduces the EDS phase analysis to a smaller set of dimensions that are now representative of the mineralogy. It is also crucial for the subsequent clustering step to avoid suffering the 'Curse of Dimensionality' (Duran et al., 2023) due to the exponentially increasing volume of data space from additional components. NMF was used to reduce the dimensionality of the spectral data from the remaining three horizons (W25, W27, W28), and the resulting NMF components from all horizons were clustered.

The unique constraints of each algorithm yield reduced components representing the original data in different forms. For example, besides reducing noise, the resulting principal component vectors of PCA maintain high variance through an orthogonal transformation (Wilkinson et al., 2019). While PCA has been used to directly distinguish particles with different morphologies and recover chemical compositions in EDS maps (Genga et al., 2012; Saghi et al., 2016), the principal component vectors are not physically interpretable because of the orthogonality constraint (Potapov, 2016). Conversely, the resulting statistically independent unmixed components from using NMF directly represent the original data structure (de La Peña et al., 2011). Unlike PCA, NMF only allows additive combinations and prevents subtraction in the matrix factors, resulting in nonnegativity components (Lee & Seung, 1999). It is from these components that Teng & Gauvin (2020) determined NMF is more suitable for EDS mapping of samples with rare earth-bearing minerals due to the smaller signal reduction compared to that from PCA. Smaragdis et al. (2014) note the NMF components correspond well to the mineral phases and components from the original data, and Jany et al. (2017) even successfully recovered the quantitative composition and nanostructures of metal alloy nanowires using a machine learning NMF-based processing. Alternatively, FA focuses on explaining the correlation within the data structure. Using the 'VARIMAX solution' which applies a rotation on the orthogonal vectors derived from PCA can benefit segmentation as it seeks single basic vectors that represent the spectral data (Wilkinson et al., 2019).

The appropriate number of components to reduce the EDS data was determined qualitatively using the scree test of the eigenvalues (Duran et al., 2023; Jany et al., 2017) in the HyperSpy library (de la Pẽna et al., 2023) and cross-referencing against the noise in the factor spectra and loading maps EDS data (Fig. 4).

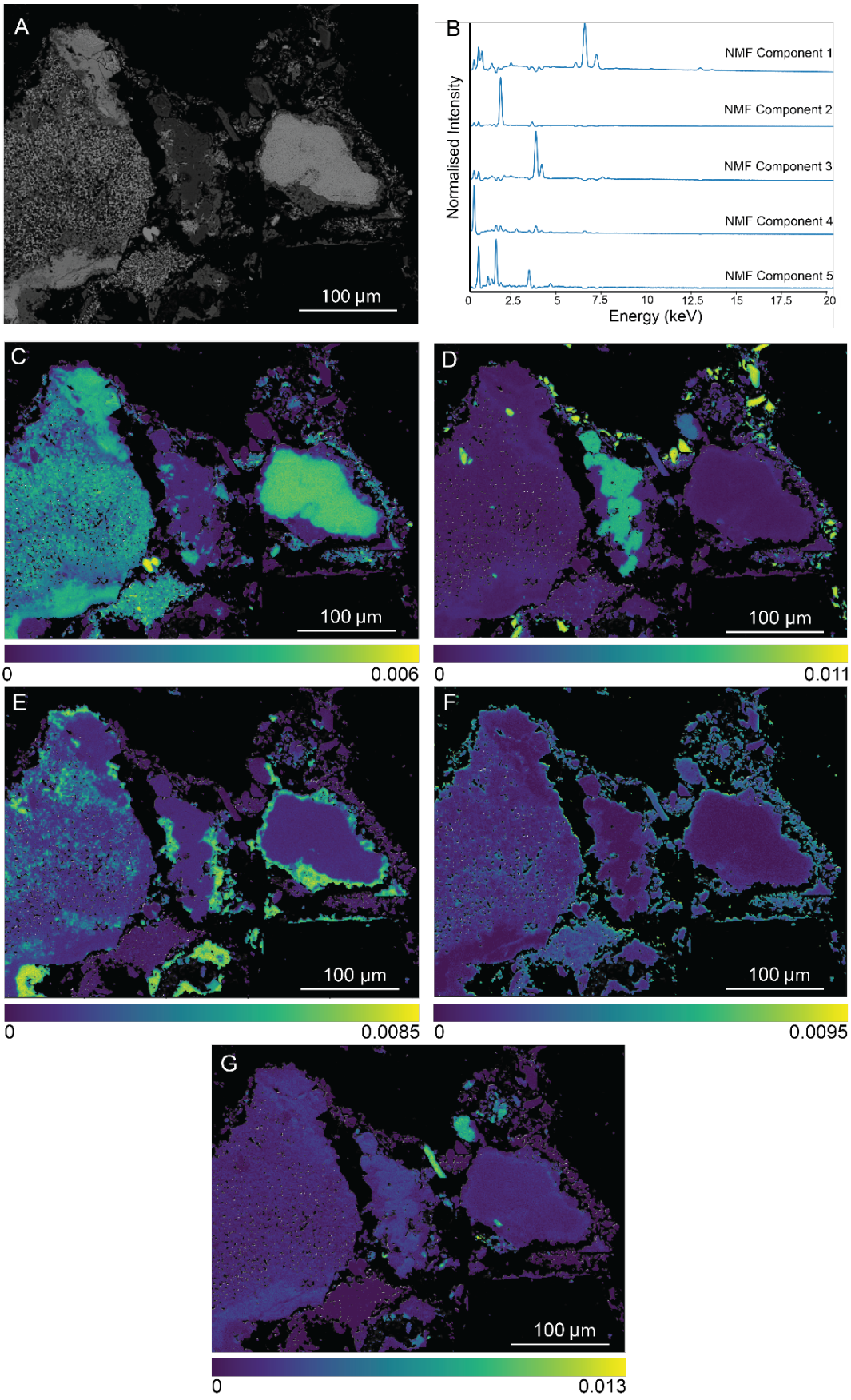

Figure 4. Dimensional reduction of region W26_T5M2 through NMF. A) BSE image. B) Chemical signature of each NMF factor. C-G) NMF loadings showing the regions where the components 1-6 are present in the sample. Pixel brightness demonstrates a stronger contribution of the spectra described by the NMF component.

Clustering is commonly used to answer questions related to the underlying structures in data but it suffers from central limitations where all data becomes equidistant when the data space becomes greater than 10 (i.e. large numbers of correlated measurements) (Koch, 2013). Thus, to identify the mineral phases and determine their quantitative compositions from the original high dimensional EDS data (2048 channels/dimensions), the clustering algorithm, Hierarchical Density-Based Spatial Clustering of Applications with Noise (HDBSCAN) was used. The components identified from preliminary NMF analysis were used to form a reduced dimensional space and then were clustered. Without prior knowledge of the data structure required in flat clustering (i.e., number of clusters), hierarchical clustering splits the data into smaller subsets until each consists of one object. The capability of HDBSCAN to determine the optimal number of clusters, identify clusters with a range in point densities (Campello et al., 2013; Campello et al., 2015; McInnes et al., 2017) and that are nested (Sander et al., 2003) resolves challenges from limited domain knowledge of legacy wastes, enabling mineral phases with varying concentrations or that formed from solid solution to be identified. Furthermore, HDBSCAN is capable of separating outlier data points using the Global-Local Outlier Scores from Hierarchies (GLOSH) algorithm by effectively and efficiently computing GLOSH scores from the HDBSCAN hierarchy based on statistical interpretation, unsupervised (Campello et al., 2015).

NMF was determined as the superior dimensional reduction algorithm for this data to cluster on. The non-negative constrains of NMF that results in components directly representing the sample is preferred given the aim of this study is to correlate the chemical data to the microstructure that they are associated with. The complete approach comprising pre-processing, dimensional reduction using only NMF, and clustering was performed on the spectral data from regions spanning the remaining stratigraphic horizons (W25, W27, W28). Based on the mineral phases where trace metals were identified from the first iteration on horizons W24 and W26, the regions analysed from horizons W25, W27, and W28 focus on: 1) where phases with high contrasting densities on the BSE image occurred together; and 2) where higher density grains less than 1000 μm localised around the edge of pore space.

2.2.5 Standardless Quantification and Stoichiometric Mineral Phase Calculations

Using HyperSpy (de la Pẽna et al., 2023), summed spectra of the hard cluster assignments were exported and the standardless quantification peak-to-background method (P/B-ZAF) using Bruker ESPRIT software was performed. Elements with > 0.45 wt% (above background which serves as the detection limit for the method) identified from both the auto-ID function and by manual selection were included in the stoichiometric mineral calculations which follow Appendix 1 in Deer et al. (2013) and used to label the mineral phase maps. Calculated mineral phases that did not correspond to those reported in iron and steel slag were named based on their chemical composition.

2.2.6 Iterative Phase Classification

Clusters from the mapped regions representing either > 30 % of the pixels of the EDS map, a mineral phase (total image pixels – surface deviation mask pixels) or that were identified

from visual inspection despite some clusters comprising <30 % of the EDS map pixels or the phase pixels (W28_M1, W26_T3, W26_T5M2), were used as a mask of the raw data for iterative phase calculation (IPC) on specific phases. These new isolated spectral datasets were pre-processed, dimensionally reduced using NMF, and clustered with HDBSCAN to create hard cluster assignments. The standardless quantification and mineral phase calculation approach described above were subsequently reapplied to these iterated clusters. Through the process of IPC, minor phases and solid solutions are identified.

2.3 Results

2.3.1 First Iteration

2.3.1.1 Dimensional reduction and clustering

Using the approach outlined above, the mineral phases represented in the five stratigraphic horizons of slag we identified and quantified, in addition to trace concentrations of metals. The clustering using HDBSCAN resulted in between four to seven, four to eight, three to nine, three to seven, and four to seven clusters in the regions from W28, W27, W26, W,25, and W24, respectively. Outliers range from 0.21 % (W27_T1) of the segmented mineral phase (EDS map pixels – mask pixels) pixels to 72.60 % (W24_T1) with averages of 20.78 %, 23.7 %, 15.29 %, 33.00%, and 39.06 % for W28, W27, W26, W25, and W24, respectively. When the outliers represent either > 30 % of the EDS map pixels or > 30 % of the segmented mineral phase pixels, IPC was applied to investigate possible microstructures that were over segmented. The outliers represent > 30 % of the pixels in both the EDS map and the segmented mineral phases for five regions, whereas they comprise < 30 % of the pixels in both the EDS map and mineral phases for thirteen regions.

The average cpp of the phase maps ranges from 499 (W24_M1) to 1676 (W28_M1) with averages of 1253, 1007, 806, 1378, and 749 for W28, W27, W26, W,25, and W24, respectively. Of the 12 regions with cpp exceeding 1000, five record outliers with > 30 % of both the EDS map pixels and the segmented mineral phase pixels (W28_T1, W27_T2M2, W25_T1, W25_M1, W24_T1), and five with outliers < 30 % of both the EDS map pixels and the segmented mineral phase pixels (W28_T3M3, W27_T1M1, W27_M4, W26_T1, W24_M2).

2.3.1.2 Quantification and identification

Various mineral phases are represented in the five stratigraphic horizons (Table 2 to 24). The mineral abundances are calculated as the percentage of the segmented mineral phase. The table symbols are defined as: - = low quantification results; * = mineral phase with IPC applied.

Table 2. Mineral phases and chemical formulas for sample W28_T1.

Mineral	Chemical composition	Mineral abundance (%)
Wollastonite	$Ca_{0.6}Si_{1.1}O_3$	1
Ca-oxide	CaO	10
Ca-Si-S	$CaSi_{0.5}S_{1.2}O_4$	23
Ca-Si	$Ca_{3.5}Si_{0.2}O_4$	21
Ca-Mg-Si-S*	$Ca_{2.9}Mg_{1.6}SiS_{0.3}O_7$	45
Iterative Phase Classification		
Ca-oxide	CaO	6
Ca-Al-Fe-Si-S	$CaAl_{0.3}Fe_{0.1}Si_{1.3}S_{0.5}O_5$	59
Ca-Al-Fe-Si-S	$CaAl_{0.7}Fe_{0.7}Si_{1.5}S_{0.5}O_7$	35

Symbol: * = mineral phase with IPC applied

Table 3. Mineral phases and chemical formulas for sample W28_M1.

Mineral	Chemical composition	Mineral abundance (%)
Anorthite	$CaAl_{1.5}Si_2O_8$	2
Fe-oxide	FeO	17
Pyrite	FeS_2	2
Fe-S	$Fe_{0.9}S_{0.1}O$	43
Fe-oxide	FeO	25
Fe-oxide*	Fe_2O_3	11
Iterative Phase Classification		
Fe-oxide	Fe_2O_3	3
Fe-S	$Fe_{1.8}S_{0.2}O_3$	82
Ca-Al-Fe-Si-S	$Ca_{0.2}Al_{0.2}Fe_2Si_{0.6}S_{0.7}O_5$	15

Symbol: * = mineral phase with IPC applied

Table 4. Mineral phases and chemical formulas for sample W28_T2M2.

Mineral	Chemical composition	Mineral abundance (%)
Fe-oxide	FeO	4
Fe-oxide	Fe_2O_3	4
Anhydrite	$CaSO_4$	1
Melilite	$Ca_{1.3}Al_{1.8}Si_{1.3}O_7$	3
-	-	
Ca-oxide	CaO	56
Melilite*	$Ca_2(Mg_{0.2}Al_{0.6})Si_{1.4}O_7$	32
Iterative Phase Classification		
Ca-Si-S	$Ca_{0.8}Si_{0.2}S_{1.3}O_4$	1
Ca-Al-Si-S	$Ca_2Al_{0.1}Si_{0.6}S_{0.3}O_4$	22
Melilite	$Ca_{1.7}(Mg_{0.2}Al_{0.7})Si_{1.5}O_7$	77

Symbol: - = Low quantification results; * = mineral phase with IPC applied.

Table 5. Mineral phases and chemical formulas for sample W28_T3M3.

Mineral	Chemical composition	Mineral abundance (%)
Fe-oxide	FeO	5
Anorthite	$Ca_{1.2}Al_{2.3}Si_{1.6}O_8$	6
Ca-Al-Si-S	$Ca_3Al_{0.4}Si_2S_{0.1}O_8$	64
Ca-Al-Fe-Si	$CaAlFe_{0.4}Si_2O_7$	2

Table 6. Mineral phases and chemical formulas for sample W27_T1M1.

Mineral	Chemical composition	Mineral abundance (%)
Quartz	SiO_2	3
Ca-Al-Si-S	$CaAl_{0.3}Si_{0.4}S_{1.2}O_4$	3
Fe-Si	$Fe_{0.7}Si_{0.1}O$	42
Ca-Al-Si	$Ca_{0.8}Al_2Si_{0.6}O_5$	3
Ca-Al-Si-S	$CaAl_{1.2}Si_{2.3}S_{0.3}O_8$	3
Melilite	$Ca_{1.5}(Mg_{0.2}Al_{0.8})(Si_{0.4}Al_{0.6})SiO_7$	4
Ca-Al-Fe-Si-S	$Ca_{2.8}Al_{0.2}Fe_{0.1}Si_{0.6}S_{0.4}O_5$	38
Ca-Al-Mg-Fe-Si-S	$CaAl_{0.7}Mg_{0.1}Fe_{0.5}SiO_5$	4

Table 7. Mineral phases and chemical formulas for sample W27_T2M2.

Mineral	Chemical composition	Mineral abundance (%)
Calcio-wüstite	$Ca_{0.3}Fe_{0.7}O$	11
Wollastonite	$Ca_{0.9}Si_{0.9}O_3$	1
Quartz	SiO_2	1
Ca-oxide	$Ca_{0.8}O$	6
Anorthite	$Ca_{1.3}Al_{1.5}Si_2O_8$	28
Quartz	SiO_2	2
Ca-Al-Mg-Fe-Si*	$CaAl_{0.6}Mg_{0.3}Fe_{0.6}Si_2O_7$	51
Iterative Phase Classification		
Fe-Si-S	$Fe_{0.5}Si_{0.1}S_{2.8}O_5$	1
Ca-Al-Mg-Fe-Si	$CaAl_{0.6}Mg_{0.3}Fe_{0.6}Si_2O_7$	97
Ca-Al-Mg-Fe-Si-S	$Ca_{0.5}Al_{0.3}Mg_{0.2}FeSi_{1.1}S_{1.6}O_7$	2

Symbol: * = mineral phase with IPC applied

Table 8. Mineral phases and chemical formulas for sample W27_M3.

Mineral	Chemical composition	Mineral abundance (%)
Fe-oxide	$Fe_{0.9}O$	10
-		-
Fe-oxide	$Fe_{1.9}O_3$	53
-		-
Ca-Fe-Si-S	$Ca_{0.2}Fe_{2.1}Si_{0.2}S_{0.1}O_4$	36

Symbol: - = Low quantification results

Table 9. Mineral phases and chemical formulas for sample W27_M4.

Mineral	Chemical composition	Mineral abundance (%)
Native Fe	Fe	28
Native Fe	Fe	68
Pyrite	FeS_2	1
Fe-Si-S	$Fe_2Si_{1.3}SO_6$	3

Table 10. Mineral phases and chemical formulas for sample W26_T1.

Mineral	Chemical composition	Mineral abundance (%)
Melilite	$Ca_{1.8}Al_1Si_{1.6}O_7$	1
Ca-Al-Si-S	$Ca_2Al_{0.4}SiS_{2.1}O_8$	8
Melilite*	$Ca_{1.4}Al_{0.7}Si_{1.5}SO_7$	91
	Iterative Phase Classification	
Melilite	$Ca_{1.6}(Mg_{0.2}Al_{0.8})(Al_{0.6}Si_{0.4})SiO_7$	31
Melilite	$Ca_2(Mg_{0.1}Al_{0.5})Si_{1.9}O_7$	13
Melilite	$Ca_{1.7}(Mg_{0.1}Al_{0.9})Si_{1.7}O_7$	56

Symbol: * = mineral phase with IPC applied

Table 11. Mineral phases and chemical formulas for sample W26_T3.

Mineral	Chemical composition	Mineral abundance (%)
Ca-Al-Si-S	$Ca_{0.4}Al_{0.1}Si_{2.6}S_{0.1}O_6$	1
Melilite	$Ca_2(Mg_{0.1}Al_{0.9})Si_{1.7}O_7$	73
Ca-Al-Si-S	$Ca_{0.9}Al_{0.2}Si_{0.6}SO_4$	23
Ca-Al-Si-S	$Ca_{0.9}Al_{0.2}Si_{0.3}S_{1.4}O_4$	1
Ca-Al-Si-S	$CaSi_{1.4}Al_{0.3}S_{1.1}O_5$	2

Table 12. Mineral phases and chemical formulas for sample W26_T4.

Mineral	Chemical composition	Mineral abundance (%)
Quartz	SiO_2	1
Olivine	$(Fe_{0.6}Ca_{0.5})Si_{1.2}O_4$	1
Ca-Al-Mg-Si-S*	$Ca_2Al_{0.9}Mg_{0.1}Si_{1.5}S_{0.3}O_7$	97
Ca-Al-Mg-Fe-Si-S	$CaAl_{0.4}Mg_{0.1}Fe_{0.1}Si_{2.2}S_{0.5}O_7$	1
Iterative Phase Classification		
Ca-Al-Si-S	$Ca_{0.9}Al_{0.2}Si_{0.7}S_{0.9}O_4$	1
Ca-Al-Mg-Si	$CaAl_{0.4}Mg_{0.5}Si_{1.4}O_5$	1
Melilite	$Ca_{1.5}(Mg_{0.1}Al_{0.9})(Al_{0.3}Si_{0.7})SiO_7$	57
Ca-Al-Si-S	$Ca_{2.2}Al_{0.2}Si_{0.7}S_{0.6}O_5$	30
Melilite	$Ca_{1.7}(Mg_{0.2}Al_{0.7})Si_{1.6}O_7$	11

Symbol: * = mineral phase with IPC applied

Table 13. Mineral phases and chemical formulas for sample W26_T5M2.

Mineral	Chemical composition	Mineral abundance (%)
Ca-Al-Fe-Si	$Ca_{0.1}Al_{0.8}Fe_{0.2}Si_{1.1}O_4$	1
Quartz	SiO_2	6
Quartz	SiO_2	4
Ca-Al-Mg-Fe-Si*	$Ca_{0.9}Al_{0.3}Mg_{0.2}Fe_{2.3}SiO_6$	64
Olivine	$(Fe_{1.7}Ca_{0.2})SiO_4$	7
Ca-Al-Fe-Si	$CaAl_{0.5}FeSi_2O_7$	18
Iterative Phase Classification		
Ca-Al-Fe-Si	$Ca_2Al_{0.2}Fe_{0.3}Si_{0.6}O_4$	8
Ca-Al-Mg-Mn-Fe-Si	$Ca_{0.5}Al_{0.2}Mg_{0.1}Mn_{0.1}Fe_{1.5}Si_{0.7}O_5$	19
Ca-Al-Fe-Si	$Ca_{0.3}Al_{0.2}Fe_{2.2}Si_{0.5}O_4$	20
Ca-Al-Mg-Mn-Fe-Si-S	$CaAl_{0.3}Mg_{0.2}Mn_{0.1}Fe_{2.2}Si\ S_{0.1}O_6$	53

Symbol: * = mineral phase with IPC applied

Table 14. Mineral phases and chemical formulas for sample W26_T6.1.

Mineral	Chemical composition	Mineral abundance (%)
Ca-Al-Si-S	$CaAl_{0.2}Si_{0.6}S_{1.9}O_6$	1
Calcite	$CaCO_3$	38
Ca-Al-Si	$Ca_{1.3}Al_{0.3}Si_2O_6$	1
Ca-Al-Mg-Si	$Ca_{0.9}Mg_{0.3}Al_{0.4}Si_{2.6}O_7$	1
Melilite	$Ca_{1.5}(Mg_{0.2}Al_{0.8})(Si_{0.5}Al_{0.5})Si_{1.1}O_7$	21
Melilite*	$Ca_{1.6}(Mg_{0.2}Al_{0.6})Si_{1.8}O_7$	38
Iterative Phase Classification		
Ca-Si-S	$Ca_{0.8}Si_2S_{0.1}O_5$	1
Ca-Al-Si-S	$Ca_{1.9}Al_{0.1}Si_{0.9}S_{0.1}O_4$	1
Ca-Al-Mg-Si	$CaAl_{0.6}Mg_{0.2}Si_2O_6$	60
Ca-Al-Si-S	$CaAl_{0.3}SiS_{0.3}O_4$	38

Symbol: * = mineral phase with IPC applied

Table 15. Mineral phases and chemical formulas for sample W26_T6.2M3.

Mineral	Chemical composition	Mineral abundance (%)
Olivine	$(Fe_{1.6}Ca_{0.4})(Si_{0.7}Al_{0.3})O_4$	1
Quartz	SiO_2	11
Olivine	$(Ca_{1.1}Mg_{0.4})Si_{1.2}O_4$	1
Monticellite	$Ca_{1.6}Mg_{0.7}Si_{0.6}O_4$	1
Ca-Al-Mg-Si	$Ca_{0.5}Al_{0.5}Mg_{0.6}Si_2O_6$	1
Wollastonite	$Ca_{0.7}Mg_{0.3}SiO_3$	1
Calcite	$CaCO_3$	25
Melilite	$Ca_{1.4}(Mg_{0.2}Al_{1.3})Si_{1.6}O_7$	20
Melilite*	$Ca_{1.3}(Mg_{0.2}Al_{0.8})Si_{1.9}Al_{0.1}O_7$	39
Iterative Phase Classification		
Quartz	SiO_2	1
Ca-Al-Mg-Fe-Si	$CaAl_{0.8}Mg_{0.2}Fe_{0.3}Si_{1.7}O_6$	87
Ca-Al-Mg-Fe-Si	$Ca_{0.9}AlMg_{0.2}Fe_{0.6}Si_{2.2}O_8$	12

Symbol: * = mineral phase with IPC applied

Table 16. Mineral phases and chemical formulas for sample W26_M4.

Mineral	Chemical composition	Mineral abundance (%)
Calcio-wüstite	$Ca_{0.1}Fe_{0.5}O$	2
Melilite	$Ca_2(Mg_{0.1}Al_{0.7})Si_{1.7}O_7$	59
Ca-Al-Si-S	$Ca_{0.8}Al_{0.1}Si_{0.3}S_{1.6}O_4$	1
Ca-Al-Si-S	$Ca_{0.8}Al_{0.2}Si_{0.4}S_{1.6}O_4$	1
Calcite	$CaCO_3$	30
Ca-Al-Fe-Si-S	$CaAl_{0.2}Fe_{0.1}Si_{0.7}S_{0.7}O_4$	7

Table 17. Mineral phases and chemical formulas for sample W25_T1.

Mineral	Chemical composition	Mineral abundance (%)
Ca-oxide	CaO	47
Larnite	$Ca_{2.2}Si_{0.8}O_4$	1
Ca-oxide*	$Ca_{0.8}O$	52
	Iterative Phase Classification	
Quartz	SiO_2	1
Melilite	$Ca_{1.6}(Mg_{0.1}Al_{0.9})Si_{1.6}O_7$	98
Ca-Al-Fe-Si-S	$Ca_{0.5}Al_{0.3}Fe_{0.1}Si_2SO_4$	

Symbol: * = mineral phase with IPC applied

Table 18. Mineral phases and chemical formulas for sample W25_M1.

Mineral	Chemical composition	Mineral abundance (%)
Quartz	SiO_2	3
Ca-oxide	$Ca_{0.8}O$	52
Ca-oxide	$Ca_{0.9}O$	5
Ca-oxide	CaO	2
Ca-Si*	$Ca_{0.7}Si_{0.1}O$	38
	Iterative Phase Classification	
Melilite	$Ca_{1.6}(Mg_{0.2}Al_{0.8})(Al_{0.8}Si_{0.2})(Si_{1.2})O_7$	21
Ca-Al-Fe-Si	$Ca_2Al_{0.2}Fe_{0.4}Si_{0.6}O_4$	1
Melilite	$Ca_{1.9}(Mg_{0.1}Al_{0.9})(Al_{0.1}Si_{0.9})Si_{0.6}O_7$	77

Symbol: - = Low quantification results; * = mineral phase with IPC applied

Table 19. Mineral phases and chemical formulas for sample W25_M2.

Mineral	Chemical composition	Mineral abundance (%)
Fe-oxide	$Fe_{0.9}O$	59
Ca-Si-S	$Ca_{1.1}Si_{0.1}S_{2.4}O_5$	1
Anorthite	$Ca_{1.5}Al_{1.4}Si_2O_8$	2
Ca-oxide	$Ca_{0.9}O$	29
Ca-Al-Fe-Si-S	$Ca_2Al_{0.7}Fe_{0.1}Si_{1.7}S_{0.8}O_8$	9

Table 20. Mineral phases and chemical formulas for sample W24_T1.

Mineral	Chemical composition	Mineral abundance (%)
Melilite	$Ca_2(Mg_{0.1}Al_{0.9})(Al_{0.6}Si_{0.4})SiO_7$	21
Melilite	$Ca_2(Mg_{0.1}Al_{0.7})Si_2O_7$	1
Rankinite	$Ca_{2.3}Si2O_7$	6
Melilite*	$Ca_{2.3}(Mg_{0.1}Al_{0.8})Si_{1.7}O_7$	72
Iterative Phase Classification		
Ca-Al-Mg-Mn-Si	$Ca_{1.2}AlMg_{0.1}Si_{1.1}O_5$	1
Melilite	$Ca_2(Mg_{0.1}Al_{0.8})Si_{1.7}O_7$	57
Melilite	$Ca_{1.8}(Mg_{0.1}Al_{0.9})Si_{1.8}O_7$	42

Symbol: * = mineral phase with IPC applied

Table 21. Mineral phases and chemical formulas for sample W24_T2.

Mineral	Chemical composition	Mineral abundance (%)
Rankinite	$Ca_3(Al_{0.6}Si_{1.4})O_7$	1
Tricalcium silicate	$Ca_{3.5}Si_{0.6}O_5$	39
Ca-Si	$Ca_{0.1}Si_{0.9}O_2$	5
Melilite	$Ca_{1.5}(Al_{0.8})(Al_{0.3}Si_{0.7})SiO_7$	13
Melilite*	$Ca_{1.3}(Al_{0.7})Si_{2.2}O_7$	42
Iterative Phase Classification		
Calcite	$CaCO_3$	1
Ca-Al-Mg-Si	$Ca_{1.2}Al_{0.6}Mg_{0.2}Si_2O_7$	80
Melilite	$Ca_{1.6}(Mg_{0.2}Al_{0.7})Si_2O_7$	19

Symbol: * = mineral phase with IPC applied

Table 22. Mineral phases and chemical formulas for sample W24_M1.

Mineral	Chemical composition	Mineral abundance (%)
Melilite	$Ca_{1.4}(Mg_{0.1}A_{0.9})(AlSi)O_7$	5
Quartz	SiO_2	1
Fe-oxide	$Fe_{1.7}O_3$	6
Melilite	$Ca_{1.9}(Mg_{0.1}Al_{0.6})Si_{1.4}O_7$	18
Tricalcium silicate	$Ca_{2.6}Si_{0.9}O_5$	53
Melilite	$Ca_{1.7}(Mg_{0.2}Al_{0.7})Si_{1.7}O_7$	17

Table 23. Mineral phases and chemical formulas for sample W24_T3M2.

Mineral	Chemical composition	Mineral abundance (%)
Ca-Fe-Si	$Ca_{0.1}Fe_{0.6}Si_{0.1}O$	3
Ca-Al-Si	$Ca_{1.5}Al_{0.5}Si_{2.1}O_7$	1
Melilite	$Ca_{1.3}(Mg_{0.2}Al_{0.8})(AlSi)SiO_7$	15
Ca-Al-Fe-Si	$CaAlFeSi_3O_{10}$	1
Ca-Al-Si	$Ca_2Al_{0.3}Si_{0.6}O_4$	40
Ca-Al-Si	$Ca_{1.7}Al_{0.4}Si_{0.7}O_4$	1
Melilite*	$Ca_{1.7}(Mg_{0.09}Al_{0.8})Si_{1.7}O_7$	39
Iterative Phase Classification		
Ca-Al-Fe-Si	$Ca_{0.1}Al_{0.1}Fe_{1.7}Si_{0.2}O_4$	1
Melilite	$Ca_{1.6}(Mg_{0.1}Al_{0.9})Si_{1.8}O_7$	96
Ca-Al-Mg-Fe-Si	$CaAl_{0.7}Mg_{0.1}Fe_{1.2}Si_2O_8$	3

Symbol: * = mineral phase with IPC applied.

Table 24. Mineral phases and chemical formulas for sample W24_T4.

Mineral	Chemical composition	Mineral abundance (%)
Fe-oxide	$Fe_{1.7}O_3$	7
Melilite	$Ca_2(Mg_{0.1}Al_{0.8})Si_{1.6}O_7$	24
Ca-Al-Si	$Ca_2Al_{0.9}Si_2O_6$	1
Ca-Al-Si	$Ca_{0.5}AlSi_2O_6$	2
Melilite	$Ca_{1.3}(Mg_{0.3}Al_{0.7})(Al_{0.1}Si_{1.9})O_7$	30
Tricalcium silicate	$Ca_{2.6}Si_{0.9}O_5$	26
Melilite	$Ca_{1.6}(Mg_{0.3}Al_{0.7})(Al_{0.2}Si_{0.8})SiO_7$	10

Melilite is the dominant phase, followed by a Ca-Al-Si-S phase, Fe-oxide, quartz, and Ca-oxide in all samples. Regions from horizon W24 comprise mostly melilite with some Ca-Al-Si, Ca-rich silicates (e.g., tricalcium silicate, larnite, rankinite), quartz, calcite, oxides (CaFeO, FeO, Fe_2O_3), and other non-conforming phases (Ca-Si, Ca-Fe-Si, Ca-Al-Mg-Si, Ca-Al-Fe-Si, Ca-Al-Mg-Mn-Si, and Ca-Al-Mg-Mn-Fe-Si). Whereas, horizon W25 has more Ca-oxide and quartz and less melilite with olivine, anorthite, Ca-Si-S, Ca-Al-Si-S, and Ca-Al-Fe-Si-S phases. Mostly Ca-Al-Si-S, melilite and quartz comprise regions from horizon W26 with olivine, calcite, Ca-Al-Mg-Si, Ca-Al-Mg-Fe-Si, some calcio-wüstite, wollastonite, monticellite, anhydrite, Ca-Al-Fe-Si, Ca-Al-Fe-Si-S, Ca-Al-Mg-Si-S, and Ca-Al-Mg-Fe-Si-S. Quartz, Fe-oxide, Fe-Si-S, Ca-Al-Mg-Fe-Si, and native Fe occur more often in regions from horizon W27 and melilite, wollastonite, anorthite, pyrite, tricalcium silicate, calcio-wüstite, Ca-oxide, Ca-Fe-Si-S, and Ca-Al-Mg-Fe-Si-S once. Horizon W28 comprises the most phases (19) of mostly Fe-oxide, melilite, Ca-oxide, anorthite, Ca-Al-Si-S, Ca-Al-Fe-Si-S and some Fe-S, Ca-Si-S, wollastonite, rankinite, anhydrite, calcite, quartz, pyrite, Ca-Si, Ca-Al-Si, Ca-Mg-Si-S, and Ca-Al-Mg-Fe-Si-S.

The results from the standardless quantification of the EDS data show more metals at higher concentrations are found in the three lower stratigraphic horizons (Table 25).

Table 25. Metal concentrations (ppm) quantified in legacy slag.

Sample	W28		W27		W26		W25		W24	
	ppm	2σ (ppm)	ppm	2σ (ppm)	ppm	2σ (ppm)	ppm	2σ (ppm)	ppm	2σ (ppm)
Ba	40	4	ND	-	ND	-	110 - 140	20, 24	30	4
Fe	1020 - 1290	63, 114	120 - 980	50, 40	240	18	90 - 780		ND	-
Mn	40	10	20 - 80	10, 12	60 - 180	14, 16	20 - 90	15, 10	10 - 230	8, 14
Ti	ND	-	20	8	50 - 120	10, 18	ND	-	40	8
Zn	ND	-	ND	-	30	8	ND	-	ND	-

Nd = not detected

Mn content ranges from 10 ppm to 190 ppm and occurs with decreasing frequency in non-conforming phases, melilite group, Fe-oxide, anorthite, quartz, calcio-wüstite, wollastonite, and larnite. Ti was identified ranging from 17 ppm to 120 ppm and is associated with melilite and non-conforming phases. Zn was detected at a concentration of 30 ppm associated with olivine. Fe occurs as a major component in minerals as well as trace metal in other minerals throughout the deposit, and occasionally as native Fe nuggets. Notable metal concentration trends include generally increasing Mn down the stratigraphic height of the deposit and the highest abundance of Mn in horizon W24.

2.3.1.2.1 Horizon W28

The mineral phases from W28_T1 (Fig. 5 and Table 2) and W28_T3M3 (Fig. 6 and Table 5) are Ca-rich compared to those from W28_T2M2 (Fig. 7 and Table 4) and W28_M1 (Fig. 8 and Table 3) which are Fe-dominant.

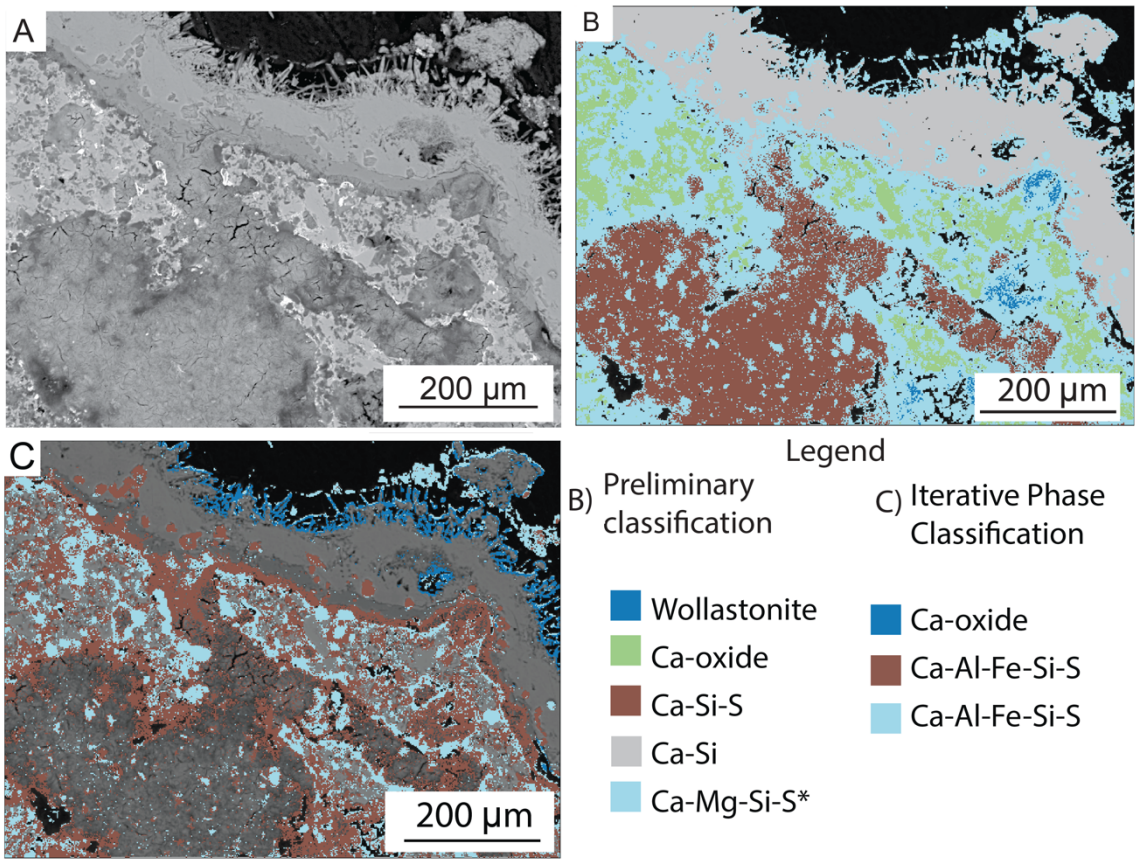

Figure 5. Region W28_T1. A) BSE image. B) Mineral phase map of wollastonite (dark blue), Ca-oxide (green), $Ca_{3.5}Si_{0.2}O_4$ (brown), $Ca_{3.5}Si_{0.2}O_4$ (grey), and $Ca_{2.9}Mg_{1.6}SiS_{0.3}O_7$ (light blue). C) IPC mineral phase map on the Ca-Mg-Si-S (light blue) in B. Ca-oxide (dark blue) and Ca-Al-Fe-Si-S ($Ca_{2.9}Mg_{1.6}SiS_{0.3}O_7$: brown; $CaAl_{0.7}Fe_{0.7}Si_{1.5}S_{0.5}O_7$: light blue). Symbol: * = mineral phase with IPC applied.

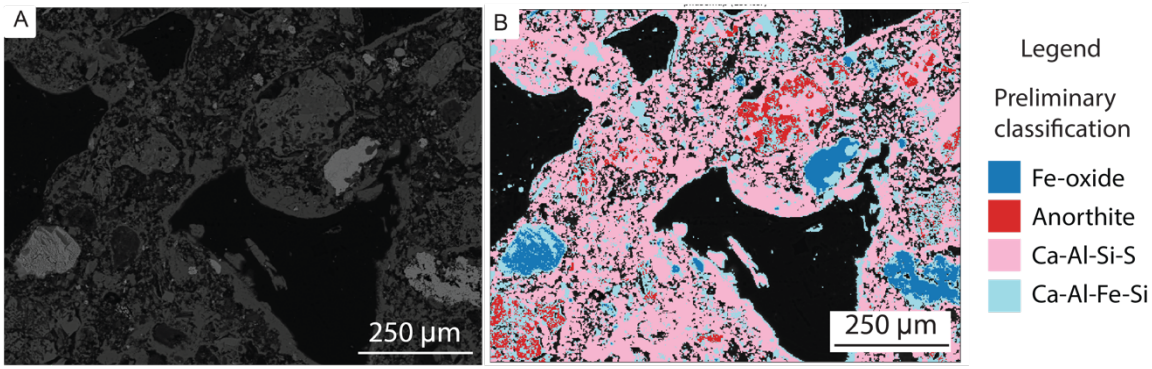

Figure 6. Region W28_T3M3. A) BSE image. B) Mineral phase map of Fe-oxide (dark blue), anorthite (red), $Ca_3Al_{0.4}Si_2S_{0.1}O_8$ (pink), and $CaAlFe_{0.4}Si_2O_7$ (light blue).

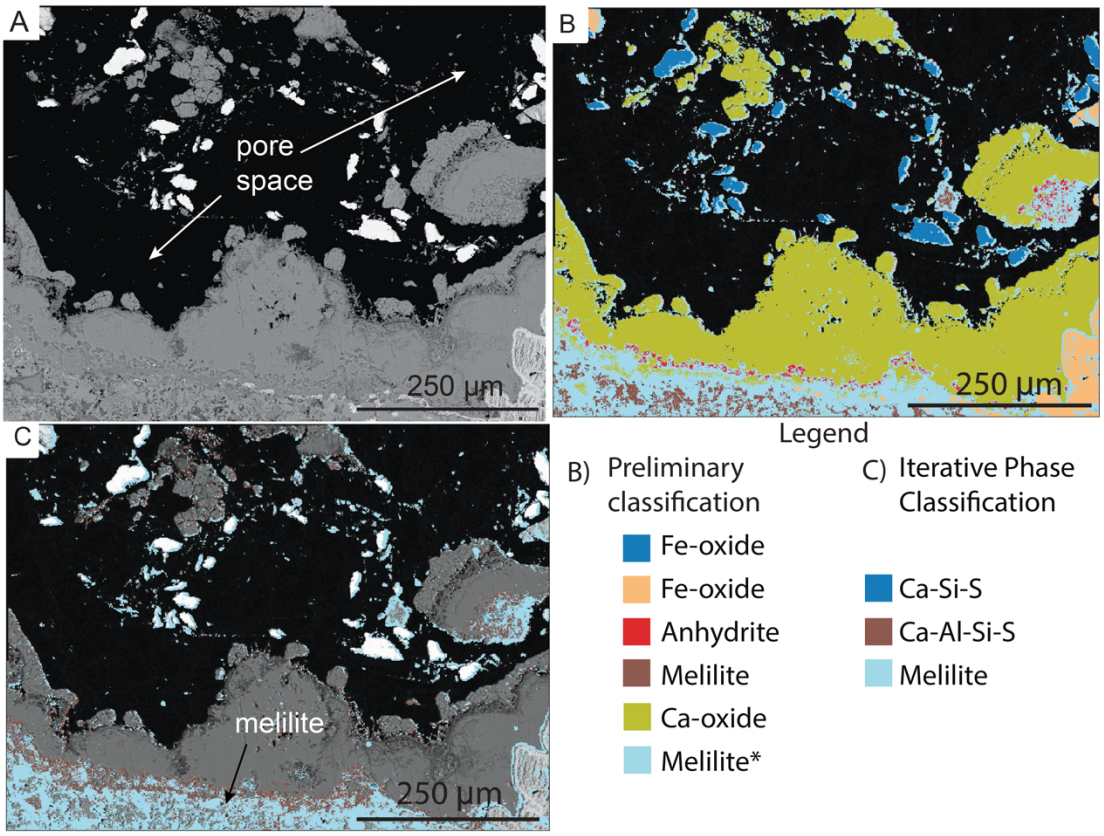

Figure 7. Region W28_T2M2. A) BSE images. B) Mineral phase map of Fe-oxide (FeO: dark blue; Fe_2O_3: orange), anhydrite (red), melilite ($Ca_{1.3}Al_{1.8}Si_{1.3}O_7$: brown; $Ca_2(Mg_{0.2}Al_{0.6})Si_{1.4}O_7$: light blue), and Ca-oxide (yellow). C) IPC mineral phase map on the melilite (light blue) in B. $Ca_{0.8}Si_{0.2}S_{1.3}O_4$ (dark blue), Ca-Al-Si-S (brown), and melilite (light blue) with 40 ppm Ba and 1020 ppm Fe. Symbol: - = low quantification results; * = mineral phase with IPC applied.

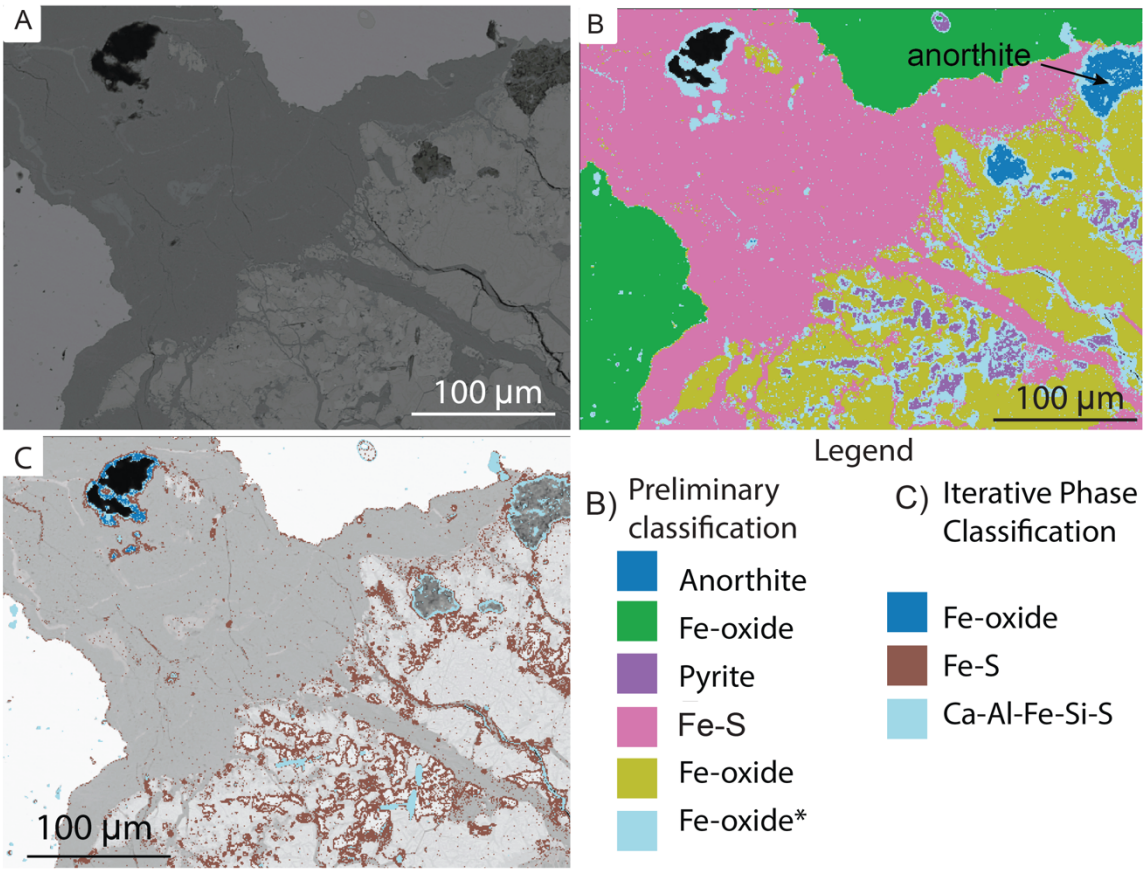

Figure 8. Region W28_M1. A) BSE image. B) Mineral phase map of anorthite (dark blue) with 40 ppm Mn and 1290 ppm Fe, Fe-oxide (FeO: green) with trace Mn, Fe-S (pink), Fe-oxide (FeO: yellow; Fe_2O_3: light blue), and pyrite (purple). C) IPC mineral phase map on the Fe-oxide (light blue) in B. Fe-oxide (Fe_2O_3: dark blue), $Fe_{1.8}S_{0.2}O_3$ (brown), and $Ca_{0.2}Al_{0.2}Fe_2Si_{0.6}S_{0.7}O_5$ (light blue). Symbol: * = mineral phase with IPC applied.

Trace Mn (40 ppm) localises in grains of anorthite within the matrix which is surrounded by Fe-oxide (W28_M1). Applying the IPC on the outlier phases from W28_T1 (Ca-Mg-Si-S) and W28_M1 (Fe-oxide) confirms rare metals are not present, whereas Ba (40 ppm) and Fe (1020 ppm) are revealed for W28_T2M2.

2.3.1.2.2 Horizon W27

Trace Ti (20 ppm) localises in Ca-Al-Si-S in pore space. The outlier Ca-Al-Mg-Fe-Si-S phase of region W27_T1M1 surrounds Ca-Al-Si-S, fills pores in the matrix, and forms phase boundaries that include 60 ppm of Mn (Fig. 9 and Table 6).

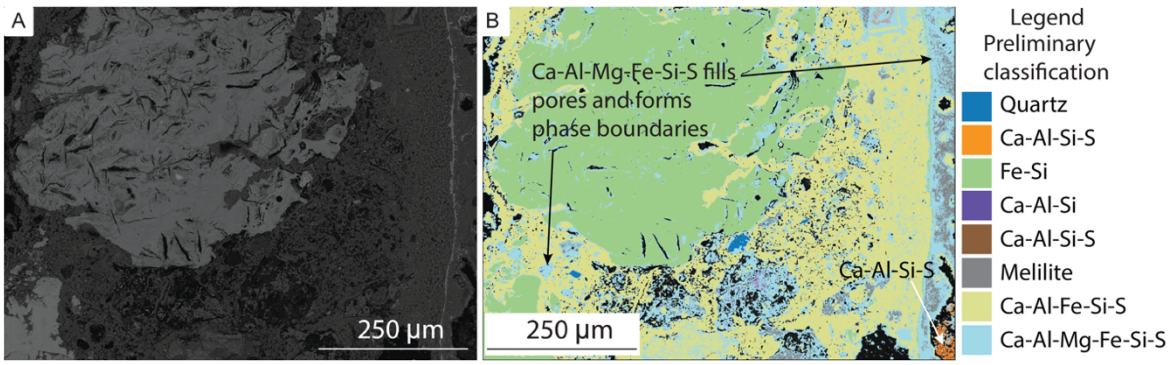

Figure 9. Region W27_T1M1. A) BSE image. B) Mineral phase map of quartz (dark blue), Ca-Al-Si-S ($CaAl_{0.3}Si_{0.4}S_{1.2}O_4$: orange with 120 ppm Ti; $CaAl_{1.2}Si_{2.3}S_{0.3}O_8$: brown), $Fe_{0.7}Si_{0.1}O$ (green), $Ca_{0.8}Al_2Si_{0.6}O_5$ (purple), melilite (grey), $Ca_{2.8}Al_{0.2}Fe_{0.1}Si_{0.6}S_{0.4}O_5$ (yellow), and $CaAl_{0.7}Mg_{0.1}Fe_{0.5}SiO_5$ (light blue) with 60 ppm Mn.

Region W27_T2M2 contains Mn and Fe in wollastonite (40 ppm and 980 ppm, respectively) and anorthite (70 ppm and 120 ppm, respectively) which are surrounded by calcio-wüstite that ranges in composition (Fig. 10 and Table 7).

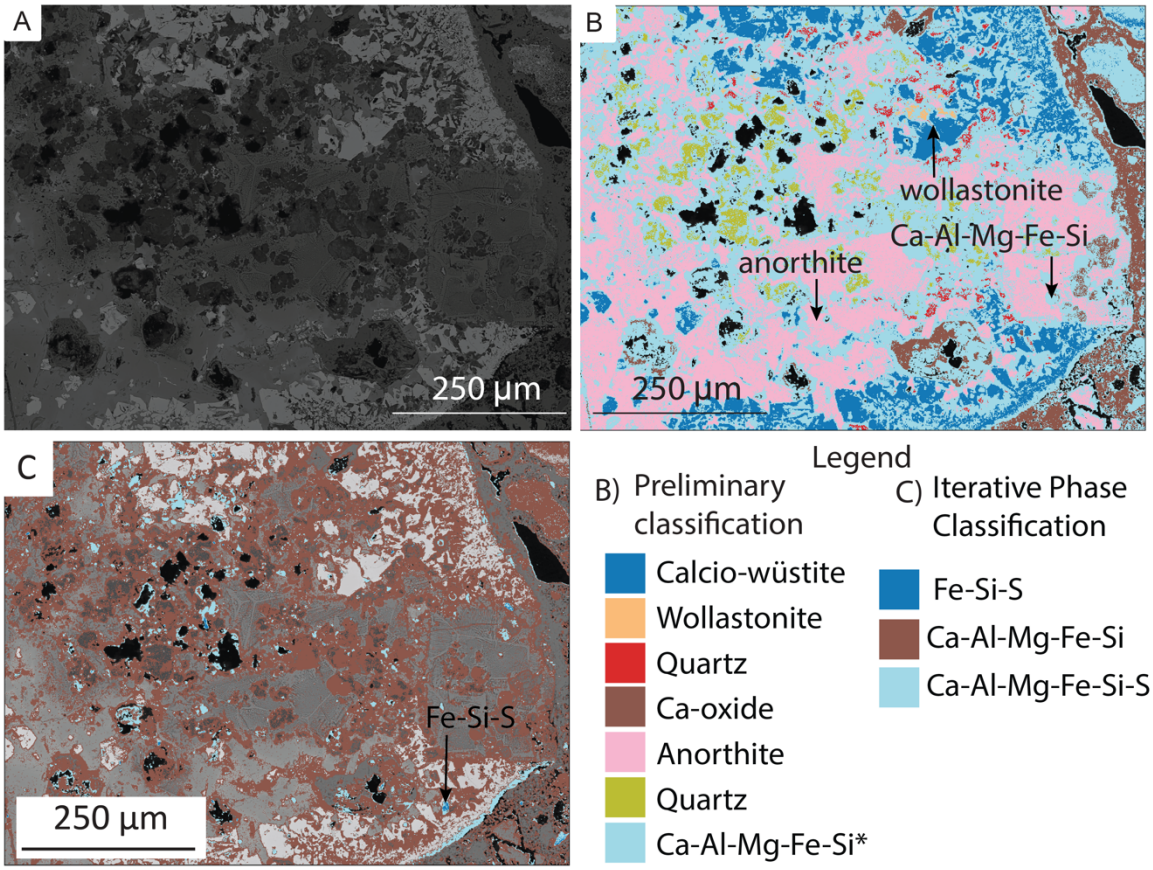

Figure 10. Region W27_T2M2. A) BSE image. B) Mineral phase map of calcio-wüstite (dark blue), wollastonite (orange) with 40 ppm Mn and 980 ppm Fe, quartz (red and yellow), Ca-oxide (brown), anorthite (pink) with 70 ppm Mn and 120 ppm Fe, and $CaAl_{0.7}Mg_{0.1}Fe_{0.5}SiO_5$ (light blue) with 60 ppm Mn. C) IPC mineral phase map on the Ca-Al-Mg-Fe-Si (light blue) in B. $Fe_{0.5}Si_{0.1}S_{2.8}O_5$ (dark blue) with 20 ppm Mn, $CaAl_{0.6}Mg_{0.3}Fe_{0.6}Si_2O_7$ (brown), and $Ca_{0.5}Al_{0.3}Mg_{0.2}FeSi_{1.1}S_{1.6}O_7$ (light blue). Symbol: * = mineral phase with IPC applied.

Mn is found throughout W27_T2M2 except for in the interior of the reaction rim. In region W27_M3, Mn localises in Fe-oxides (40 ppm to 80 ppm) near pores of the slag and in Ca-Fe-Si-S (30 ppm) (Fig. 11 and Table 8), while no trace metals were identified in W27_M4 (Fig. 12 and Table 9).

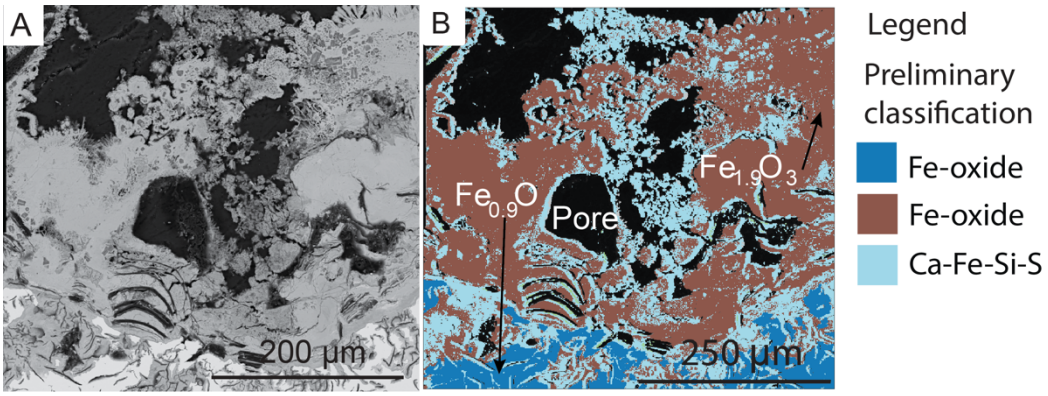

Figure 11. Region W27_M3. A) BSE image. B) Mineral phase map of Fe-oxide ($Fe_{0.9}O$: dark blue; $Fe_{1.9}O_3$: brown) with between 40 ppm to 80 ppm Mn and $Ca_{0.2}Fe_{2.1}Si_{0.2}S_{0.1}O_4$ (light blue) with 30 ppm Mn. Symbol: - = low quantification results.

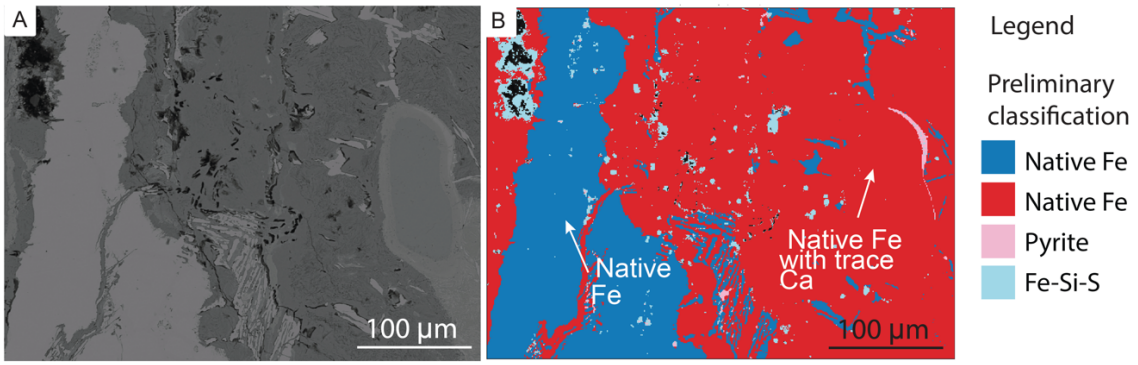

Figure 12. Region W27_M4. A) BSE image. B) Mineral phase map of native Fe (dark blue). Native Fe (red) with trace Ca, pyrite (pink), and $Fe_2Si_{1.3}SO_6$ (light blue).

Reiterating the Ca-Al-Mg-Fe-Si outlier phase from region W27_T2M2 containing 60 ppm of Mn confirms the presence of the trace metals that were identified from the preliminary clustering.

2.3.1.2.3 Horizon W26

In region W26_T3, 120 ppm of Ti in grains of Ca-Al-Si-S localising in pore space and within both the melilite and another slightly compositionally different Ca-Al-Si-S phase (Fig. 13 and Table 11).

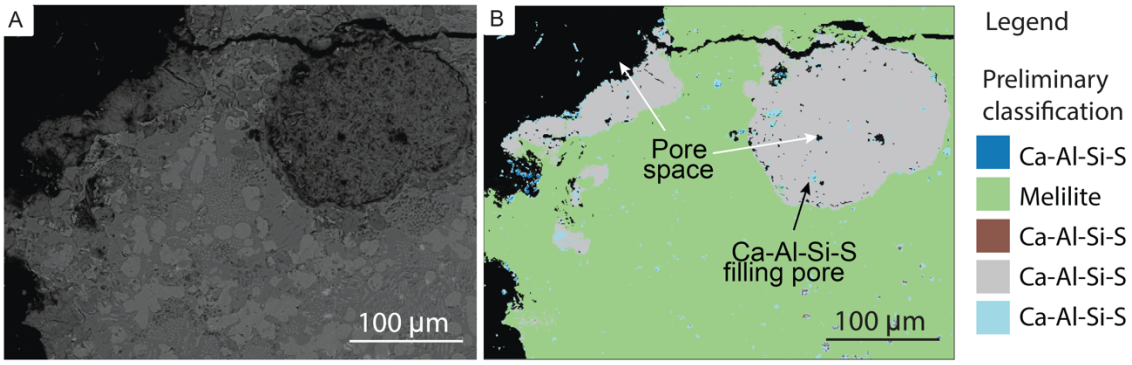

Figure 13. Region W26_T3. A) BSE image. B) Mineral phase map of Ca-Al-Si-S ($Ca_{0.4}Al_{0.1}Si_{2.6}S_{0.1}O_6$: dark blue; $Ca_{0.9}Al_{0.2}Si_{0.6}SO_4$: brown; $Ca_{0.9}Al_{0.2}Si_{0.3}S_{1.4}O_4$: grey; $CaSi_{1.4}Al_{0.3}S_{1.1}O_5$: light blue with 120 ppm Ti) and melilite (green).

Preliminary clustering on W26_T1 did not reveal trace Fe (150 ppm) and Mn (130 ppm) that were identified from reiterating on the outliers resulting in three compositionally variable melilite phases displaying exsolution textures (Fig. 14 and Table 10).

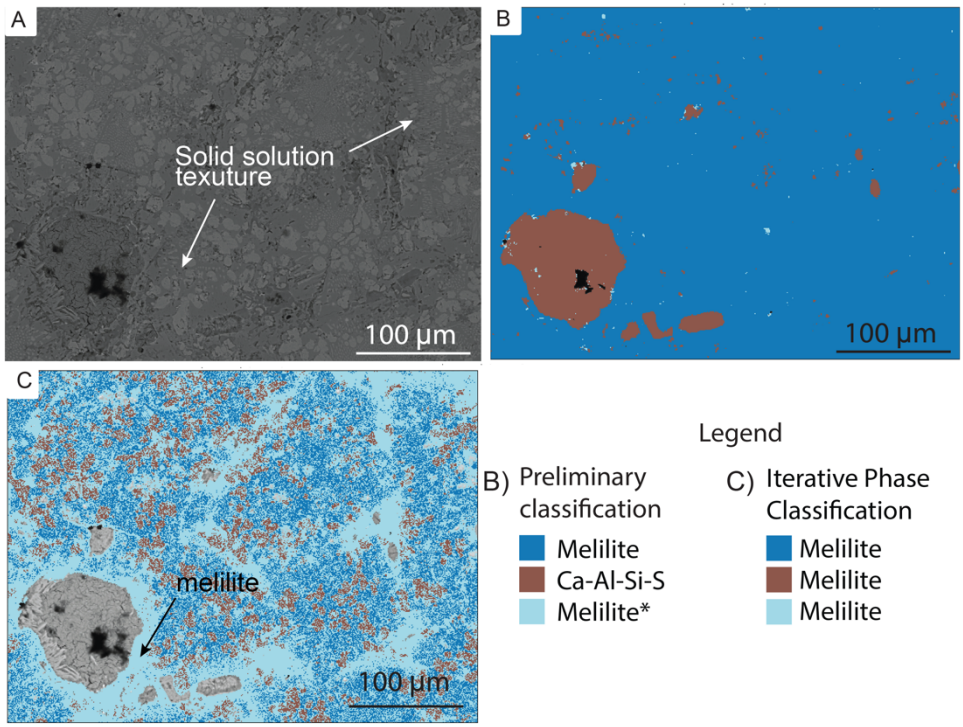

Figure 14. Region W26_T1. A) BSE image. B) Mineral phase map of melilite ($Ca_{1.8}Al_1Si_{1.6}O_7$: dark blue; $Ca_{1.4}Al_{0.7}Si_{1.5}SO_7$: light blue) and $Ca_2Al_{0.4}SiS_{2.1}O_8$ (brown). C) IPC mineral phase map on the melilite (dark blue) in B. Three compositionally variable melilite ($Ca_{1.6}(Mg_{0.2}Al_{0.8})(Al_{0.6}Si_{0.4})SiO_7$: dark blue; $Ca_2(Mg_{0.1}Al_{0.5})Si_{1.9}O_7$: brown; $Ca_{1.7}(Mg_{0.1}Al_{0.9})Si_{1.7}O_7$: light blue with 130 ppm Mn) Symbol: * = mineral phase with IPC applied.

Conversely, in region W26_T6.1 where Ti was detected in outliers, Ti was not found after the IPC. The Ti localising within a Ca-Al-Si phase and melilite are associated with melilite within the matrix and surrounding the exterior of the slag that is exposed to pore space (Fig.15 and Table 14).

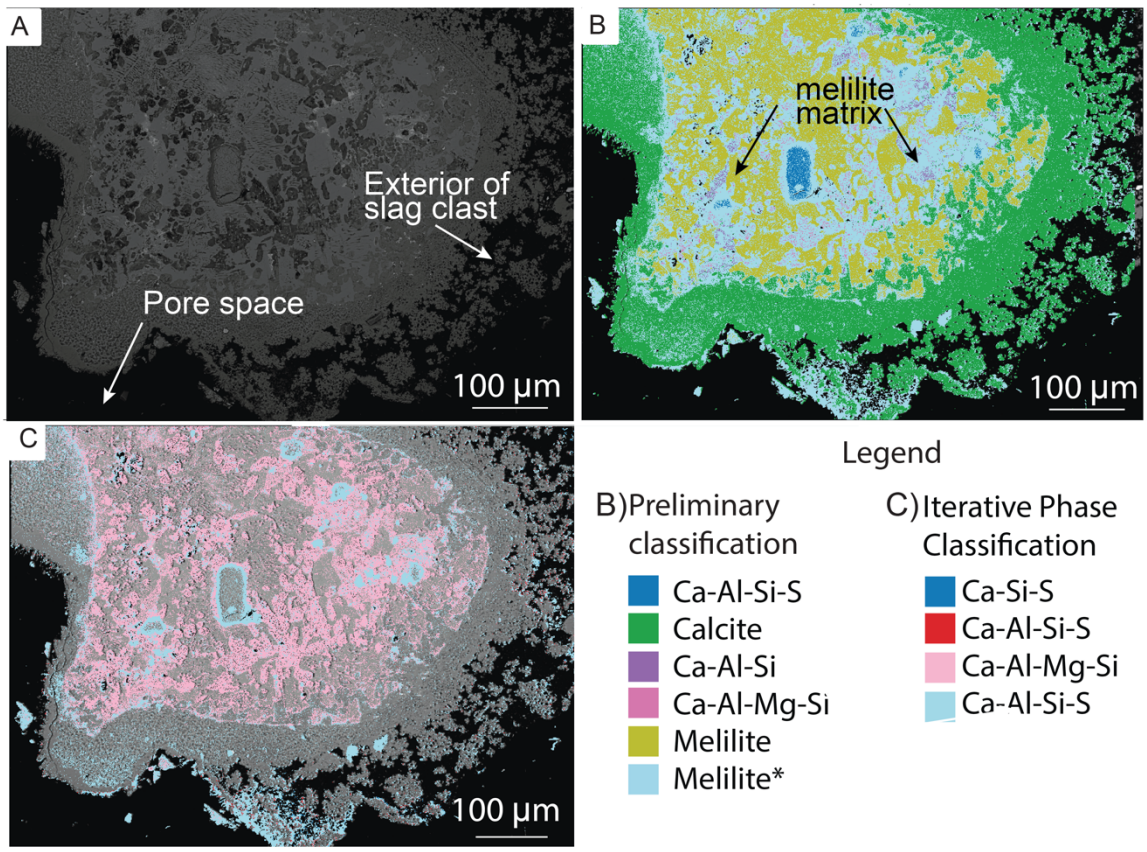

Figure 15. Region W26_T6.1. A) BSE image. B) Mineral phase map of $CaAl_{0.2}Si_{0.6}S_{1.9}O_6$ (dark blue), calcite (green), $Ca_{1.3}Al_{0.3}Si_2O_6$ (purple) with 51.47 ppm Ti, $Ca_{0.9}Mg_{0.3}Al_{0.4}Si_{2.6}O_7$ (pink), melilite ($(Ca_{1.5}(Mg_{0.2}Al_{0.8})(Si_{0.5}Al_{0.5})Si_{1.1}O_7$: yellow; $Ca_{1.6}(Mg_{0.2}Al_{0.6})Si_{1.8}O_7$: light blue with 60 ppm Ti). C) IPC mineral phase map on melilite (light blue) in B. $Ca_{0.8}Si_2S_{0.1}O_5$ (dark blue), Ca-Al-Si-S ($Ca_{1.9}Al_{0.1}Si_{0.9}S_{0.1}O_4$: red; $CaAl_{0.3}SiS_{0.3}O_4$: light blue), and $CaAl_{0.6}Mg_{0.2}Si_2O_6$ (pink). Symbol: * = mineral phase with IPC applied.

Mn occurs in region W26_T5M2 in a Ca-Al-Mg-Fe-Si (180 ppm) and a Ca-Al-Fe-Si (60 ppm) phase (Fig. 16 and Table 13).

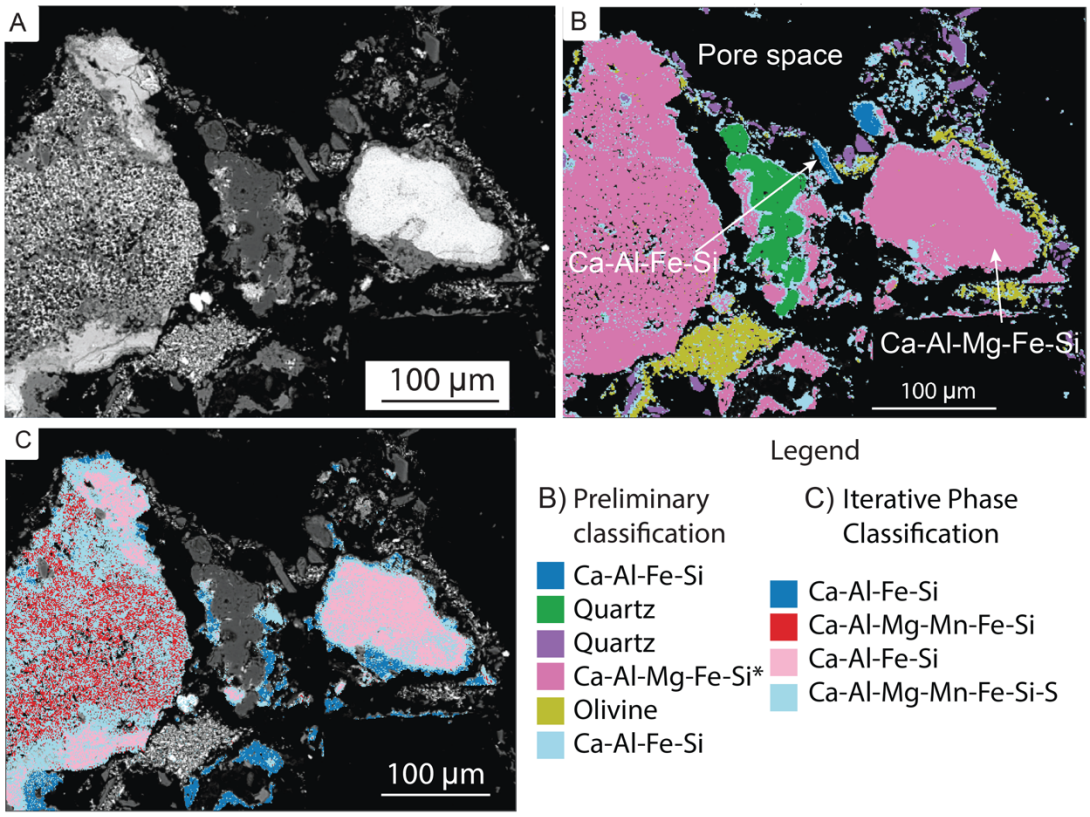

Figure 16. Region W26_T5M2. A) BSE image. B) Mineral phase map of Ca-Al-Fe-Si ($Ca_{0.1}Al_{0.8}Fe_{0.2}Si_{1.1}O_4$: dark blue with 60 ppm Mn; $CaAl_{0.5}FeSi_2O_7$: light blue, quartz (green and purple), $Ca_{0.9}Al_{0.3}Mg_{0.2}Fe_{2.3}SiO_6$ (pink) with 175.41 ppm Mn, and olivine (yellow). C) IPC mineral phase map on Ca-Al-Mg-Fe-Si (pink) in B. Ca-Al-Fe-Si ($Ca_2Al_{0.2}Fe_{0.3}Si_{0.6}O_4$: dark blue; $Ca_{0.3}Al_{0.2}Fe_{2.2}Si_{0.5}O_4$: pink), $Ca_{0.5}Al_{0.2}Mg_{0.1}Mn_{0.1}Fe_{1.5}Si_{0.7}O_5$ (red), and $Ca_{0.5}Al_{0.2}Mg_{0.1}Mn_{0.1}Fe_{1.5}Si_{0.7}$ $S_{0.1}O_5$ (light blue). Symbol: * = mineral phase with IPC applied.

In region W26_T6.2M3, olivine and monticellite are associated with 30 ppm Zn and 240 ppm Fe, respectively. Calcite forms a reaction rim around melilite that displays an exsolution texture (Fig. 17 and Table 15).

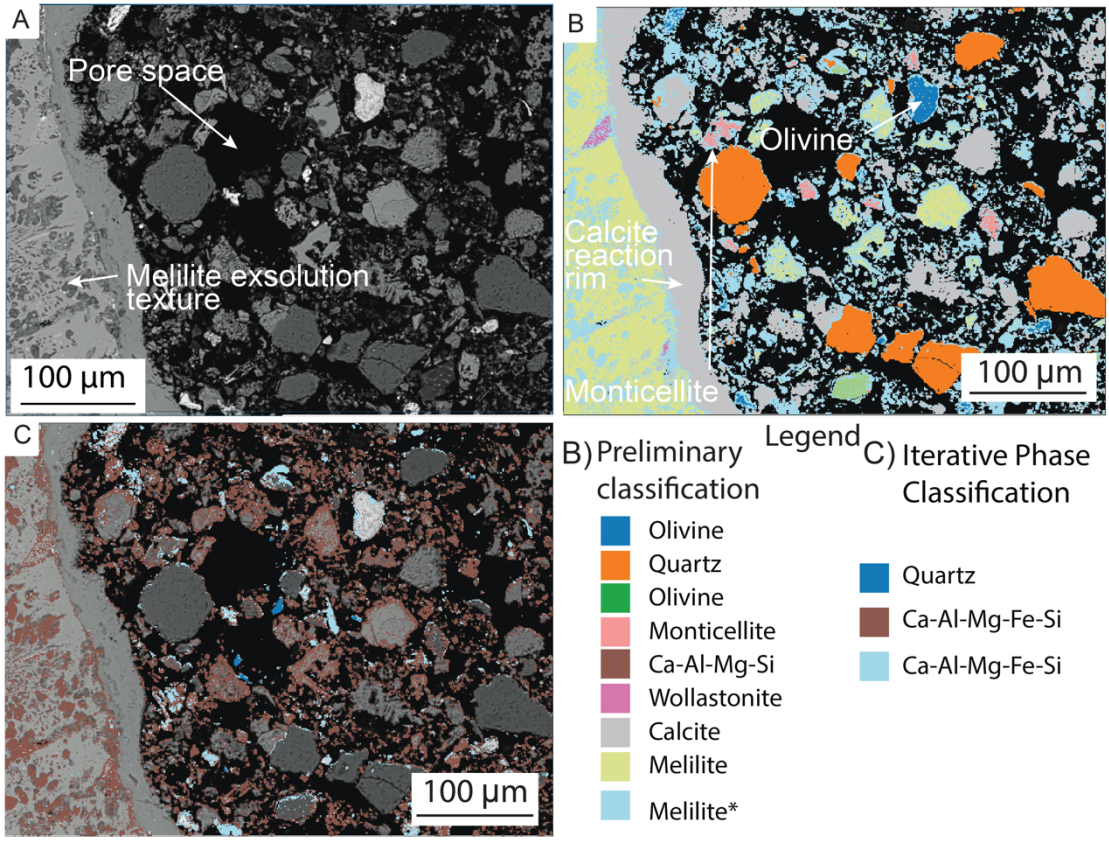

Figure 17. Region W26_T6.2M3. A) BSE image. B) Mineral phase map of olivine ($(Fe_{1.6}Ca_{0.4})(Si_{0.7}Al_{0.3})O_4$: dark blue with 30 ppm Zn; $(Ca_{1.1}Mg_{0.4})Si_{1.2}O_4$: green), quartz (orange), monticellite (salmon) with 240 ppm Fe, $Ca_{0.5}Al_{0.5}Mg_{0.6}Si_2O_6$ (brown), wollastonite (pink), calcite (grey), and melilite ($Ca_{1.4}(Mg_{0.2}Al_{1.3})Si_{1.6}O_7$: yellow; $Ca_{1.3}(Mg_{0.2}Al_{0.8})Si_{1.9}Al_{0.1}O_7$: light blue). C) IPC mineral phase map on melilite (light blue) in B. Quartz (dark blue), Ca-Al-Mg-Fe-Si ($CaAl_{0.8}Mg_{0.2}Fe_{0.3}Si_{1.7}O_6$: brown; $Ca_{0.9}AlMg_{0.2}Fe_{0.6}Si_{2.2}O_8$: light blue). Symbol: * = mineral phase with IPC applied.

No trace metals were found localising in regions W26_T4 (Fig. 18 and Table 12) and W26_M4 (Fig. 19 and Table 16).

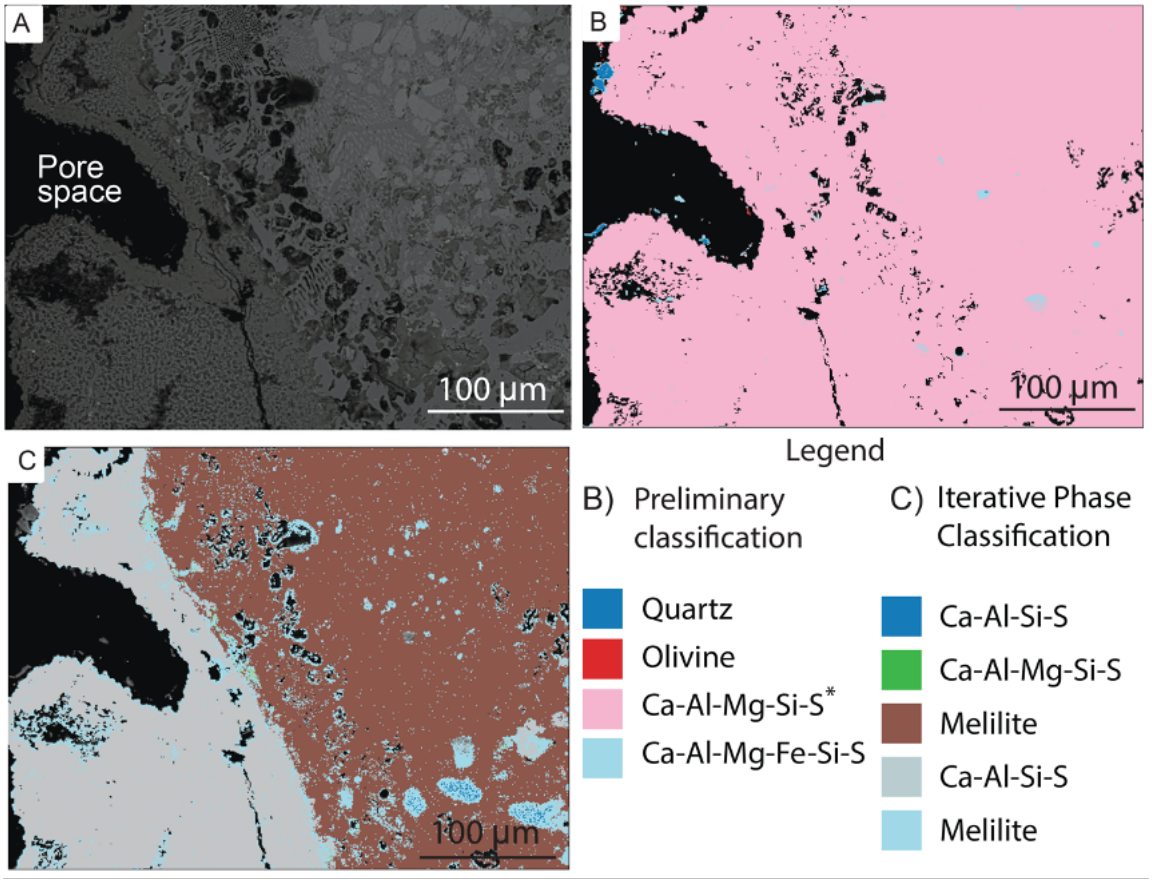

Figure 18. Region W26_T4. A) BSE image. B) Mineral phase map of quartz (dark blue), olivine (red), $Ca_2Al_{0.9}Mg_{0.1}Si_{1.5}S_{0.3}O_7$ (pink), and $CaAl_{0.4}Mg_{0.1}Fe_{0.1}Si_{2.2}S_{0.5}O_7$ (light blue). C) IPC mineral phase map on the Ca-Al-Mg-Si-S (pink) in B. Ca-Al-Si-S ($Ca_{0.9}Al_{0.2}Si_{0.7}S_{0.9}O_4$: dark blue; $Ca_{2.2}Al_{0.2}Si_{0.7}S_{0.6}O_5$: grey), Ca-Al-Mg-Si-S (green), and melilite ($Ca_{1.5}(Mg_{0.1}Al_{0.9})(Al_{0.3}Si_{0.7})SiO_7$: brown; $Ca_{1.7}(Mg_{0.2}Al_{0.7})Si_{1.6}O_7$: light blue). Symbol: * = mineral phase with IPC applied.

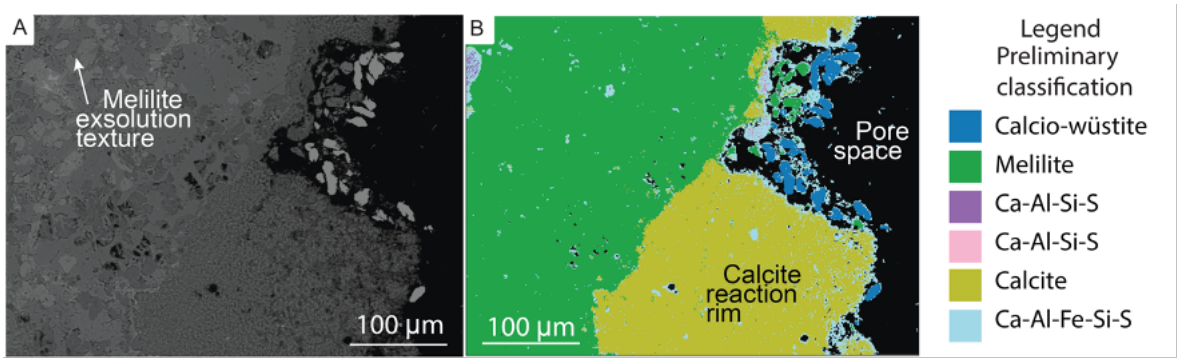

Figure 19. Region W26_M4. A) BSE image. B) Mineral phase map of calcio-wüstite (dark blue), melilite (green), Ca-Al-Si-S ($Ca_{0.8}Al_{0.1}Si_{0.3}S_{1.6}O_4$: purple; $Ca_{0.8}Al_{0.2}Si_{0.4}S_{1.6}O_4$: pink), calcite (yellow), and $CaAl_{0.2}Fe_{0.1}Si_{0.7}S_{0.7}O_4$ (light blue).

2.3.1.2.4 Horizon W25

Regions W25_T1 and W25_M1 are dominantly CaO with larnite occurring in the former (Fig. 20 and Table 17), and quartz and a Ca-Si phase in the latter (Fig. 21 and Table 18).

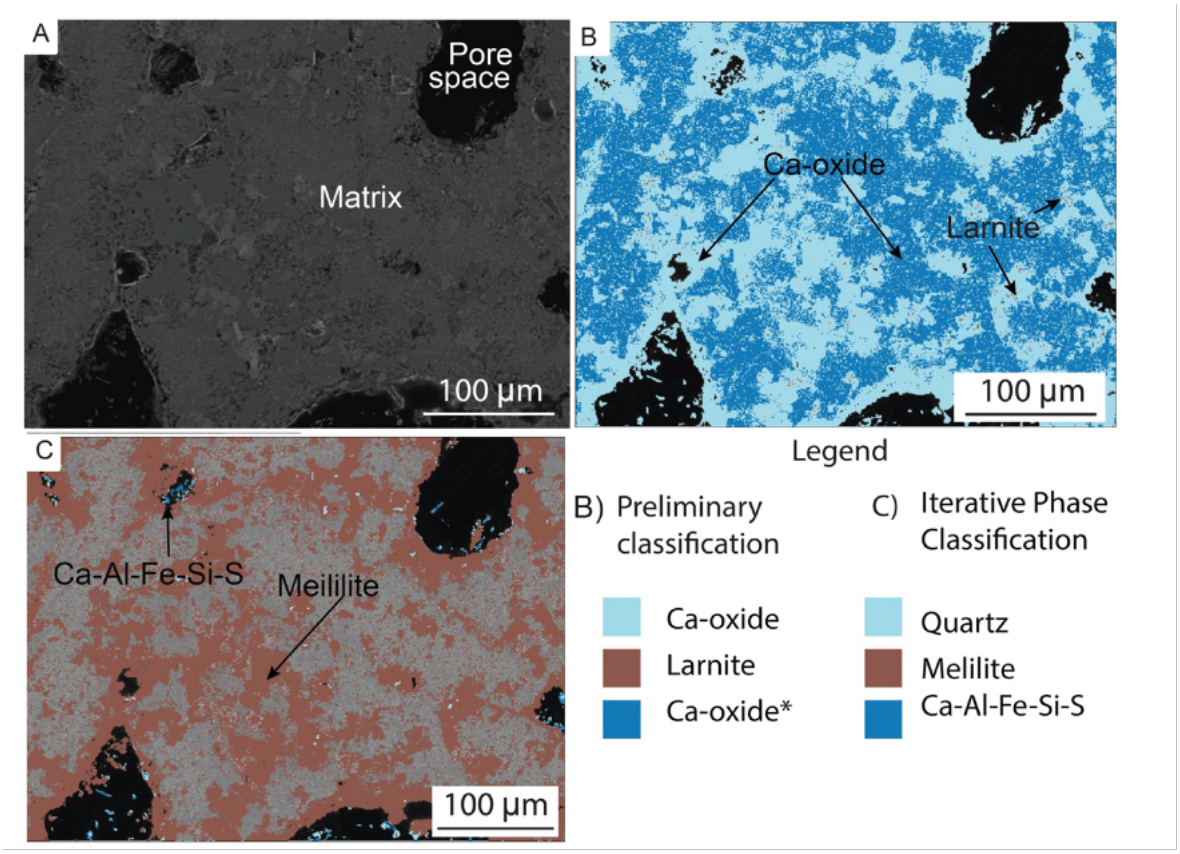

Figure 20. Region W25_T1. A) BSE image. B) Mineral phase map of Ca-oxide (CaO: light blue; $Ca_{0.8}O$: dark blue with 140 ppm Ba), and larnite (brown) with 90 ppm Mn. C) IPC mineral phase map on Ca-oxide (dark blue) in B. Quartz (light blue), melilite (brown) with 20 ppm Mn, and $Ca_{0.5}Al_{0.3}Fe_{0.1}Si_2SO_4$ (dark blue) with 110 ppm Ba. Symbol: * = mineral phase with IPC applied.

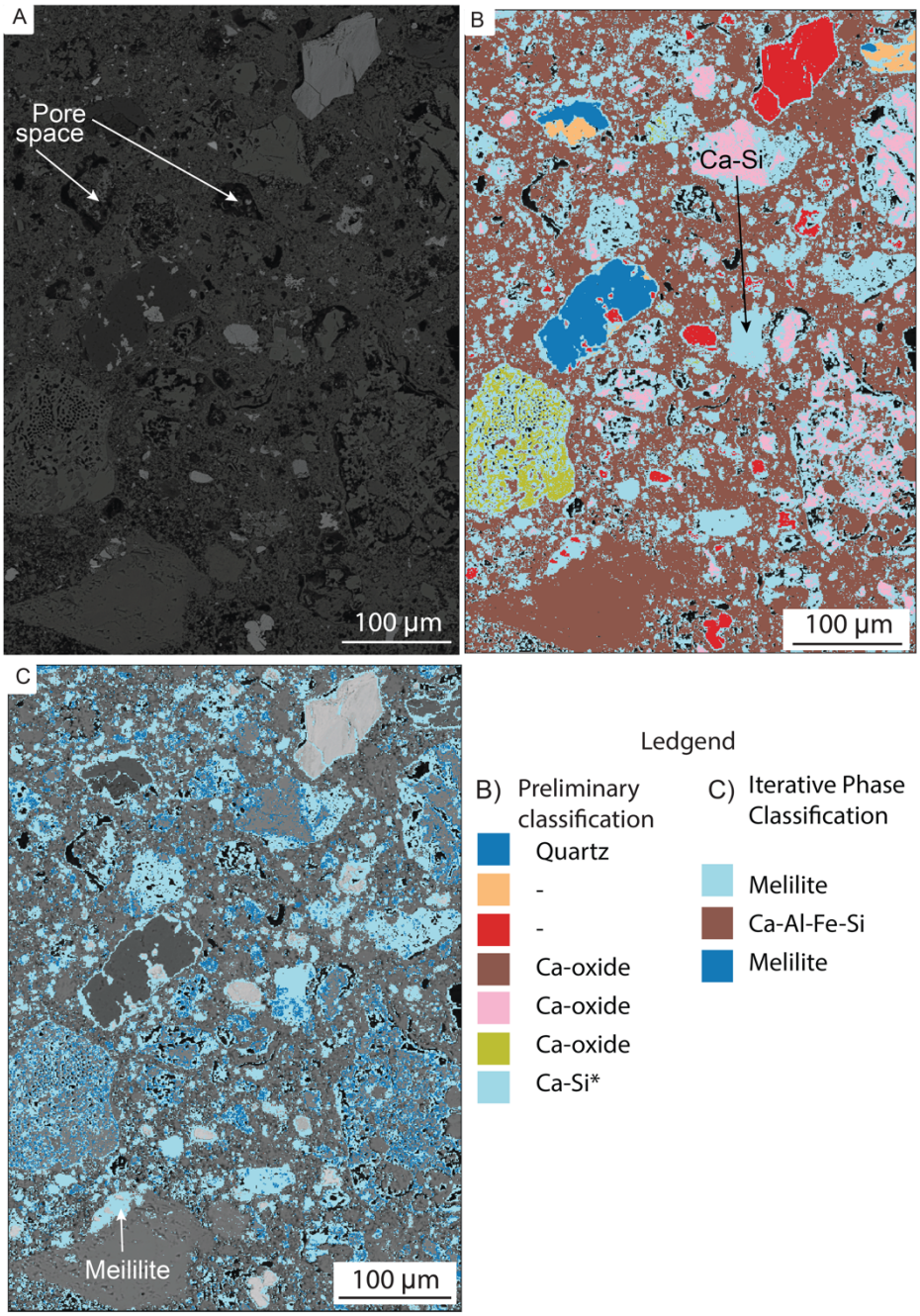

Figure 21. Region W25_M1. A) BSE image. B) Mineral phase map of quartz (dark blue), Ca-oxide ($Ca_{0.8}O$: brown; $Ca_{0.9}O$: pink; CaO: yellow), and $Ca_{0.7}Si_{0.1}O$ (light blue) with 230 ppm Fe. C) IPC mineral phase map on Ca-Si (light blue) in B. Melilite ($Ca_{1.6}(Mg_{0.2}Al_{0.8})(Al_{0.8}Si_{0.2})(Si_{1.2})O_7$: light blue with 30 ppm Mn; $Ca_{1.9}(Mg_{0.1}Al_{0.9})(Al_{0.1}Si_{0.9})Si_{0.6}O_7$: dark blue with 780.64 ppm Fe and 140 ppm Ba), and $Ca_2Al_{0.2}Fe_{0.4}Si_{0.6}O_4$ (brown). Symbol: - = low quantification results; * = mineral phase with IPC applied.

Larnite includes 90 ppm Mn in W25_T1 and the outlier cluster quantified as Ca-oxide is associated with 140 ppm Ba. Both Fe-oxide and anorthite in region W25_M2 contain Mn (80 ppm and 80 ppm, respectively). Appling the IPC on the outliers from regions W25_T1 and W25_M1 reveals Mn (20 ppm) in melilite and Ba (110 ppm) in a Ca-Al-Fe-Si-S phase in the former, and Fe (780 ppm) in melilite, Mn (20 ppm to 60 ppm) in melilite and a Ca-Al-Fe-Si phase, and Ba (140 ppm) in melilite in the latter. Region W25_M2 includes Ca-oxide with 90 ppm Fe, trace Mn localising with nuggets of Fe (80 ppm) that are exposed to pore space and are associated with needles of anorthite (80 ppm) (Fig. 22 and Table 19).

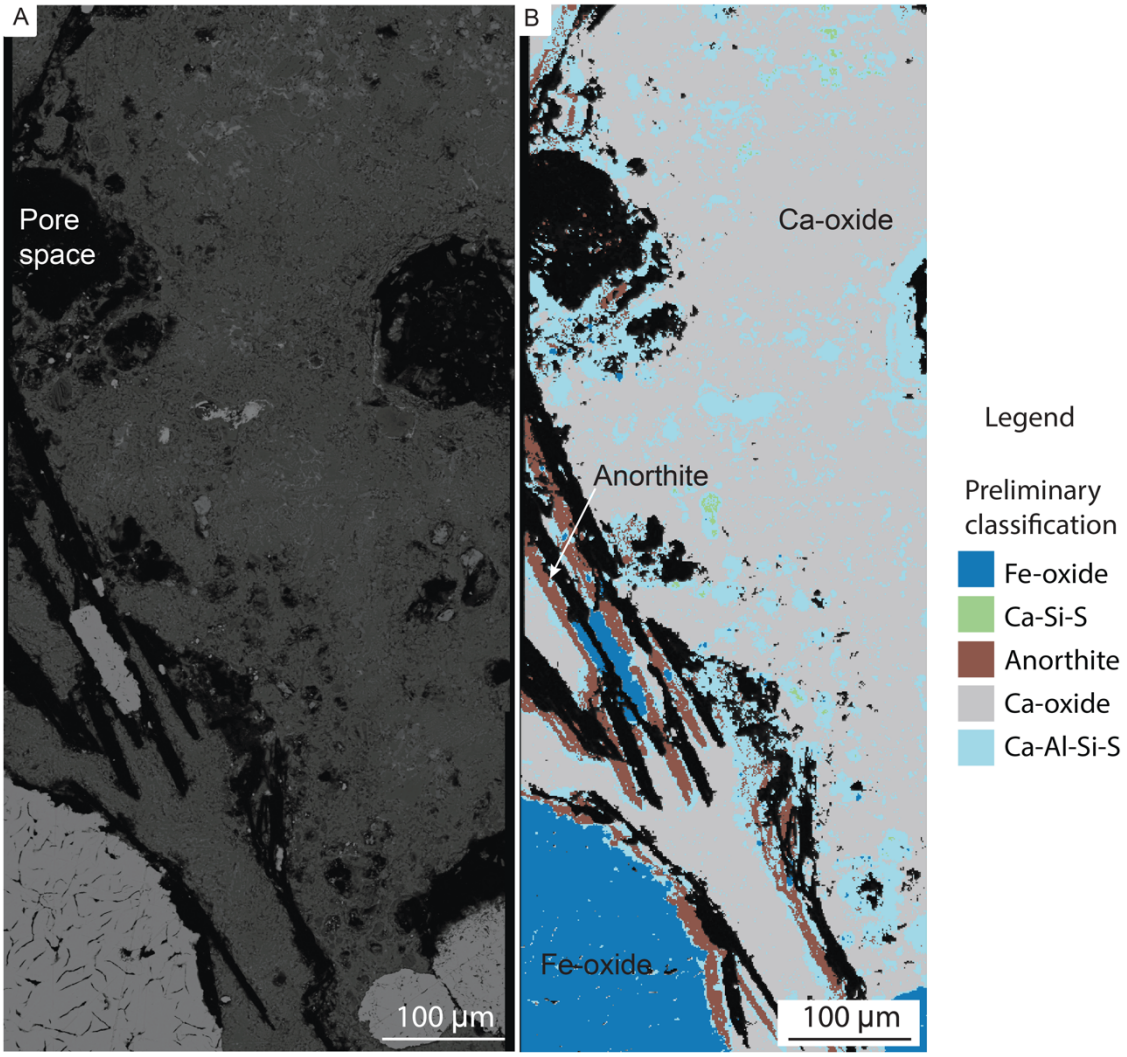

Figure 22. Region W25_M2. A) BSE image. B) Mineral phase map of Fe-oxide ($Fe_{0.9}O$: dark blue) with 80 ppm Mn, $Ca_{1.1}Si_{0.1}S_{2.4}O_5$ (green), anorthite (brown) with 80 ppm Mn, Ca-oxide (grey) with 90 ppm Fe, and $Ca_2Al_{0.7}Fe_{0.1}Si_{1.7}S_{0.8}O_8$ (light blue).

2.3.1.2.5 Horizon W24

Melilite dominates regions in horizon W24, followed by Ca-Si silicates (larnite, rankinite, tricalcium silicate). In both W24_T1 (Fig. 23 and Table 20) and W24_T2 (Fig. 24 and Table 21), the outliers comprising melilite revealed trace Mn (up to 40 ppm and up to 50 ppm, respectively) that was not detected from the preliminary clustering.

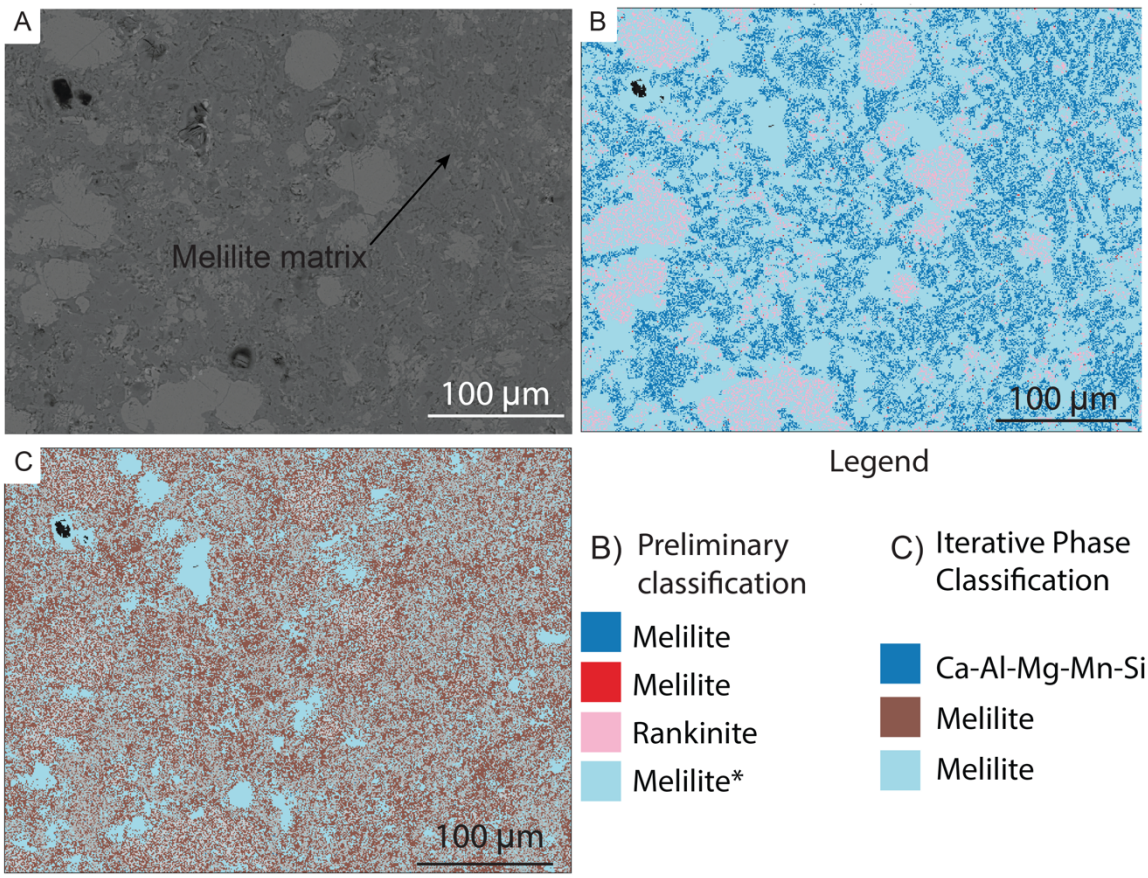

Figure 23. Region W24_T1. A) BSE image. B) Mineral phase map of melilite ($Ca_2(Mg_{0.1}Al_{0.9})(Al_{0.6}Si_{0.4})SiO_7$: dark blue; $Ca_2(Mg_{0.1}Al_{0.7})Si_2O_7$: red; $Ca_{2.3}(Mg_{0.1}Al_{0.8})Si_{1.7}O_7$: light blue) and rankinite (pink). C) IPC mineral phase map on melilite (light blue) in B. $Ca_{1.2}AlMg_{0.1}Mn_{0.1}Si_{1.1}O_5$ (dark blue) with 30 ppm Mn, and melilite ($Ca_2(Mg_{0.1}Al_{0.8})Si_{1.7}O_7$: brown; $Ca_{1.8}(Mg_{0.1}Al_{0.9})Si_{1.8}O_7$: light blue) with up to 40 ppm Mn. Symbol: * = mineral phase with IPC applied.

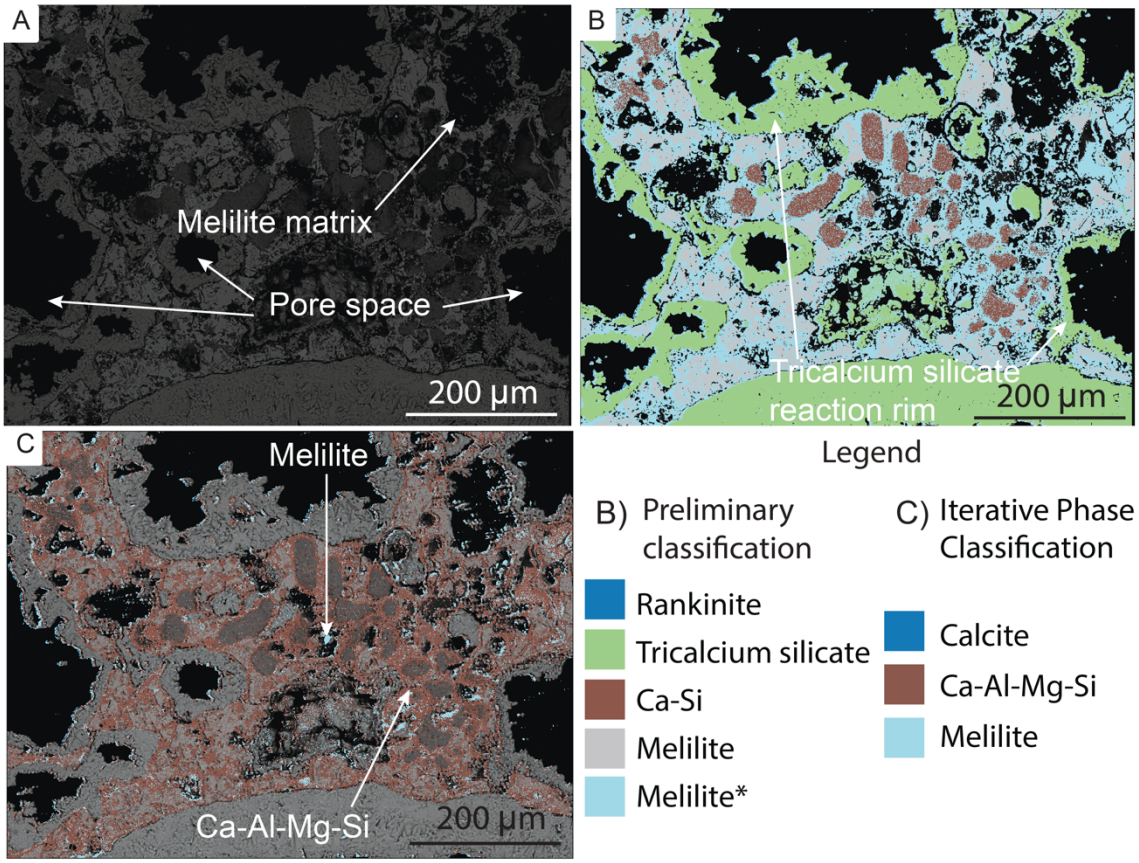

Figure 24. Region W24_T2. A) BSE image. B) Mineral phase map of rankinite (dark blue), tricalcium silicate (green), $Ca_{0.1}Si_{0.9}O_2$ (brown), and melilite ($Ca_{1.5}(Al_{0.8})(Al_{0.3}Si_{0.7})SiO_7$: grey; $Ca_{1.3}(Al_{0.7})Si_{2.2}O_7$: light blue). C) IPC mineral phase map on melilite (light blue) in B. Calcite (dark blue), $Ca_{1.2}Al_{0.6}Mg_{0.2}Si_2O_7$ (brown) with 50 ppm Mn, and melilite (light blue) with up to 40 ppm Mn. Symbol: * = mineral phase with IPC applied.

While region W24_M1 is dominantly pore space (84.66 % of pixels of EDS map), the highest Mn (230 ppm) content is associated with Fe-oxide within the pore space that is surrounded by grains of tricalcium silicate (Fig. 25 and Table 22).

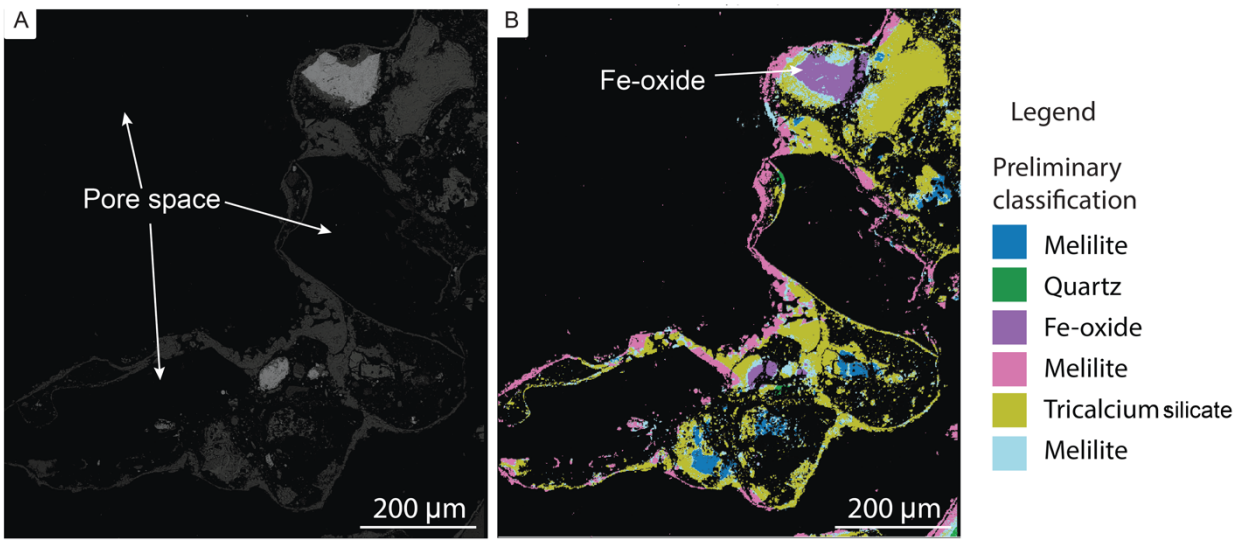

Figure 25. Region W24_M1. A) BSE image. B) Mineral phase map of melilite ($Ca_{1.4}(Mg_{0.1}A_{0.9})(AlSi)O_7$: dark blue; $Ca_{1.9}(Mg_{0.1}Al_{0.6})Si_{1.4}O_7$: pink; $Ca_{1.7}(Mg_{0.2}Al_{0.7})Si_{1.7}O_7$: light blue), quartz (green), Fe-oxide (purple) with 230 ppm Mn, and tricalcium silicate (yellow).

The Ca-Fe-Si phase in W24_T3M2 associated with Mn (190 ppm) localises around higher Al regions or is surrounded by a Ca-Al-Si phase that is exposed to pore space (Fig. 26 and Table 23).

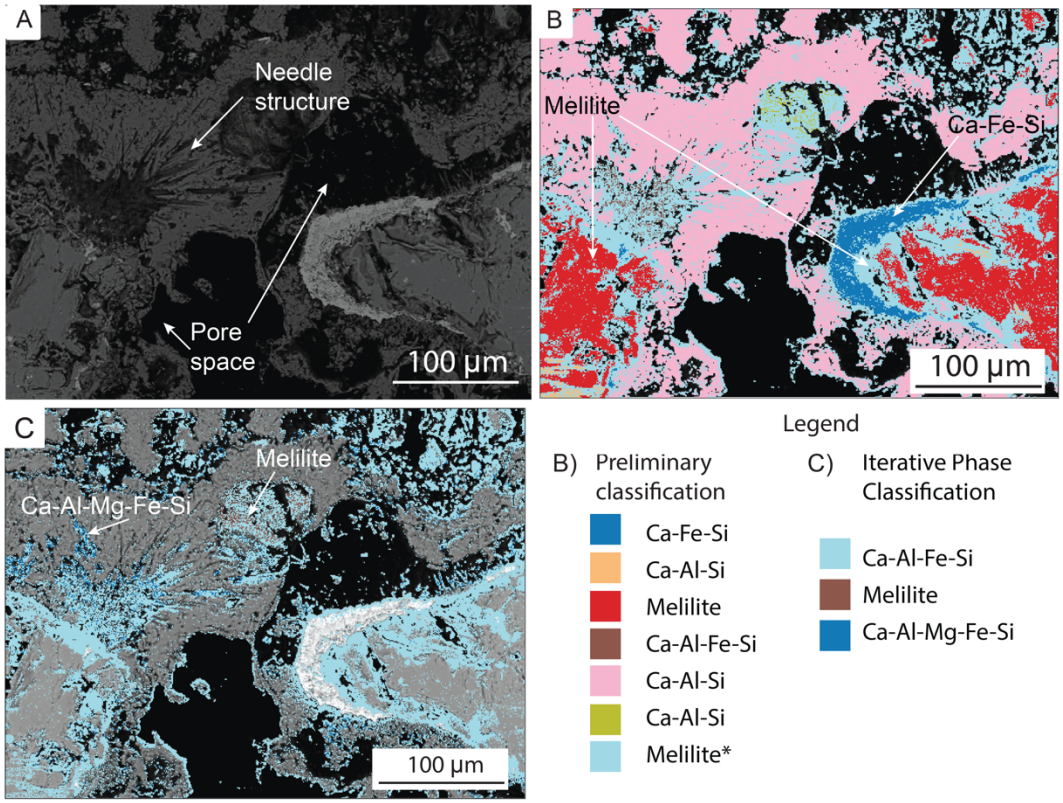

Figure 26. Region W24_T3M2. A) BSE image. B) Mineral phase map of Ca-Fe-Si (dark blue) with 190 ppm Mn, melilite (red) with 40 ppm Mn, melilite (light blue) with 90 ppm Mn, Ca-Al-Fe-Si (light blue), Ca-Al-Si ($Ca_{1.5}Al_{0.5}Si_{2.1}O_7$: orange; $Ca_2Al_{0.3}Si_{0.6}O_4$: pink; $Ca_{1.7}Al_{0.4}Si_{0.7}O_4$: yellow). C) IPC mineral phase map on melilite (light blue) in B. $Ca_{0.1}Al_{0.1}Fe_{1.7}Si_{0.2}O_4$ (dark blue) 160 ppm Mn, $CaAl_{0.7}Mg_{0.1}Fe_{1.2}Si_2O_8$ (light blue), and melilite ($Ca_{1.6}(Mg_{0.1}Al_{0.9})Si_{1.8}O_7$: brown) with 10 ppm Mn. Symbol: * = mineral phase with IPC applied.

Applying the IPC on the W24_T3M2 outliers revealed phases of Ca-Al-Fe-Si, melilite with 10 ppm Mn, and Ca-Al-Mg-Mn-Fe-Si with 160 ppm Mn. In W24_T4, Ti (40 ppm) is associated with melilite in the slag matrix, Mn (10 ppm) is associated with Fe-oxide in close proximity to the clast edge, and Ba (30 ppm) is associated with the melilite outlier phase (Fig. 27 and Table 24).

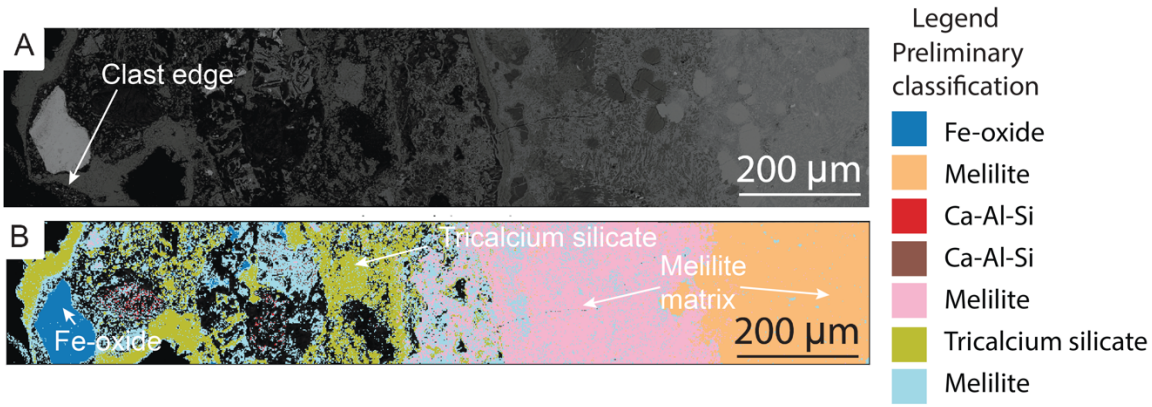

Figure 27. Region W24_T4. A) BSE image. B) Mineral phase map of Fe-oxide ($Fe_{1.7}O_3$: dark blue) with 10 ppm Mn, melilite ($Ca_2(Mg_{0.1}Al_{0.8})Si_{1.6}O_7$: orange with 40 ppm Ti; $Ca_{1.3}(Mg_{0.3}Al_{0.7})(Al_{0.1}Si_{1.9})O_7$: pink; $Ca_{1.6}(Mg_{0.3}Al_{0.7})(Al_{0.2}Si_{0.8})SiO_7$: light blue with 30 ppm Ba), Ca-Al-Si ($Ca_2Al_{0.9}Si_2O_6$: red; $Ca_{0.5}AlSi_2O_6$: brown), and tricalcium silicate (yellow). Symbol: * = mineral phase with IPC applied.

2.3.1.2.6 Microstructures and mineral associations

Melilite often dominates the matrix and varies in composition, evident as exsolution textures or discrete homogeneous regions. Quartz grains usually within the melilite matrix are found within tricalcium silicate (W24_M1: Fig. 25) or in pores near slag clast edges (W26_T3: Fig. 13; W26_T4: Fig.18; W26_T5M2:16). Calcite can comprise reaction rims around slag clasts growing needle structures into the pore space (W26_M4: Fig. 19; W26_T6.1: Fig. 15; W26_T6.2M3: Fig. 17). Wollastonite occurs with Fe-oxides (W27_T2M2: Fig. 10; W28_T1: Fig. 5) or is associated with melilite (W26_T6.1: Fig. 15). Larnite is found within CaO (W25_T1: Fig. 20). Olivine grains occur with clasts of quartz and are surrounded by a rim of calcite (W26_T6.2M3: Fig. 17). Monticellite occurs with clasts of olivine and is surrounded by a rim of calcite (W26_T6.2M3: Fig. 17). Tricalcium silicate matrix displaying exsolution texture (W24_T4: Fig. 27), occurring as remnants of clasts (W24_M1: Fi. 25) and forming reaction rims (W24_T2: Fig. 24) are associated with quartz and melilite. Within the melilite matrix (W24_T1: Fig. 23) semi-round clusters of rankinite grains occur and can dominate with increasing porosity and grains of quartz and CaO. Anorthite can comprise the matrix (W25_M2: Fig. 22; W27_T2M2: Fig. 10). Ca-oxide forms within the matrix (W28_T1: Fig. 5; W28_T2M2: Fig. 7; W25_T1: Fig. 20; W25_M1: Fig. 21), as a reaction rim with needle structures growing into a pore (W28_T1: Fig. 5), and as clasts with slightly varying composition (W25_M1: Fig. 21). The Fe-oxide FeO displays exsolution texture (W27_M4: Fig. 12) and zoning (W27_M4: Fig. 12) in addition to forming nuggets within cracks (W27_T1M1: Fig. 9) and isolated in pore space (W28_T2M2: Fig. 7). Fe_2O_3 mineralisation resembling a melted state and can be association with a CaO reaction rim. The Ca-Fe oxide calcio-wüstite can form a rim around melilite (W24_T3M2: Fig. 26), as grains in the pore space near a calcite reaction rim (W26_M4: Fig. 19), and surround anorthite matrix sharing a similar cracking texture to FeO (W27_T2M2: Fig. 10). Pyrite occurs with both zoned FeO (W27_M4: Fig. 12) and where fractures in those grains have been filled (W28_M1: Fig. 8). Anhydrite occurs in the melilite matrix forming needle structures (W26_T3: Fig. 13). Occasionally, the stoichiometric calculations did not yield mineral phase formulas previously reported in iron or steel slag. Horizon 26 had the most non-conforming phases.

2.3.2 Iterative Phase Classification

Results from applying the IPC on select mineral phases and outliers were variable and are categorised as: 1) IPC revealing trace metal (s) that were not identified in the preliminary clustering (Ba, Fe: W28_T2M2; Mn: W26_T1; Mn: W25_T1; Ba, Mn: W25_M1; Mn: W24_T1; Mn: W24_T2); 2) IPC not revealing metals that were identified from the preliminary clustering (Ti: W26_T6.1); 3) IPC confirming no trace metals (W28_T1, W28_M1, W26_T4); 4) IPC confirming trace metals identified from the preliminary clustering (Mn: W27_T2M2; Mn: W26_T5M2).

'Coincidence peaks' were detected at In Lβ1(3.487 keV) and Sn Lα1 (3.443 keV) in 14 phase spectra produced from both the first iteration and the IPC steps. High resolution BSE imaging (5 to 15 keV) and point analysis in Aztec that did not reveal the trace metals support this incorrect signal binning.

2.4 Discussion

Common quantification methods (i.e., MLA, QEMSCAN) require considerable domain knowledge of samples for accurate results. Instead, the IPC workflow that leverages unsupervised machine learning enables quick and reproducible results by modifying the simple parameters of each algorithm. The abundances of trace Ba, Fe, Mn, and Ti and 37 mineral phases were quantified from the five stratigraphic horizons. This was done without a comprehensive list of the possible slag mineral phases that the user would need and use to populate the input mineral library for mineral calculation and identification by MLA (Fandrich et al., 2007). The data-driven approach that leverages the density of measurements made helps users decide where to perform more detailed analysis. It does this by requiring IPC analysis based on statistical properties of each phase, rather than subjective and error-prone details in BSE images.

2.4.1 Dimensional reduction and clustering

Applying a dimensional reduction and clustering algorithm on the EDS data provides a chemical correlation of the segmented mineral phases to the physical microstructures of the samples. Subsequent standardless quantification and stoichiometric mineral phase calculations of the clustered NMF components reflect even the slightly variable compositions evident in the contrasting densities in the associated BSE image (e.g., W28_T1: Fig. 5 and Table 2; W26: Fig. 14 and Table 10; W26_T6.1: Fig. 15 and Table 14). This is attributed to the non-negative constraint of NMF that forces clustering in positive dataspace which directly represents microstructures in the samples. The normalised intensity spectra of the six NMF components in Figure 4 represent the reduced EDS data into components directly associated with the various microstructures evident in the BSE. Jany et al. (2017) and Teng and Gauvin (2020) used NMF compared to PCA for phase identification, which included rare earth metals, and found NMF more effective due to the smaller signal reduction. These findings are relevant for choosing which dimensional reduction algorithm to use in this study that has a similar aim of trace metal identification. It is worth considering that without the non-negative constraint defining NMF, reducing data dimensionality using PCA allows components to occupy more dimensional space and subsequent clustering could reflect more of the spectral data variance. However, with the focus of this research on developing an optimised method for quantifying slag mineralogy

and metal concentrations and identifying the microstructures where the trace constitutes are localising, representing the data variance in maximised data space is not worth compromising the direct physical representation NMF components have to the sample. PCA is frequently applied to reduce noise prior to spectral data processing (Lucas et al., 2013; Teng & Gauvin, 2020), especially when the abstract nature of the loading does not interfere with further interpretation such as mineral phase characterisation. This suggests PCA might be the more appropriate choice for studies that do not require detailed microstructural information. Therefore, NMF is the more suitable choice for this study as it can handle overlapping signals in microstructural data, allowing it to directly represent the physical microstructures of the slag.

Applying HDBSCAN enabled the identification of mineral phases with slight compositional variation. The phase maps from all regions except two (W28_T3M3 and W25_M2) depict separate clusters with the same elemental components but with varying quantities. This segmentation between mineral phase members occurs in silicates (melilite, Ca-Al-Fe-Si-S, Ca-Al-Si-S, Ca-Al-Fe-Si, Ca-Al-Fe-Si, Ca-Al-Mg-Fe-Si, Ca-Al-Si) and oxides (Ca, Fe). Wilkinson et al. (2019) recognised image segmentation from clustering strongly influences mineral phase identification and quantification. As such, the combination of using HDBSCAN that can identify clusters with varying densities or that are nested and manipulating the 'min_cluster_size' and 'min_samples' hyperparameters to optimise the image segmentation are inferred to explain the identification of slight chemical variation in the mineral phases. Computing the number of pixels comprising each mineral phase following the first clustering attempt provided a reference point to test alternative parameter values and combinations. The range of the number of clusters identified and the percentages of outliers can be attributed to the heterogeneous nature of slag (e.g., ore rock, fluxes, scrap metal).

Traditional segmentation methods requiring labels would not be capable of resolving the complex slag mineralogy found in this study. Alternatives to mineral phase segmentation by clustering including converting elemental f-ratio maps into phase maps to decomposed EDS spectra (Teng & Gauvin, 2020), and directly loading the dimensional reduction components into the Bruker ESPRIT software (Jany et al., 2017) could improve segmentation. However, the previously stated benefits of using a hierarchical, density-based clustering algorithm would be compromised. Furthermore, optimisation of the mineral phase identification that leverages multiple statistically robust algorithms to process the data and drive the analysis of significant microstructures and trace metals would not be possible. While it is outside the scope of this research, steps to optimise clustering such as the hyper-parameter described by Parker and Barnard (2019) that recognises the characteristics expected of successful clustering, could be integrated into future workflows. The success of clustering the NMF components with minimal manual inspection to reveal slight compositional variation in addition to trace metals from big data sets provides valuable insight for optimising unsupervised learning approaches aimed at material characterisation.

2.4.2 Iterative Phase Classification

More specific mineralogic and chemical compositions were identified from the 15 regions that IPC was applied to, including six where trace metal (s) not identified in the preliminary clustering were revealed. This included Ba (40 ppm to 140 ppm) in melilite, Fe

(780 ppm to 1020 ppm) in melilite, and Mn (10 ppm to 130 ppm) in Ca-Al-Mg-Si, Ca-Al-Fe-Si, Fe-Si-S, and melilite. The more precise mineral phase segmentation and trace metal localisation from IPC provide a chemical and spatial association that helped to distinguish the five stratigraphic horizons. In letting the percentage of pixels of the outliers or another cluster from the EDS map (>30%) dictate which cluster to apply IPC, higher microstructural detail was recovered. As such, the results from applying unsupervised learning methods to highly dimensional data can be used to develop data controls. The traditional quantification methods previously listed lack this optimisation capabilities that enabled easily tailored data-driven analysis of the Warton slag deposit A. The more specific compositional distinction between samples that not only revealed trace metal which would have been missed, but also helped to associate the metallurgical process responsible for the slag, demonstrates unsupervised learning can resolve the challenges of not knowing *a priori* the representative constitutes (Kotula et al., 2006).

Some textural variations evident on the BSE images that were not segmented even after IPC could reflect the limitations of the algorithms. Using a specific BSE contrast and brightness calibration to standardise BSE image grey scale could provide an additional differentiation criterion for chemical composition identification of minerals that crystallisation as solid solutions resulting in similar-looking spectra (Schulz et al., 2020).

2.4.3 Quantification

The mineral phases and trace metals identified in this study are dominantly consistent with those reported in both modern and legacy iron and steel slag (Piatak et al., 2021). Ba (140 ppm), Fe (90 ppm to 1300 ppm), Mn (10 ppm to 230 ppm), Ti (20 ppm to 120 ppm), and Zn (30.28 ppm) from the preliminary clustering and Ba, Fe, and Mn from IPC differentiate the stratigraphic horizons and demonstrate CRM localises in this legacy slag deposit (Table 26).

Table 26. Summary of trace element abundances quantified (ppm) from the Warton slag deposit B and compiled by Piatak et al. (2021).

	This study		Piatak et al. (2021)		
Metal (ppm)	Preliminary Clustering	IPC	Modern BF	Pre-1900 BF	Steel and Legacy sites
Ba	140	40 - 140	417	579	415
Fe	90 - 1300	120 - 780	26000	339000	196000
Mn	10 - 230	20	8000	7000	49000
Ti	20 - 120	ND	7000	5000	6000
Zn	30	ND	67.7	15.4	650

ND = not detected

The chemical compositions of mineral phases that did not conform to those previously identified are likely the result of the slag cooling. Similar to the spectral artefact produced

from a Si-Kα sum peak during the attempted detection of low levels of Sn in a SiO_2 matrix (Hurban, 2003), 'coincidence peaks' resulted from the pulse-pile up of Si Kα X-rays in nine phase spectra, appearing as In Kβ X-rays. These spectral artefacts identified prior to the final quantification and mineral calculations highlight the importance of optimising SEM settings to achieve the best EDS data quantification and avoid misplaced EDS events that distort spectral results (Newbury & Ritchie, 2013).

2.4.4 Resource recovery

The quantification results confirm that both iron and steel slags are represented in the deposit from the different slag horizon compositions which is inferred as the result of metallurgical processes evolution. Olivine, anorthite, more frequent melilite, and higher Fe-oxide content typical of iron slags, suggest the horizons W24, W26, and W28 are associated with pre-1900 iron recovery. Separating the iron slags are two horizons, W25 and W27, with lower Fe-oxide and higher Ca-oxide content, characteristic of steel slag and reflects the use of Ca-rich fluxes that improve slag formation (Piatak et al., 2021). Thus, it is inferred that the inland legacy deposit A represents the simultaneous iron and steelmaking at the Carnforth Iron Works from the quantification results. While iron and steel production are confirmed at Carnforth, historic documentation does not specify which metallurgical process is responsible for which deposit (Harris, 1960; Riden & Owen, 1995; Taylor, 2013). Higher Al_2O_3, MgO, and trace metal content in the stratigraphically lowest horizon could be evidence of the early Bessemer iron pig production which likely would have been less efficient at metal recovery.

The quantified rare metal content of Ba, Fe, Mn, and Ti in the slag deposit is lower compared to that reported by Piatak et al. (2021) from pre-1900 BF (439 ppm to 539 ppm less of Ba; 337,700 ppm to 3378,910 ppm less of Fe; 6,770 ppm to 6,990 ppm less of Mn; 4,880 ppm to 4,980 ppm less of Ti), and steel and legacy slag sites (275 ppm to 375 ppm for Ba; 194,700 ppm to 195,910 ppm less of Fe; 48,770 ppm to 48,990 ppm less of Mn; 5,880 ppm to 5,980 ppm less of Ti) (Table 26). The quantified Zn content is 14.6 ppm higher than that reported from pre-1900 BF and 620 ppm lower than that reported from steel and legacy slag sites (Piatak et al., 2021) (Table 26). However, compared to the metal abundances from the horizons W25 and W27, the relatively higher Mn and Ti quantified in horizon W26 (at most 80 ppm to 150 ppm more Mn; at most 100 ppm more Ti) and the relatively higher Mn quantified in horizon W24 (at most 150 ppm more) associated with the iron slag, differentiate the two types of slag (Table 26).

The 37 studies that Piatak et al. (2021) compiled to summarise the chemical composition of pre-1900 BF, modern BF, steel, and legacy slag, used a variety of techniques including XRD, X-ray fluorescence spectroscopy (XRF), laser ablation inductively coupled plasma mass spectrometry (LA-ICP-MS), and inductively coupled plasma-atomic emission spectrometry (ICP-AES). While these four analytical methods can be used for element identification and quantification, they have limitations and lack the capabilities of the approach detailed in this study. The presented method bypasses pre-existing mineral libraries used by XRD for data comparison (M. Lee, 2017). Instead, the standardless quantification and stoichiometric calculations applied to the clusters enabled the quantification and identification of unreported mineral phases and trace Ba, Fe, and Mn. Furthermore, as a result of using SEM-EDS to collect the data instead of the more

destructive ICP-AES (Murray et al., 2000), and using NMF to process the spectral data, the quantified metals are spatially associated with the mineral phase that they localise in, and to the host microstructures. This facilitated the microstructural analysis to determine that Ba, Fe, Mn, Ti, and Zn dominantly localise in reactive phases in close proximity to pores (melilite: Fig. 7; Ca-Al-Si-S: Fig. 9; anorthite, Ca-Al-Mg-Fe-Si, Ca-oxide: Fig. 10; Fe-oxide: Fig. 11; melilite: Fig. 14; melilite, Ca-Al-Si: Fig. 15; Ca-Al-Fe-Si: Fig. 16; Ca-oxide, larnite: Fig. 20; Ca-Si, melilite: Fig. 21; Fe-oxide, Ca-oxide: Fig. 22; Ca-Al-Mg-Si, melilite: Fig. 24; Fe-oxide: Fig. 25; Ca-Fe-Si, Ca-Al-Mg-Mn-Fe-Si, melilite: Fig. 26; Fe-oxide, melilite: Fig. 27). Even though XRF and LA-ICP-MS can quantify elemental compositions while preserving spatial correlation to the host mineral phase (Durrant, 1999; Sharma, 2012), it cannot identify mineral phase as the method presented in the study does by clustering and performing stoichiometric mineral composition calculations.

The influence of ‘Biogeochemical Weathering’ (Potysz et al., 2018) which may cause the release of metals from the slag deposit in the environment would impact the potential CRM recovery estimates. Analysing a combination of drill core and samples from the surface of the deposit and with increasing depth into the horizon could be used to account for ‘Biogeochemical Weathering’ impacts. Thus, providing more precise metal content estimates for legacy slag deposits.

The smaller concentrations of Ba, Fe, Mn, and Ti (Table 25) compared to those that are typically found in pre-1900 BF, steel, and legacy slag sites make non-bio hydrometallurgical processing impractical for resource recovery from this deposit as this method is favoured for higher concentrations of recoverable metals (Habib et al., 2020). Alternatively, biohydrometallurgical processing which uses microorganisms to dissolve metals from their mineral sources is an environmentally friendly alternative to conventional recovery methods since it produces smaller quantities of waste (Brandl & Faramarzi, 2006; J. Lee & Pandey, 2012) and has lower energy and landfill space demands (Habib et al., 2020). The reactive phases previously listed offer more surface reaction potential and allow access for reactive fluids to grain boundaries (Librandi et al., 2019; Postma, 1993; Shen & Forssberg, 2003). Notably, bioleaching with Mn solubilising microorganisms has been shown to recover Mn from lean grade ores (Ghosh et al., 2016; Panda et al., 2015; Srichandan et al., 2013). Thus, the findings of this study, determined by identifying trace metal localisation and the potential for bioleaching with the data-driven microstructural approach, support the viability of extracting the revealed trace metals with bioleaching. Employing bioleaching on the industrial scale could reduce treatment expenses for slags with lower metal concentrations (Solisio & Lodi, 2002). Furthermore, by linking the metallurgical processes to the slag composition and metal content, metal recovery from legacy industrial waste deposits could be improved. This could facilitate the development of more precise resource recovery methods with lower energy demands, environmental impact, and costs, ultimately promoting the integration of CE practices into industrial waste management.

2.5 Conclusion

The data-driven unsupervised machine learning approach outlined in this study was used to quantify and identify the mineral phases and trace metal content from a legacy iron and steel slag deposit. Using dimensional reduction and clustering enables efficient processing

of many high-dimensional spectral datasets. The chemical composition of the mineral phases identified by the standardless quantification and the stochiometric mineral calculations is associated with the microstructures where they are localising. Using unsupervised learning methods (1. NMF, 2. HDBSCAN, 3. IPC) for quantification decreases human-dependent data processing and the need for substantial domain knowledge of samples. NMF is more suitable for identifying the mineralogy and the trace metal content as directly represents the physical microstructures of the slag. Application of the IPC step improves the accuracy of trace metal identification. From both confirming the presence of Ba, Fe, and Mn found from preliminary clustering, and revealing Ba, Fe, and Mn that was not initially identified, the capabilities of this approach to drive further analysis and act as data control are demonstrated.

Identification of the multiple metallurgical processes represented in the legacy slag deposits allowed for the recommendation of more precise and environmentally sensitive metal recovery methods. The less energy-intense bioleaching approach that shows promise is suggested to help release Mn from iron production slags due to Mn concentrating in mineral phases in close proximity to pores and reaction rims, facilitating bioleaching solutions' access.

By leveraging highly dimensional spatially and chemically correlated datasets, the metal content can be quantified to inform the potential for CRM recovery from legacy industrial wastes. This insight can then be used to optimise slag repurposing and resource recovery methods, ultimately integrating CE principles into industrial waste management.

3. Chapter 3: Heterogeneous lithification across a legacy coastal slag bank: the creation of new sedimentary rock from anthropogenic material

3.1 Introduction

Artificial ground is a defining characteristic of the Anthropocene resulting from humans acting as geological agents in landscape evolution (Cooper et al., 2018; Price et al., 2011; Wilkinson, 2005). Heterogenous in nature, artificial ground ranging from spoil heaps from deep mining to furnace slag and waste tips (Price et al., 2011) contributed more than 316 gigatonne (Gt) of sediment in 2015, greatly surpassing the annual sediment supply by major rivers to oceans (more than 24 times) (Cooper et al., 2018). Population growth, a wider range of minerals being exploited, and technological advancements are increasing the volume of anthropogenic sediment (Cooper et al., 2018).

As well as being significant in terms of volume, artificial ground deposits also pose a range of challenges (e.g., toxic metal contamination: Hobson et al. (2017)) but also many opportunities. Slag generated from the smelting of ore, coke, and fluxes to be casted into pig iron or used for steel making can be reused due to its high stability and ability to neutralise acidity (Ahmedzade & Sengoz, 2009; Huijgen et al., 2005; Piatak & Ettler, 2021). The world iron and steel slag production in 2022 is estimated between 299 and 354 Mt and between 172 and 263 Mt (USGS, 2023), respectively and may increase to 2.2 and 0.7 Gt/yr^{-1} by 2100 (Pullin et al., 2019). The significant quantities of waste produced during the Industrial Revolution in the UK could be used in Circular Economic practices for sustainable action (Branca et al., 2020). Possible resource recovery (Gomes et al., 2016; Habib et al., 2020) from the estimated 490 to 640 million tonnes of slag generated in the UK since 1875 (Renforth et al., 2011) would reduce the extraction of new raw materials (Bianco & Porisiensi, 2016). Mineral carbonation as a form of greenhouse gas removal (Sanna et al., 2014) mimicking natural weathering processes (Doucet, 2010; Gomes et al., 2016; Huijgen et al., 2005) has been applied to alkaline iron and steel slags (Eloneva et al., 2008; Huijgen et al., 2005; Huijgen & Comans, 2006; Pan et al., 2012). The passive in-situ storage of atmospheric CO_2 documented in legacy slag-dominated artificial ground (MacDonald, et al., 2023a; MacDonald,, et al., 2023b; Mayes et al., 2018; Pullin et al., 2019) aids in the removal of greenhouse gasses. Considering over 190 million tonnes of legacy iron and steel slag exist at current and former workings across the UK (Riley et al., 2020), and the increasing volumes of artificial ground in general (Cooper et al., 2018), it is necessary to understand the processes altering these materials.

Given this range of potential opportunities which artificial ground may offer, it is important to understand how processes such as lithification (MacDonald, et al., 2023a) affect their physical and mechanical properties. As the preservation of artificial ground is contingent on its ability to endure the transformative and erosional effects of nature and humans (Price et al., 2011), the degree of lithification of the typically loose and unconsolidated material will yield variable chemical and physical changes (MacDonald, et al., 2023a). Instead, most studies investigating the long-term fate of legacy slag deposits are focused on the carbon capture potential (Chukwuma et al., 2021), emplacement method (Pullin et al.,

2019), drainage waters (Mayes et al., 2018), and the surrounding environment (Yi et al., 2012).

Lithification of a slag deposit by calcite precipitation from ingassed atmospheric CO_2 reacting with dissolved Ca from the slag has been documented at a small inland legacy slag deposit at Glengarnock, Scotland (MacDonald, et al., 2023a). However, in the UK, volumetrically the majority of legacy slag is located in coastal settings (Riley et al., 2020), where more chemically complex interactions with seawater will occur. This study documents the mechanisms driving the lithification of a coastal legacy slag-dominated artificial ground deposit through X-Ray Diffraction (XRD), EDS, thermogravimetric analysis (TGA), and stable Carbon and Oxygen isotope analysis. We present new insight into the influences natural weathering processes and various water sources have on the lithification of artificial ground, which will inform future repurposing (Renforth, 2019)

3.2 Materials and methods

Slag samples were collected in a transect orthogonal to the sea across the Warton slag heap in South Lancashire, England (54.129483°, -2.80018°: Fig. 28) where iron and steel works were active from 1864 to 1929 (LCC, 2006; Riden & Owen, 1995).

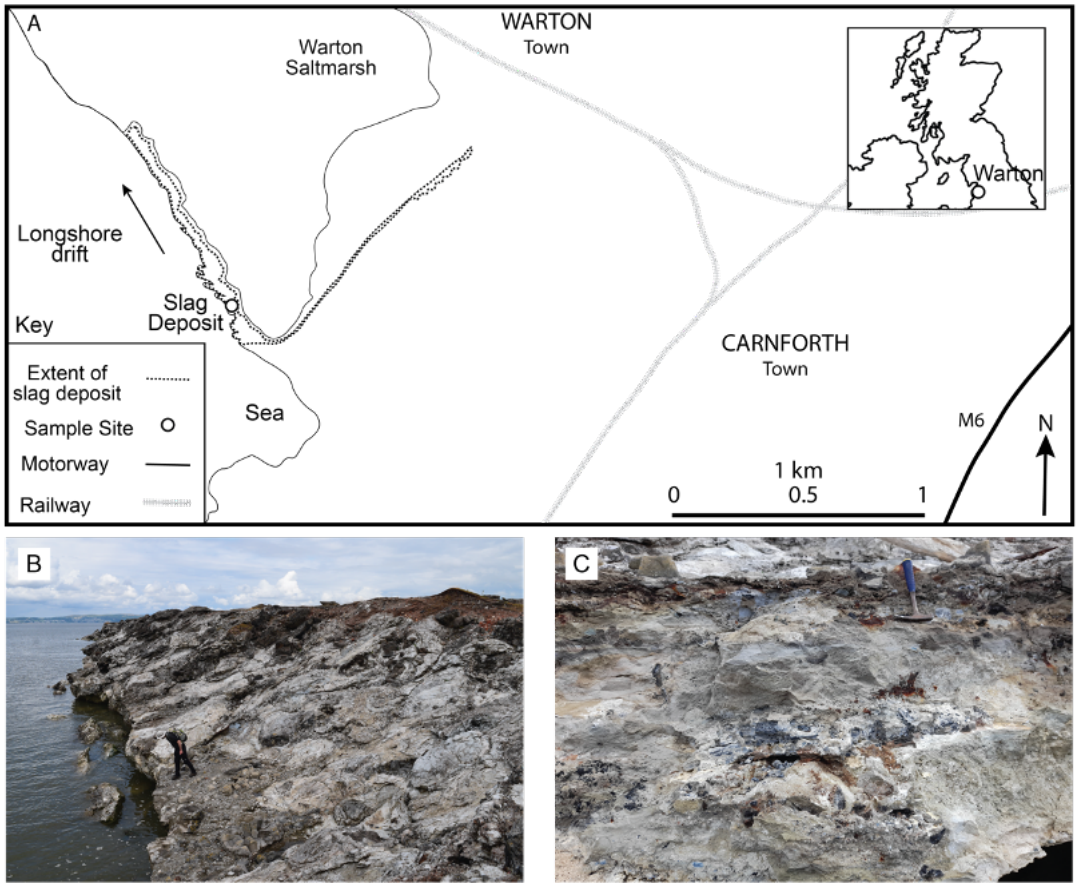

Figure 28. A) Location of sampling site in South Lancashire, England. B) Field photograph showing the lithified nature of the seaward side of the approximately 10 m thick deposit; 1.82 m height person for scale. C) Field photograph showing lithified vertical succession through the lower part of the seaward side of the deposit, where samples W5-W9 were obtained from.

Historical accounts suggest the slag was piled to form sea embarkments and has continued to prevent extensive erosion at the Warton Saltmarsh (Harwood & Scott, 1999; Skelcher, 2014). All samples appear to be made of particles or clasts of grey slag with a cream-colored material between that vigorously effervesces when in contact with diluted hydrochloric acid. Samples W5, W6, W7, W8, and W9 (Fig. 28B, C and S1A-E) were collected below the mean high watermark (MHWM) in the intertidal zone and below where W13 was collected (Fig. S1F). Sample W15 (Fig. S1G) is from above the MHWM in a zone washed by seawater during storms, whereas W18 (Fig. S1H) dominantly experiences rainfall on the top surface of the deposit. Sample W20 (Fig. S1I) is topographically lower and from the eastern side of the deposit, where inland the Warton Saltmarsh contributes more saline water to rainwater puddles where W23 was collected (Fig. S1J).

Samples were cut using a cool-water diamond saw, pulverised with an agate mortar and pestle, and passed through a 53 μm sieved for TGA and XRD analysis. Cream-coloured material from between slag clasts (hypothesised to be a carbonate mineral) was drilled for stable C and O isotope analysis.

Thermogravimetric analysis was conducted using an SDT Q600 (TA Instruments, USA) under Ar atmosphere at 100ml/min with a 10° C per minute heating rate from 0 °C to 1000°C at the School of Chemistry. The weight loss at decomposition temperatures for slag components was determined using the modified Thermogravimetric analysis - derivative TGA-DTG interpretation (Chiang & Pan, 2017) to quantify carbonate content (Table S1).

Sample mineralogy was identified by XRD on a Malvern Panalytical Empyrean with PIXcel3D-Medipix3 1x1 detector using Cu Kα radiation (wavelength 1.541874 (Å)) at the School of Chemistry, University of Glasgow. Data collection was collected in Bragg-Brentano reflection geometry 5-80° 2θ, with a step size 0.0131°. Phase identification was performed with reference to the Crystallographic Open Database.

$\delta^{13}C$ and $\delta^{18}O$ values, to determine the source of CO_2 in the powdered cream-coloured material, were acquired using an Isoprime 100 mass spectrometer at the School of Geographical and Earth Sciences, University of Glasgow. The drilled powder was acidified using phosphoric acid (≥1.90 SG) and heated for 1 hour at 60 °C on an Elementar GasBench. Triplicates of the sample were run and the average reported with 1 standard deviation except for W6 as the carbonate content was below the detection level. The reference standards NBS-18 and IAEA-603 were used and reported values were calibrated to Vienna-Pe De Belemnite (V-PDB). The secondary standard IA-RO22 (Iso-Analytical Ltd.) was used to calibrate linearity for more depleted values of $\delta^{13}C$ and $\delta^{18}O$. The analytical uncertainty for the $\delta^{13}C$ and $\delta^{18}O$ analysis (0.10 and 0.1 per mille ‰, respectively), was determined from IAEA-603 (n=39) measurements during the analytical bath.

Polished thin sections with a ~20 nm conductive carbon layer from selected samples were imaged and mapped by SEM-EDS analysis using a Zeiss Sigma VP-FEG SEM equipped with a BSE detector and an Oxford Instruments Ultimax 170 mm^2 EDS detector at the GEMS facility at the School of Geographical and Earth Sciences, University of Glasgow. EDS mapping was conducted with an accelerating voltage of 20 keV, in a high vacuum

using high current mode, with a working distance of 8.0 mm, and an aperture of 60 µm. EDS maps that were acquired and processed using Oxford Instrument AZtec ® 4.3 and AZtec ® Flex software have had the AZtec ® Trumap function applied which resolves element peak overlap and removes artefacts and background.

3.3 Results

Visual inspection during fieldwork indicates the seaward side of the deposit comprising a sloping bank experiencing sea washing has more cream-coloured material covering the slag than on the top of the heap. Gehlenite ($Ca_2Al_2SiO_7$) and/or åkermanite ($Ca_2MgSi_2O_7$) (end-members of the melilite solid solution) were identified by XRD analysis (Table 27) in all but one (W6) of the ten samples, with other common slag phases such as larnite (Ca_2SiO_4) and pseudowollastonite ($CaSiO_3$) occurring in a smaller number of samples. The CSH minerals thaumasite $Ca_3Si(OH)_6(CO_3)(SO_4)\cdot 12H_2O$) and jouravskite ($Ca_3Mn^{4+}(SO_4)(CO_3)(OH)_6\cdot 12H_2O$) occur in several samples, while all except for one (W6) sample contain carbonate minerals (dominantly calcite ($CaCO_3$) but occasionally aragonite and vaterite).

Table 27. Mineral phases identified by XRD of slag from South Lancashire, England. Symbols: * = detected; - = not detected.

Sample	W5	W6	W7	W8	W9	W13	W15	W18	W20	W23
Gh	*	-	*	*	*	*	*	*	*	*
Ak	*	-	*	*	*	-	*	*	-	*
Cal	-	-	*	*	*	*	*	*	*	*
Arg	*	-	-	-	*	-	-	-	-	-
Vtr	-	-	*	*	-	-	-	-	*	-
Qtz	*	-	-	-	-	*	-	*	-	-
SiO_2	-	*	-	-	-	-	-	-	-	-
Rnk	-	-	-	-	-	*	-	-	-	*
Lrn	-	-	*	-	-	-	-	-	-	-
Fa	-	*	-	-	-	-	-	-	-	-
Wus	-	*	-	-	-	-	-	-	-	-
Lws	-	*	-	-	-	-	-	-	-	-
Jouravskite	*	*	*	*	-	-	*	-	-	-
Thaumasite	*	*	-	-	-	-	*	-	-	-
Ettringite	-	-	-	-	-	-	-	-	*	-
Pseudo-wollastonite	-	-	-	*	*	*	-	-	*	-

There was some correlation between mineralogy and the location of the sample along the transect from the seaward side to the landward side. Notably, samples W5 and W6 from the intertidal zone containing thaumasite and jouravskite do not occur with calcite. Gehlenite and åkermanite are absent in W6 and fayalite ($Fe^{2+}{}_2SiO_4$), wüestite (FeO), and lawsonite

($CaAl_2(Si_2O_7)(OH)_2 \cdot H_2O$) are associated with the elevated thaumasite and jouravskite content. The Ca-rich silicates pseudowollastonite and rankinite ($Ca_3Si_2O_7$) occurring around the MHWM (W13) are not present in samples from the top of the slag bank (W18).

Different regions of the deposit show variable textures and spatial distribution of elements within microstructures in the multi-element EDS maps from the SEM analysis (Fig. 29).

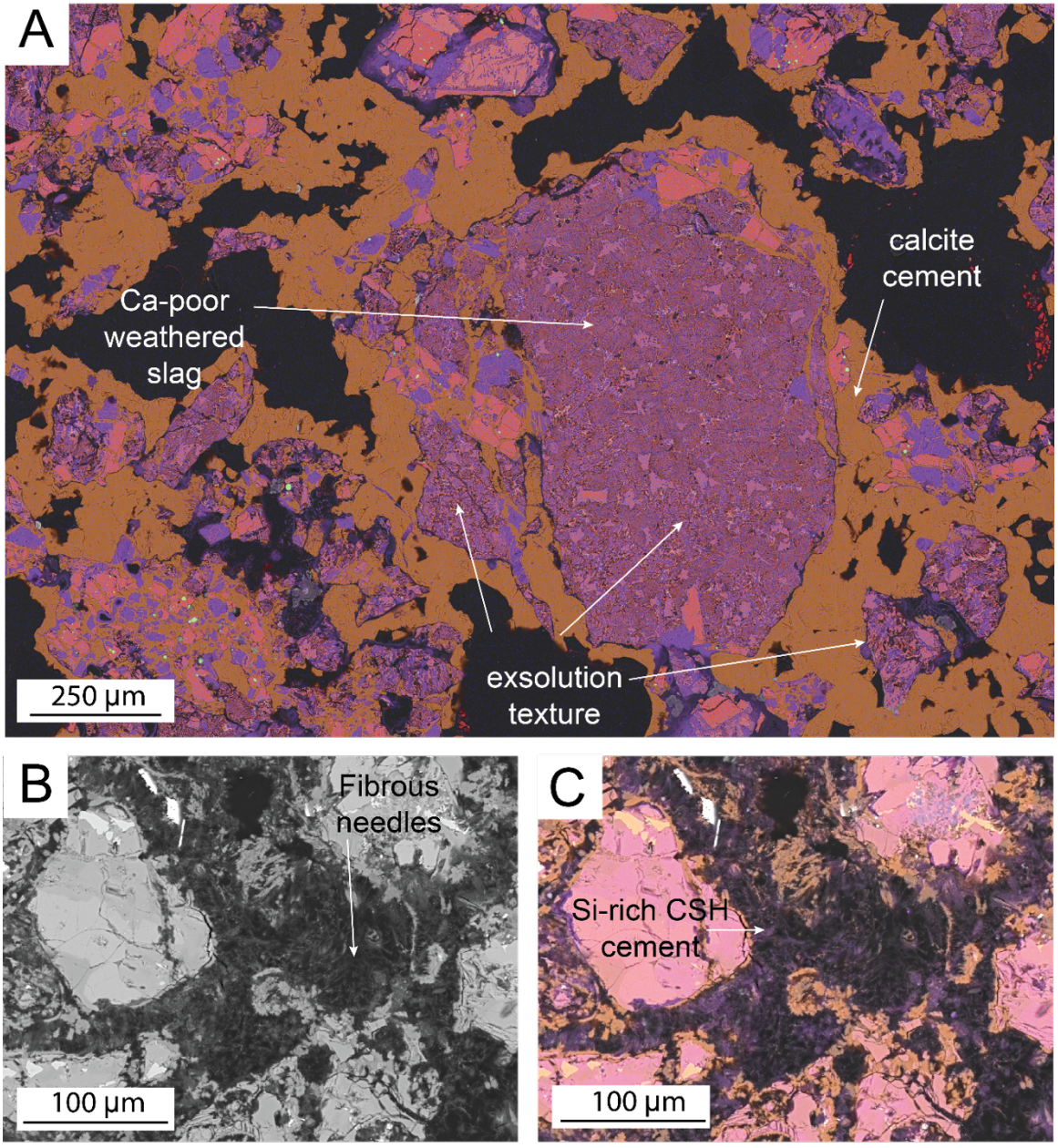

Figure 29. SEM analysis of microstructures. A) EDS map (orange = Ca; purple = Si; blue = Mg; red = Al; green = Fe) showing calcite cement lithifying slag clasts together. Weathered slag is Ca-poor where there is Si-rich exsolution texture. B) BSE image showing fibrous needle structures between slag clasts. C) EDS map of the same area as B showing the Si-rich CSH cement lithifying slag clasts together.

The slag dominantly comprises clasts often displaying exsolution textures where the Si-rich portions can vary in size (50 µm to 750 µm) and concentration. The finer-grained Si-rich regions are associated with weathered slag that is Ca-poor and more porous (Fig. 29A). The material cementing clasts together differ in size, shape, texture, and proportions

of Ca and Si. The cement from below storm wave base (W17) is Ca-rich, varies in thickness from ~10 µm to ~ 175 µm, and forms an amorphous-shaped network that surrounds the slag clasts (Fig. 29A). The cement from the intertidal zone (W1) is Si-rich and forms fine fibrous needles that both fill pores and surrounds Ca-rich rims on the exterior of clasts (Fig. 29B, C).

Thermogravimetric analysis of the slag samples recorded weight loss spanning 628 °C to 759 °C with carbonate content reaching 16.2 wt% on the top of the bank (W18) and decreased towards the seaward side to 0.6 wt% in sample W5 (Fig. 30).

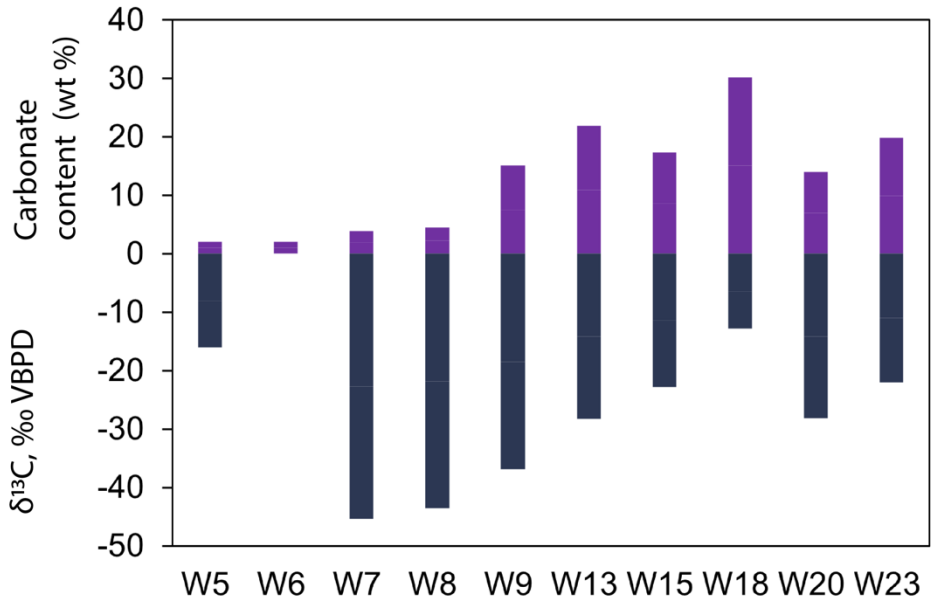

Figure 30. Carbonate content of the slag samples and $\delta^{13}C$ values of the cream- coloured material from TGA and stable isotope analysis, respectively. No $\delta^{13}C$ data for W6.

Weight loss exceeding 105 °C associated with the expulsion of surface water up to 200 °C, and the dehydration of crystalline water from weight loss between 400 °C to 500 °C, corroborates the presence of the CSH in samples W5 and W6. Carbon and oxygen isotopic analysis of the powdered cream-coloured material between and around the slag clasts gave $\delta^{13}C$ values between -6.4 ‰ and -22.7 ‰ and $\delta^{18}O$ between -4.2 ‰ and -11.3 ‰ (Fig. 30). There is a correlation between samples with more depleted (-22.6 ‰: W7) $\delta^{13}C$ values in closer proximity to the sea, whereas samples from the top of the slag bank (farther from the sea) were less depleted (-6.4 ‰: W18). The sample from within a puddle on the saltmarsh side of the deposit (W23) is similarly depleted to that of those exposed to seawater during storms (W15).

3.4 Discussion

Similar material found lithifying rock-like masses of slag that is associated with the Glengarnock Steelworks in North Ayrshire, Scotland is dominated by calcite (MacDonald et al., 2023a). Calcium from the edges of the slag clasts sourcing the calcite cement is leached by water (MacDonald et al., 2023a; Mayes et al., 2018) from the Kilbirnie Loch (a

freshwater lake) as in Equation 1 (Equation 1: Mayes et al., 2018; Pullin et al., 2019), where the slag forms approximately a quarter of the lake shoreline.

$$Ca_2SiO_4 + 4H_2O \rightleftharpoons 2Ca^{2+} + 4H_4SiO_4 + 4OH^- \quad (1)$$

As the lake water is driving calcite precipitation, the fluctuating level allowed for leached Ca to react with temporarily isolated highly alkaline water that was pooling on the rough surface of the slag heap, promoting the ingassing and hydroxylation of atmospheric CO_2. The strongly negative $\delta^{13}C$ value recorded at Glengarnock (-20.05±0.23 ‰) supports the interpretation that the calcite cement comprises atmospheric CO_2 and that there was minor dissolved inorganic carbon (DIC) equilibration in the pooled water prior to calcite precipitation (MacDonald et al., 2023a). While the stockpiled slag from Glengarnock is in an inland lake, most legacy iron and steel slags in the UK were deposited in coastal settings (Riley et al., 2020) such as Warton, where the mechanisms and drivers of lithification may be more complex.

3.4.1 Mechanisms of lithification

3.4.1.1 Calcite cement precipitation

The cream-coloured material covering the slag heap and found cementing clasts together results from lithification mechanisms that are driven by Ca leaching and water (MacDonald et al., 2023a). While Ca leaching from the edge of slag grains is the mechanism for sourcing Ca for the calcite cement (MacDonald et al., 2023a) across the three distinct regions of the slag bank (Fig. 31), it is impacted by conditions that vary across the width of the deposit.

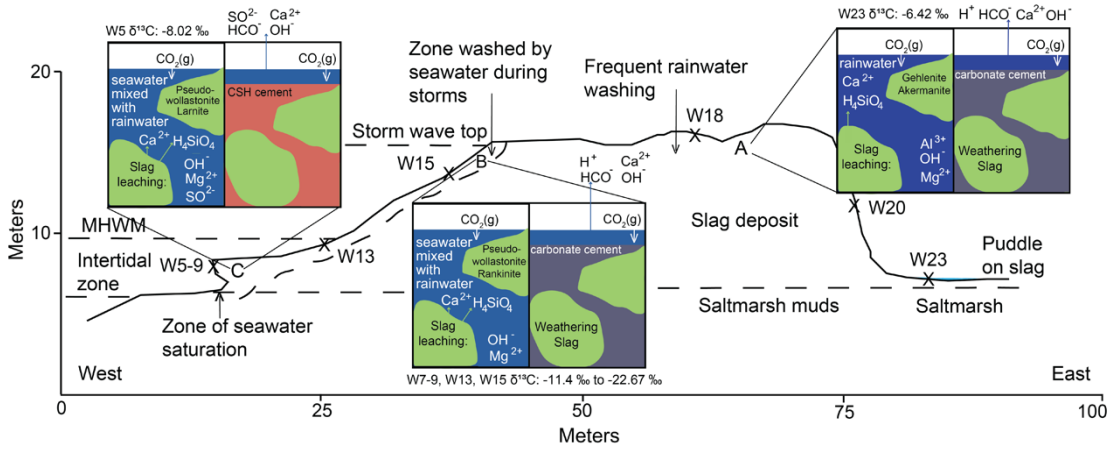

Figure 31. Conceptual model of the mechanism lithifying slag-dominated artificial ground. A) Rainwater facilitating melilite dissolution drive carbonation precipitation. B) Rain and seawater facilitate more Ca-rich phase (i.e., pseudowollastonite, rankinite) dissolution by buffering the rising pH. C) Seawater driving secondary CSH precipitation where erosion is undercutting the deposit.

The source of Ca is dependent on the solubility of the minerals comprising the slag (Huijgen et al., 2005), thus affecting the mechanisms of lithification. Samples from the top of the slag bank (Fig. 31A) are dominated by melilite group end-members gehlenite and åkermanite with the cement material recording 15.08 wt% calcite. On the seaward side

(Fig. 31B and C), additional Ca-rich phases (i.e., pseudowollastonite, rankinite: $Ca_3Si_2O_7$) were detected and the calcite content in the cement reaches 10.9 wt% (W13). Notably, as calcite content in the cement decreases westerly along the transect with increasing proximity to the sea, the $\delta^{13}C$ values become more depleted except for W5 (Fig. 31 and 32).

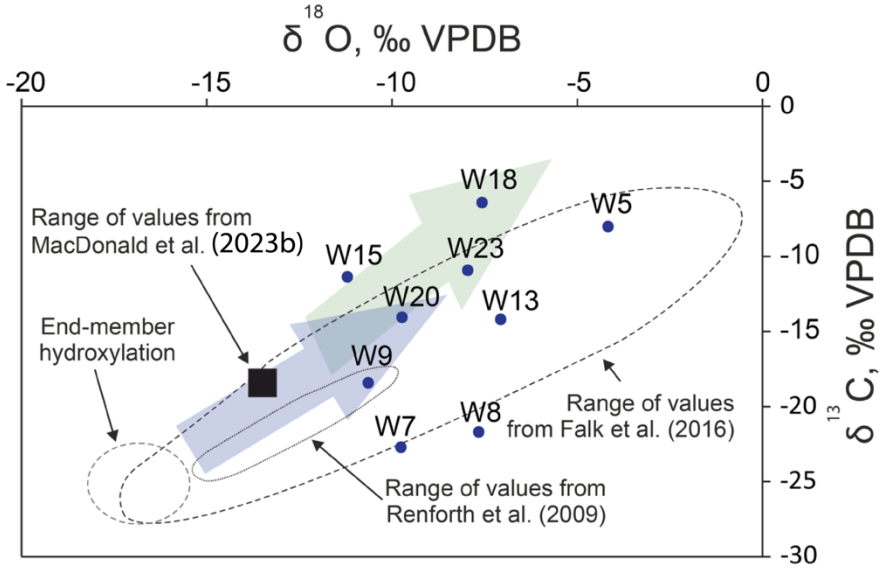

Figure 32. $\delta^{13}C$ and $\delta^{18}O$ values from this study (blue circles) and analogous studies (Falk et al., 2016; Renforth et al., 2009); partial DIC equilibrium (blue arrow) and recrystallisation (green arrow) trends and hydroxylation fields from (Falk et al., 2016). The error bars are smaller than the data point symbol size where they are not visible. Modified from (MacDonald et al., 2023b).

Together, these results suggest the influence of environmental parameters are larger drivers than the mineralogy for the calcite precipitation lithifying the slag deposit.

3.4.1.1.1 pH

The carbonation of the slag surface is controlled by the diffusion of Ca through the solid matrix to the surface, implying mineral solubility will affect the secondary precipitation of carbonate cement (Huijgen et al., 2005). Due to the crystal structure, the dissolution of gehlenite and åkermanite is generally slower at higher pH values (gehlenite at pH 7 and pH 10 and åkermanite at pH 7: Engström et al., 2013). Combined with the larger driving force for Ca dissolution compared to that of Mg at neutral to alkaline pH (Engström et al., 2013), rainwater would drive Ca leaching and increase the alkalinity (Fig. 31A and Equation 1). Similar to at Glengarnock, pooling rainwater could get caught on the rough surface of the slag heap (MacDonald et al., 2023a), refresh the water and slow the increasing pH. This would explain the higher calcite content (15.08 wt%) from the top of the slag bank. However, calcite precipitating from a stream draining a slag heap at Consett, U.K. with a pH of >11, attributed to the ingassing and hydroxylating of atmospheric CO_2, demonstrates sufficient Ca was released from the slag for carbonate mineralisation (Mayes et al., 2018).

As demonstrated in Equation 1, the leached Ca^{2+} increases water alkalinity, promoting the ingassing of atmospheric CO_2 into solution where it is hydroxylated and precipitated as solid calcium carbonate (Equations 2 and 3) (MacDonald et al., 2023a; Mayes et al., 2018). This calcium carbonate cement lithifies the slag clasts.

$$CO_2\ (g) \rightleftharpoons CO_2\ (aq) + H_2O\ (l) \rightleftharpoons HCO^-\ (aq) + H^+ \rightleftharpoons CO_3^{2-}\ (aq) + 2H^+ \quad (2)$$

$$2Ca^{2+} + 2HCO^-\ (aq) \rightleftharpoons CaCO_3\ (s) + H_2O\ (l) + CO_2\ (aq) \quad (3)$$

3.4.1.1.2 Seawater

More frequent and abundant seawater introducing Mg^{2+} on the seaside of the deposit (Fig. 30A, B), especially around the MHWM, acts as a buffer (Equation 4: Miki et al., 2004) to the rising pH from slag dissolution (Equation 1).

$$CaO\ (s) + H_2O + Mg_2\ (aq) \rightleftharpoons Ca^{2+}\ (seawater) + Mg(OH)_2\ (s) \quad (4)$$

These more neutral conditions would facilitate faster Ca dissolution from gehlenite and åkermanite (Engström et al., 2013) enabling more carbonate to precipitate. The EDS map (Fig. 30A) indicates that Ca leaching from the edge of slag clasts is precipitating to form the calcite cement. Furthermore, when more available Ca can continuously dissolve and react with ingassed CO_2, more atmospheric CO_2 can be captured and stored in the carbonate cement (Equations 2 and 3) as evident in the low $\delta^{13}C$ values (-11.4 ‰ to -22.7 ‰: W7, W8, W9) from the seaward side of the slag bank (Fig. 31B).

3.4.1.1.3 Atmospheric CO_2 input

The range of $\delta^{13}C$ values from the two regions of the slag bank (Fig. 30A, B) where calcite cement is lithifying the deposit indicate multiple processes are affecting the isotope composition. Given there is minimal vegetation on the slag deposit and the calcite precipitation is in situ, there is little to no scope for biogenic carbon input; therefore, the carbon was most likely atmospheric CO_2 and was ingassed and hydroxylated prior to calcite precipitation. The low $\delta^{13}C$ values of -18.5 ‰ and -14.1 ‰ (W9 and W20, respectively) falling within the range of partial dissolved inorganic carbon (DIC) equilibrium (Fig. 31) from calcites in a hyperalkaline setting of springs in the Semail ophiolite in Oman (Falk et al., 2016), similar to the carbonated slag with hydroxylated atmospheric CO_2 from Glengarnock (-20.05 ± 0.23 ‰: MacDonald et al., 2023a).

Hydroxylation and instant calcite precipitation would yield $\delta^{13}C$ values between -25 ‰ to -27.5 ‰ (Dietzel et al., 1992; Falk et al., 2016; Renforth et al., 2009) suggesting the DIC remained in solution long enough for gradual DIC equilibrium to proceed, resulting in the more intermediate isotopic composition (Falk et al., 2016). The slightly less depleted $\delta^{13}C$ values ranging from -14.13 ‰ to -6.42 ‰ could reflect calcite with DIC $\delta^{13}C$ values that were closer to equilibrium values following precipitation, then recrystallised with hydroxylated atmospheric CO_2 (Falk et al., 2016). Therefore, the $\delta^{13}C$ values from the calcite cement lithifying the slag at Warton are interpreted to reflect the ingassing and hydroxylation of atmospheric CO_2 where partial DIC equilibrium occurred prior to initial calcite cement precipitation, followed by some subsequent calcite recrystallisation in some samples.

3.4.1.2 Calcium-Silicate-Hydrate cement precipitation

Similar cream coloured material found covering the slag heap in the intertidal zone (Fig. S1A) resembling the secondary calcite cement is inferred to be comprised dominantly of CSH. The samples with the CSH phases jouravskite and thaumasite (W5 and W6) recorded more weight loss over 50°C to 200°C during TGA analysis corresponding to CSH decomposition (Haha et al., 2011; Jiang et al., 2018; Pane & Hansen, 2005) compared to that from calcium carbonate which decomposes at 600 °C to 750 °C (Chiang & Pan, 2017). The sulphur in the CSH minerals could have been sourced from the original ore rock, inclusions in melilites commonly found in blast furnace slag (Pullin et al., 2019; Scott et al., 1986), or from dissolved species in seawater (Gregor et al., 1988). The same drivers that impact the calcite cement described above are likely affecting the CSH cement similarly. The associated phases pseudowollastonite and larnite would be contributing Ca leached by seawater, however, only slightly lower $\delta^{13}C$ values (-8.02 ‰) from the calcalitic component of the cement suggest the CSH phases are affecting subsequent calcite precipitation.

3.4.1.2.1 Surface Reaction

The Ca dissolved from the slag minerals that is from and/or diffuses to the slag surface (Huijgen et al., 2005) must have sufficient surface area to be able to precipitate (Ragipani et al., 2019). In this study, we found CSH preferentially precipitates over calcite in the intertidal zone (Fig. 31C). The BSE and EDS map shows the Si-rich fibrous needles, indicative of the presence of CSH, surrounding slag clasts with Ca-rich rims are cementing the clasts together (Fig. 30B, C). The CSH acts as a Ca sink for ions that would have been used to form carbonates (Béarat et al., 2006) and reduces the permeability of the slag (Pullin et al., 2019). A hydration front between secondary CSH surrounding a Ca-, Si-, and S-depleted inner alteration layer where the most reactive phases (i.e., larnite) were absent indicates water diffusion is limited in carbonated slag (Pullin et al., 2019). Without sufficient water to drive the leaching of Ca (MacDonald et al., 2023a) following CSH formation that is reducing exposed slag, subsequent calcite cement precipitation is unlikely. Similar weathering documented in a basic oxygen furnace slag with larnite dissolution and CSH precipitation (Hobson et al., 2017) supports secondary CSH precipitation as the mechanism lithifying the heap in the intertidal zone.

3.4.1.2.2 Atmospheric CO_2 input

The $\delta^{13}C$ values from calcite in samples with CSH fall outside the range of values from samples located on the top of the deposit, except for that from W18. Calcite is a minor component in these samples with CSH from the intertidal zone. Recrystallisation of the CSH comprising ingassed and hydroxylated atmospheric CO_2 that underwent partial DIC equilibrium could explain the deviation of calcite $\delta^{13}C$ values from the hydroxylation end-member (-25 ‰: Dietzel et al. (1992)).

3.4.2 Implication

The lithification mechanisms documented in this study are driven by the two compositionally distinct regions of the slag bank. With increasing volumes of artificial

ground produced annually (Cooper et al., 2018), understanding how it interacts with the environment following deposition will inform repurposing capabilities and possible remediation measures. The composition of artificial ground will continue to change alongside the technological advancements that now allow modern extraction techniques to exploit lower quality resources (Cooper et al., 2018). Historic accounts claiming the slag bank has prevented coastal erosion of the Warton Saltmarsh support the use of slag for 'hard' protection and coastal defence once lithified (Pranzini & Williams, 2013; Riley et al., 2020). Slag replacement in Portland cement has been found to reduce the degradation from sulphate attack by reducing the cement permeability (McGrath & Hooton, 1997) as a result of the dense microstructures of slag (Brown et al., 2003). Cement with a higher slag content was found to be more effective at reducing sulphate attack due to shallow ettringite formation (Brown et al., 2003). While the CSH documented in this study has been attributed to improve the durability of steel slag building material (Lizarazo-Marriaga et al., 2011; Zhang et al., 2011), the physical integrity of cement is often compromised from ettringite and thaumasite formation (Mehta, 1983; Shi et al., 2012). The expansion and cracking from secondary ettringite (Mehta, 1983; Tian & Cohen, 2000), cement degradation in marine environments attributed to thaumasite formation (Irassar et al., 2003), and decreased strength in concrete with ettringite and thaumasite (Shi et al., 2012; Tian & Cohen, 2000) highlight the importance of understanding how lithified slag of varying compositions evolves in the presence of seawater.

The mechanisms responsible for the lithification of slag-dominated artificial ground present the opportunity to remove atmospheric CO_2. Using the reported density range minimum of BF (1150 to 1440 kg/m^3) and maximum of BOF (1600 to 1760 kg/m^3) slag (Lee, 1974) and the average percentage of carbonate of the total sample mass (7.95 %), the estimated carbon sequestration potential is 38,694 to 59,218 t of CO_2. Even with less carbonate precipitation where the slag is more frequently washed by seawater, more atmospheric CO_2 is drawn down and mineralised. However, as a result of the armouring effect from CSH precipitation and the resulting reduction in surface reaction (Ragipani et al., 2019) limiting slag mineral dissolution and available Ca, additional sources of Ca and agitation to restore the surface reaction is necessary for subsequent CO_2 mineralisation. Calculation of the CO_2 capture potential of lithified slag-dominated artificial ground must consider how secondary precipitates affect the total extent and rate of carbonation (Hobson et al., 2017) in field-size situations spanning various environments and time scales. Additionally, experiments determining the impact mineralogy has on atmospheric CO_2 capture could further elucidate the processes responsible for the variable $\delta^{13}C$ values that deviate from the hydroxylation end member.

Nevertheless, the cream-coloured material covering the slag bank identified as secondary CSH may mitigate one of the challenges posed by artificial ground. The dissolution of slag minerals comprising potentially toxic elements such as V and Cr (Mayes et al., 2018) is limited by the armouring effect from CSH formation. Even though the tetrahedral Si site of dicalcium silicate can accommodate V(V), the presence of V(V) in secondary CSH suggests the released vanadate was reincorporated (Hobson et al., 2017). Furthermore, the long-term release of Cr from steel slag and other alkaline wastes in similar open systems controlled by the solubility of secondary CSH release tends to be in stable forms. The incorporation of Cr(III) into CSH during leaching experiments prevented oxidation in the solid slag matrix (De Windt et al., 2011). Therefore, the lithification of slag-dominated

artificial ground by secondary CSH precipitation may prevent the release of toxic metals at ambient conditions.

3.5 Conclusions

This study identifies the mechanisms lithifying a coastal legacy iron and steel slag deposit in South Lancashire, England. Compositionally diverse (identified by XRD) slag samples spanning the width of the deposit are lithified by cream-coloured material with variable calcite content (confirmed by TGA) and a range of $\delta^{13}C$ values.

Where rainfall drove the dissolution of gehlenite and åkermanite by facilitating the leaching Ca, more atmospheric CO_2 mineralised in the calcite cement that is lithifying the top of the deposit. Comparatively, where there are more Ca-rich phases that are washed by seawater on the seaward side of the deposit above the MHWM, there is less calcite but records more depleted $\delta^{13}C$ values. Secondary CSH covering and lithifying the deposit below the mean low-water mark inhibit further mineral dissolution and carbonation, potentially limiting the release of toxic metals.

Given the mineralogic and external environmental parameters influencing the mechanisms of lithification, the results shown here suggest opportunities for slag valorisation. The repurposing and management of slag-dominated artificial ground could be optimised to facilitate in-situ atmospheric CO_2 capture by mineralization.

4. Chapter 4: Conclusion

4.1 Metal recovery potential

4.1.1 Slag characterisation and quantification

Deeper investigation and detailed characterisation of slags needed to guide resource recovery greatly benefit from using statistically robust machine learning analytical methods. The spatial and chemical correlation gained from processing SEM-EDS data with a dimensional reduction and clustering algorithm enables the pinpointing of trace elements. By averaging large numbers of pixels, weaker signals are amplified above spectral background, facilitating the identification and quantification of trace metals that are challenged by alternative methods. NMF is more suited than PCA for analysing historic slag due to the non-negative constraint of the algorithm that directly links revealed trace metals such as Ba, Fe, and Mn found in this study, to the host phase segmented by clustering, and the physical microstructures of the sample. Uncertainties due to analysing spectral data of historic slags are easily overcome by applying these unsupervised learning approaches. Using IPC which allows the data to guide the analysis, revealed phases and trace Ba, Fe, and Mn that were not segmented and identified during the preliminary dimensional reduction and clustering. This higher detailed characterisation improved the accuracy of the data-driven approach and helped to confirm that iron and steel production are represented in the Warton slag deposit A from the variable slag composition and metal concentrations. Stratigraphic analysis revealed olivine, anorthite, more frequent melilite, and higher Fe-oxide content in horizons W24, W26, and W28, and lower Fe-oxide and higher Ca-oxide content in horizons W25 and W27, indicating the metallurgical process evolution from solely iron production to combined iron and steel production. This suggests co-deposition rather than separate disposal based on process which has implications for both metal recovery methods and the application of the most suitable techniques.

4.1.2 Recovery method

Elevated Mn found in close proximity to pores in both the iron and steel slag horizons during compositional and microstructural analysis inform the recommendation of bioleaching for metal recovery. The reactive phases (anorthite, Ca-oxide, Ca-Si, Ca-Al-Si, Ca-Fe-Si, Ca-Al-Fe-Si, Ca-Al-Mg-Si, Ca-Al-Si-S, Ca-Al-Mg-Fe-Si, Ca-Al-Mg-Mn-Fe-Si, Fe-oxide, larnite, and melilite) and the larger surface reaction potential allow for Mn solubilising microorganism containing fluid to interact with the slag, facilitating the release of the metal. This demonstrates that the approach can be used to suggest less-energy demanding recovery methods which could help to determine the feasibility of CRM recovery from legacy slag. Therefore, it will be necessary to associate structures from the deposit to the micro- and nanoscale with the identified trace metal concentrations for various types of slags.

4.2 Lithification mechanisms

Legacy iron and steel slags are promising waste materials that can be reused for positive climate action if understood and managed properly. This work ultimately provides insight into the opportunities for atmospheric CO_2 storage and CRM recovery from legacy iron and steel slag deposits. While natural environmental processes result in the lithification of

these anthropogenically derived rocks, variable atmospheric CO_2 content occurs across the deposit in the cream-coloured material cementing the slag. The interactions between compositionally variable weathering slag and fresh water and seawater water facilitate lithification by multiple mechanisms. Even though lithification by secondary CSH inhibits future carbonate mineralisation from seawater washing that recorded the most depleted $\delta^{13}C$ values, the weathering product could limit the release of toxic metals.

4.3 Future investigation

The heterogeneous nature of the Warton slag including variable metal content of horizons in the inland deposit and various types of lithifications across the coastal deposit have implications for reuse opportunities. Sampling from the interior of the inland deposit could reveal metal concentrations that more closely represent the slag composition just after deposition. After testing the recommended metal recovery method, a comparison between the metal content and the microstructures from this study would help to inform how biochemical weathering impacts metal mobilisation from the deposit to the microscale. Additional LA-ICP-MS analysis could help to verify the metal concentrations determined by the outlined approach. Spectral artefacts that challenge accurate data interpretation could be limited from evaluating how different combinations of process times and dwell times affect the cpp, thus the cluster spectral resolution. This would benefit higher-resolution imaging and mapping to more precisely locate micro- to nanoscale metal structures.

Further research characterising slag deposits in coastal and non-coastal settings would improve the understanding of how the depositional setting impacts lithification as well as atmospheric CO_2 storage. Identifying and describing the lithification processes of deposits from different ages with a series of samples will address unknowns regarding the long-term potential of these wastes. This would also contribute to the limited understanding of historic slag deposit evolution. Combined with detailed microstructural analysis (SEM-EDS), the outlined areas for further investigation would help in determining which type of repurposing would be the most effective and informative for method development.

Appendices

Appendix A: additional tables

Table S1. Carbonate content quantified from TGA using the modified TGA-DTG interpretation (Chaing and Pan, 2017).

Sample	T_1	T_m	T_2	Weight loss (%)	Weight loss (mg)
JM21_W5A	619	636.5	654	1.25	0.10
JM21_W5B	630	645.5	661	1.1	0.12
JM21_W5C	719	757	795	0.8	0.05
JM21_W5 Average	656	679.67	703.33	1.05	0.09
JM21_W6A	641	659.5	678	1.35	0.29
JM21_W6B	681	729	777	0.25	0.04
JM21_W6C	709	735	761	1.5	0.25
JM21_W6 Average	677	707.83	738.67	1.03	0.20
JM21_W7A	619	637	655	1.8	0.08
JM21_W7B	651	669.5	688	2.25	0.35
JM21_W7C	630	652	674	1.75	0.20
JM21_W7 Average	633.33	652.83	672.33	1.93	0.21
JM21_W8A	642	659	676	2	0.25
JM21_W8B	643	661	679	1.5	0.30
JM21_W8C	600	644	688	3.25	0.38
JM21_W8 Average	628.33	654.67	681	2.25	0.31
JM21_W9A	666	701.5	737	8.25	1.92
JM21_W9B	671	703	735	8.65	1.84
JM21_W9C	670	694	718	5.75	1.11
JM21_W9 Average	669	699.5	730	7.55	1.62

Sample	T_1	T_m	T_2	Weight loss (%)	Weight loss (mg)
JM21_W13A	681	716	751	11.24	2.37
JM21_W13B	673	711	749	12	2.46
JM21_W13C	678	704.5	731	9.5	2.01
JM21_W13 Average	677.33	710.50	743.67	10.91	2.28
JM21_W15A	679	704	729	5.75	0.83
JM21_W15B	687	714	741	11.625	1.35
JM21_W15C	672	696.5	721	8.625	0.64
JM21_W15 Average	679.33	704.83	730.33	8.67	0.94
JM21_W18A	703	732	761	13.7	1.78
JM21_W18B	689	722.5	756	16.05	1.48
JM21_W18C	695	727	759	15.5	1.82
JM21_W18 Average	695.67	727.17	758.67	15.08	1.69
JM21_W20A	681	705.5	730	6.2	0.66
JM21_W20B	653	693.5	729	4.75	0.65
JM21_W20C	708	734.5	761	10	1.58
JM21_W20 Average	680.67	711.17	740	6.98	0.96
JM21_W23A	670	699.5	729	9.2	1.60
JM21_W23B	679	712	745	11.5	2.10
JM21_W23C	663	695.5	728	9.05	2.86
JM21_W23 Average	670.67	702.33	734	9.92	2.19

Table S2. Mineral phase identified in each stratigraphic horizon in the legacy iron and steel slag.

Mineral	W28	W27	W26	W25	W24
Mll	*****^^	*	********^^^^^	^^^	**********^^^^
Wo	*	*	*		
Rnk	*				*
Lrn				*	*
Mtc			*		
Anh	*		*		
An	***	*		*	
Ol			****		
Cal	*		**		^
Qtz	*	**	*****^^^^	*^	*
Py	*	*			
Tricalcium silicate		*		^	**
Calcio-wüstite		*	*		
Ca-oxide	***^	*		******	
Fe-oxide	*********^^	**		*	**
Ca-Si	*			*	*
Fe-S	*^^				
Ca-Al-Si	*		*		****
Ca-Si-S	*^		^	*	
Ca-Fe-Si					*
Fe-Si-S		*^			
Ca-Al-Mg-Si			**^		*^
Ca-Al-Fe-Si	*		**		^
Ca-Al-Si-S	***^		********^^^^	*	
Ca-Fe-Si-S		*			
Ca-Mg-Si-S	*				
Ca-Al-Mg-Fe-Si		*^	*^^		
Ca-Al-Mg-Mn-Si					^
Ca-Al-Fe-Si-S	*^^^^		*	^	
Ca-Al-Mg-Si-S			*		
Ca-Al-Mg-Mn-Fe-Si					^
Ca-Al-Mg-Fe-Si-S	*	^	*		
Native Fe		**			

Symbols: * = identified from preliminary clustering; ^ = identified from IPC on a mineral phase.

Appendix B: additional figures

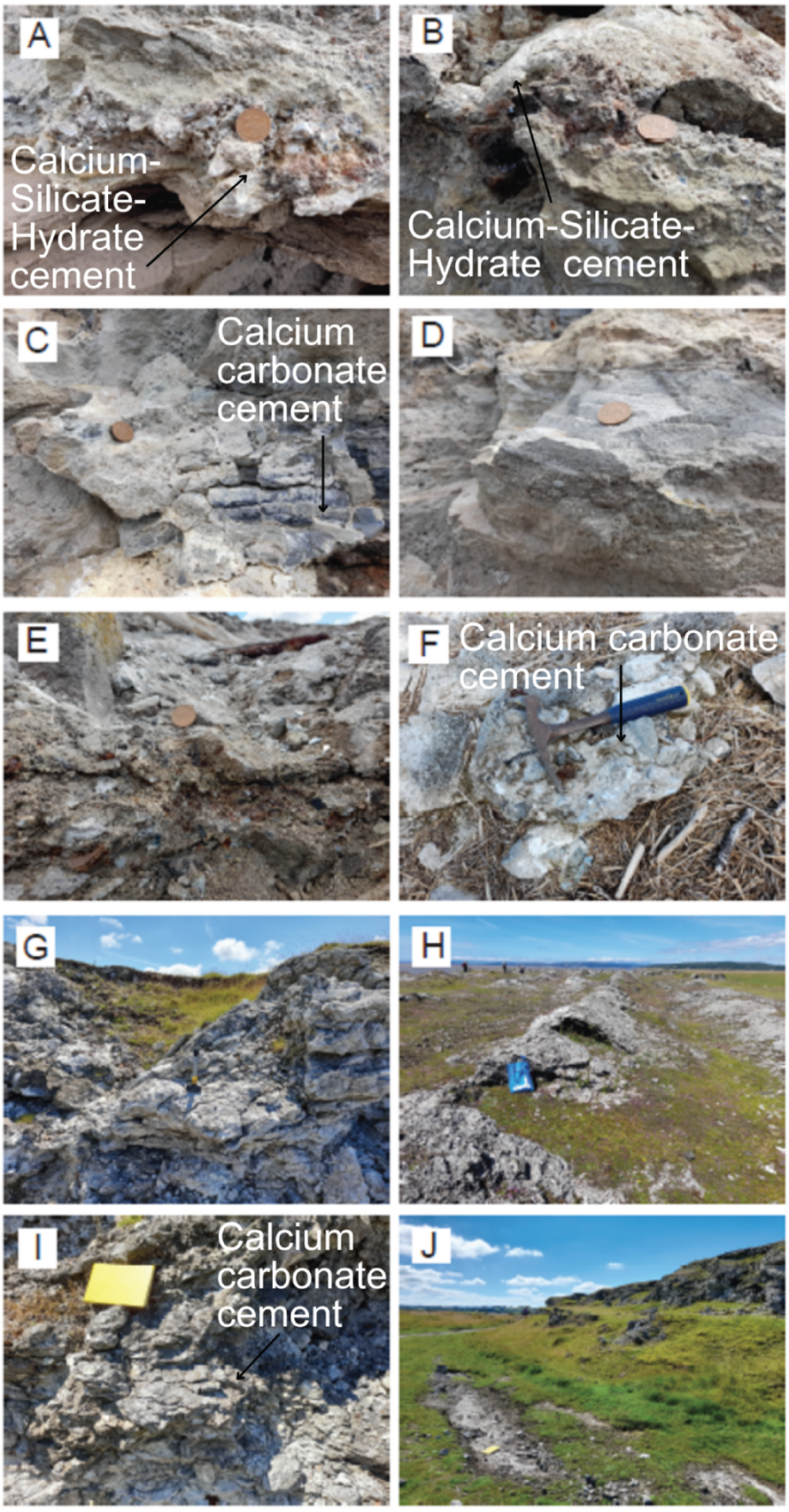

Figure S1. Sample locations of the coastal (B) legacy slag deposit. A) W5. B) W6. C) W7. D) W8. E) W9. F) W13. G) W15. H) W18. I) W20. J) W23.

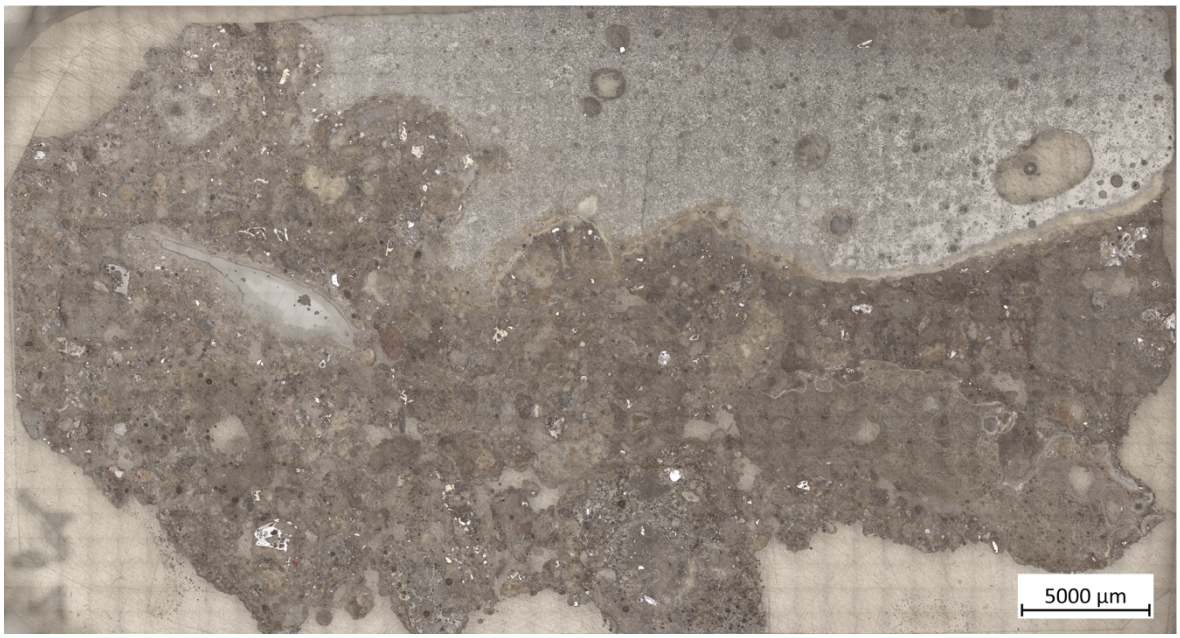

Figure S2. Stitched optical microscopy image of the polished thin section representing horizon W24 at 10x magnification in plain polarised reflected light.

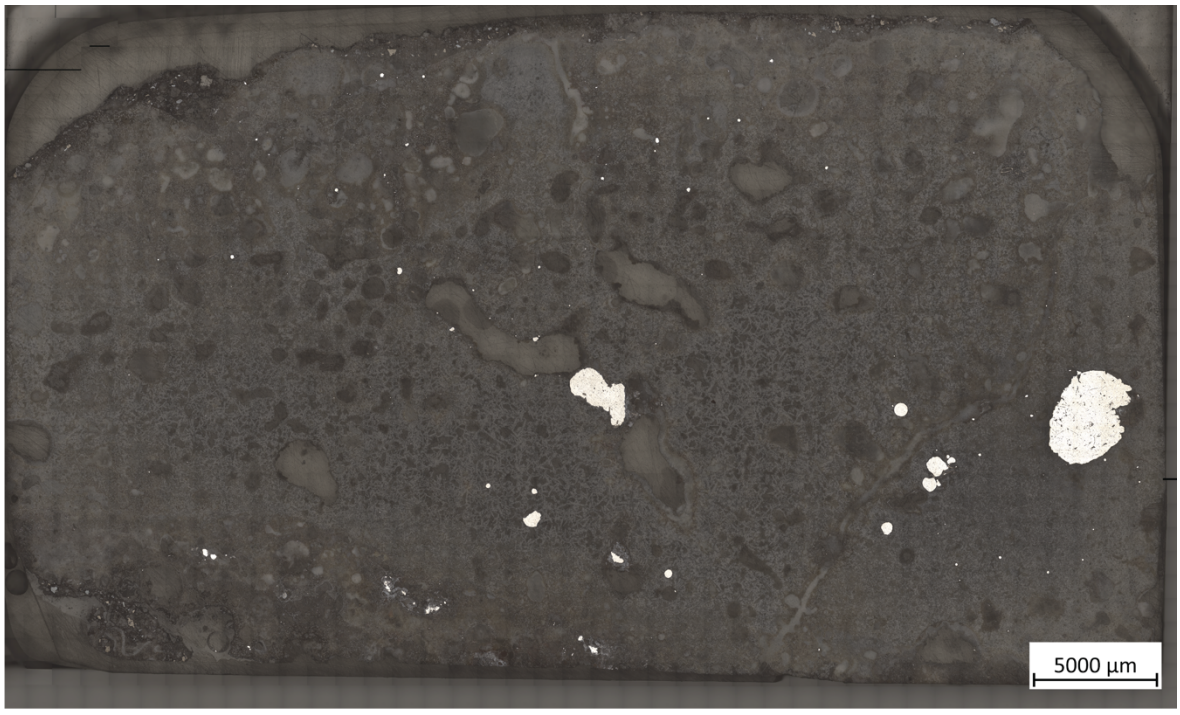

Figure S3. Stitched optical microscopy image of the polished thin section representing horizon W25 at 10x magnification in plain polarised reflected light.

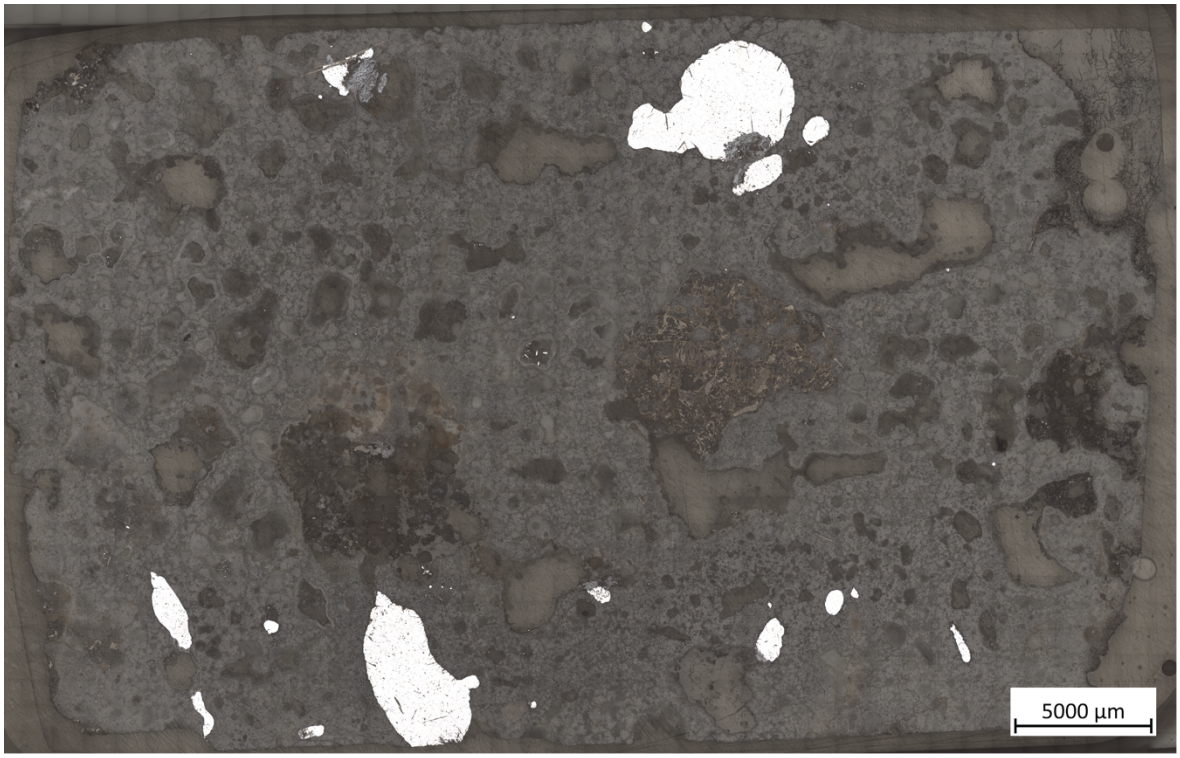

Figure S4. Stitched optical microscopy image of the polished thin section representing horizon W26 at 10x magnification in plain polarised reflected light.

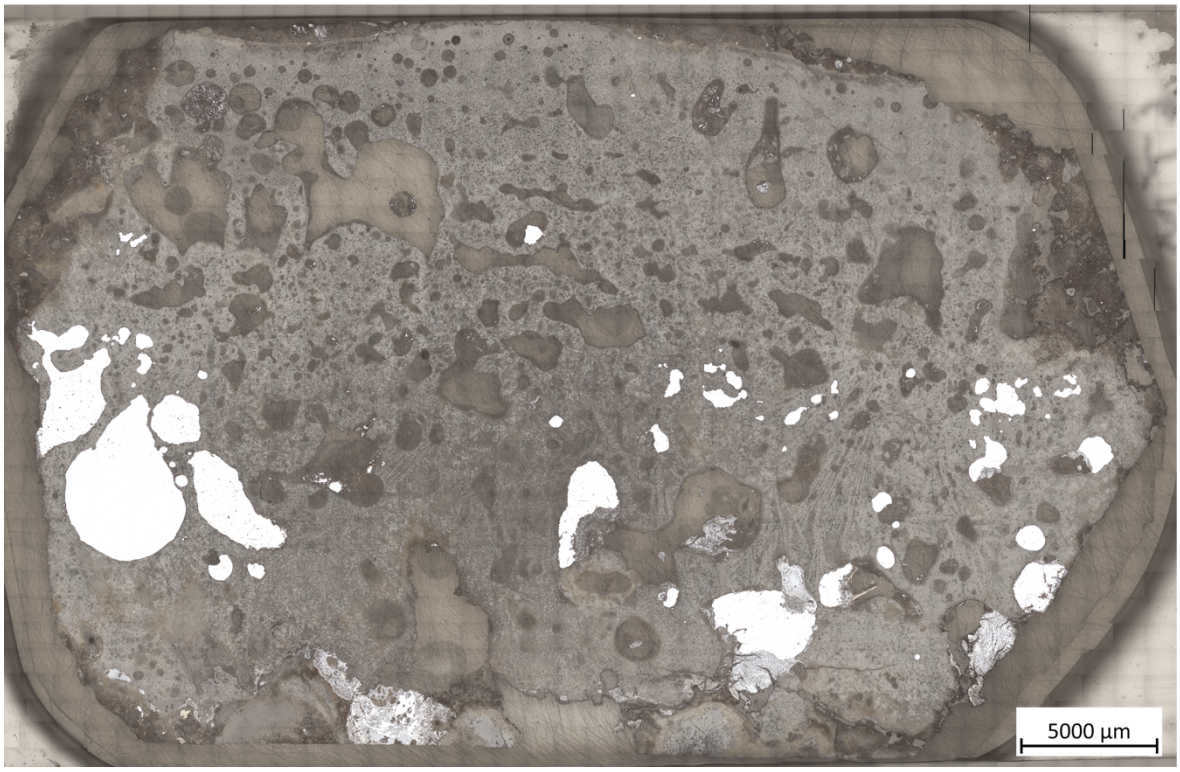

Figure S5. Stitched optical microscopy image of the polished thin section representing horizon W27 at 10x magnification in plain polarised reflected light.

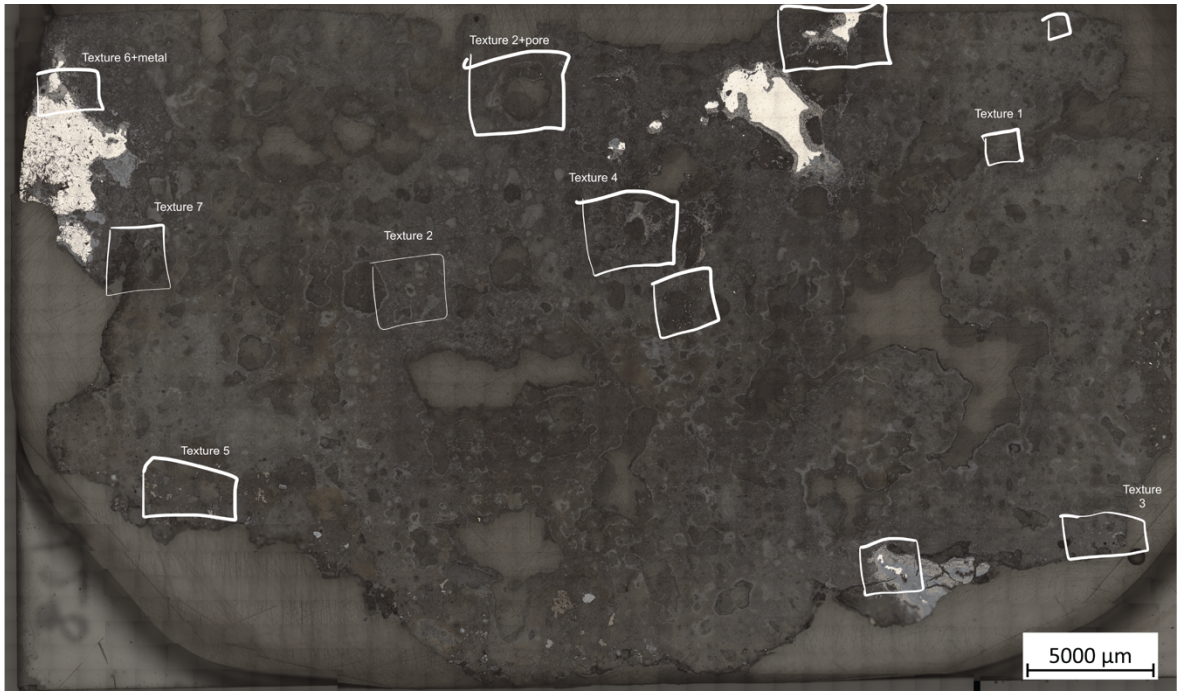

Figure S6. Stitched optical microscopy image of the polished thin section representing horizon W28 at 10x magnification in plain polarised reflected light.

Appendix C: Python code for the unsupervised machine learning approach

1. Load libraries and functions

In [1]:
```
import os
import scipy
import hyperspy.api as hs
import numpy as np
import h5py
import pandas as pd
import seaborn as sns
import skimage.io as io
import hdbscan

import matplotlib.pyplot as plt
import matplotlib.patches as patches
from matplotlib import cm

import sklearn as skl
import sklearn.cluster as cluster
from sklearn.decomposition import PCA, NMF

import skimage as ski
import skimage.morphology as mph
from skimage import measure
```

In [ ]:
```
os.chdir('Your:File/Path')
```

In [2]:
```
def h5printR(item, leading = ''):
    for key in item:
        if isinstance(item[key], h5py.Dataset):
            print(leading + key + ': ' + str(item[key].shape))
        else:
            print(leading + key)
            h5printR(item[key], leading + '  ')

# Print structure of a `.h5` file
def h5print(filename):
    with h5py.File(filename, 'r') as h:
        print(filename)
        h5printR(h, '  ')
```

In [ ]:
```
def add_xrl_labels(data_array, amplitude_thresh, ax, elements_list, colors_list,
                   scale, offset):

    ele_dic = hs.material.elements.as_dictionary()  # call element dictionary from
                                                    #hyperspy library
    ofs = offset/scale

    for e_idx in range(0, len(elements_list)):
        # find peak position of element
        peak_ka = round((ele_dic[elements_list[e_idx]]['Atomic_properties']
                         ['Xray_lines']['Ka']['energy (keV)']/scale)-ofs)

        # if element peak exceeds upper or lower threshold
        if data_array[peak_ka] > amplitude_thresh*data_array.max() or
        data_array[peak_ka] < amplitude_thresh*data_array.min():
            # draw vline of Ka peak
            ax.vlines(x = peak_ka, ymin = 0, ymax = data_array[peak_ka],
                      color = e_colors[e_idx])

            # draw vline of Kb peak
            if 'Kb' in ele_dic[elements_list[e_idx]]['Atomic_properties'] \
```

```
            ['Xray_lines']:
                peak_kb = round((ele_dic[elements_list[e_idx]]['Atomic_properties']
                                 ['Xray_lines']['Kb']['energy (keV)']/scale)-ofs)
                ax.vlines(x = peak_kb, ymin = 0, ymax = data_array[peak_kb],
                          color = e_colors[e_idx])
            # draw vline of La peak
            if 'La' in ele_dic[elements_list[e_idx]]['Atomic_properties'] \
            ['Xray_lines']:
                peak_la = round((ele_dic[elements_list[e_idx]]['Atomic_properties']
                                 ['Xray_lines']['La']['energy (keV)']/scale)-ofs)
                ax.vlines(x = peak_la, ymin = 0, ymax = data_array[peak_la],
                          color = e_colors[e_idx])
            # draw vline of Ll peak
            if 'Ll' in ele_dic[elements_list[e_idx]]['Atomic_properties'] \
            ['Xray_lines']:
                peak_ll = round((ele_dic[elements_list[e_idx]]['Atomic_properties']
                                 ['Xray_lines']['Ll']['energy (keV)']/scale)-ofs)
                ax.vlines(x = peak_ll, ymin = 0, ymax = data_array[peak_ll],
                          color = e_colors[e_idx])
            # draw vline of Ln peak
            if 'Ln' in ele_dic[elements_list[e_idx]]['Atomic_properties']\
            ['Xray_lines']:
                peak_ln = round((ele_dic[elements_list[e_idx]]['Atomic_properties']
                                 ['Xray_lines']['Ln']['energy (keV)']/scale)-ofs)
                ax.vlines(x = peak_ln, ymin = 0, ymax = data_array[peak_ln],
                          color = e_colors[e_idx])

            # place peak name and bounding box for positive peaks
            #Ka peaks
            if data_array[peak_ka] > 0:
                ax.text(x = peak_ka, y = data_array[peak_ka]+(0.05*data_array.max()),
                        s = elements[e_idx], ha = 'center',
                        color = 'black')
                rect_height = (data_array.max() - data_array.min())*0.04
                e_rect = patches.Rectangle(xy = (peak_ka-30, data_array[peak_ka]+
                                                 (0.05*data_array.max())),
                                           color = e_colors[e_idx], width = 60,
                                           height = rect_height+(0.5*rect_height))
                ax.add_patch(e_rect)

            if data_array[peak_ka] < 0:
                ax.text(x = peak_ka, y = data_array[peak_ka]+(0.05*data_array.max()),
                        s = elements[e_idx], ha = 'center',
                        color = 'black')
                rect_height = (data_array.max() - data_array.min())*0.04
                e_rect = patches.Rectangle(xy = (peak_ka-30, data_array[peak_ka]+
                                                 (0.05*data_array.max())),
                                           color = e_colors[e_idx], width = 60,
                                           height = rect_height+(0.5*rect_height))
                ax.add_patch(e_rect)
```

In [4]:

```
def poisson_noise_norm(signal):
    """normalises hyperspy style signal for poissonian noise. based on [Keenan2004].

    Parameters
    ----------'
    signal - a hyperspy data stack

    Returns
    -------
    normalised Signal in a vector format
        The decomposition loadings, as a Signal with same dimension as the original
        navigation dimensions.
    data_factor_signals : tuple of Signals
```

```
    """
    # retreive original data shape
    y, x, e = signal.data.shape

    print('inital mean=', signal.data.mean(),' inital max =', signal.data.max(),
          ' inital min=', signal.data.min())
    with signal.unfolded():
            # The rest of the code assumes that the first data axis
            # is the navigation axis. We transpose the data if that
            # is not the case
            #navigation_shapes = np.asarray(signal.axes_manager.navigation_shape) \
                #.squeeze()
            # array with x & y size
            #signal_shape = signal.axes_manager.signal_shape # value equal to
                #number of energy channels

            if signal.axes_manager[0].index_in_array == 0:

                dc = signal.data.copy()
            else:
                dc = signal.data.T.copy()

            # make sure dc is correct data type for scaling
            dc = dc.astype('float64')

            aG = dc[:, :].sum(1).squeeze()
            bH = dc[:, :].sum(0).squeeze()
            #print(aG,bH)
            root_aG = np.sqrt(aG)[:, np.newaxis]
            root_bH = np.sqrt(bH)[np.newaxis, :]

            # We ignore numpy's warning when the result of an
            # operation produces nans - instead we set 0/0 = 0

            with np.errstate(divide="ignore", invalid="ignore"):
                # this is quation 8 of (Keenan & Kotula, 2004)
                dc[:, :] /= root_aG * root_bH
                dc[:, :] = np.nan_to_num(dc[:, :])


    print(dc.shape)
    print('scaled mean=',dc.mean(),' scaled max =',dc.max(),' scaled min=',dc.min())

    # convert dc array shape ((y*x), energy_channels) into d_norm
        #(y, x, energy_channels)
    d_norm = dc.reshape(y, x, e)

    # convert d_norm numpy array into hyperspy EDSSEMSpectrum
    s_norm = hs.signals.EDSSEMSpectrum(d_norm)
    # copy metadata and axes_manager from original signal
    s_norm.metadata = signal.metadata
    s_norm.axes_manager = signal.axes_manager

    return s_norm, d_norm, dc   # return the hyperspy object s_norm, numpy array
                                    #d_norm (y,x,energy)
                                # and vectorised numpy array dc (y*x,energy)
```

In [5]:

```
def flatten_masked_array(im, mask):
    """Flatten an image array containing NaN values, or excluding False values
    from mask.

    Parameters
    ----------
    im - an np array that requires masking (shape = (y, x, ...))
    mask - a binary boolean array (shape = (y, x)), True = data to be included
```

```
    in vect
                    False = NaN values excluded from vect

    Returns:
    --------
    vect - a flattened array from im, excluding NaN values
        (shape = ((y*x)-(number of NaN)), ...)
    """

    # for 2D images
    if len(im.shape) == 2:
        vect = np.empty([])
        vect = np.vstack(im[mask == 1])
    # for EDS spectral images
    elif len(im.shape) == 3:
        vect = np.empty([])
        vect = np.vstack(im[mask == 1, :])

    return vect
```

In [6]:

```
def reconstruct_masked_image(arr, mask, im_shape):
    """Reconstruct an image from a flattened array to contain masked NaN values.

    Parameters
    ----------
    arr - a flattened array, excluding NaN values from mask
    (shape = ((y*x)-(number of NaN)), ...)
    mask - a binary boolean array (shape = (y, x)), True = data belonging to arr,
    False = NaN values excluded from arr
    im_shape - tuple of desired image shape (e.g. (y, x, e))

    Returns:
    --------
    im - an image array (shape = (y, x, ...)), containing NaN values where
    (mask == False)
    """

    # for 2D images
    if len(im_shape) == 2:
        # find desired image shape
        y_pix = im_shape[0]
        x_pix = im_shape[1]

        # create empty NaN array
        im = np.zeros((y_pix, x_pix))
        im[:] = np.nan

        # replace True values on mask array with the data from the flattened array
        index = 0
        for i in range(0, y_pix):
            for j in range(0, x_pix):
                if mask[i,j] == 1:
                    im[i,j] = arr[index]
                    index += 1

    # for EDS spectral images
    elif len(im_shape) == 3:
        # find desired image shape
        y_pix = im_shape[0]
        x_pix = im_shape[1]
        e_len = im_shape[2]

        # create empty NaN array
        im = np.zeros((y_pix, x_pix, e_len))
        im[:] = np.nan
```

```
        # replace True values on mask array with the data from the flattened array
        index = 0
        for i in range(0, y_pix):
            for j in range(0, x_pix):
                if mask[i,j] == 1:
                    im[i,j,:] = arr[index]
                    index += 1

    return im
```

In [7]:
```
def poisson_scale_mask(data):
    """normalises numpy array signal for poissonian noise. based on [Keenan2004]_.

    Parameters
    ----------'
    data - a numpy array

    Returns
    -------
    normalised Signal in a vector format
        The decomposition loadings, as a Signal with same dimension as the original
        navigation dimensions.
    data_factor_signals : tuple of Signals

    """
    # retreive original data shape
    n, e = data.shape

    print('inital mean=', data.mean(),' inital max =', data.max(),' inital min=',
          data.min())

    dc = np.copy(data)

    # make sure dc is correct data type for scaling
    dc = dc.astype('float64')

    aG = dc[:, :].sum(1)
    bH = dc[:, :].sum(0)
    #print(aG,bH)
    root_aG = np.sqrt(aG)[:, np.newaxis]
    root_bH = np.sqrt(bH)[np.newaxis, :]

    # We ignore numpy's warning when the result of an
    # operation produces nans - instead we set 0/0 = 0
    with np.errstate(divide = "ignore", invalid = "ignore"):
        # this is quation 8 of (Keenan & Kotula, 2004)
        dc[:, :] /= root_aG * root_bH
        dc[:, :] = np.nan_to_num(dc[:, :])


    print(dc.shape)
    print('scaled mean=',dc.mean(),' scaled max =',dc.max(),' scaled min=',dc.min())

    return dc   # return the hyperspy object s_norm, numpy array d_norm (y,x,energy)
                                # and vectorised numpy array dc (y*x,energy)
```

In [8]:
```
def plt_phasemap(labelled_im, bse_im = None, scale = 1, mpl_cmap = None,
                 legend_labels = None, phasemap_title = ''):
    """Plot a phase map with scale

    """
    # create figure to the correct size for document
    plt.figure(figsize = (7.51181*2,5.51181*2))
```

```
    if type(bse_im) == np.ndarray:
        # plot the labels map as pcolormesh to get best quality image
        plt.imshow(bse_im, cmap ='gray')
        im = plt.pcolormesh(labelled_im, cmap = mpl_cmap, alpha = 1)

    else:
        im = plt.imshow(labelled_im, cmap = mpl_cmap)

    # add additional plot parameters: title, no x/y ticks, colorbar
    plt.title(phasemap_title)
    plt.tick_params(axis = 'both',which = 'both',bottom = False,top = False,
                    left = False,right = False,labelbottom = False,
                    labelleft = False)
    plt.colorbar()
```

2.0 Load annd calibrate the raw data

Export the h5py, .raw, and .rpl formats so they can be analysed

2.1 Load data

In [11]:
```
file = h5py.File('/Volumes/Tobisha/Warten_use_13_4_2023/h5oina/Warten_use_12_4_2023
                 'Specimen 1 W26_T5M2 Site 1 W26_T5M2_EDS.h5oina','r')
```

2.2 Extract the Metadata and assign to variables

In [12]:
```
energy_scale = file['1']['EDS']['Header']['Channel Width'][0]
energy_offset = file['1']['EDS']['Header']['Start Channel'][0]

x_pix = file['1']['EDS']['Header']['X Cells'][0]
x_scale = file['1']['EDS']['Header']['X Step'][0]

y_pix = file['1']['EDS']['Header']['Y Cells'][0]
y_scale = file['1']['EDS']['Header']['Y Step'][0]

total_map_pixels = file['1']['EDS']['Header']['X Cells'][0]*file['1']['EDS'] \
    ['Header']['Y Cells'][0]
print(total_map_pixels)

peaks_list = list(file['1']['EDS']['Data']['Window Integral'])
print(peaks_list)
```

```
196608
['Al Kα1', 'C Kα1,2', 'Ca Kα1', 'Cl Kα1', 'Fe Kα1', 'K Kα1', 'Mg Kα1,2', 'Mn Kα1', 'O
Kα1', 'P Kα1', 'S Kα1', 'Si Kα1', 'Ti Kα1']
```

2.3 Import raw data and convert to hyperspy HDF5

note even if this is **SEM** data due to a hyperspy bug need to treat as **TEM**. does not really effect spectra, but does mean that the quantification tool in hyperspy for TEM signals is not correct for SEM data.

In [103…
```
raw_map = hs.load('/Volumes/Tobisha/W26/W26_T5M2/W26_T5M2_EDS_Data.rpl') \
    .transpose(navigation_axes=(1,2))
raw_map = hs.signals.EDSTEMSpectrum(raw_map)
raw_map.plot()
```

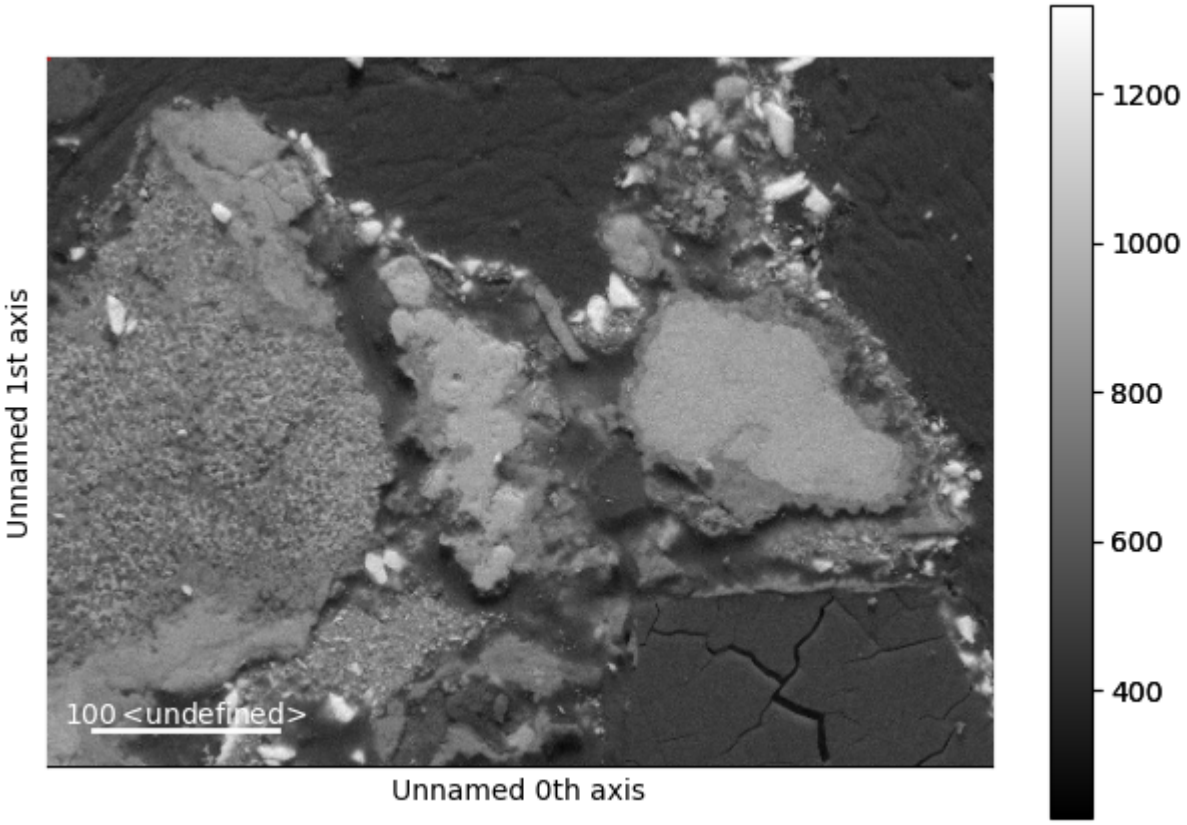

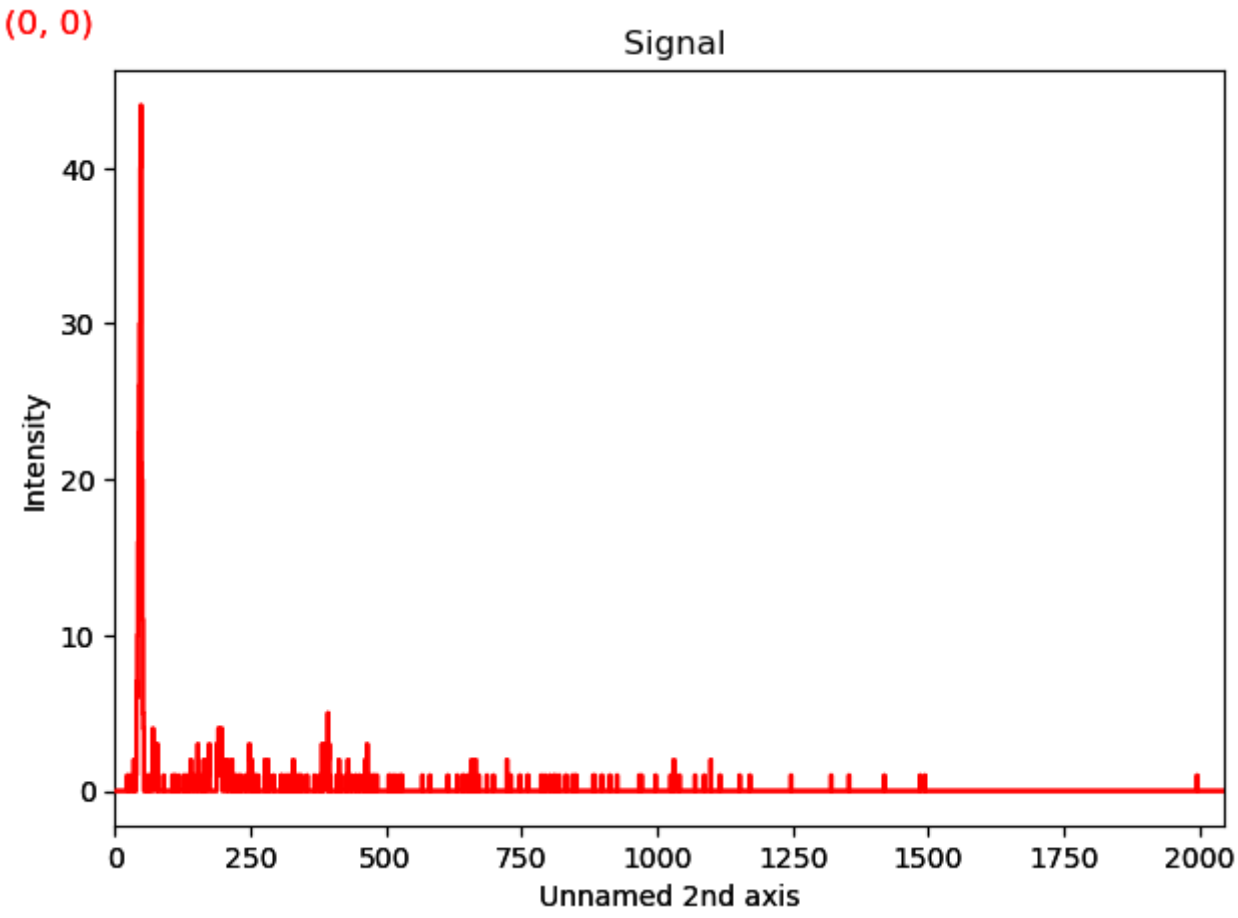

In [15]:
```
print(raw_map.data.shape)
```

```
(384, 512, 2048)
```

2.4 Bring in all the metadata from the H5OINA file

In [16]:
```
# Create a new list to store the extracted elements
elements_list = []

# Iterate over each element in the peaks_list
for peak in peaks_list:
```

```
# Split the element based on space and retrieve the first part
    element = peak.split()[0]
    elements_list.append(element)

print(elements_list)
```

```
['Al', 'C', 'Ca', 'Cl', 'Fe', 'K', 'Mg', 'Mn', 'O', 'P', 'S', 'Si', 'Ti']
```

2.5 Assign metadata and calibration information to spectral map

In [17]:
```
raw_map.axes_manager[0].name = 'X'
raw_map.axes_manager['X'].units = 'um'
raw_map.axes_manager['X'].scale = x_scale
raw_map.axes_manager[1].name = 'Y'
raw_map.axes_manager['Y'].units = 'um'
raw_map.axes_manager['Y'].scale = y_scale

raw_map.axes_manager[2].name = 'Energy'
raw_map.axes_manager['Energy'].units = 'keV'
raw_map.axes_manager['Energy'].scale = (energy_scale/1000)
raw_map.axes_manager['Energy'].offset = (energy_offset/1000)

raw_map.metadata.Acquisition_instrument.TEM.beam_energy = file['1']['EDS']['Header']
    ['Beam Voltage'][0]
raw_map.axes_manager
```

Out[17]: **< Axes manager, axes: (512, 384|2048) >**

Navigation axis name	size	index	offset	scale	units
X	512	0	0.0	0.8125022053718567	um
Y	384	0	0.0	0.8125022053718567	um

Signal axis name	size	offset	scale	units
Energy	2048	-0.19739768981934595	0.009999934196472168	keV

2.6 Crop the raw spectral data and backscatter electron image if needed

In [19]:
```
raw_map.plot()
```

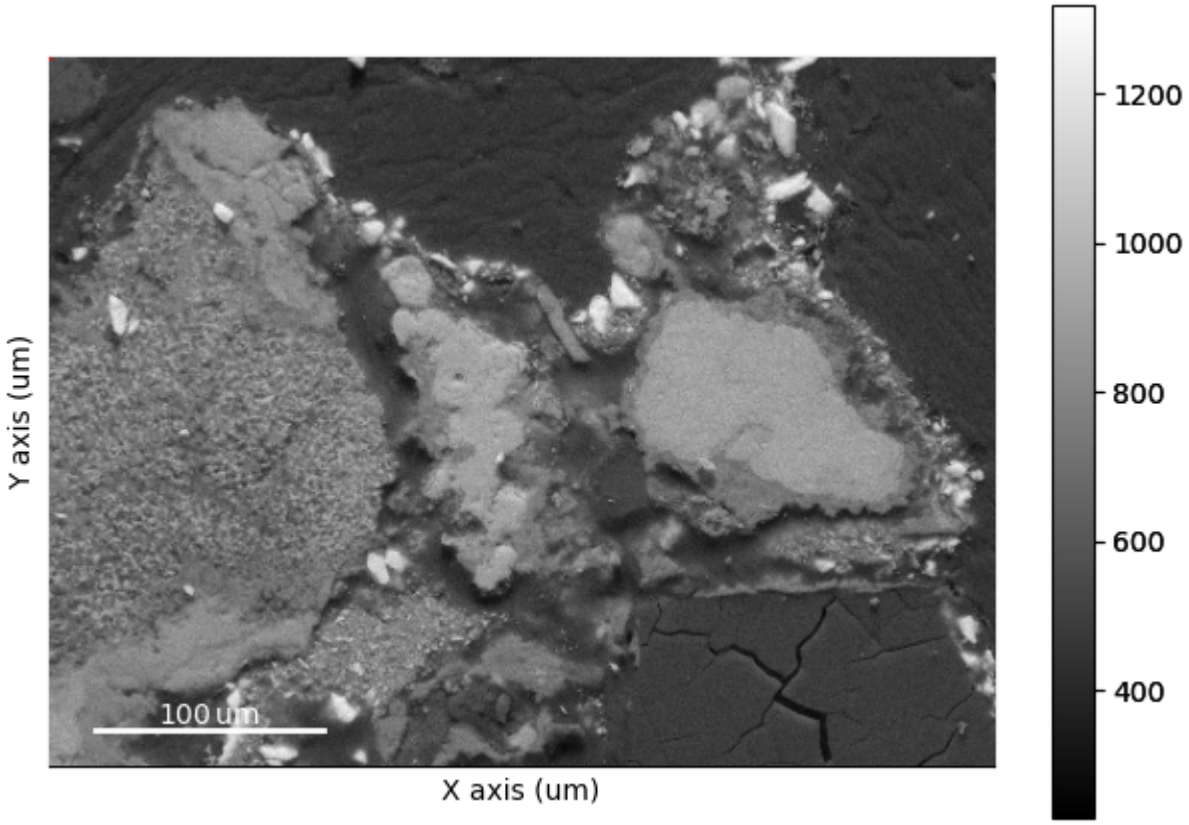

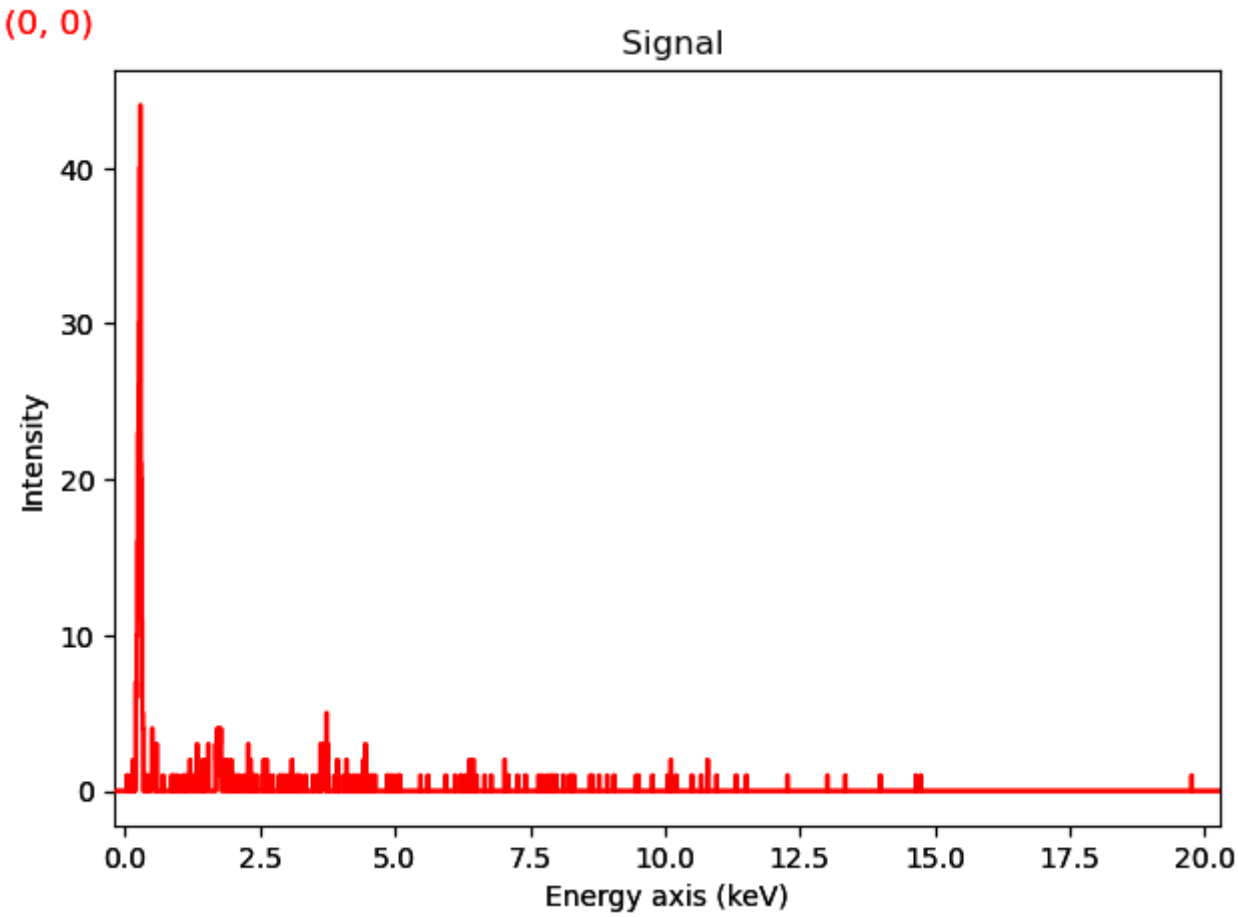

In [30]:
```
#Crop x-axis if necessary
raw_map.crop(axis = 'X',  start = 0, end = 972)
```

In [ ]:
```
#Crop y-axis if nevessary
raw_map.crop(axis = 'Y', start = 0, end = 728)
```

In [20]:
```
print(raw_map.data.shape)
```

```
(384, 512, 2048)
```

In [21]:
```
bse = io.imread('/Volumes/Tobisha/W26/W26_T5M2/W26_T5M2_BSE.tif')
```

```
print(bse.shape)
```

```
(768, 1024)
```

In [38]:
```
#Crop the BSE
bse = bse[0:1454,0:1944]
print(bse.shape)
```

```
(1454, 1944)
```

In [46]:
```
#Check to see if the bse is 2x the size of the raw data
bse_ds = ski.measure.block_reduce(bse, block_size = (2,2))
print(bse_ds.shape)
print(raw_map.data.shape)
```

```
(384, 512)
(384, 512, 2048)
```

In [23]:
```
#Check raw map before saving
raw_map.sum(axis = (0,1)).plot()
```

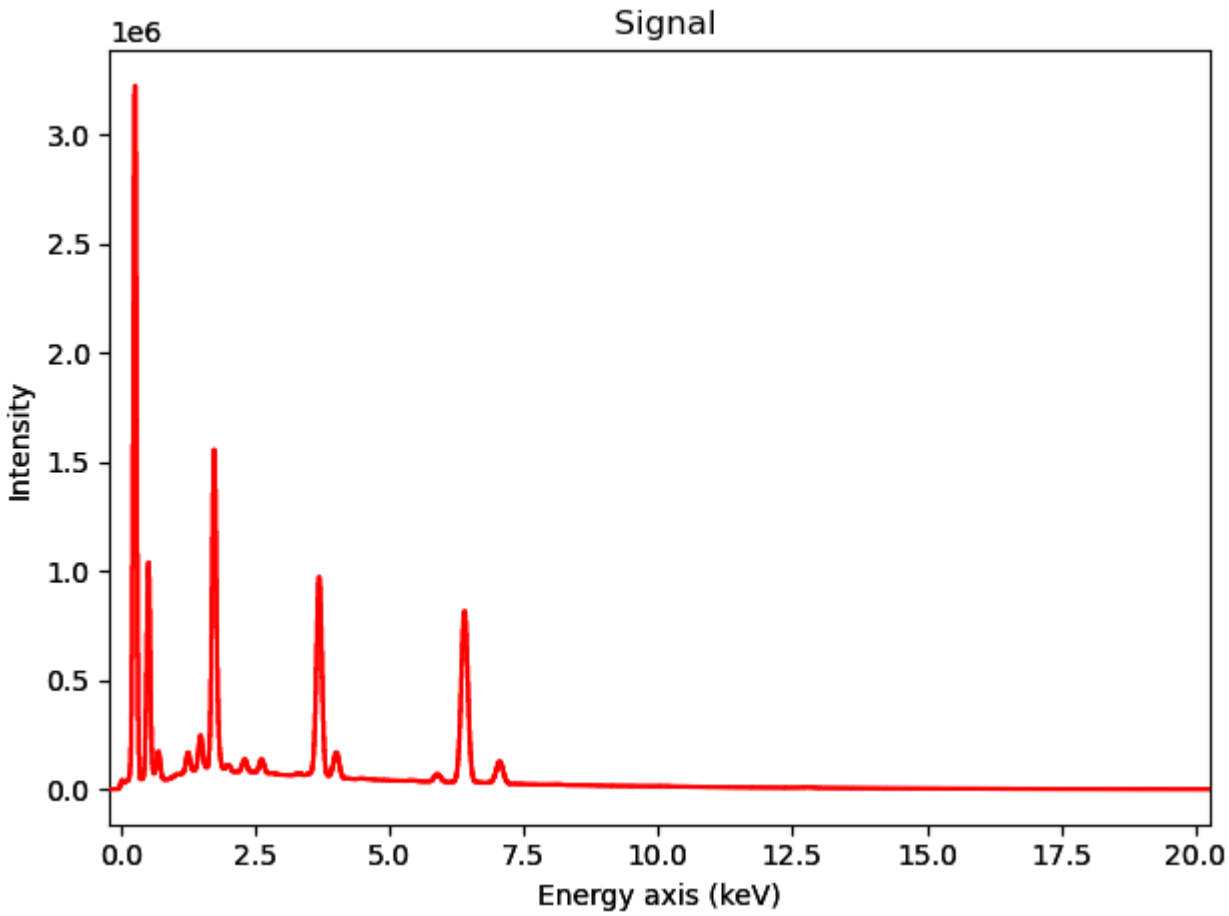

2.7 Save off the calibrated spectral map as a hyperspy file

In [60]:
```
raw_map.save('W26_T6.2M3_HR_EDS_data_raw_calib_RH_G16.hspy')
```

3.0 Load preprocessed data

In [10]:
```
# Calibrated hs
s_calib = hs.load('/Volumes/Tobisha/W26/W26_T5M2/W26_T5M2_EDS_data_raw_calib_RH.hspy'

y, x, e = s_calib.data.shape

offset = s_calib.axes_manager[0].offset
scale = s_calib.axes_manager[0].scale

# BSE
```

```
bse = io.imread('/Volumes/Tobisha/W27/W27_T2M2/BSE.tiff')
bse_ds = ski.measure.block_reduce(bse, block_size = (2,2))

# Poisson normalised vector
#d_vect = np.load('/Volumes/Tobisha/W24/W24_M1/poisson_vect.npy')

# Pore mask
mask = np.load('/Volumes/Tobisha/W26/W26_T5M2/mask.npy')

# Poisson scaled mask data
d_msk_norm = np.load('/Volumes/Tobisha/W26/W26_T5M2/poisson_vect_pore_mask.npy')


#NMF components
compz = np.load('/Volumes/Tobisha/W26/W26_T5M2/NMF/NMF.npy', allow_pickle = True)
```

In [26]:
```
#Set colors labels and elements to be labeled
elements = ['Si', 'Ca', 'Al', 'S', 'C', 'O', 'Cl', 'Fe', 'K', 'Cr', 'Na','Mg', 'Al',
            'P', 'Sc', 'Ti', 'V','Mn', 'Co', 'Ni', 'Cu', 'Ga', 'Ge','Br','Rb','Sr',
            'Nb','Mo']

e_colors = ['red', 'brown', 'darkred', 'tomato', 'salmon', 'indianred','orangered',
            'darkorange', 'chocolate', 'sandybrown', 'peru', 'navajowhite', 'wheat',
            'bisque', 'khaki', 'lightyellow', 'yellow', 'greenyellow', 'olive',
            'olivedrab','honeydew', 'limegreen', 'mediumseagreen', 'springgreen',
            'forestgreen', 'darkgreen', 'aquamarine', 'turquoise']
```

In [27]:
```
#Check that the energy axis is calibration
s_calib.axes_manager
```

Out[27]: **< Axes manager, axes: (512, 384\|2048) >**

Navigation axis name	size	index	offset	scale	units
X	512	0	0.0	0.8125022053718567	um
Y	384	0	0.0	0.8125022053718567	um

Signal axis name	size	offset	scale	units
Energy	2048	-0.19739768981936[illegible]9934196472168		keV

4.0 Poisson noise scaling

This step reduces the Poisson noise in the data

In [28]:
```
counts = s_calib.data.sum(axis = (0,1,2))
print(f'total map counts: {counts}')
cpp = counts/(y*x)
print(f'counts per pixel: {cpp}')
```

```
total map counts: 124833225
counts per pixel: 634.9346160888672
```

In [29]:
```
s_calib.sum(axis=(0,1)).plot(True)
```

```
WARNING:hyperspy._signals.eds:No elements defined, set them with `add_elements`
```

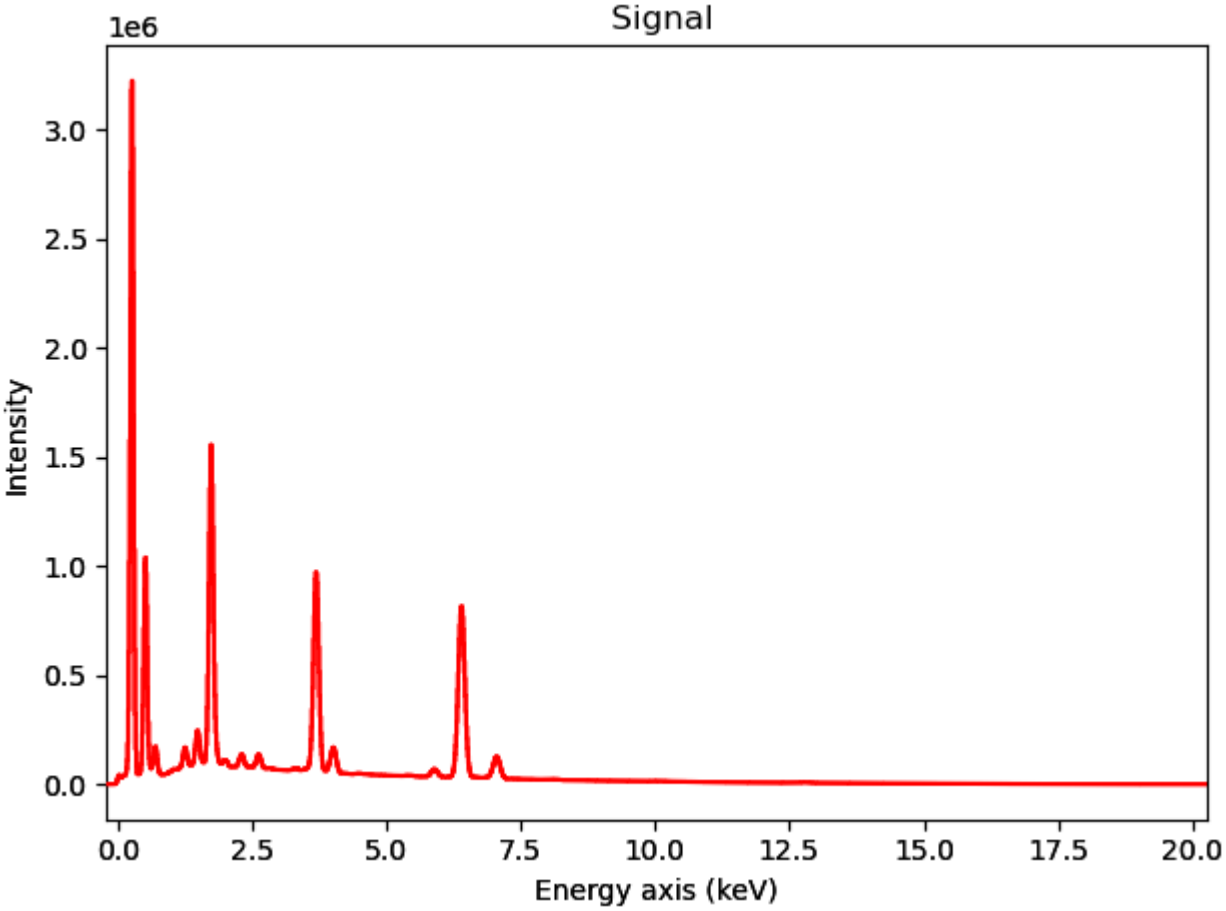

4.1 Mask Surface Defect

In [33]:
```
fig, (ax1,ax2) = plt.subplots(1,2)

ax1.imshow(bse_ds, cmap = 'gray')
ax2.hist(bse_ds.reshape(bse_ds.shape[0]*bse_ds.shape[1]), bins = 2**8)
ax2.set_box_aspect(bse_ds.shape[0]/bse_ds.shape[1])
ax2.set_ylim((0, 8000))
ax2.set_xlim((0, 2**16))
```

Out[33]: (0.0, 65536.0)

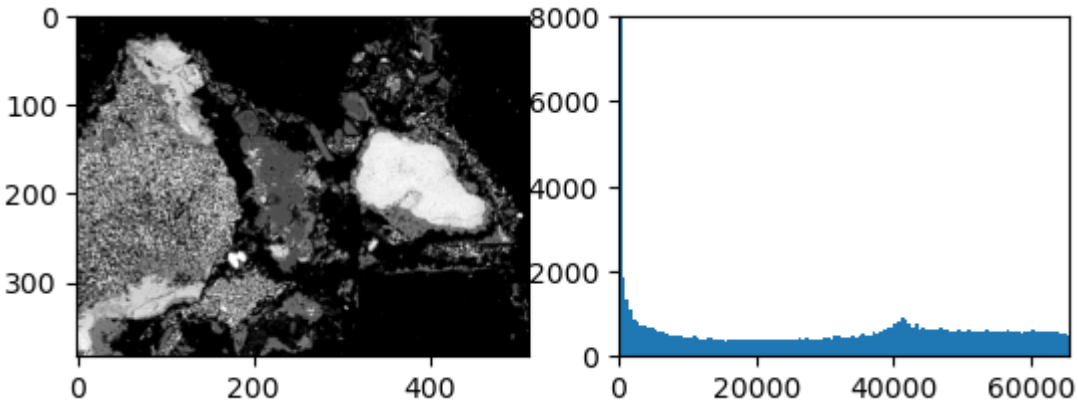

In [34]:
```
thresh_value = 20000
print(thresh_value)
```

```
20000
```

In [35]:
```
mask = np.ones((384, 512))
mask[bse_ds<=thresh_value] = 0

plt.figure()
plt.imshow(mask)
```

Out[35]: <matplotlib.image.AxesImage at 0x1d19ea990>

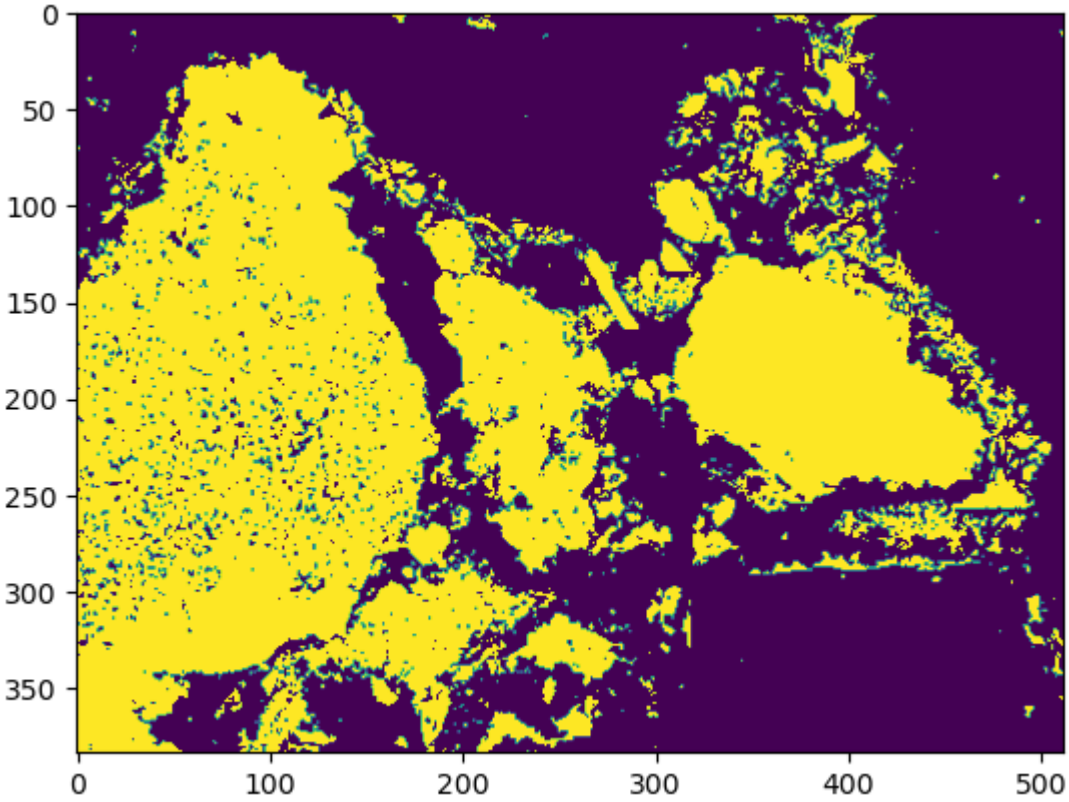

In [38]:
```
# save mask
np.save('mask.npy', mask)
```

4.2 Apply Poisson scaling

In [36]:
```
d_msk = flatten_masked_array(s_calib.data, mask)
d_im = reconstruct_masked_image(d_msk, mask, (y,x,e))
d_msk_norm = poisson_scale_mask(d_msk)
```

```
inital mean= 0.38371133422194326  inital max = 105  inital min= 0
(88223, 2048)
scaled mean= 5.0241918037074754e-05  scaled max = 0.019702760155977515  scaled min= 0.
0
```

In [37]:
```
plt.plot(d_msk.sum(0), color = 'r', label = 'Poisson of mask')
```

Out[37]: [<matplotlib.lines.Line2D at 0x1d1aa9750>]

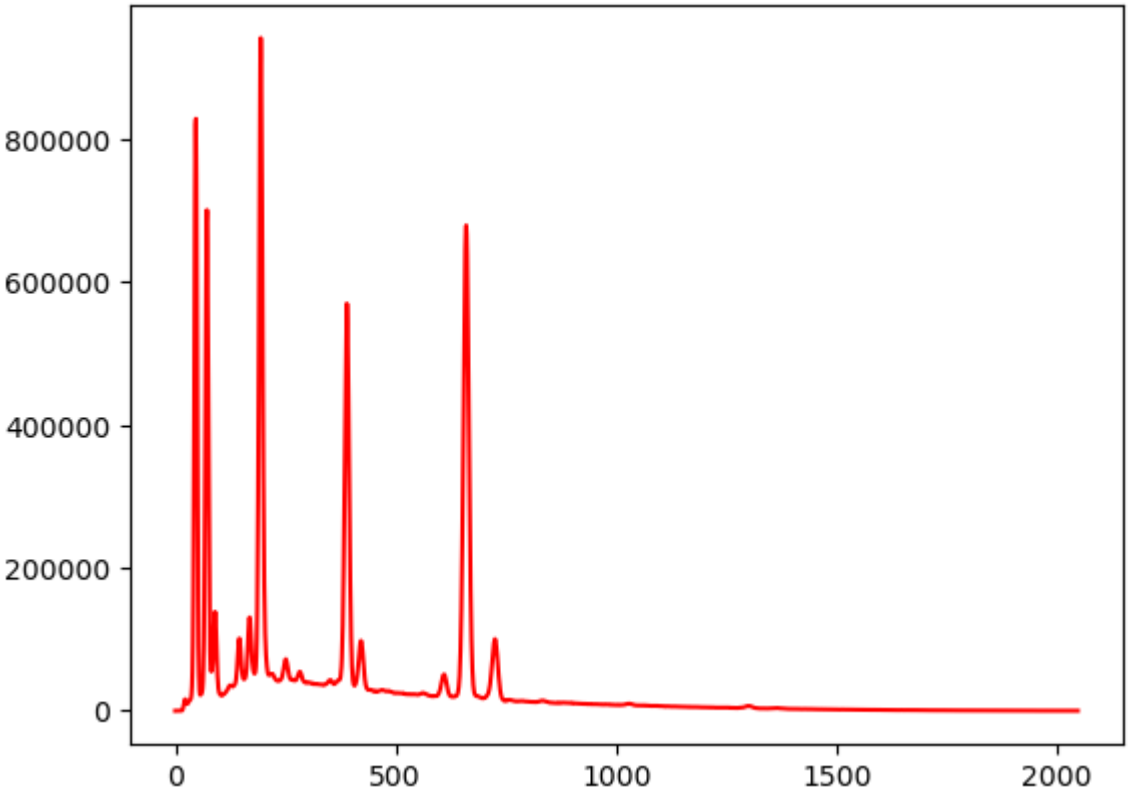

In [38]:
```
plt.figure()
plt.imshow(bse, cmap = 'gray')
plt.pcolormesh(d_im.sum(axis = 2), cmap = 'gray')
plt.gca().set_box_aspect(384/512)
```

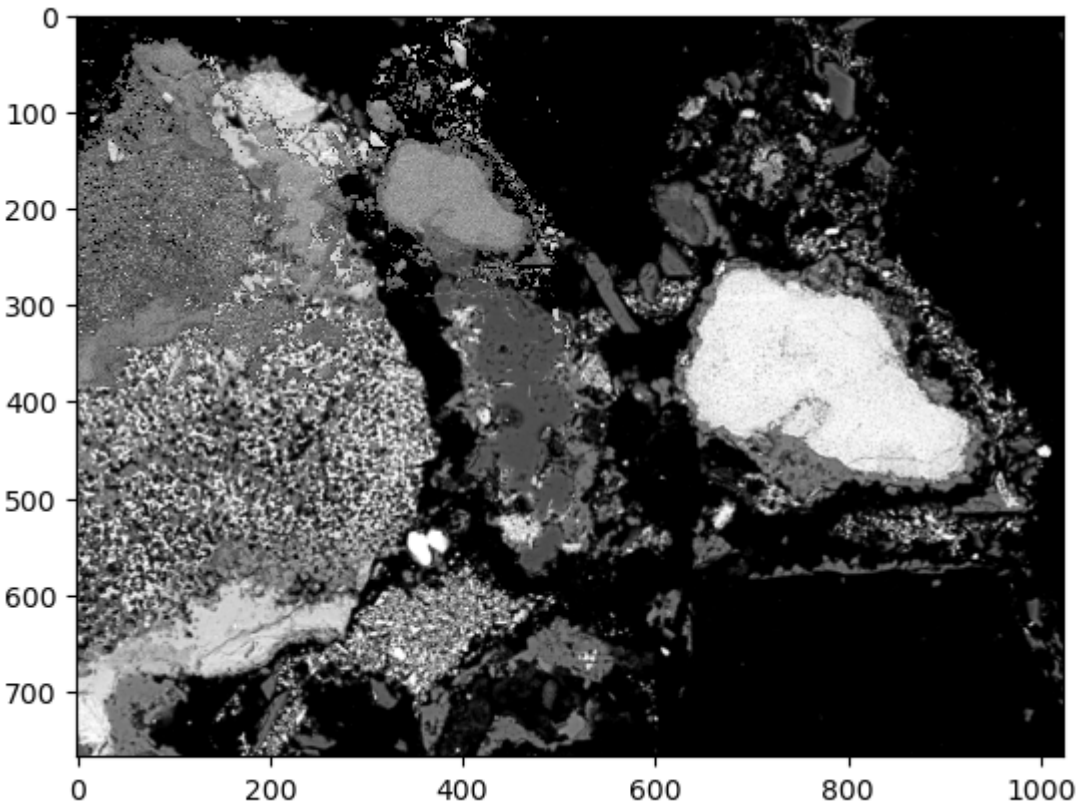

In [39]:
```
plt.figure(figsize = (16,6))
plt.plot(d_msk_norm.sum(0), color = 'r', label = 'Poisson of mask')
plt.plot(d_norm.sum((0,1)), color = 'black', linestyle = 'dashed',
         label = 'Poisson of raw')
plt.legend()
```

Out[39]: <matplotlib.legend.Legend at 0x1d1aa3cd0>

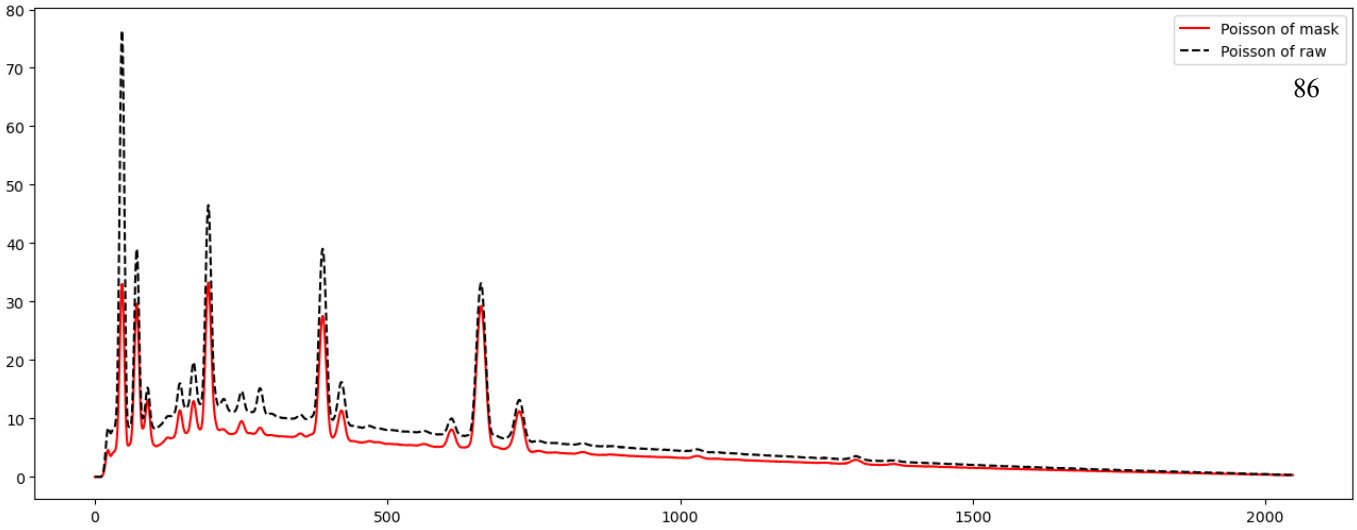

In [48]:
```
# save masked poisson scaled data
np.save('poisson_vect_pore_mask_.npy', d_msk_norm)
d_msk_norm.shape
```

Out[48]:
```
(106215, 2048)
```

5.0 Dimentional Reduction

5.1 PCA

In [40]:
```
s_calib.change_dtype('float32')
s_calib
```

Out[40]:
```
<EDSTEMSpectrum, title: , dimensions: (512, 384|2048)>
```

Run PCA using HyperSpy with 15 components to explore the data

In [41]:
```
s_calib.decomposition(normalize_poissonian_noise = True, algorithm = 'SVD',
                      output_dimension = 15)
```

```
Decomposition info:
  normalize_poissonian_noise=True
  algorithm=SVD
  output_dimension=15
  centre=None
```

Plot PCA Scree to see the total varience explained by each PCA component and use the number of components indicated by the 'elbow' to use in NMF

In [42]:
```
s_calib.plot_explained_variance_ratio(log = True,vline = True)
```

Out[42]:
```
<Axes: title={'center': '\nPCA Scree Plot'}, xlabel='Principal component index', yla
bel='Proportion of variance'>
```

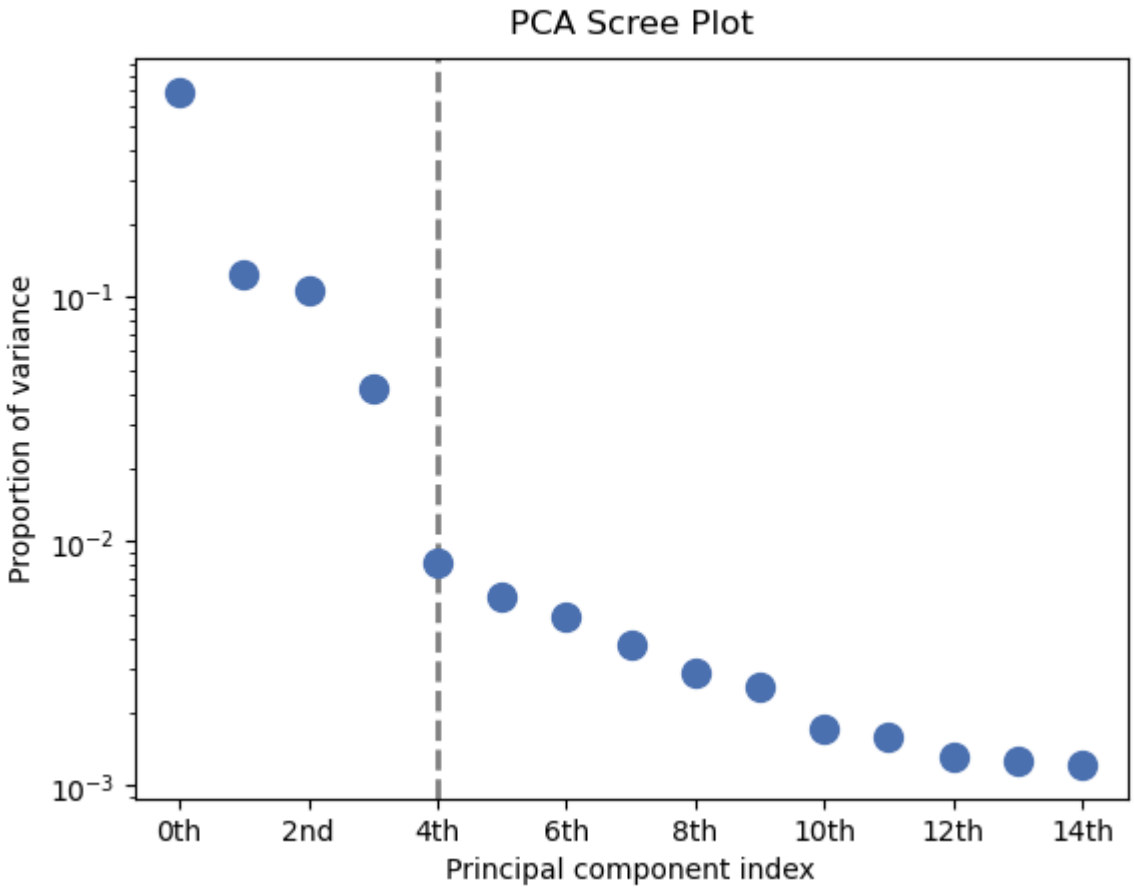

Based on the number of components that describe the data we will re-run the PCA with that number of components from the scree plot

In [43]:
```
forpca = d_msk_norm

pca = skl.decomposition.PCA(n_components = 5)
pca.fit(forpca)

f = plt.figure(figsize = (7,5))
plt.plot(np.cumsum(pca.explained_variance_ratio_))
plt.xlabel('number of components')
plt.ylabel('cumulative explained variance')
compz = pca.transform(forpca)
```

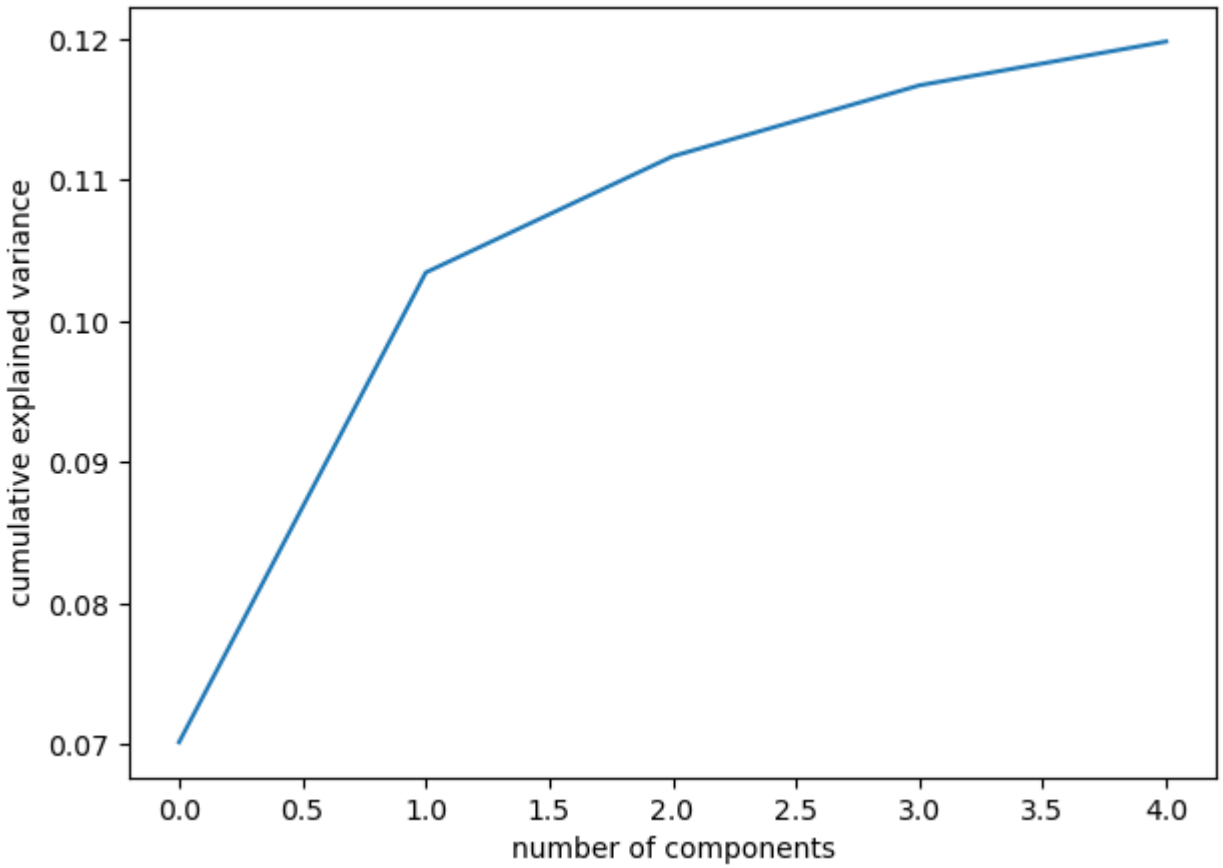

In [106…

```
#Plot the PCA components on the BSE image
compz_im = reconstruct_masked_image(compz, mask, (y, x, 5))

for i in range(0,5):
    plt.figure()
    plt.title(f'PCA{i+1}')
    plt.imshow(bse_ds, cmap = 'gray')
    plt.pcolormesh(compz_im[:,:,i])
    plt.colorbar()
```

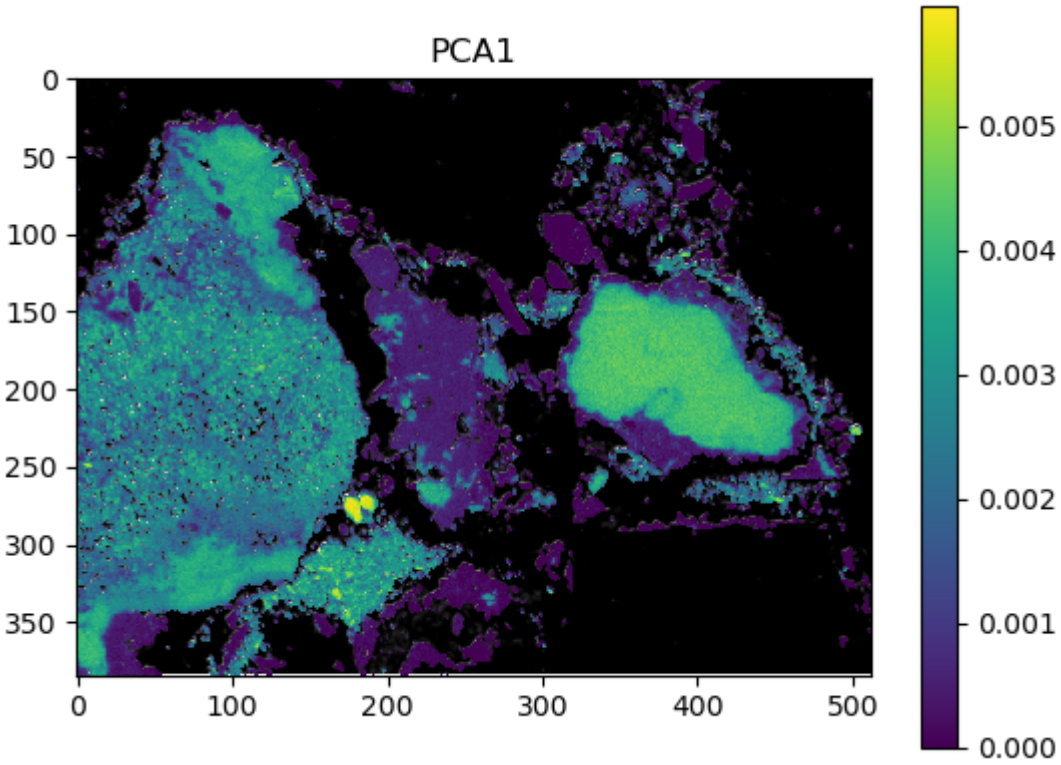

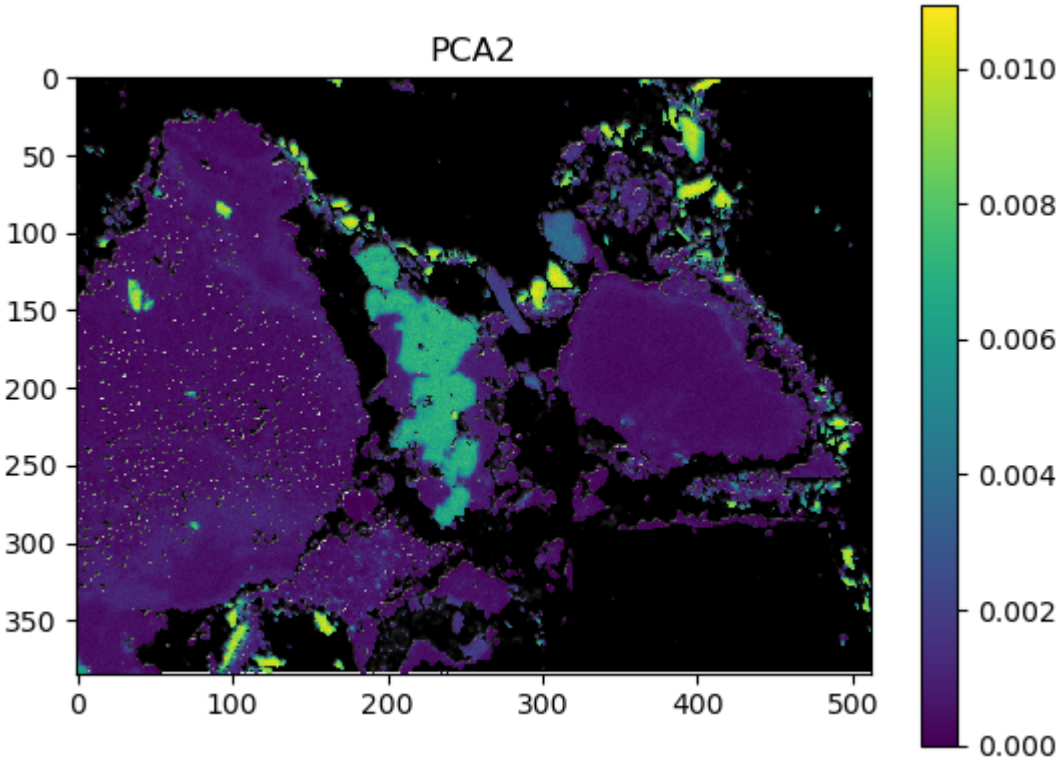
PCA2
0
50
100
150
200
250
300
350
0
100
200
300
400
500
0.010
0.008
0.006
0.004
0.002
0.000

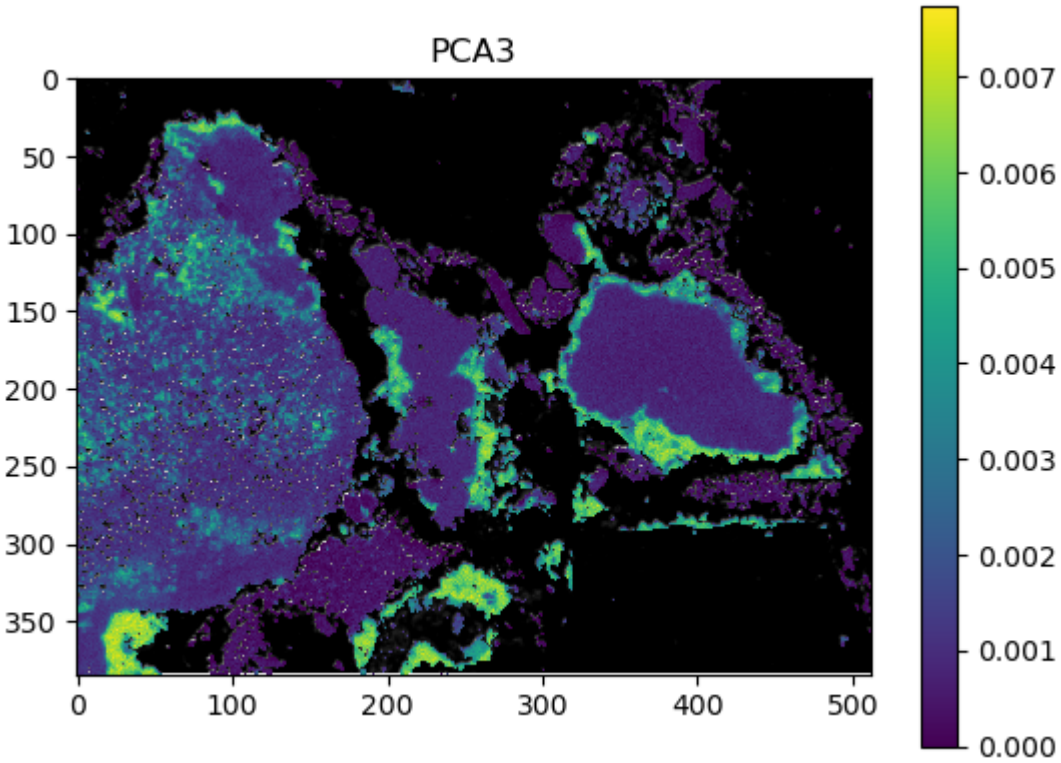
PCA3
0
50
100
150
200
250
300
350
0
100
200
300
400
500
0.007
0.006
0.005
0.004
0.003
0.002
0.001
0.000

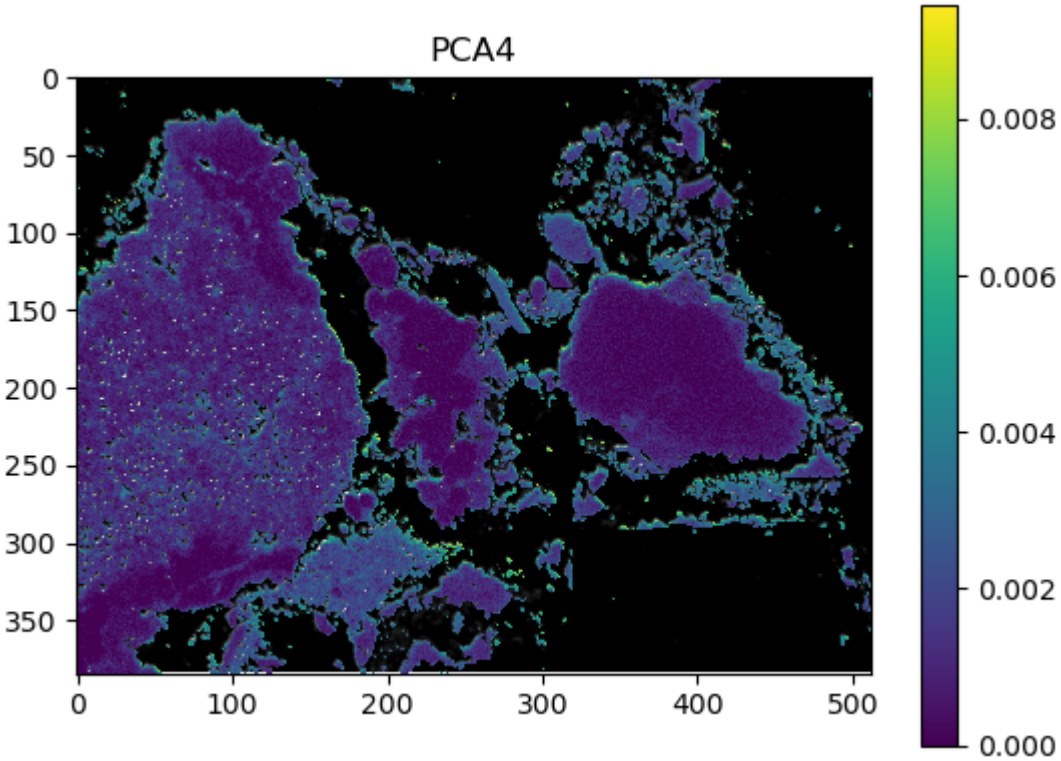

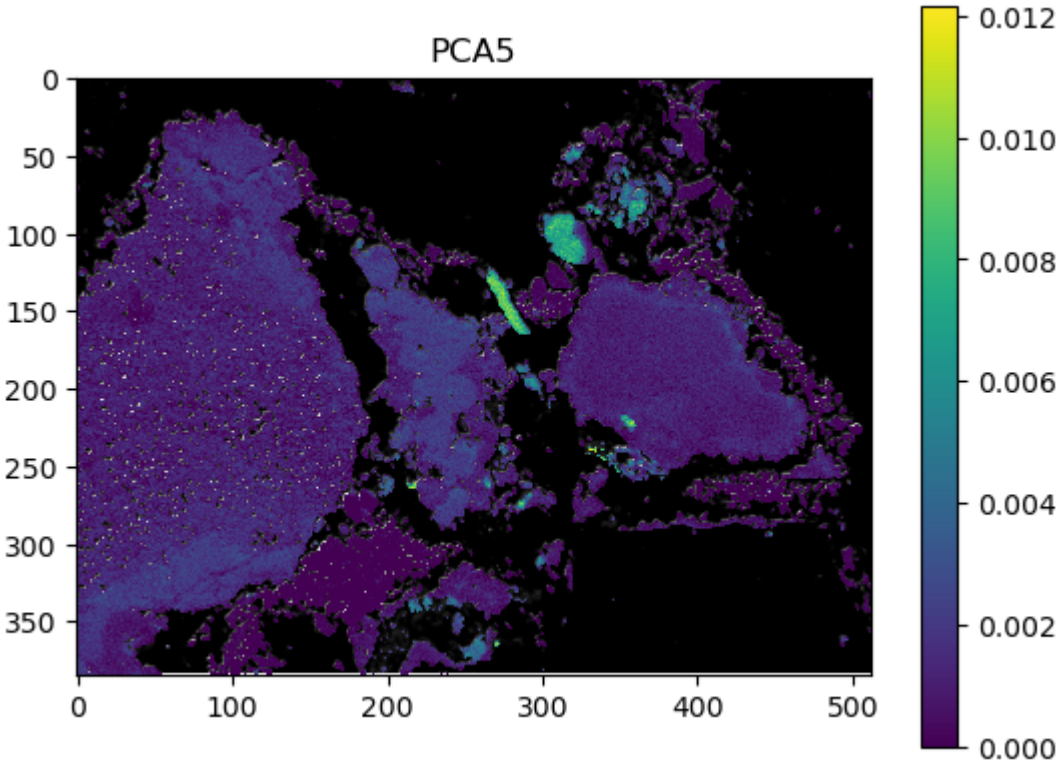

5.2 NMF

In [49]:
```
# Run NMF with the number of components that describe the data well from the PCA
    # Scree plot and from qualitatitly
# checking the noise of the component factors and loadings
fornmf = d_msk_norm

nmf = NMF(n_components = 5)
nmf.fit(fornmf)
compz = nmf.transform(fornmf)
```

```
/Users/robbinhilderman/opt/anaconda3/envs/hspy_environment/lib/python3.11/site-packages/sklearn/decomposition/_nmf.py:1665: ConvergenceWarning: Maximum number of iterations 200 reached. Increase it to improve convergence.
  warnings.warn(
```

In [37]:
```
# Save the NMF components
```

```
np.save('E:/W26/W26_T6.2M3/High_Resolution/compz', arr = compz, allow_pickle = True)
```

In [51]:
```
# Plot the NMF components on the BSE
compz_im = reconstruct_masked_image(compz, mask, (y, x, 5))

for i in range(0,5):
    plt.figure()
    plt.title(f'NMF{i+1}')
    plt.imshow(bse_ds, cmap = 'gray')
    plt.pcolormesh(compz_im[:,:,i], cmap = 'viridis')
    plt.colorbar()
```

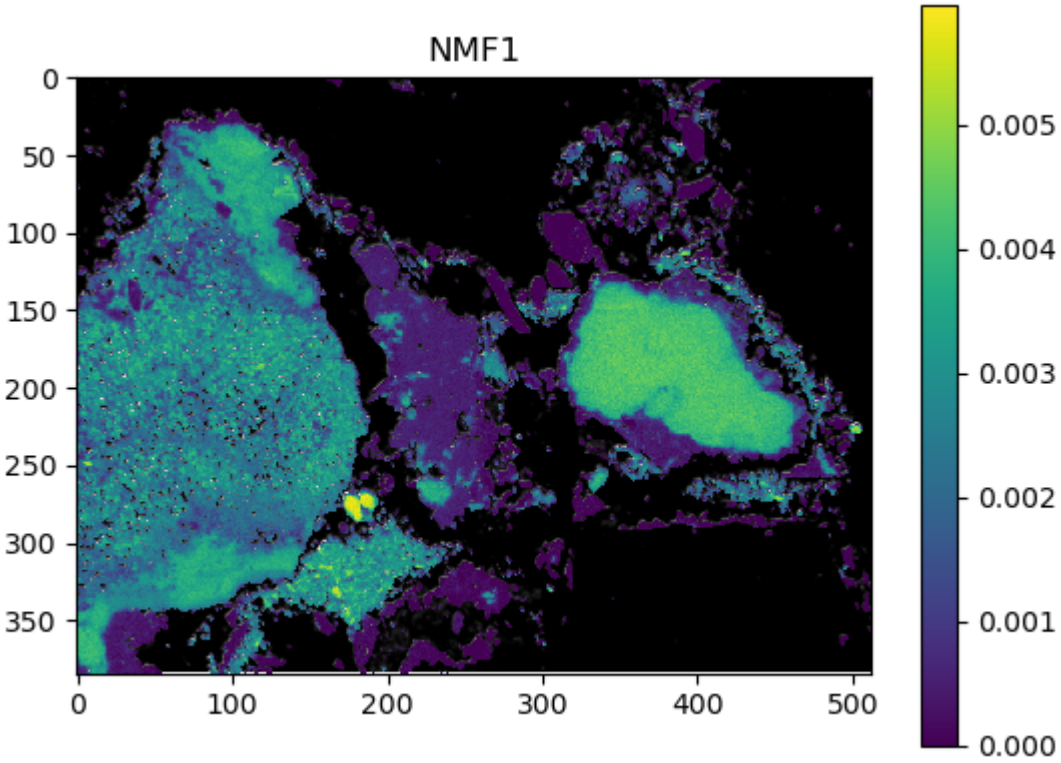

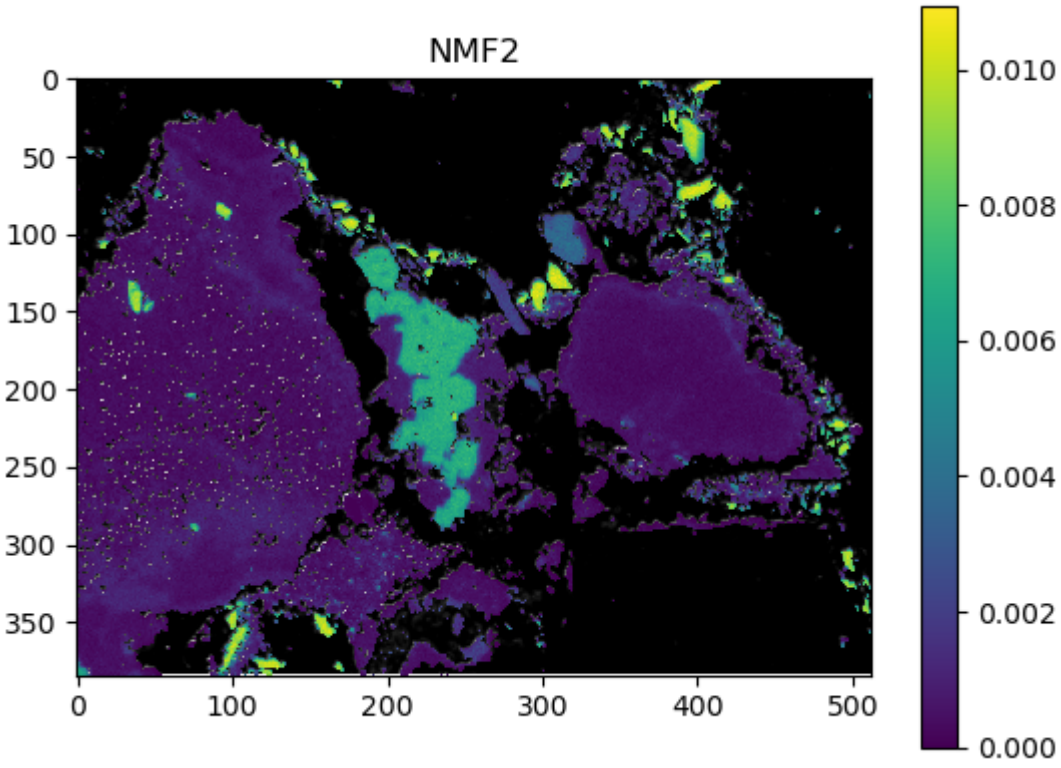

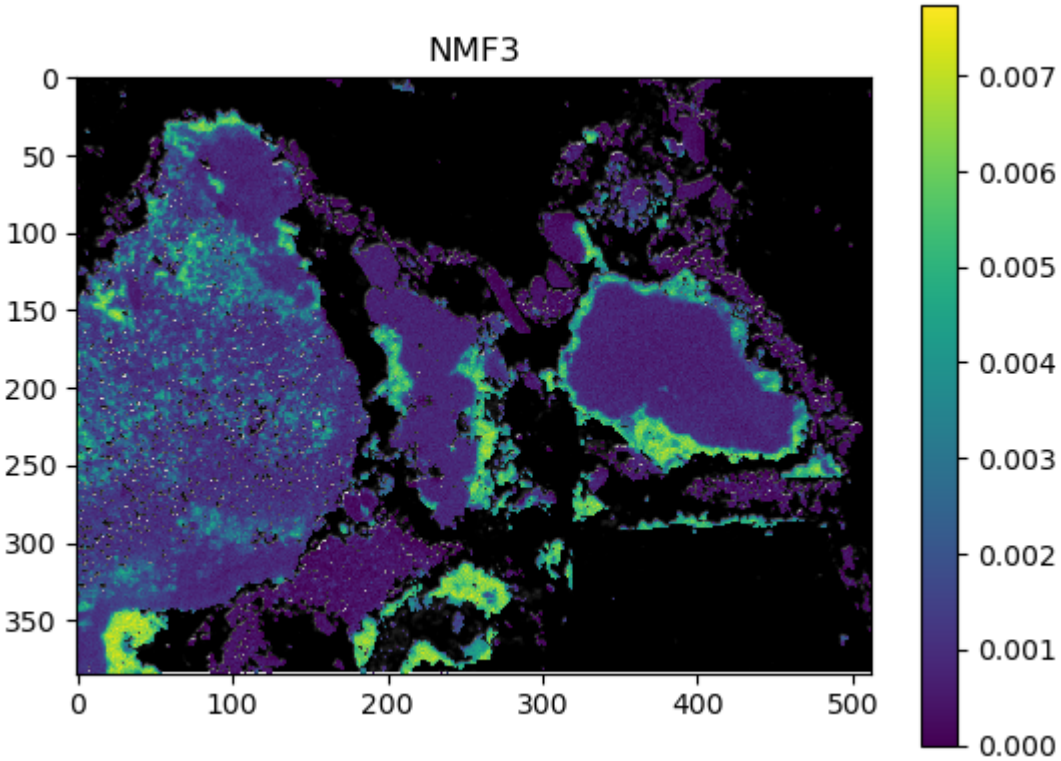
NMF3
0
50
100
150
200
250
300
350
0
100
200
300
400
500
0.007
0.006
0.005
0.004
0.003
0.002
0.001
0.000

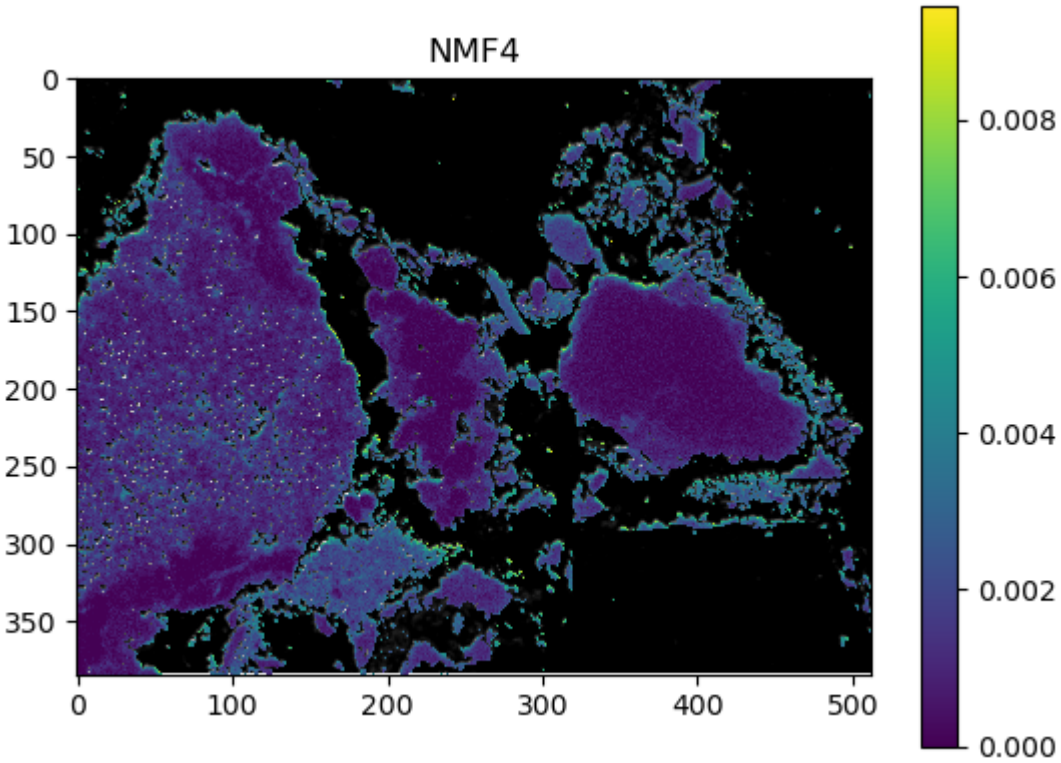
NMF4
0
50
100
150
200
250
300
350
0
100
200
300
400
500
0.008
0.006
0.004
0.002
0.000

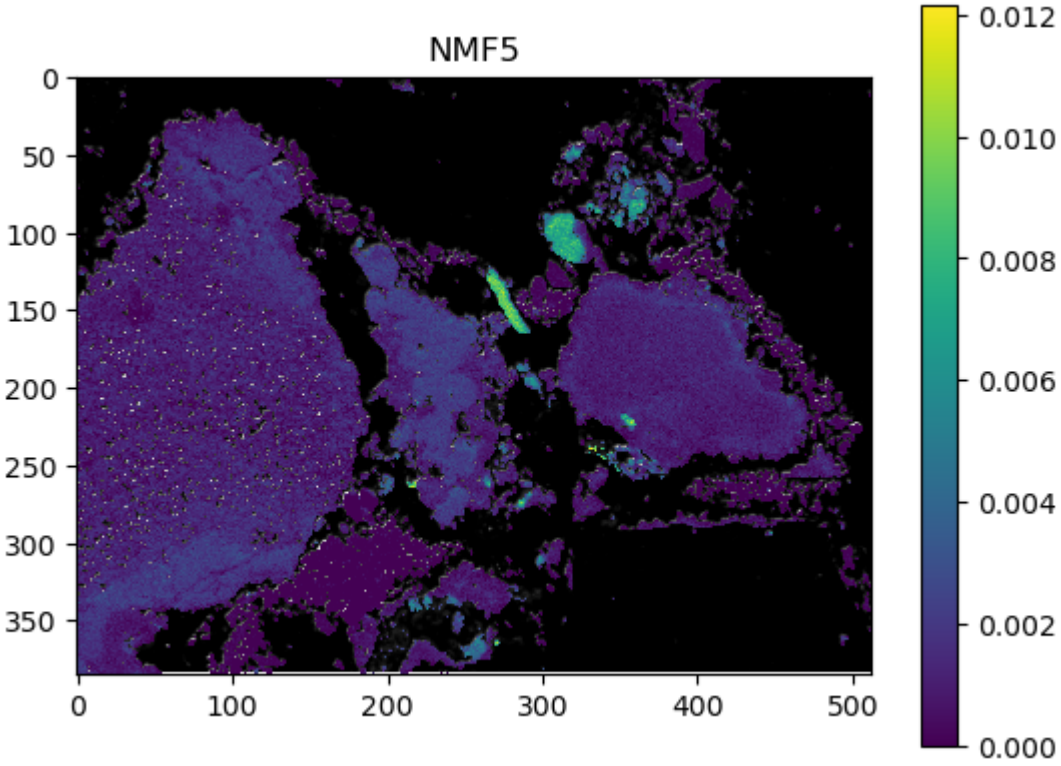

In [52]:
```
nmf_loads = nmf.components_
```

In [57]:
```
# Plot the NMF component loadings
%matplotlib inline
scale = s_calib.axes_manager[2].scale
offset = s_calib.axes_manager[2].offset
ofs = offset/scale

fig, axs = plt.subplots(5, 1)
fig.xlim =[0-ofs , 2048-ofs]
x_label = np.arange(0, 21, 2)
x_ticks = (x_label/scale) - ofs
fig.subplots_adjust(hspace = 0)

axs[0].plot(nmf_loads[0], linewidth = 1)
axs[0].set_yticks([])
axs[0].spines['bottom'].set_visible(False)
axs[0].set_xlim(0-ofs,2048)

axs[1].plot(nmf_loads[1], linewidth=1)
axs[1].set_yticks([])
axs[1].spines['top'].set_visible(False)
axs[1].spines['bottom'].set_visible(False)
axs[1].set_xlim(0-ofs,2048)

axs[2].plot(nmf_loads[2], linewidth=1)
axs[2].set_yticks([])
axs[2].spines['top'].set_visible(False)
axs[2].spines['bottom'].set_visible(False)
axs[2].set_xlim(0-ofs,2048)

axs[3].plot(nmf_loads[3], linewidth=1)
axs[3].set_yticks([])
axs[3].spines['top'].set_visible(False)
axs[3].spines['bottom'].set_visible(False)
axs[3].set_xlim(0-ofs,2048)

axs[4].plot(nmf_loads[4], linewidth=1)
axs[4].set_yticks([])
axs[4].spines['top'].set_visible(False)
axs[4].spines['bottom'].set_visible(False)
```

```
axs[4].set_xlim(0-ofs,2048)

plt.show()
#plt.savefig(f'NMF Factors_new', dpi = 600)
```

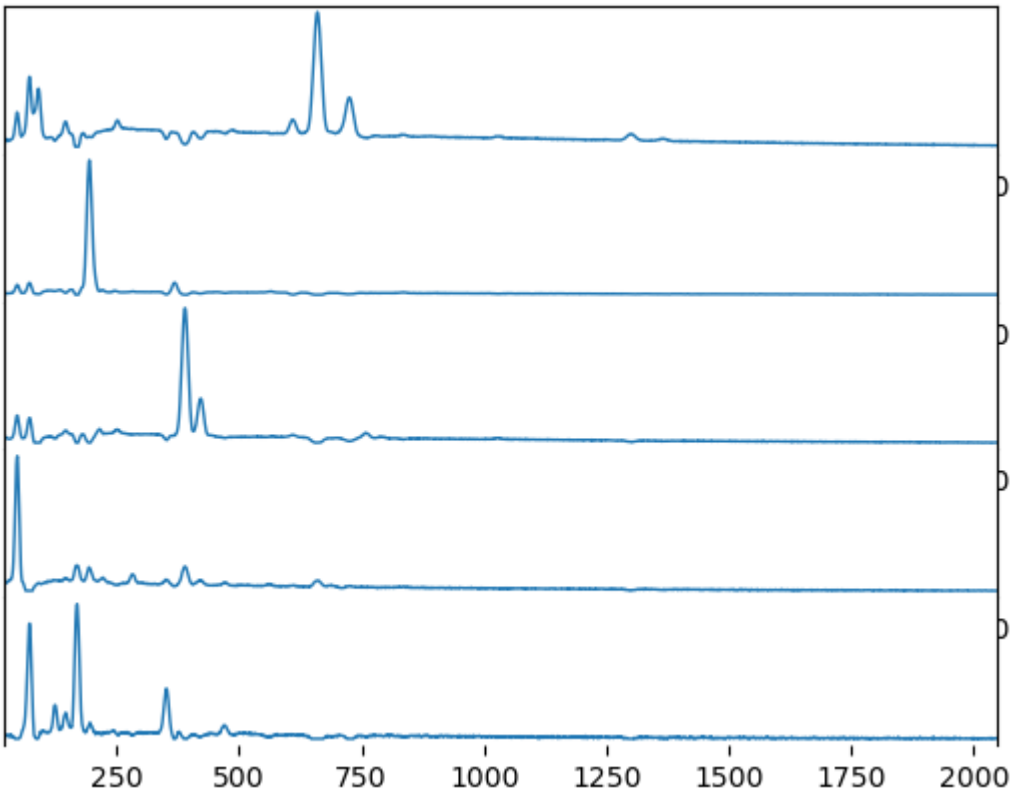

6.0 Clustering

6.1 HDBSCAN

In [60]:
```
clust = hdbscan.HDBSCAN(min_cluster_size = 100,min_samples = 150,
                        prediction_data = True)
clust.fit(compz)

# Hard cluster label for each data point, including outlier cluster of '-1'
labels = clust.labels_
print(labels.shape)

# Total number of clusters, inclusive of 'outliers' cluster
n_cluster = len(set(labels))
print('Number of clusters:',str(n_cluster))

# Assign the largest cluster number as outlier cluster
labels[np.where(labels == -1)[0]] = n_cluster-1
```

```
(88223,)
Number of clusters: 6
```

In [61]:
```
# calculate % of cluster 9 assigned as outliers
n_outliers = 0
for i in range(0,int(compz.shape[0])):
    if labels[i] == n_cluster-1:
        n_outliers+= 1
print('Percent outliers: '+str((n_outliers/compz.shape[0])*100))
```

```
Percent outliers: 18.658399737030027
```

In [64]:
```
# reconstruct hard cluster assignments
label_map = reconstruct_masked_image(arr = labels, mask = mask, im_shape = (y, x))
```

```
# create binary segmentations per cluster
labels_seg = []
labels_spec = []
clus_count = []
zero_count = []

for i in range(0, n_cluster):

    labels_seg.append(np.zeros((y, x)))
    labels_seg[i][label_map==i] = 1
    labels_spec.append(s_calib.data[label_map==i, :].sum(axis = (0)))

    plt.figure()
    plt.imshow(bse_ds, cmap='binary_r')
    plt.imshow(labels_seg[i],cmap = 'binary_r')
    plt.title(f'cluster {i+1}')

    clus_count.append(labels_seg[i].sum())
    zero_count.append((labels_seg[i]==0).sum())
    print(clus_count[i]==((y*x)-zero_count[i]))


labels_seg = np.asarray(labels_seg)
print(labels_seg.shape)
print(clus_count)
```

```
True
True
True
True
True
True
(6, 384, 512)
[795.0, 4813.0, 3190.0, 57500.0, 5464.0, 16461.0]
```

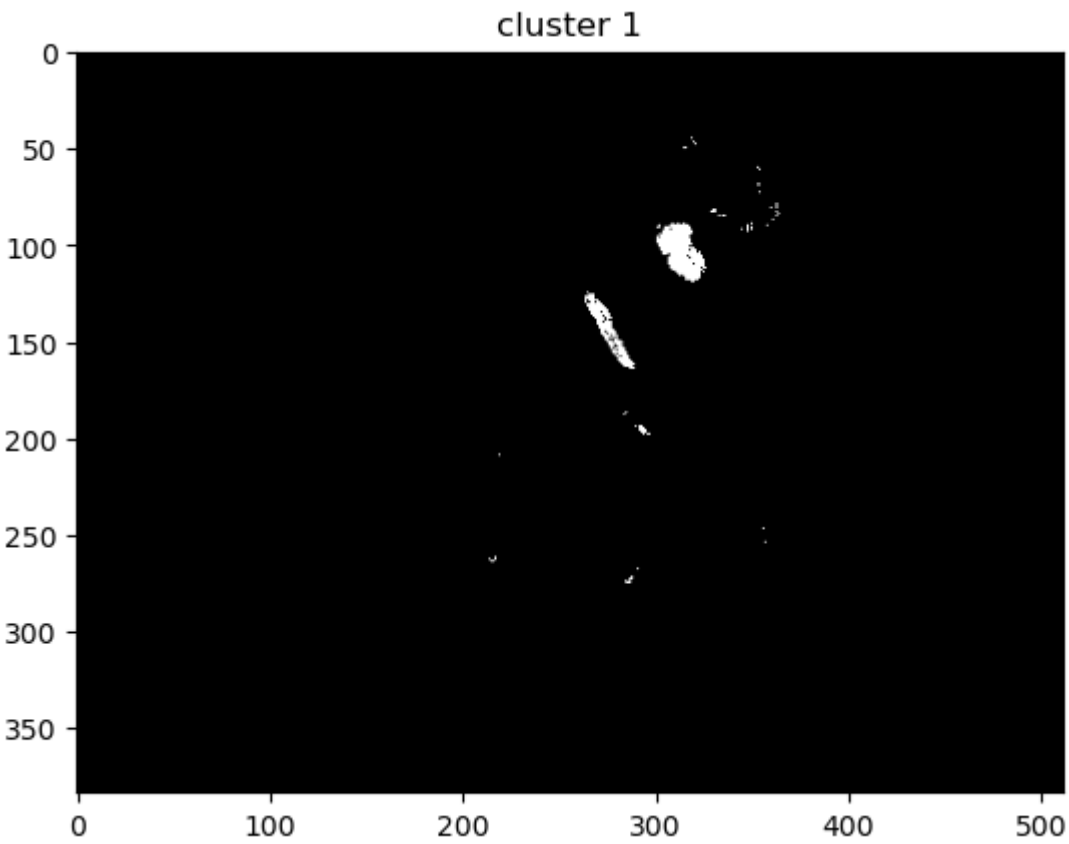

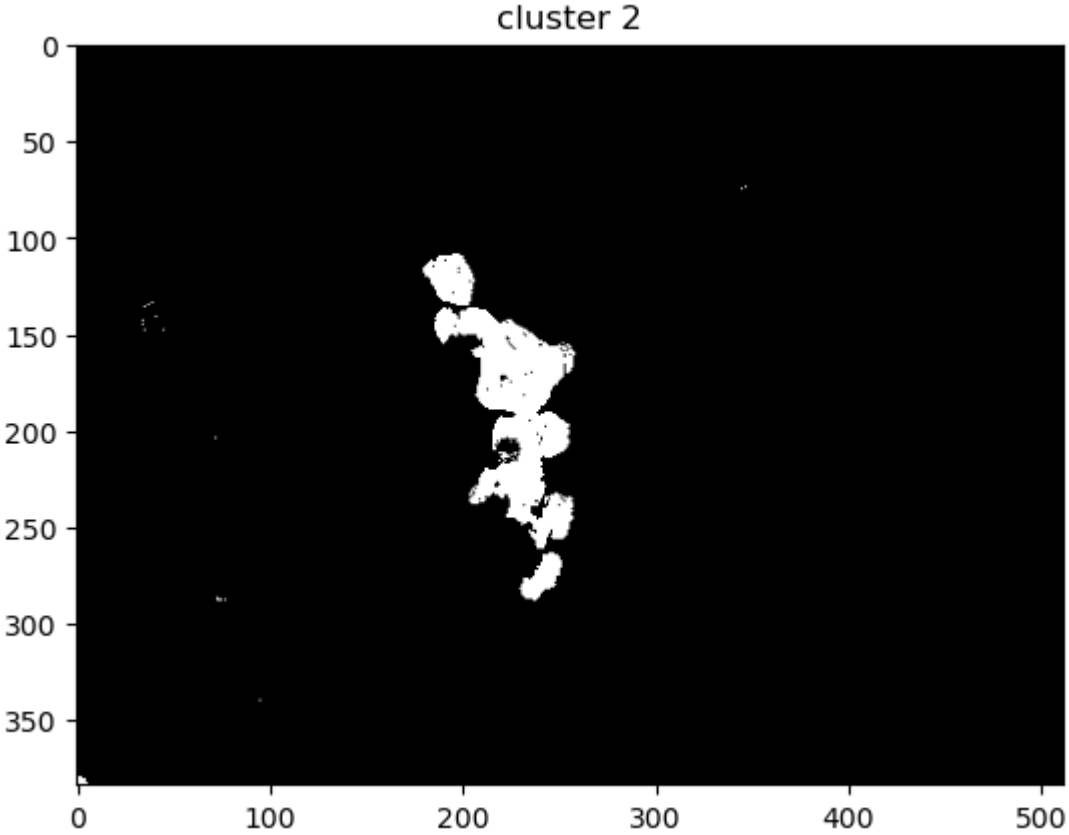
cluster 2
0
50
100
150
200
250
300
350
0
100
200
300
400
500

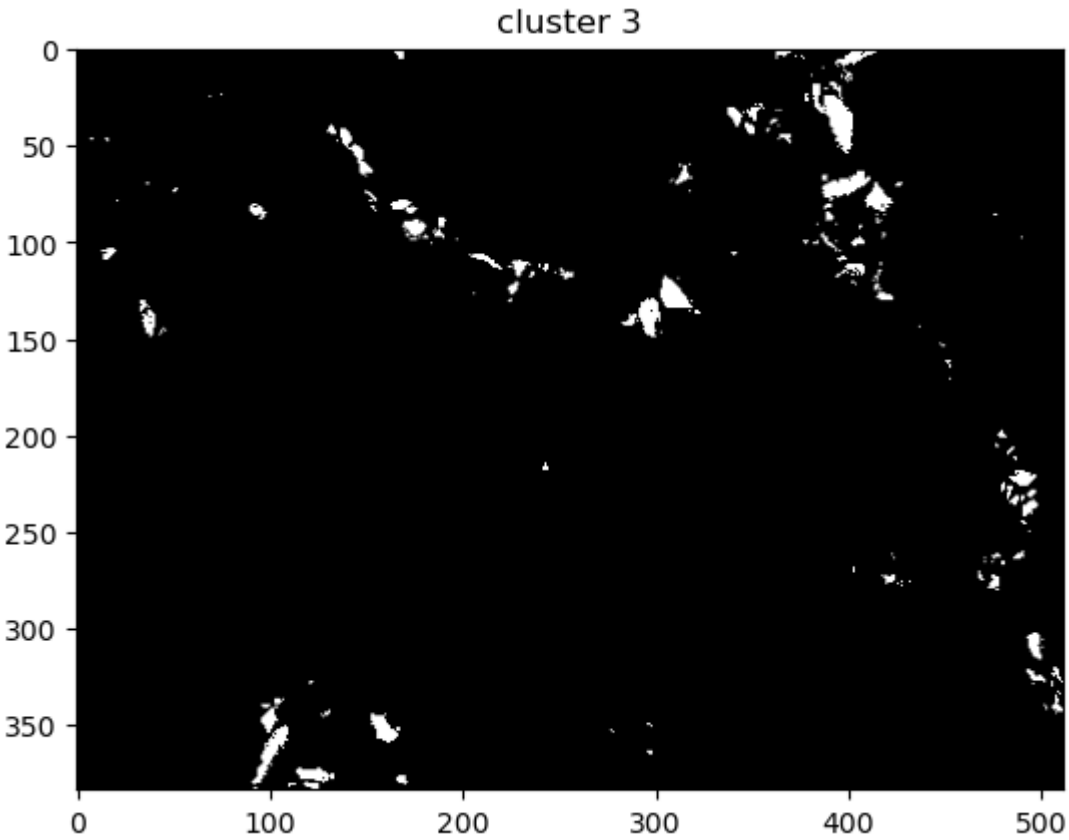
cluster 3
0
50
100
150
200
250
300
350
0
100
200
300
400
500

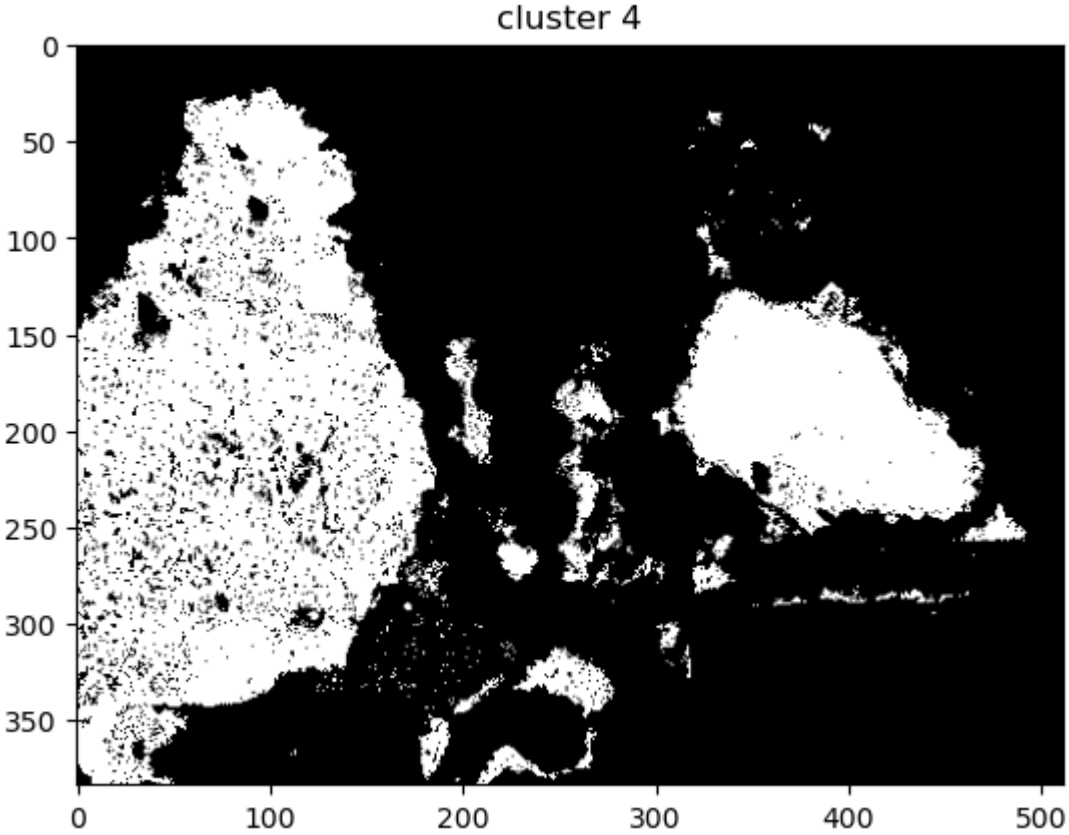
cluster 4
0
50
100
150
200
250
300
350
0
100
200
300
400
500

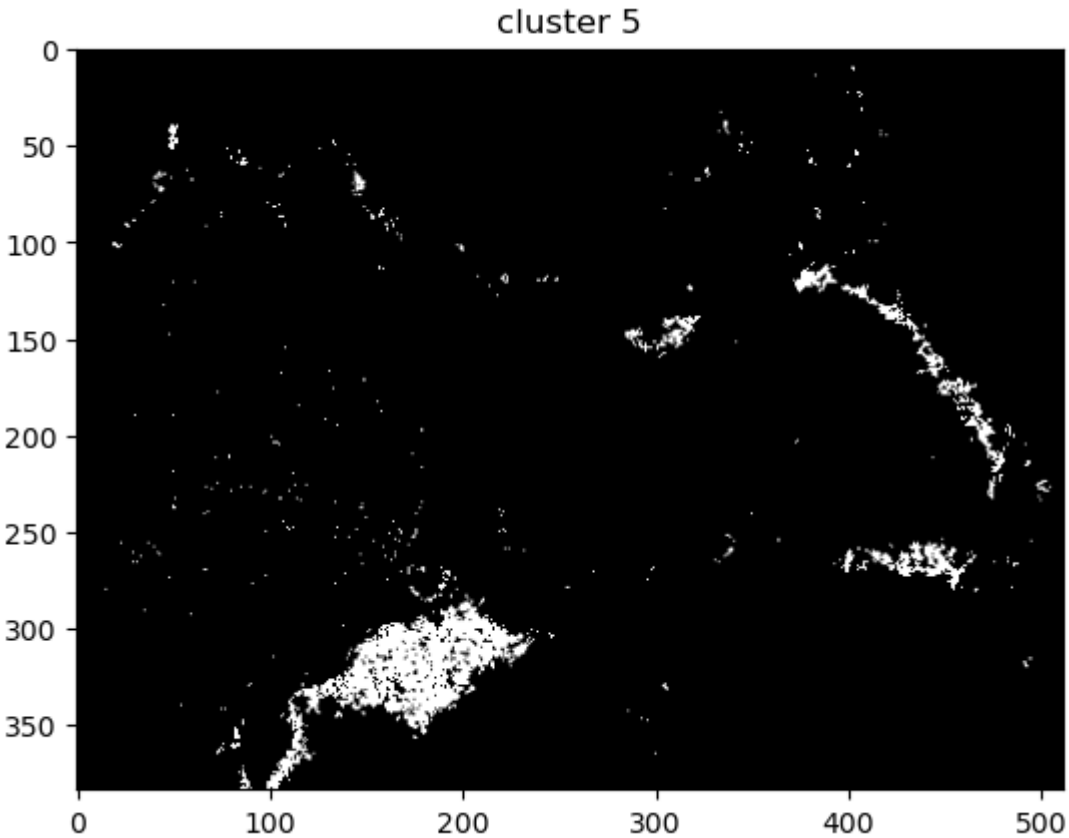
cluster 5
0
50
100
150
200
250
300
350
0
100
200
300
400
500

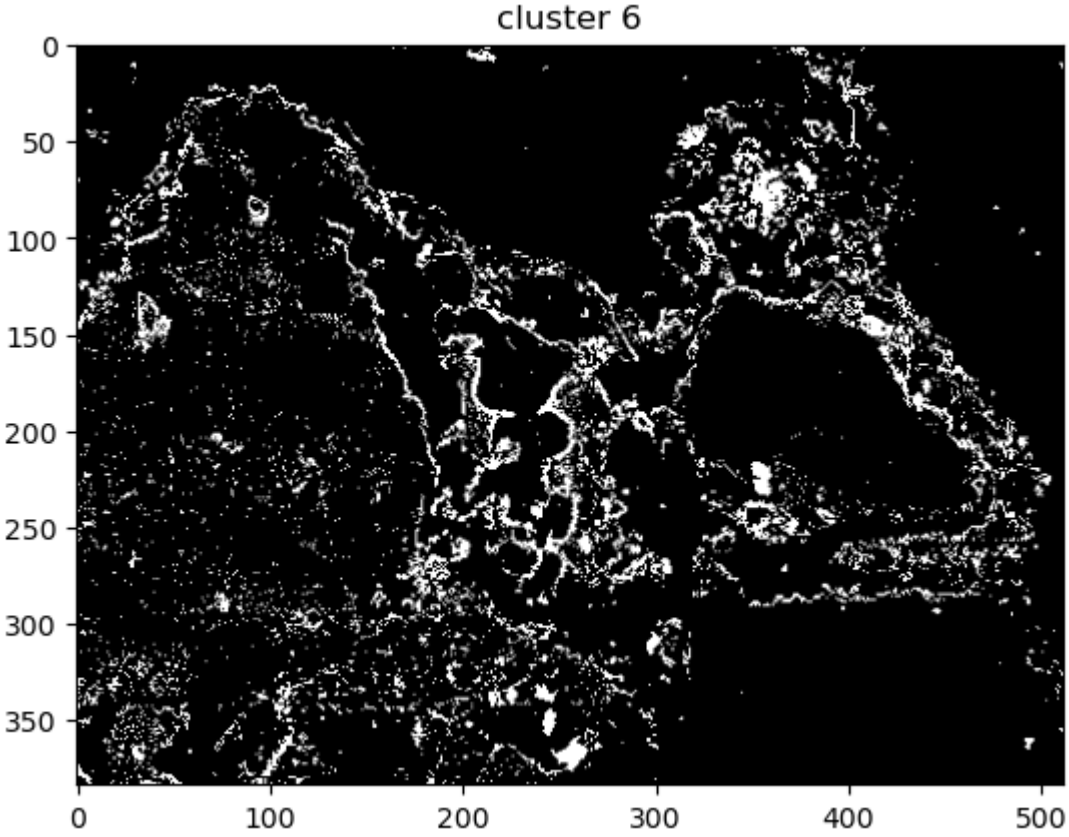

In [ ]:
```
#Save any cluster of interest to do reiterate
np.save('COI_P4_spec', arr = labels_seg[3], allow_pickle = True)
```

In [65]:
```
#Plot the phase map
plt_phasemap(label_map, bse_im = bse_ds, scale = s_calib.axes_manager[0].scale,
             mpl_cmap = 'tab20', phasemap_title = 'phasemap')
```

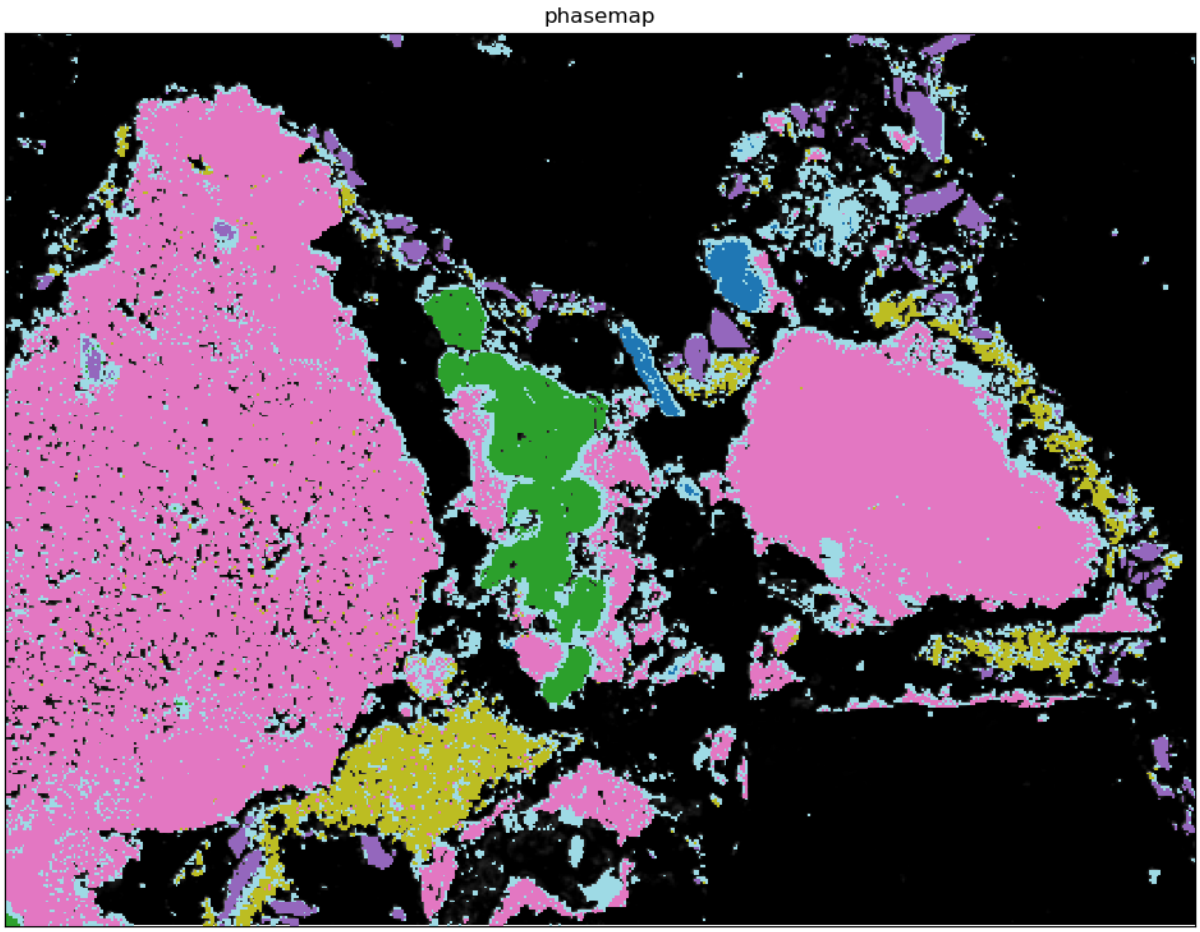

7.0 Save cluster spectra for back projection

In [74]:
```
# Create summed spectra as % of total counts per cluster
clus_spec = []

for i in range(0,n_cluster):
    clus_spec.append((s_calib.data[labels_seg[i] == 1,:]).sum(axis = 0))
```

In [97]:
```
# Plot each spectra to explore
c_idx = 0
for spec in clus_spec:
    plt.figure()
    plt.imshow(labels_seg[c_idx])
    plt.title(f'Cluster {c_idx+1}')
    c_idx+= 1
```

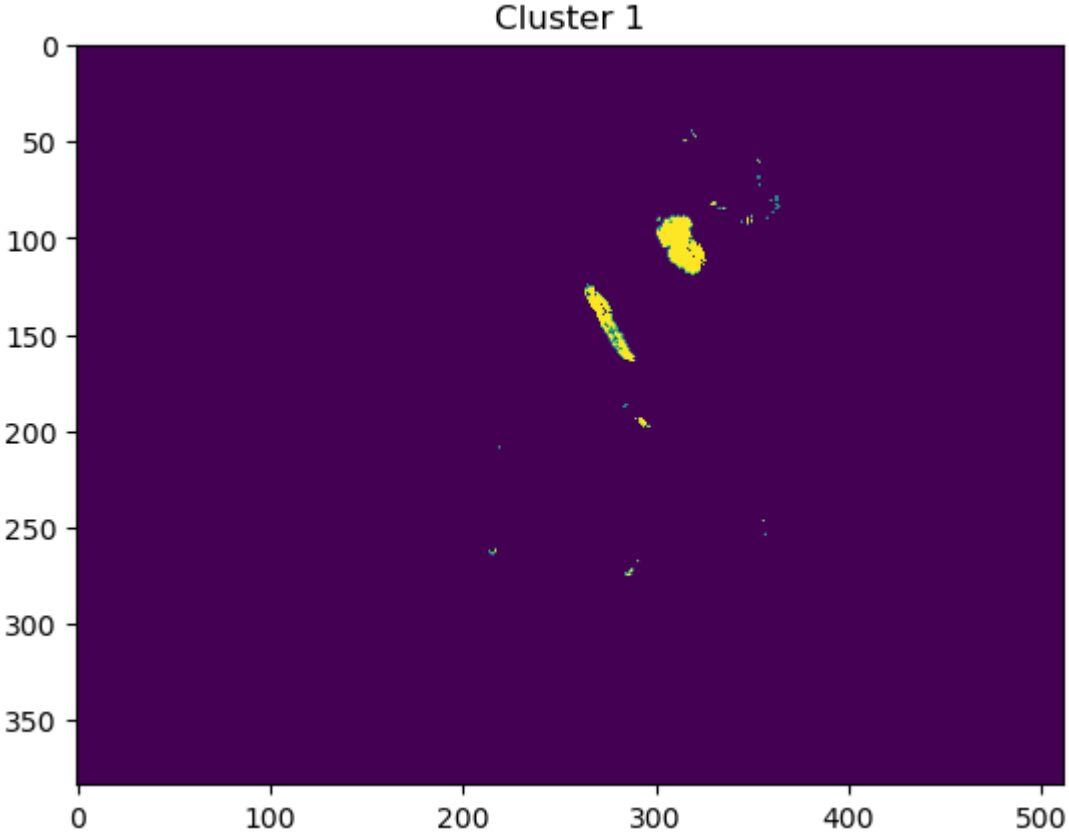
Cluster 1
0
50
100
150
200
250
300
350
0
100
200
300
400
500

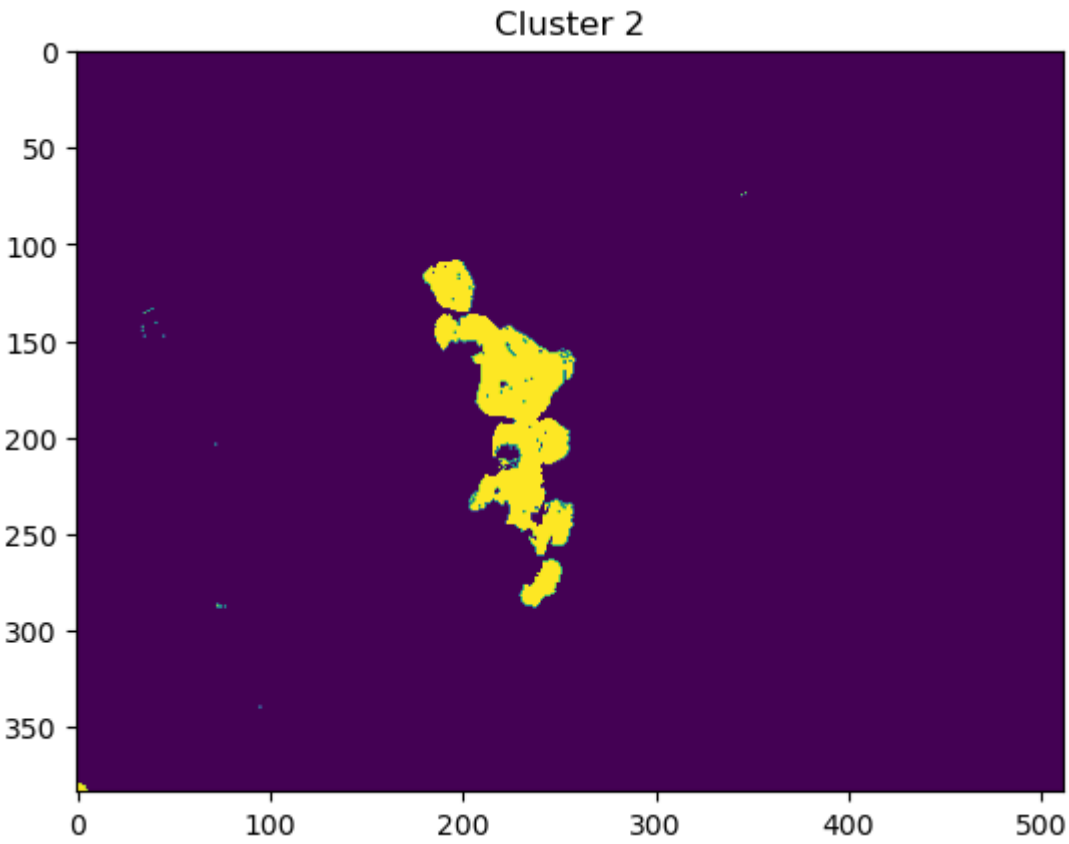
Cluster 2
0
50
100
150
200
250
300
350
0
100
200
300
400
500

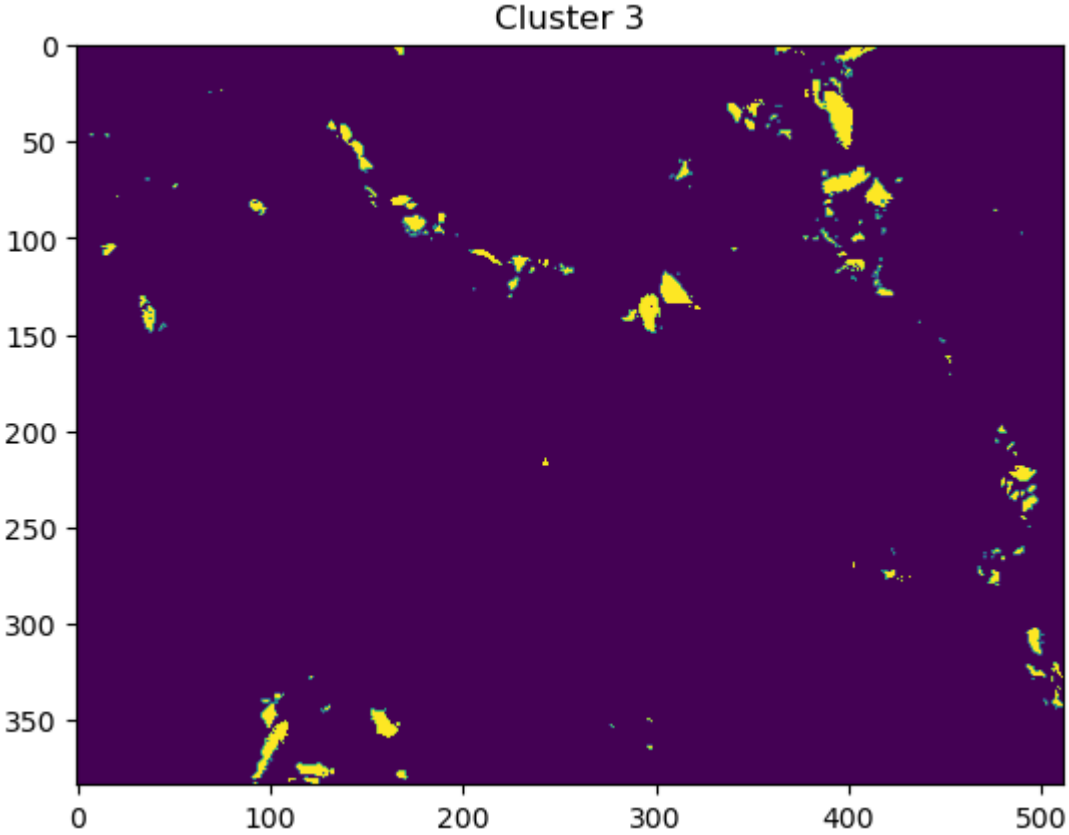
Cluster 3
0
50
100
150
200
250
300
350
0
100
200
300
400
500

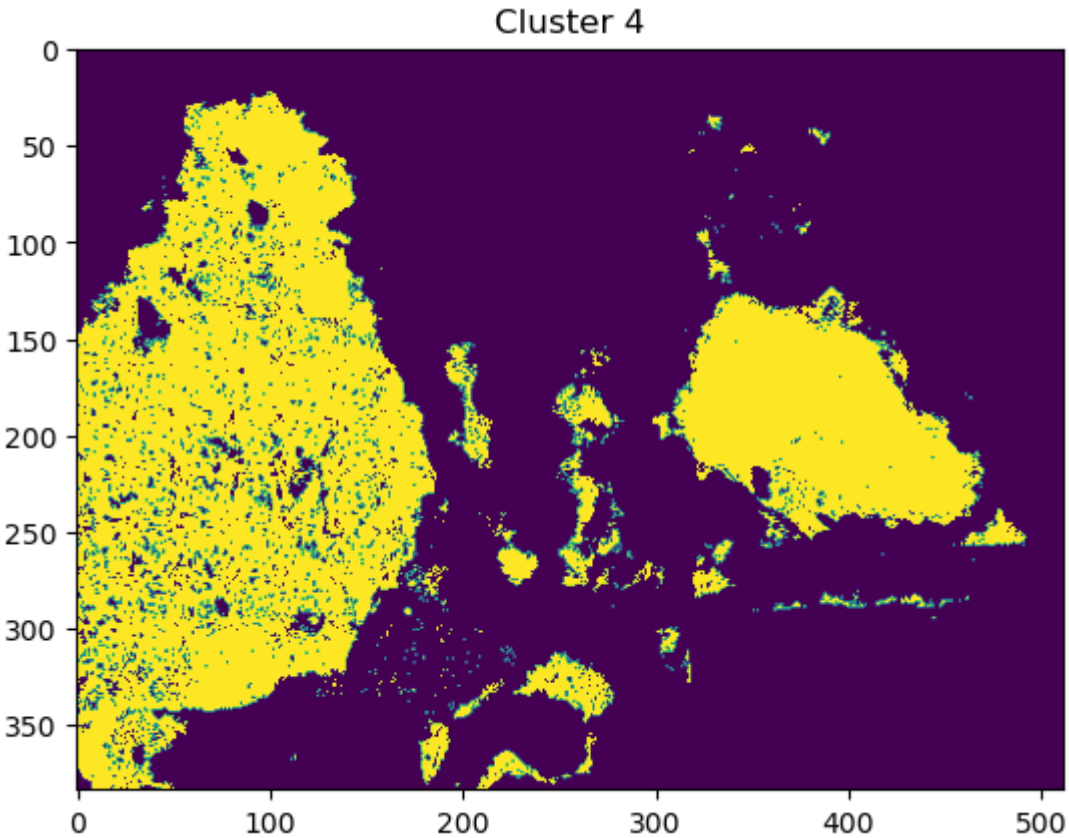
Cluster 4
0
50
100
150
200
250
300
350
0
100
200
300
400
500

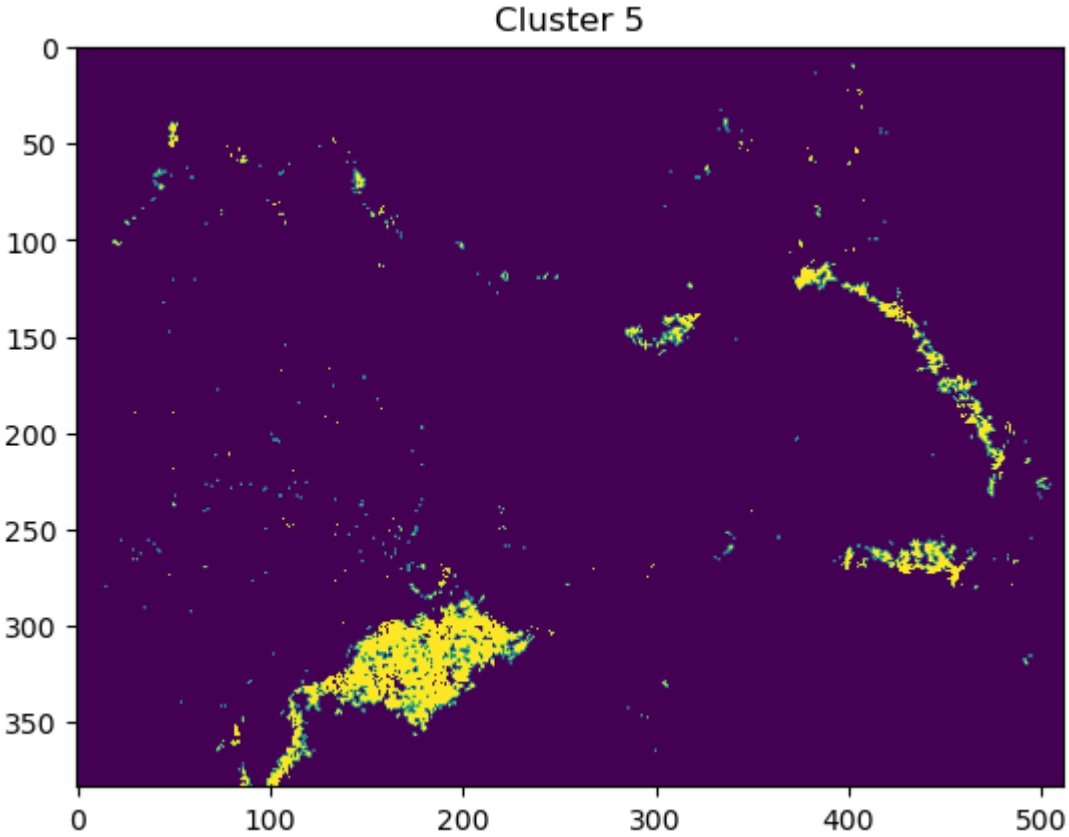

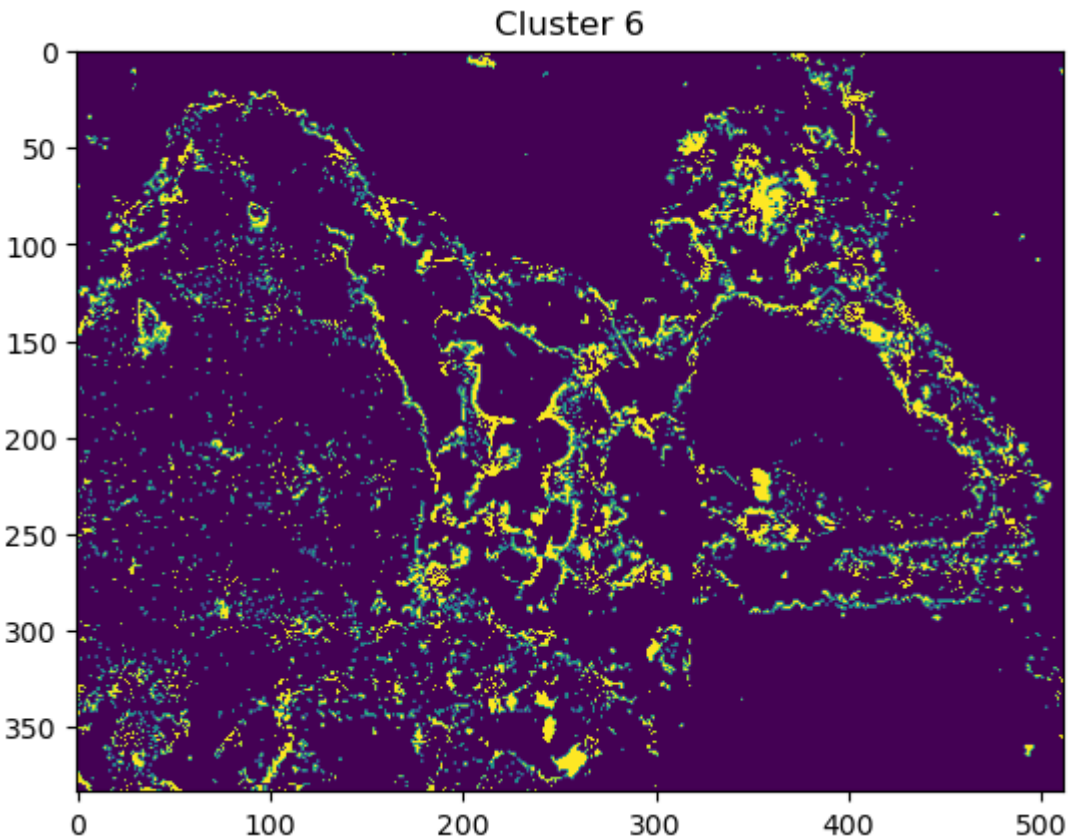

In [ ]:
```
# Plot the spectra of each cluster
%matplotlib inline

c_idx = 0
for spec in clus_spec:
    plt.figure()
    plt.plot(spec, c = 'firebrick')
    plt.xlim(right = 1000)
    plt.xlim(left = 0)
    plt.title(f'Cluster {c_idx}')


    add_xrl_labels(data_array = spec, amplitude_thresh = 0.03,
```

```
            ax = plt.gca(), elements_list = elements, colors_list = e_colors,
                   scale = s_calib.axes_manager[2].scale,
            offset = s_calib.axes_manager[2].offset)

    #plt.savefig(f'Cluster {c_idx}')
    c_idx+=1
```

8.0 Conversion from .msa to .spx file and exporting to Bruker Espirit format

This step creates spectra files that can be read in the Bruker Espirit software

In [ ]:
```
for i in range(0, n_cluster):

    COI = flatten_masked_array(s_calib.data, labels_seg[i])
    clus_spec = hs.signals.Signal1D(COI.sum(0))
    clus_spec.set_signal_type("EDS_SEM")
    clus_spec.change_dtype('float32')
    clus_spec.axes_manager[0].name = 'E'
    clus_spec.axes_manager[0].offset = s_calib.axes_manager['Energy'].offset
    clus_spec.axes_manager[0].scale = s_calib.axes_manager['Energy'].scale
    clus_spec.axes_manager[0].units = s_calib.axes_manager['Energy'].units
    to_spx(clus_spec, f_name = f'Cluster{i+1}')
    clus_spec.save(f'W28_T2M2_2_NMF8_cluster{i+1}', extension = 'msa', format = 'XY')
```

9.0 Reiteration on a Cluster of Interest (COI)

Using COI, follow the same workflow as that for the calibrated spectral data

In [79]:
```
COI_clus = np.load('/Volumes/Tobisha/W26/W26_T5M2/NMF/COI_P4/COI_P4_cluster_BI.npy')
print(COI_clus.shape)
plt.figure()
plt.imshow(COI_clus)
```

```
(384, 512)
```

Out[79]:
```
<matplotlib.image.AxesImage at 0x1d0ba9250>
```

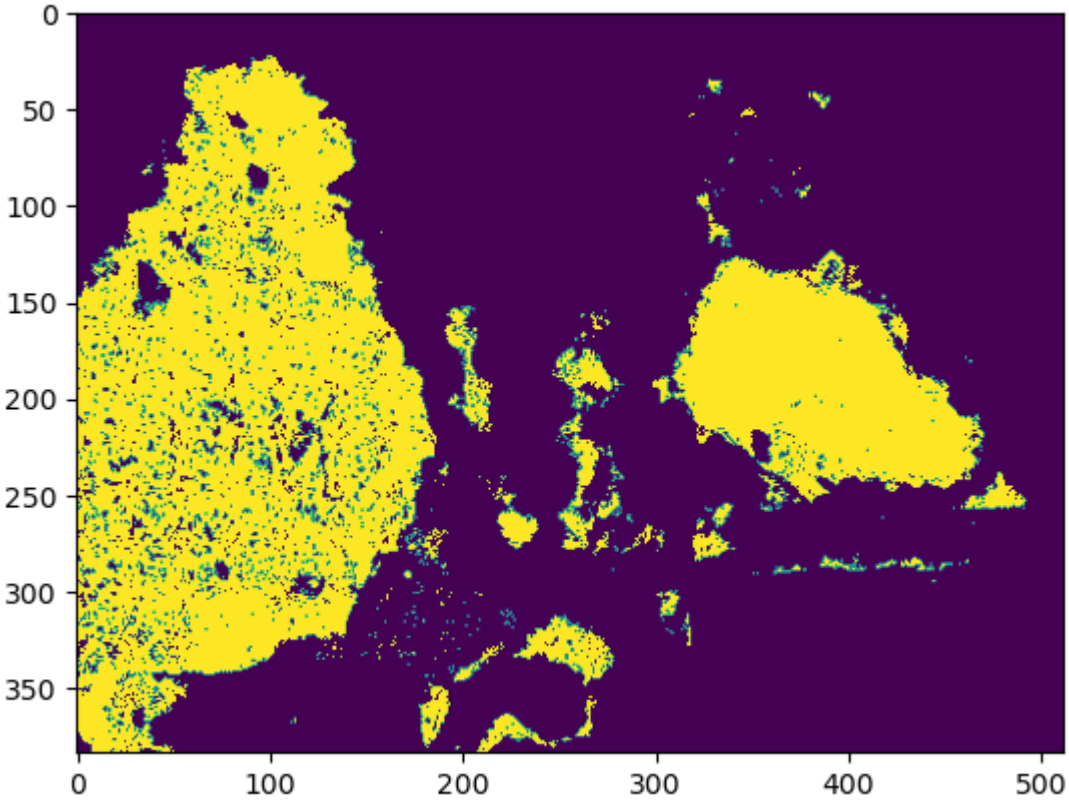

9.1 Apply poisson scaling

In [80]:
```
COI = flatten_masked_array(s_calib.data, COI_clus)
COI_im = reconstruct_masked_image(COI, COI_clus, (y, x, e))
COI_norm = poisson_scale_mask(COI)
```

```
inital mean= 0.38006088  inital max = 41.0  inital min= 0.0
(57500, 2048)
scaled mean= 6.349569151535403e-05  scaled max = 0.022750787759664506  scaled min= 0.0
```

In [23]:
```
np.save('/Volumes/Tobisha/W27/W27_T2M2/NMF', arr = COI_norm, allow_pickle = True)
```

9.2 Dimentional Reduction

In [81]:
```
# Use the same number of components as indicated by the PCA scree plot
fornmf = COI_norm

nmf = NMF(n_components = 5)
nmf.fit(fornmf)
compz_COI = nmf.transform(fornmf)
```

```
/Users/robbinhilderman/opt/anaconda3/envs/hspy_environment/lib/python3.11/site-packages/sklearn/decomposition/_nmf.py:1665: ConvergenceWarning: Maximum number of iterations 200 reached. Increase it to improve convergence.
  warnings.warn(
```

In [180…
```
# Save the COI NMF components
np.save('compz_COI', 'E:/W26/W26_T5M2/NMF/COI_P4', allow_pickle = True)
```

In [115…
```
# Plot the NMF component factors
compz_im_COI = reconstruct_masked_image(compz_COI, noise_clus, (y, x, 5))
%matplotlib inline
for i in range(0,5):
    plt.figure()
    plt.title(f'NMF_COI{i+1}')
    plt.imshow(bse_ds, cmap = 'gray')
    plt.pcolormesh(compz_im_COI[:,:,i])
```

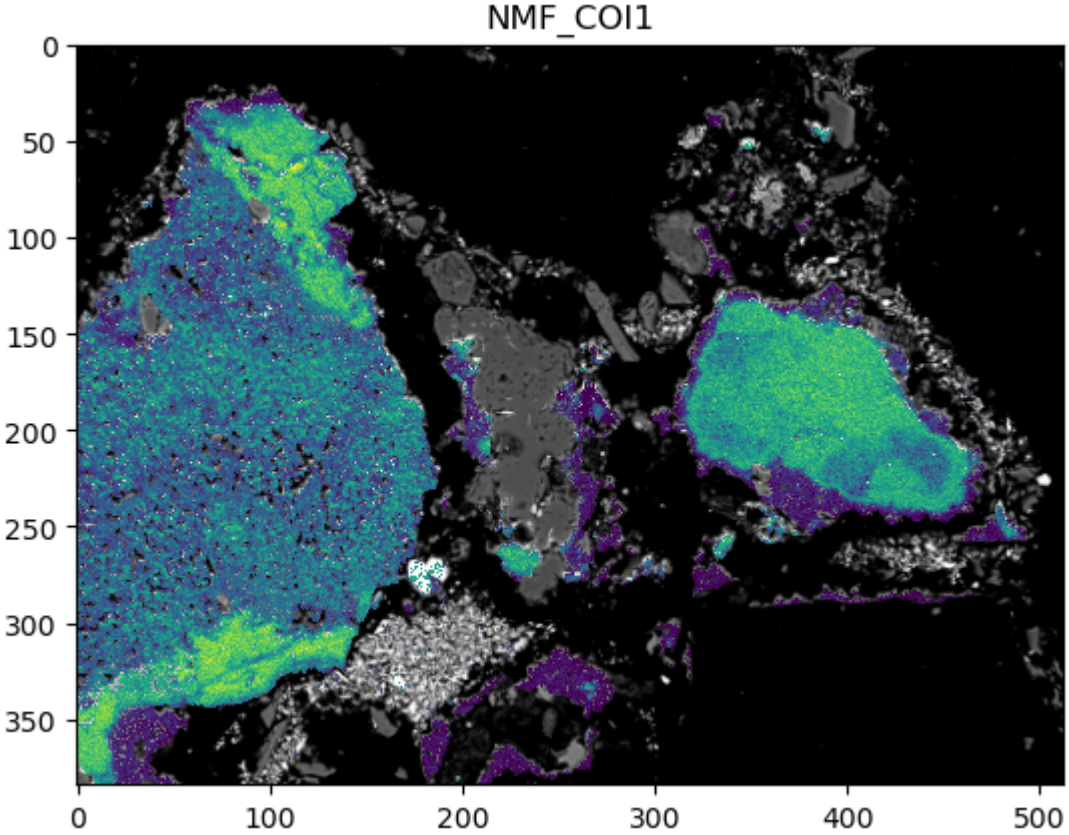
NMF_COI1
0
50
100
150
200
250
300
350
0
100
200
300
400
500

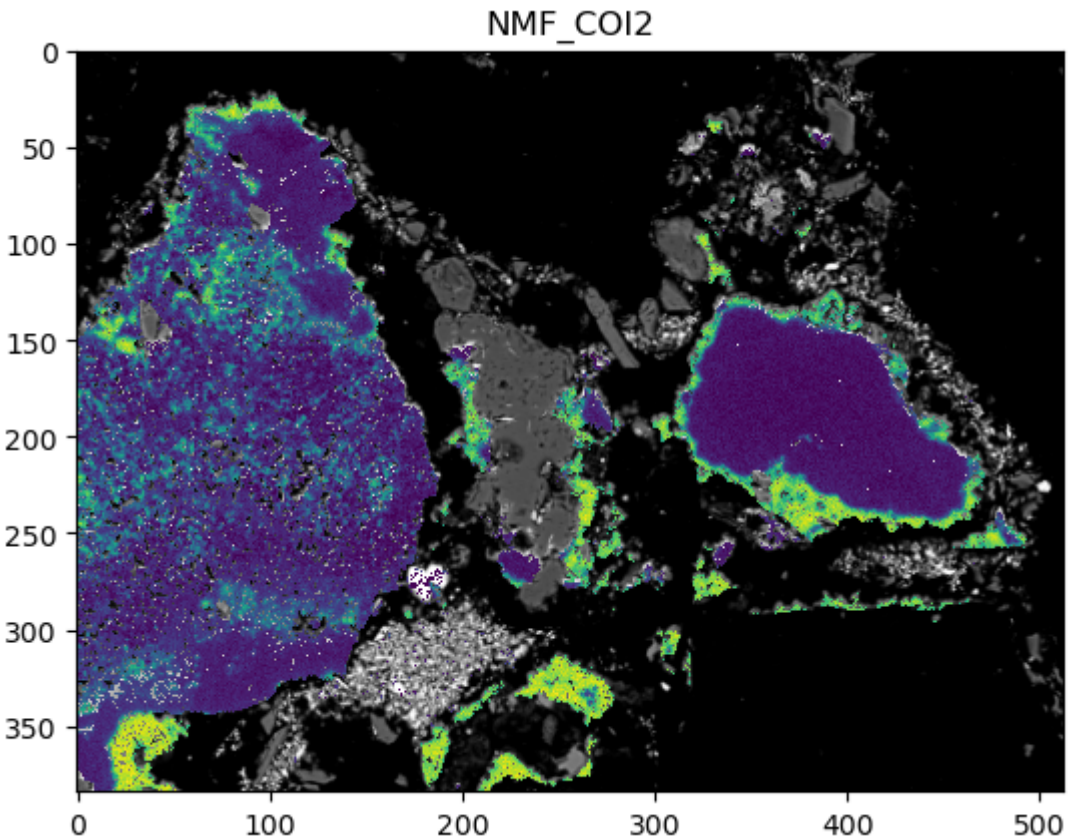
NMF_COI2
0
50
100
150
200
250
300
350
0
100
200
300
400
500

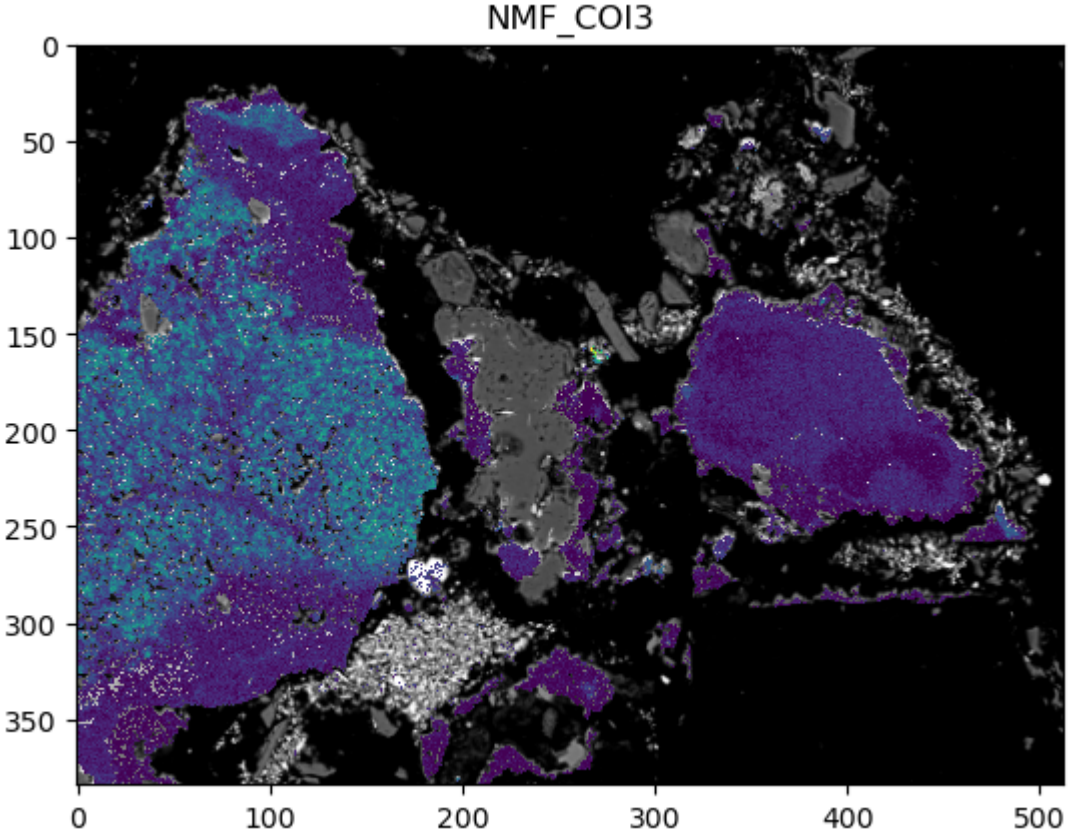
NMF_COI3
0
50
100
150
200
250
300
350
0
100
200
300
400
500

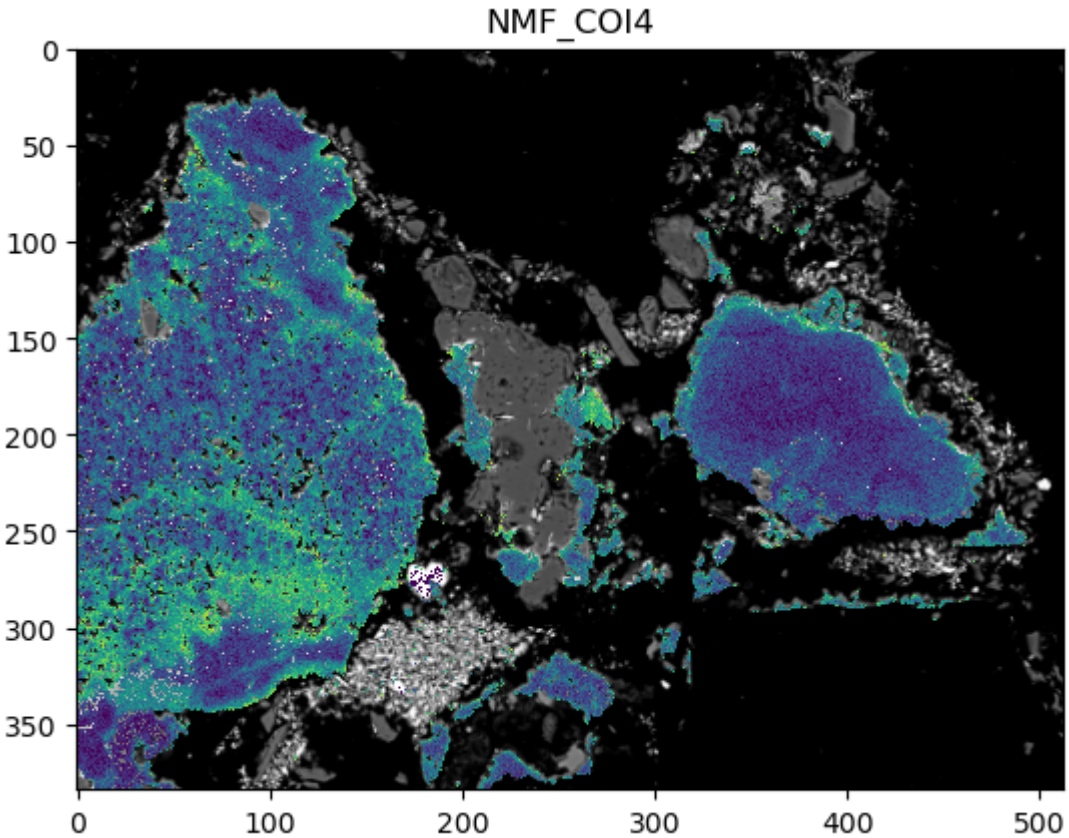
NMF_COI4
0
50
100
150
200
250
300
350
0
100
200
300
400
500

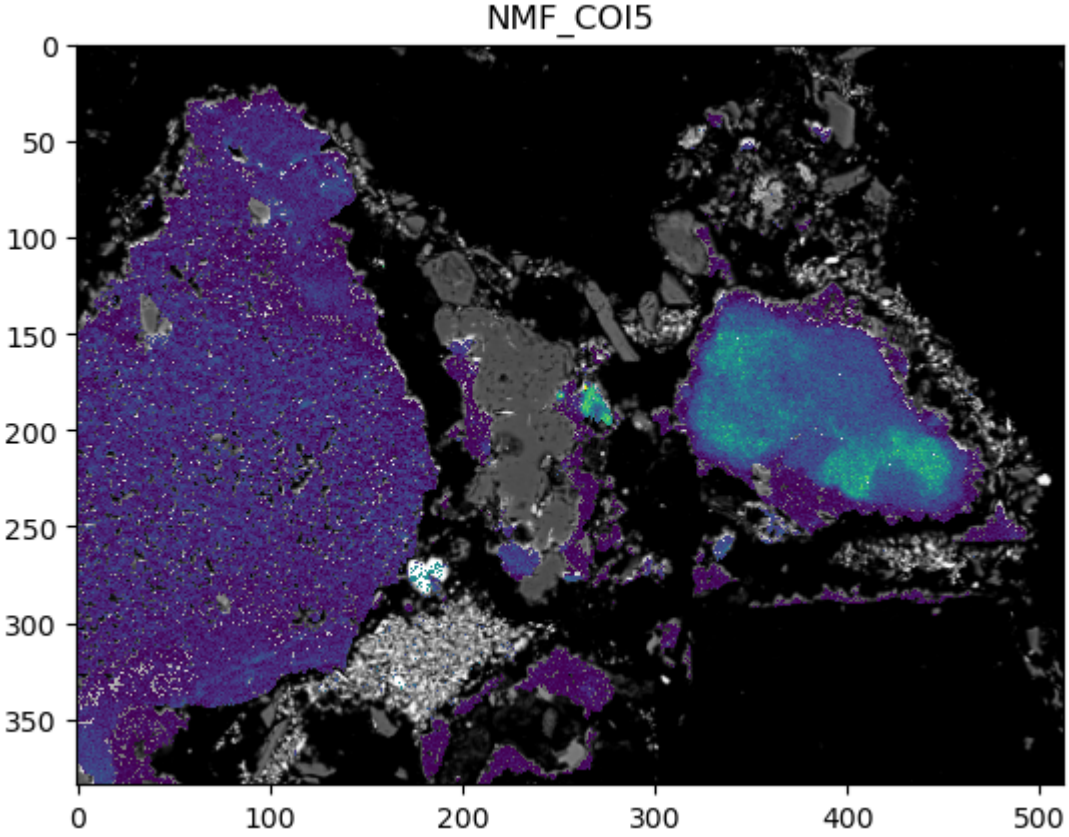

In [84]:
```
nmf_loads_COI = nmf.components_
```

In [86]:
```
# Plot the NMF component loadings
%matplotlib inline
scale = s_calib.axes_manager[2].scale
offset = s_calib.axes_manager[2].offset
ofs = offset/scale

fig, axs = plt.subplots(5, 1)
fig.xlim =[0-ofs , 2048-ofs]
x_label = np.arange(0, 21, 2)
x_ticks = (x_label/scale) - ofs
fig.subplots_adjust(hspace = 0)

axs[0].plot(nmf_loads_COI[0], linewidth = 1)
axs[0].set_yticks([])
axs[0].spines['bottom'].set_visible(False)
axs[0].set_xlim(0-ofs,2048)

axs[1].plot(nmf_loads_COI[1], linewidth=1)
axs[1].set_yticks([])
axs[1].spines['top'].set_visible(False)
axs[1].spines['bottom'].set_visible(False)
axs[1].set_xlim(0-ofs,2048)

axs[2].plot(nmf_loads_COI[2], linewidth=1)
axs[2].set_yticks([])
axs[2].spines['top'].set_visible(False)
axs[2].spines['bottom'].set_visible(False)
axs[2].set_xlim(0-ofs,2048)

axs[3].plot(nmf_loads_COI[3], linewidth=1)
axs[3].set_yticks([])
axs[3].spines['top'].set_visible(False)
axs[3].spines['bottom'].set_visible(False)
axs[3].set_xlim(0-ofs,2048)

axs[4].plot(nmf_loads_COI[4], linewidth=1)
```

```
axs[4].set_yticks([])
axs[4].spines['top'].set_visible(False)
axs[4].spines['bottom'].set_visible(False)
axs[4].set_xlim(0-ofs,2048)

plt.show()
#plt.savefig(f'NMF Factors_new', dpi = 600)
```

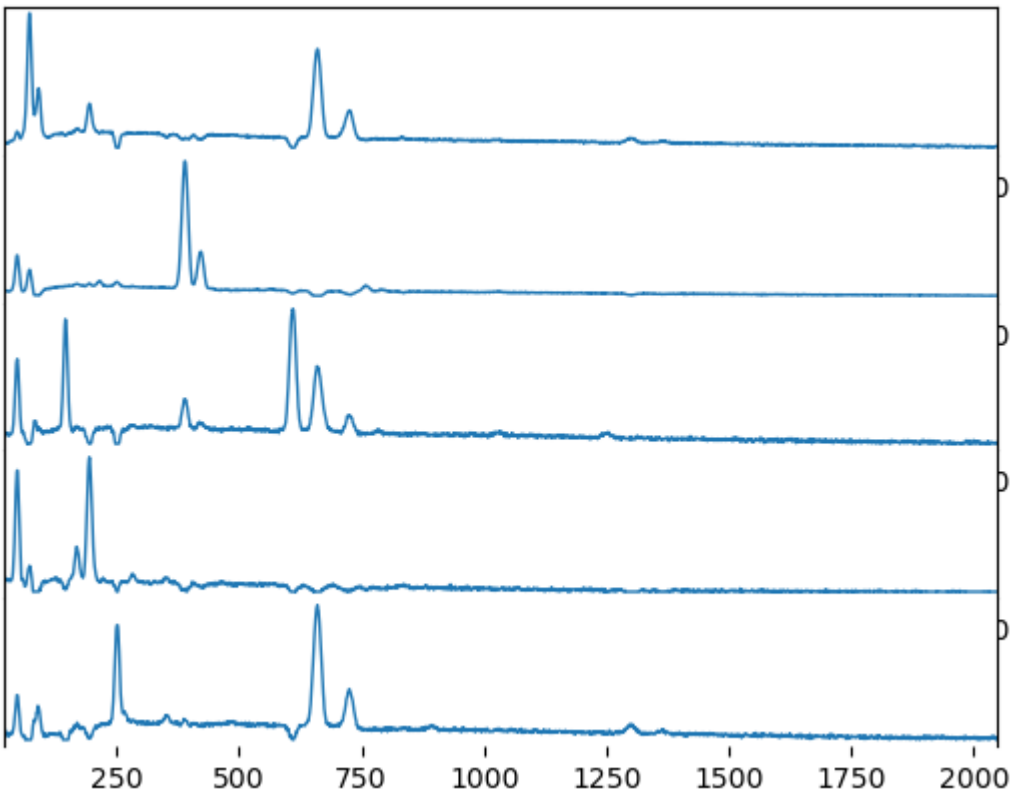

9.3 HDBSCAN Clustering on COI

In [87]:
```
clust = hdbscan.HDBSCAN(min_cluster_size = 500,min_samples = 100,
                        prediction_data = True)
clust.fit(compz_COI)

# Hard cluster label for each data point, including outlier cluster of '-1'
labels_COI = clust.labels_
print(labels_COI.shape)

# Total number of clusters, inclusive of 'outliers' cluster
n_cluster = len(set(labels_COI))
print('Number of clusters:',str(n_cluster))

# Assign the largest cluster number as outlier cluster
labels_COI[np.where(labels_COI == -1)[0]] = n_cluster-1
```

```
(57500,)
Number of clusters: 4
```

In [252…
```
# Save COI cluster labels
np.save('E:/W26/W26_T5M2/NMF/COI_P4/P4_HDBSCAN', arr = labels_COI,
        allow_pickle = True)
```

In [88]:
```
# reconstruct hard cluster assignments
label_map_COI = reconstruct_masked_image(arr = labels_COI, mask = noise_clus,
                                         im_shape = (y, x))
# create binary segmentations per cluster
labels_COI_seg = []
labels_COI_spec = []
clus_COI_count = []
zero_COI_count = []
```

```
for i in range(0, n_cluster):

    labels_COI_seg.append(np.zeros((y, x)))
    labels_COI_seg[i][label_map_COI == i] = 1
    labels_spec.append(s_calib.data[label_map_COI == i, :].sum(axis = (0)))

    plt.figure()
    #plt.imshow(bse_ds, cmap='binary_r')
    plt.imshow(labels_COI_seg[i],cmap='binary_r')
    plt.title(f'cluster {i+1}')

    clus_COI_count.append(labels_COI_seg[i].sum())
    zero_COI_count.append((labels_COI_seg[i] == 0).sum())
    print(clus_COI_count[i] == ((y*x)-zero_COI_count[i]))


labels_COI_seg = np.asarray(labels_COI_seg)
print(labels_COI_seg.shape)
print(clus_COI_count)
```

```
True
True
True
True
(4, 384, 512)
[4722.0, 10606.0, 11544.0, 30628.0]
```

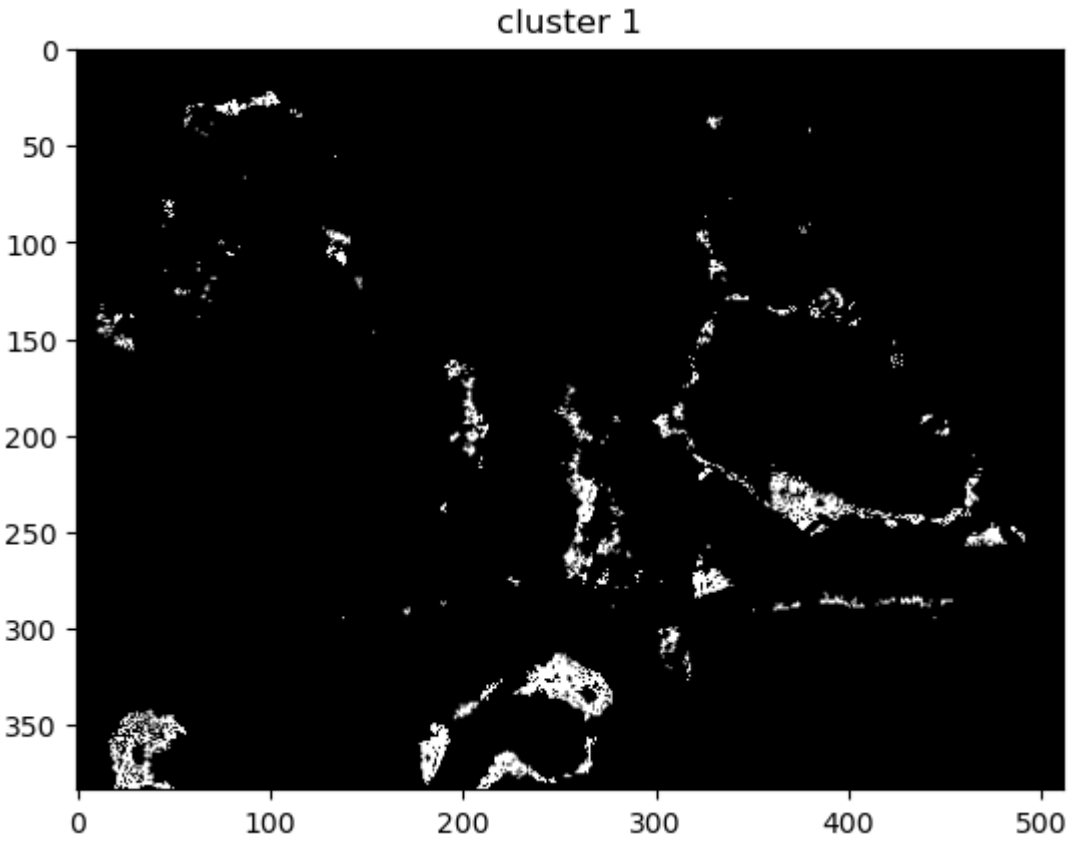

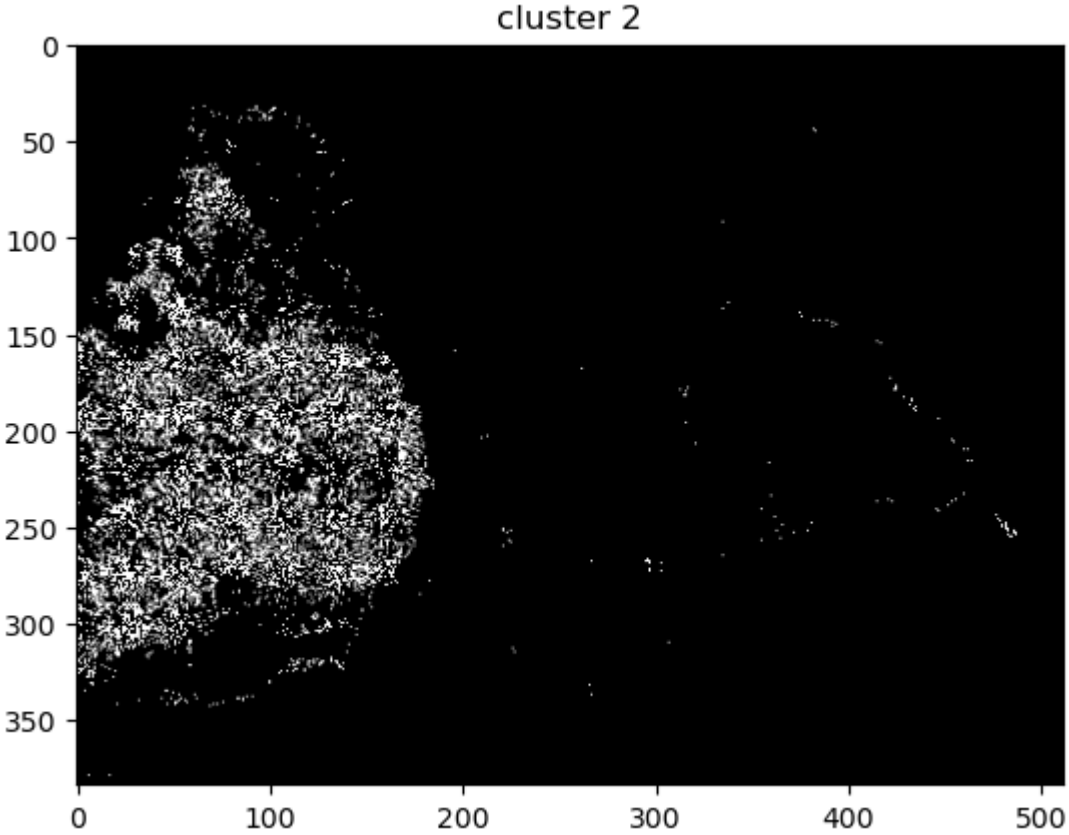
cluster 2
0
50
100
150
200
250
300
350
0
100
200
300
400
500

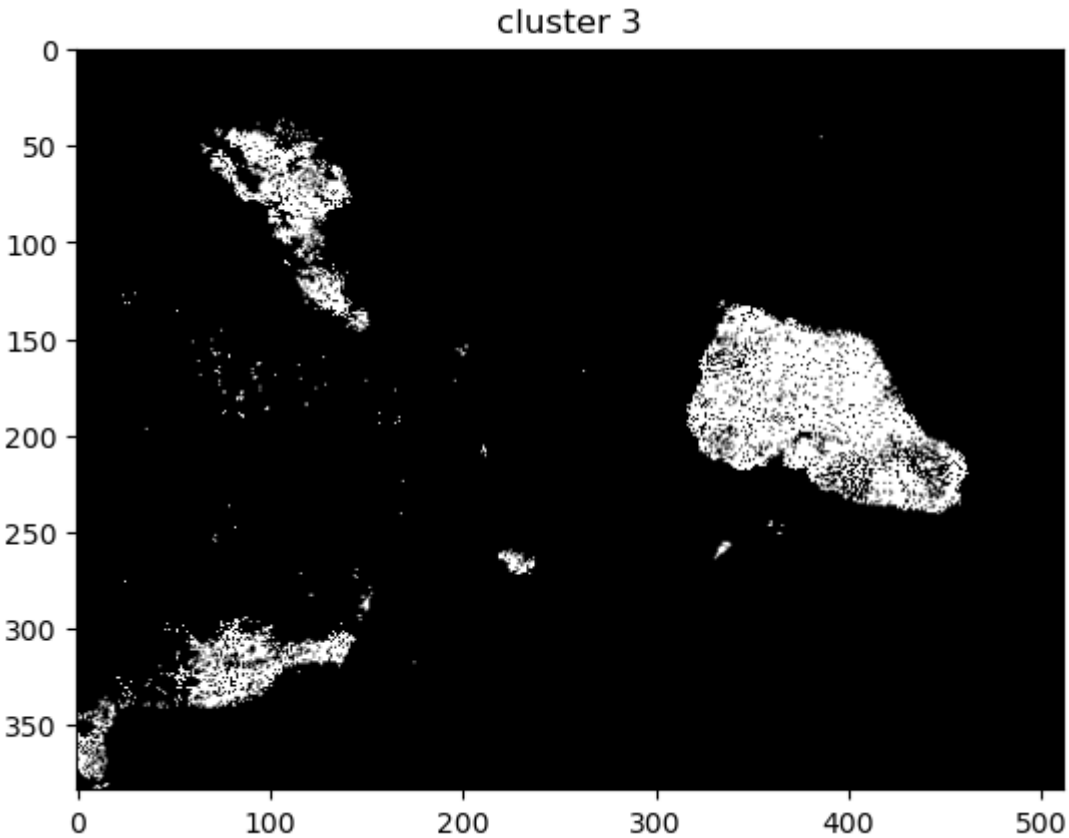
cluster 3
0
50
100
150
200
250
300
350
0
100
200
300
400
500

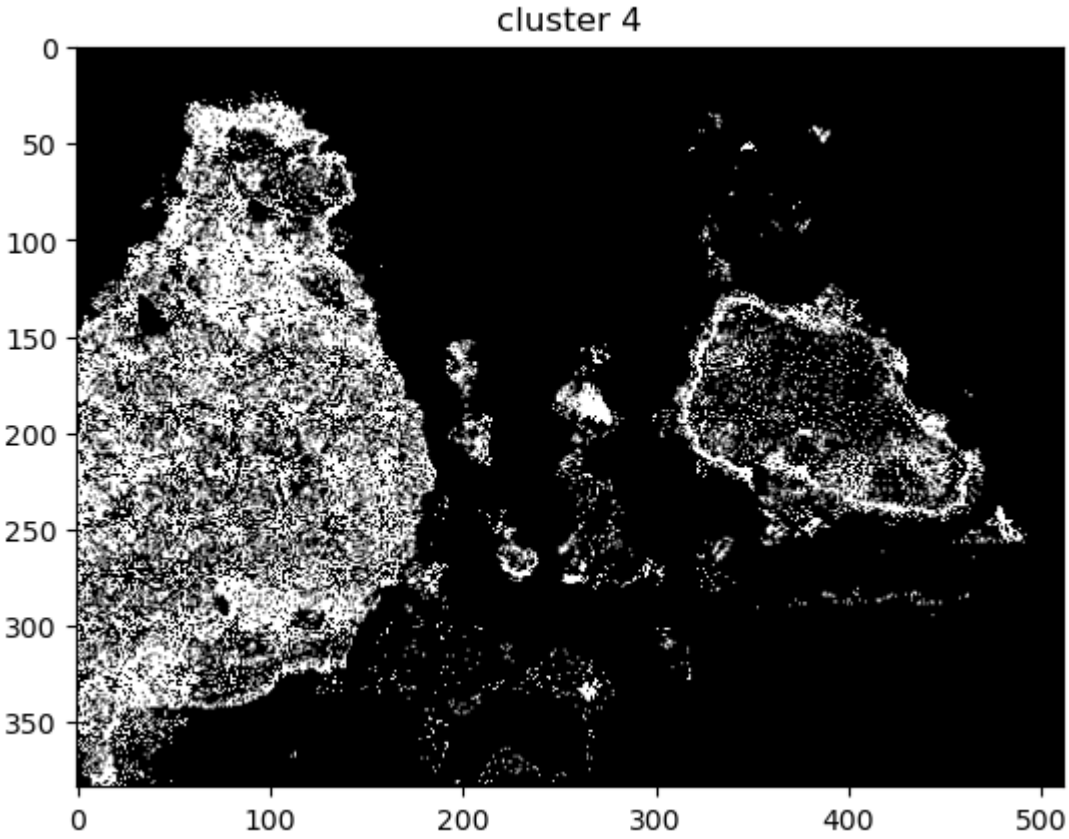

In [89]:
```
# Plot the phase map
plt_phasemap(label_map_COI, bse_im = bse_ds, scale = s_calib.axes_manager[0].scale,
             mpl_cmap = 'tab20', phasemap_title = 'phasemap_COI_4')
```

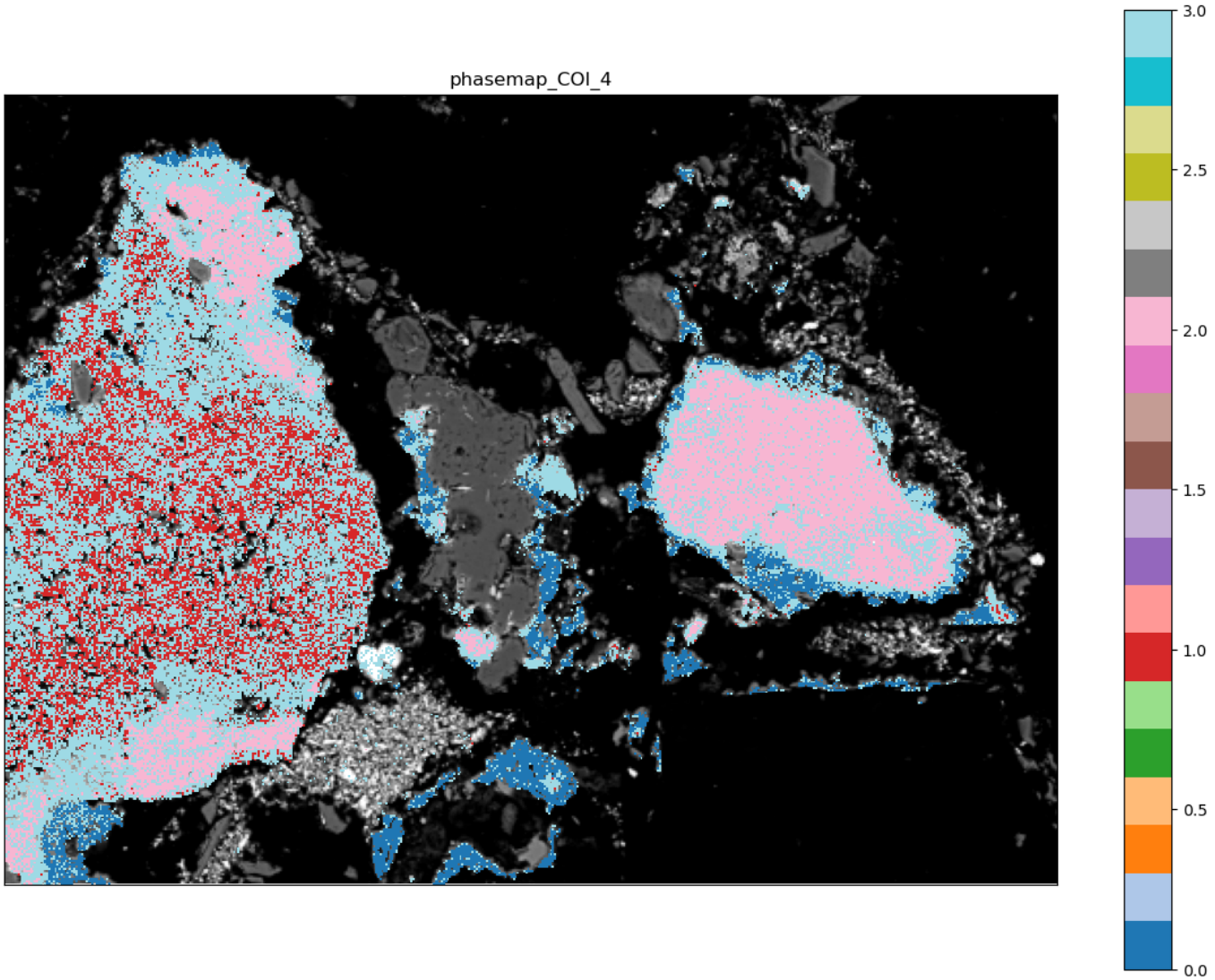

9.4 Save COI cluster spectra for back projection

In [90]:
```
# create summed COI spectra as % of total counts per cluster
clus_COI_spec = []

for i in range(0,n_cluster):
    clus_COI_spec.append((s_calib.data[labels_COI_seg[i] == 1,:]).sum(axis = 0))
```

In [94]:
```
# Plot each spectra to explore
c_idx = 0
for spec in clus_COI_spec:
    plt.figure()
    plt.imshow(labels_COI_seg[c_idx])
    plt.title(f'P4_Cluster {c_idx+1}')
    c_idx+=1
```

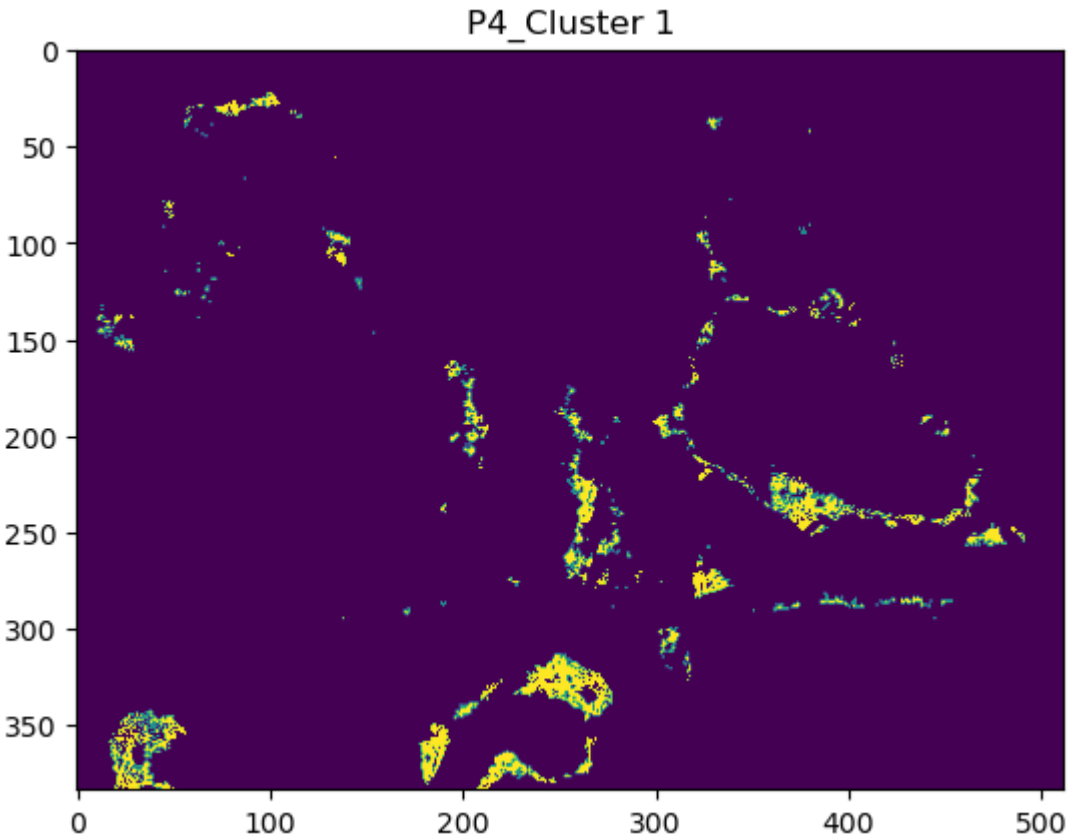

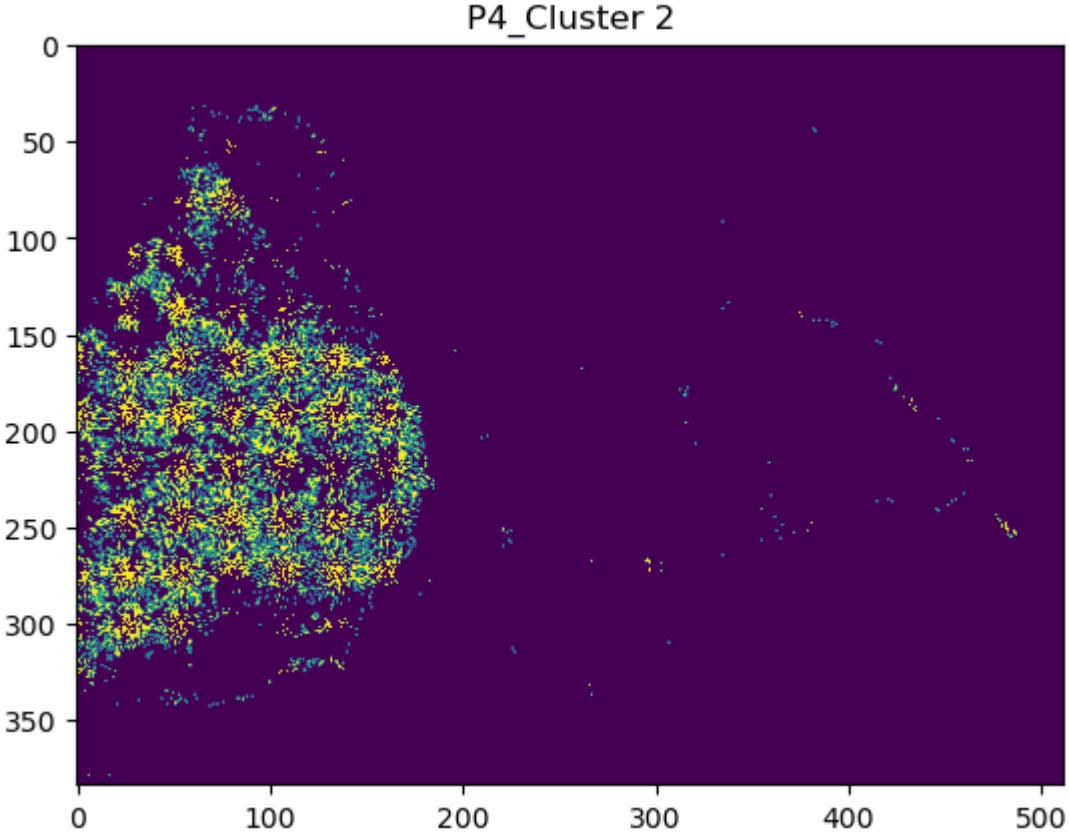
P4_Cluster 2
0
50
100
150
200
250
300
350
0
100
200
300
400
500

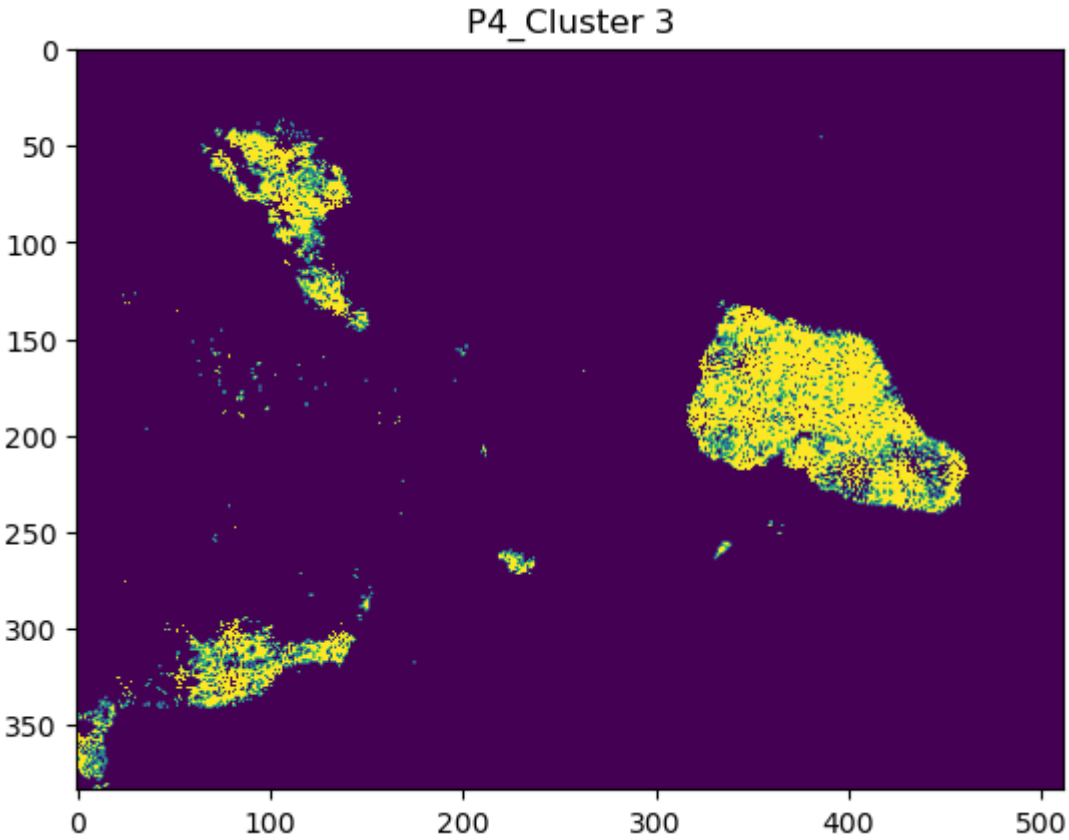
P4_Cluster 3
0
50
100
150
200
250
300
350
0
100
200
300
400
500

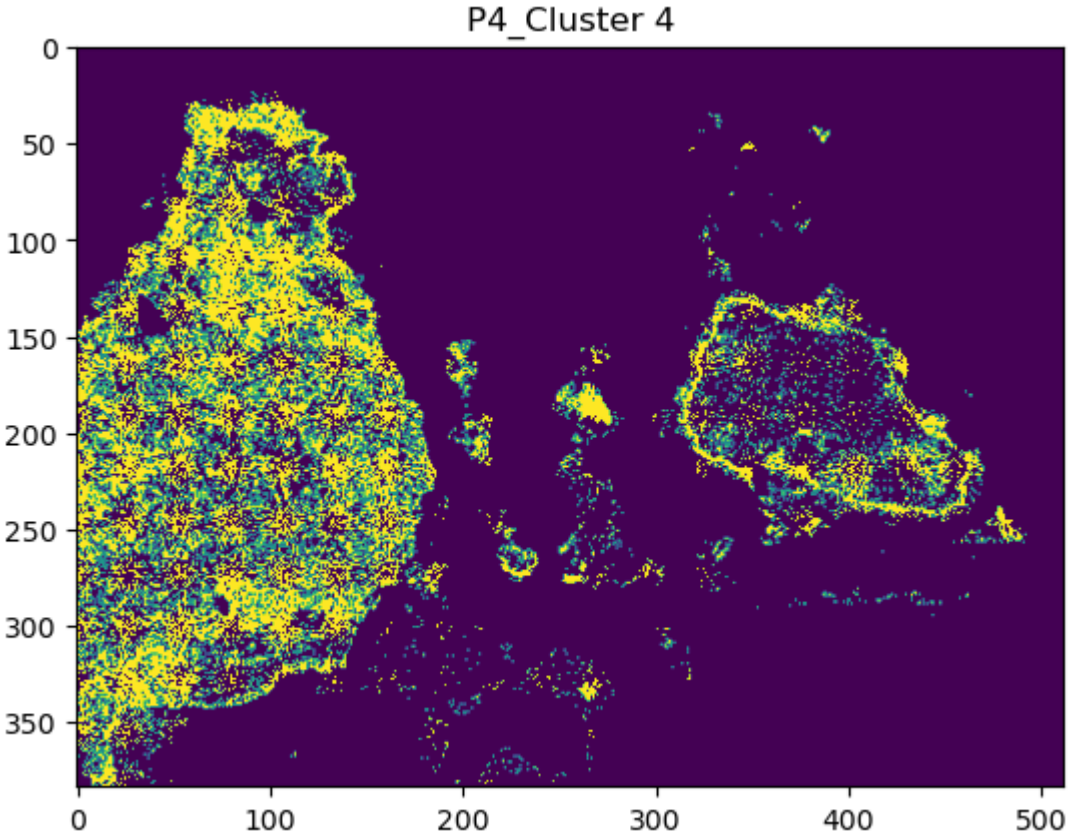

In [ ]:
```
# Plot the spectra of each cluster
c_idx = 0
for spec in clus_COI_spec:
    plt.figure()
    plt.plot(spec, c = 'firebrick')
    plt.xlim(right = 1000)
    plt.xlim(left = 0)
    plt.title(f'Cluster {c_idx}')

    xtick_labels = np.arange(0, 21, 2) # create a range from 0 to max kV(+1),
                                       #and step of 2kV (tick labels)
    xticks = xtick_labels/scale - (offset/scale) # get tick label positions in
                                                 #channels


    ax = plt.gca()
    ax.set_xticks(xticks)
    ax.set_xticklabels(xtick_labels)

    add_xrl_labels(data_array = spec, amplitude_thresh = 0.04,
            ax = plt.gca(), elements_list = elements, colors_list = e_colors,
                   scale = s_calib.axes_manager[2].scale,
            offset = s_calib.axes_manager[2].offset)

    #plt.savefig(f'COI_Cluster {c_idx}')

    c_idx+=1
```

9.5 COI conversion from .msa to .spx file and exporting to Bruker Espirit format

In [ ]:
```
for i in range(0, n_cluster):

    COI = flatten_masked_array(s_calib.data, labels_COI_seg[i])
    clus_COI_spec = hs.signals.Signal1D(COI.sum(0))
    clus_COI_spec.set_signal_type("EDS_SEM")
    clus_COI_spec.change_dtype('float32')
    clus_COI_spec.axes_manager[0].name = 'E'
    clus_COI_spec.axes_manager[0].offset = s_calib.axes_manager['Energy'].offset
    clus_COI_spec.axes_manager[0].scale = s_calib.axes_manager['Energy'].scale
```

```
    clus_COI_spec.axes_manager[0].units = s_calib.axes_manager['Energy'].units
    to_spx(clus_COI_spec, f_name = f'COI_Cluster{i+1}')
    clus_COI_spec.save(f'W26_T6.2M3_COI_P5_COI_cluster{i+1}', extension = 'msa',
                       format = 'XY')
```

List of References

Ahmedzade, P., & Sengoz, B. (2009). Evaluation of steel slag coarse aggregate in hot mix asphalt concrete. *Journal of Hazardous Materials*, *165*(1), 300–305. https://doi.org/10.1016/j.jhazmat.2008.09.105

Béarat, H., McKelvy, M. J., Chizmeshya, A. V. G., Gormley, D., Nunez, R., Carpenter, R. W., Squires, K., & Wolf, G. H. (2006). Carbon Sequestration via Aqueous Olivine Mineral Carbonation: Role of Passivating Layer Formation. *Environmental Science & Technology*, *40*(15), 4802–4808. https://doi.org/10.1021/es0523340

Bianco, L., & Porisiensi, S. (2016). *Economia circolare e Sostenibilità*. *10*.

Bobicki, E. R., Liu, Q., Xu, Z., & Zeng, H. (2012). Carbon capture and storage using alkaline industrial wastes. *Progress in Energy and Combustion Science*, *38*(2), 302–320. https://doi.org/10.1016/j.pecs.2011.11.002

Bonenfant, D., Kharoune, L., Sauve´, S., Hausler, R., Niquette, P., Mimeault, M., & Kharoune, M. (2008). CO2 Sequestration Potential of Steel Slags at Ambient Pressure and Temperature. *Industrial & Engineering Chemistry Research*, *47*(20), 7610–7616. https://doi.org/10.1021/ie701721j

Branca, T. A., Colla, V., Algermissen, D., Granbom, H., Martini, U., Morillon, A., Pietruck, R., & Rosendahl, S. (2020). Reuse and Recycling of By-Products in the Steel Sector: Recent Achievements Paving the Way to Circular Economy and Industrial Symbiosis in Europe. *Metals*, *10*(3), Article 3. https://doi.org/10.3390/met10030345

Brandl, H., & Faramarzi, M. A. (2006). Microbe-metal-interactions for the biotechnological treatment of metal-containing solid waste. *China Particuology*, *4*(2), 93–97.

Brandt, D. (1985). Metallurgy fundamentals. *Goodheart-Willcox Company, Inc., 1985,* 256.

Brown, P. W., Hooton, R. D., & Clark, B. A. (2003). The co-existence of thaumasite and ettringite in concrete exposed to magnesium sulfate at room temperature and the influence of blast-furnace slag substitution on sulfate resistance. *Cement and Concrete Composites*, *25*(8), 939–945. https://doi.org/10.1016/S0958-9465(03)00152-5

Butler, B. (1977). Al-rich pyroxene and melilite in a blast-furnace slag and a comparison with the Allende meteorite. *Mineralogical Magazine*, *41*(320), 493–499.

Campello, R. J. G. B., Moulavi, D., Zimek, A., & Sander, J. (2015). Hierarchical Density Estimates for Data Clustering, Visualization, and Outlier Detection. *ACM Transactions on Knowledge Discovery from Data*, *10*(1), 5:1-5:51. https://doi.org/10.1145/2733381

Campello, R. J., Moulavi, D., & Sander, J. (2013). *Density-based clustering based on hierarchical density estimates*. 160–172.

Chiang, P.-C., & Pan, S.-Y. (2017). Iron and Steel Slags. In P.-C. Chiang & S.-Y. Pan, *Carbon Dioxide Mineralization and Utilization* (pp. 233–252). Springer Singapore. https://doi.org/10.1007/978-981-10-3268-4_11

Chukwuma, J. S., Pullin, H., & Renforth, P. (2021). Assessing the carbon capture capacity of South Wales' legacy iron and steel slag. *Minerals Engineering*, *173*, 107232. https://doi.org/10.1016/j.mineng.2021.107232

Cooper, A. H., Brown, T. J., Price, S. J., Ford, J. R., & Waters, C. N. (2018). Humans are the most significant global geomorphological driving force of the 21st century. *The Anthropocene Review*, *5*(3), 222–229. https://doi.org/10.1177/2053019618800234

Council, L. C. (2006). *Lancashire Historic Town Survey Programme: Preston with Walton-le-Dale and Penwortham, Historic Town Assessment Report*.

Cravotta III, C. A. (2005). *Assessment of characteristics and remedial alternatives for abandoned mine drainage: Case study at Staple Bend Tunnel unit of Allegheny*

Portage Railroad National Historic Site, Cambria County, Pennsylvania, 2004. GEOLOGICAL SURVEY RESTON VA.

de La Peña, F., Berger, M.-H., Hochepied, J.-F., Dynys, F., Stephan, O., & Walls, M. (2011). Mapping titanium and tin oxide phases using EELS: An application of independent component analysis. *Ultramicroscopy*, *111*(2), 169–176.

de la Pẽna, F., Prestat, E., Fauske, V. T., Burdet, P., Lähnemann, J., Jokubauskas, P., Furnival, T., Nord, M., Ostasevicius, T., MacArthur, K. E., Johnstone, D. N., Sarahan, M., Taillon, J., Aarholt, T., Migunov, V., Eljarrat, A., Caron, J., Francis, C., Nemoto, T., … Åne, H. W. (2023). *Hyperspy*. https://doi.org/10.5281/zenodo.592838

De Windt, L., Chaurand, P., & Rose, J. (2011). Kinetics of steel slag leaching: Batch tests and modeling. *Waste Management*, *31*(2), 225–235. https://doi.org/10.1016/j.wasman.2010.05.018

Deer, W. A., Howie, R. A., & Zussman, J. (2013). *An introduction to the rock-forming minerals* (Third edition). The Minerological Society.

Dietzel, M., Usdowski, E., & Hoefs, J. (1992). Chemical and 13C/12C- and 18O/16O-isotope evolution of alkaline drainage waters and the precipitation of calcite. *Applied Geochemistry*, *7*(2), 177–184. https://doi.org/10.1016/0883-2927(92)90035-2

Doucet, F. J. (2010). Effective CO2-specific sequestration capacity of steel slags and variability in their leaching behaviour in view of industrial mineral carbonation. *Minerals Engineering*, *23*(3), 262–269. https://doi.org/10.1016/j.mineng.2009.09.006

Douglas, G., Wendling, L., & Coleman, S. (2012). Productive use of steelmaking by-product in environmental applications (I): Mineralogy and major and trace element geochemistry. *Minerals Engineering*, *35*, 49–56.

Duran, E. C., Kho, Z., Einsle, J. F., Azaceta, I., Cavill, S. A., Kerrigan, A., Lazarov, V. K., & Eggeman, A. S. (2023). Correlated electron diffraction and energy-dispersive X-ray for automated microstructure analysis. *Computational Materials Science*, *228*, 112336. https://doi.org/10.1016/j.commatsci.2023.112336

Durrant, S. F. (1999). Laser ablation inductively coupled plasma mass spectrometry: Achievements, problems, prospects. *Journal of Analytical Atomic Spectrometry*, *14*(9), 1385–1403. https://doi.org/10.1039/A901765H

Eloneva, S., Teir, S., Salminen, J., Fogelholm, C.-J., & Zevenhoven, R. (2008). Fixation of CO2 by carbonating calcium derived from blast furnace slag. *Energy*, *33*(9), 1461–1467.

Engström, F., Adolfsson, D., Samuelsson, C., Sandström, Å., & Björkman, B. (2013). A study of the solubility of pure slag minerals. *Minerals Engineering*, *41*, 46–52. https://doi.org/10.1016/j.mineng.2012.10.004

Falk, E. S., Guo, W., Paukert, A. N., Matter, J. M., Mervine, E. M., & Kelemen, P. B. (2016). Controls on the stable isotope compositions of travertine from hyperalkaline springs in Oman: Insights from clumped isotope measurements. *Geochimica et Cosmochimica Acta*, *192*, 1–28. https://doi.org/10.1016/j.gca.2016.06.026

Fandrich, R., Gu, Y., Burrows, D., & Moeller, K. (2007). Modern SEM-based mineral liberation analysis. *International Journal of Mineral Processing*, *84*(1–4), 310–320. https://doi.org/10.1016/j.minpro.2006.07.018

Geissdoerfer, M., Savaget, P., Bocken, N. M. P., & Hultink, E. J. (2017). The Circular Economy – A new sustainability paradigm? *Journal of Cleaner Production*, *143*, 757–768. https://doi.org/10.1016/j.jclepro.2016.12.048

Genga, A., Baglivi, F., Siciliano, M., Siciliano, T., Tepore, M., Micocci, G., Tortorella, C., & Aiello, D. (2012). SEM-EDS investigation on PM10 data collected in Central

Italy: Principal Component Analysis and Hierarchical Cluster Analysis. *Chemistry Central Journal*, *6*(2), S3. https://doi.org/10.1186/1752-153X-6-S2-S3

Georget, F., Schmatz, J., Wellmann, E., & Matschei, T. (2023). A critical catalogue of SEM-EDS multispectral maps analysis methods and their application to hydrated cementitious materials. *Journal of Microscopy*, *n/a*(n/a). https://doi.org/10.1111/jmi.13245

Georget, F., Wilson, W., & Scrivener, K. L. (2022). Simple automation of SEM-EDS spectral maps analysis with Python and the edxia framework. *Journal of Microscopy*, *286*(2), 185–190. https://doi.org/10.1111/jmi.13099

Ghosh, S., Mohanty, S., Akcil, A., Sukla, L. B., & Das, A. P. (2016). A greener approach for resource recycling: Manganese bioleaching. *Chemosphere*, *154*, 628–639. https://doi.org/10.1016/j.chemosphere.2016.04.028

Goldstein, J. I., Newbury, D. E., Michael, J. R., Ritchie, N. W., Scott, J. H. J., & Joy, D. C. (2017). *Scanning electron microscopy and X-ray microanalysis*. springer.

Gomes, H. I., Mayes, W. M., Rogerson, M., Stewart, D. I., & Burke, I. T. (2016). Alkaline residues and the environment: A review of impacts, management practices and opportunities. *Journal of Cleaner Production*, *112*, 3571–3582. https://doi.org/10.1016/j.jclepro.2015.09.111

Grandell, L., Lehtilä, A., Kivinen, M., Koljonen, T., Kihlman, S., & Lauri, L. S. (2016). Role of critical metals in the future markets of clean energy technologies. *Renewable Energy*, *95*, 53–62. https://doi.org/10.1016/j.renene.2016.03.102

Gregor, C. B., Garrels, R. M., Mackenzie, F. T., & Maynard, J. B. (1988). *Chemical Cycles in the Evolution of the Earth*. Wiley New York.

Grilli, M., Bellezze, T., Gamsjäger, E., Rinaldi, A., Novak, P., Balos, S., Piticescu, R., & Ruello, M. (2017). Solutions for Critical Raw Materials under Extreme Conditions: A Review. *Materials*, *10*(3), 285. https://doi.org/10.3390/ma10030285

Gunn, G. (2014). *Critical metals handbook*. John Wiley & Sons.

Habib, A., Bhatti, H. N., & Iqbal, M. (2020). Metallurgical Processing Strategies for Metals Recovery from Industrial Slags. *Zeitschrift Für Physikalische Chemie*, *234*(2), 201–231. https://doi.org/10.1515/zpch-2019-0001

Hagelüken, B. C. (2012). Recycling the platinum group metals: A European perspective. *Platinum Metals Review*, *56*(1), 29–35.

Haha, M. B., Lothenbach, B., Le Saout, G., & Winnefeld, F. (2011). Influence of slag chemistry on the hydration of alkali-activated blast-furnace slag — Part I: Effect of MgO. *Cement and Concrete Research*, *41*(9), 955–963. https://doi.org/10.1016/j.cemconres.2011.05.002

Harwood, T. R., & Scott, R. (1999). *A report on Spartina anglica control Grange-over-Sands 1998-1999 for South Lakeland District Council*.

Hatayama, H., & Tahara, K. (2018). Adopting an objective approach to criticality assessment: Learning from the past. *Resources Policy*, *55*, 96–102. https://doi.org/10.1016/j.resourpol.2017.11.002

Historical society of lancashire and cheshire, & Harris, A. (1960). *Carnforth, 1840-1900: The Rise of a North Lancashire Town*. As author 1.

Hobson, A. J., Stewart, D. I., Bray, A. W., Mortimer, R. J. G., Mayes, W. M., Rogerson, M., & Burke, I. T. (2017). Mechanism of Vanadium Leaching during Surface Weathering of Basic Oxygen Furnace Steel Slag Blocks: A Microfocus X-ray Absorption Spectroscopy and Electron Microscopy Study. *Environmental Science & Technology*, *51*(14), 7823–7830. https://doi.org/10.1021/acs.est.7b00874

Hofmann, M., Hofmann, H., Hagelüken, C., & Hool, A. (2018). Critical raw materials: A perspective from the materials science community. *Sustainable Materials and Technologies*, *17*, e00074. https://doi.org/10.1016/j.susmat.2018.e00074

Hudson-Edwards, K. (2016). Tackling mine wastes. *Science*, *352*(6283), 288–290.

Huijgen, W. J. J., & Comans, R. N. J. (2006). Carbonation of Steel Slag for CO_2 Sequestration: Leaching of Products and Reaction Mechanisms. *Environmental Science & Technology*, *40*(8), 2790–2796. https://doi.org/10.1021/es052534b

Huijgen, W. J. J., Witkamp, G.-J., & Comans, R. N. J. (2005). Mineral CO_2 Sequestration by Steel Slag Carbonation. *Environmental Science & Technology*, *39*(24), 9676–9682. https://doi.org/10.1021/es050795f

Humphries, M. (2013). *Rare earth elements: The global supply chain. CRS Report for Congress R41347. Congressional Research Service, Washington DC, USA.[cited 2017 August 15]*.

Humphris, J., & Carey, C. (2016). New methods for investigating slag heaps: Integrating geoprospection, excavation and quantitative methods at Meroe, Sudan. *Journal of Archaeological Science*, *70*, 132–144. https://doi.org/10.1016/j.jas.2016.04.022

Hurban, S. S. (2003). EDS Spectral Artifacts / Sum Peaks: A Reminder. *Microscopy Today*, *11*(3), 43–43. https://doi.org/10.1017/S1551929500052706

International Energy Agency. (2021). *The role of critical minerals in clean energy transitions*. OECD Publishing.

IPCC. (2014). Climate Change 2014: Mitigation of Climate Change. Contribution of Working Group III to the Fifth Assessment Report of the Intergovernmental Panel on Climate Change [Edenhofer, O., R. Pichs-Madruga, Y. Sokona, E. Farahani, S. Kadner, K. Seyboth, A. Adler, I. Baum, S. Brunner, P. Eickemeier, B. Kriemann, J. Savolainen, S. Schlömer, C. von Stechow, T. Zwickel and J.C. Minx (eds.)]. *Cambridge University Press, Cambridge, United Kingdom and New York, NY, USA*.

Irassar, E. F., Bonavetti, V. L., & González, M. (2003). Microstructural study of sulfate attack on ordinary and limestone Portland cements at ambient temperature. *Cement and Concrete Research*, *33*(1), 31–41. https://doi.org/10.1016/S0008-8846(02)00914-6

Jany, B. R., Janas, A., & Krok, F. (2017). Retrieving the Quantitative Chemical Information at Nanoscale from Scanning Electron Microscope Energy Dispersive X-ray Measurements by Machine Learning. *Nano Letters*, *17*(11), 6520–6525. https://doi.org/10.1021/acs.nanolett.7b01789

Jiang, N.-J., Du, Y.-J., & Liu, K. (2018). Durability of lightweight alkali-activated ground granulated blast furnace slag (GGBS) stabilized clayey soils subjected to sulfate attack. *Applied Clay Science*, *161*, 70–75. https://doi.org/10.1016/j.clay.2018.04.014

Jones, W. (1920). The improvement of low grade basic slag. *Transactions of the Faraday Society*, *16*(December), 324–327.

Keenan, M. R., & Kotula, P. G. (2004). Accounting for Poisson noise in the multivariate analysis of ToF-SIMS spectrum images. *Surface and Interface Analysis*, *36*(3), 203–212. https://doi.org/10.1002/sia.1657

Khudhur, F. W. K., Divers, M., Wildman, M., MacDonald, J. M., & Einsle, J. F. (2024). Interrogation of ecotoxic elements distribution in slag and precipitated calcite through a machine learning-based approach aided by mass spectrometry. *Advanced Sustainable Systems*.

Khudhur, F. W. K., Macente, A., MacDonald, J. M., & Daly, L. (2022). Image-Based Analysis of Weathered Slag for Calculation of Transport Properties and Passive Carbon Capture. *Microscopy and Microanalysis*, *28*(5), 1514–1525. https://doi.org/10.1017/S1431927622000915

Koch, I. (2013). *Cluster Analysis. In Analysis of Multivariate and High-Dimensional Data* (pp. 183–222). Cambridge University Press.

Kotula, P. G., Keenan, M. R., & Michael, J. R. (2006). Tomographic Spectral Imaging with Multivariate Statistical Analysis: Comprehensive 3D Microanalysis. *Microscopy and Microanalysis*, *12*(1), 36–48. https://doi.org/10.1017/S1431927606060193

Lee, A. R. (1974). Blastfurnace and steel slag: Production, properties and uses. *(No Title)*.

Lee, D. D., & Seung, H. S. (1999). Learning the parts of objects by non-negative matrix factorization. *Nature*, *401*(6755), Article 6755. https://doi.org/10.1038/44565

Lee, J., & Pandey, B. D. (2012). Bio-processing of solid wastes and secondary resources for metal extraction–a review. *Waste Management*, *32*(1), 3–18.

Lee, M. (2017). *X-Ray Diffraction for Materials Research: From Fundamentals to Applications*. CRC Press.

Lewis, D. (1982). *Properties and uses of iron and steel slags*. 182–186.

Lizarazo-Marriaga, J., Claisse, P., & Ganjian, E. (2011). Effect of steel slag and portland cement in the rate of hydration and strength of blast furnace slag pastes. *Journal of Materials in Civil Engineering*, *23*(2), 153–160. Scopus. https://doi.org/10.1061/(ASCE)MT.1943-5533.0000149

Lucas, G., Burdet, P., Cantoni, M., & Hébert, C. (2013). Multivariate statistical analysis as a tool for the segmentation of 3D spectral data. *Micron*, *52–53*, 49–56. https://doi.org/10.1016/j.micron.2013.08.005

Lundén, R., & Paulsson, B. (2009). 1—Introduction to wheel–rail interface research. In R. Lewis & U. Olofsson (Eds.), *Wheel–Rail Interface Handbook* (pp. 3–33). Woodhead Publishing. https://doi.org/10.1533/9781845696788.1.3

Lusty, P., Shaw, R., Gunn, A., & Idoine, N. (2021). *UK criticality assessment of technology critical minerals and metals*.

MacDonald, J. M., Brolly, C. V., Slaymark, C., Spruženiece, L., Wilson, C., & Hilderman, R. (2023). The mechanisms and drivers of lithification in slag-dominated artificial ground. *The Depositional Record*, dep2.230. https://doi.org/10.1002/dep2.230

MacDonald, J. M., Khudhur, F. W. K., Carter, R., Plomer, B., Wilson, C., & Slaymark, C. (2023). The mechanisms and microstructures of passive atmospheric CO2 mineralisation with slag at ambient conditions. *Applied Geochemistry*, *152*, 105649. https://doi.org/10.1016/j.apgeochem.2023.105649

Martineau, B. H., Johnstone, D. N., van Helvoort, A. T. J., Midgley, P. A., & Eggeman, A. S. (2019). Unsupervised machine learning applied to scanning precession electron diffraction data. *Advanced Structural and Chemical Imaging*, *5*(1), 3. https://doi.org/10.1186/s40679-019-0063-3

Martins, F. F., & Castro, H. (2020). Raw material depletion and scenario assessment in European Union – A circular economy approach. *Energy Reports*, *6*, 417–422. https://doi.org/10.1016/j.egyr.2019.08.082

Mayes, W. M., Hull, S. L., & Gomes, H. I. (2022). Chapter 22 - From linear economy legacies to circular economy resources: Maximising the multifaceted values of legacy mineral wastes. In A. Stefanakis & I. Nikolaou (Eds.), *Circular Economy and Sustainability* (pp. 409–431). Elsevier. https://doi.org/10.1016/B978-0-12-819817-9.00009-0

Mayes, W. M., Riley, A. L., Gomes, H. I., Brabham, P., Hamlyn, J., Pullin, H., & Renforth, P. (2018). Atmospheric CO2 Sequestration in Iron and Steel Slag: Consett, County Durham, United Kingdom. *Environmental Science & Technology*, *52*(14), 7892–7900. https://doi.org/10.1021/acs.est.8b01883

McGrath, P. F., & Hooton, R. D. (1997). Influence of Binder Composition on Chloride Penetration Resistance of Concrete. *Special Publication*, *170*, 331–348. https://doi.org/10.14359/6829

McInnes, L., Healy, J., & Astels, S. (2017). hdbscan: Hierarchical density based clustering. *The Journal of Open Source Software*, *2*(11), 205. https://doi.org/10.21105/joss.00205

Mehta, P. K. (1983). Mechanism of sulfate attack on portland cement concrete—Another look. *Cement and Concrete Research*, *13*(3), 401–406. https://doi.org/10.1016/0008-8846(83)90040-6

Miki, T., Futatsuka, T., Shitogiden, K., Nagasaka, T., & Hino, M. (2004). Dissolution Behavior of Environmentally Regulated Elements from Steelmaking Slag into

Seawater. *ISIJ International*, *44*(4), 762–769. https://doi.org/10.2355/isijinternational.44.762

Montour, M. (1994). *Aqueous solubility of solid forms of lead in mining and smelting wastes, Leadville, Colorado: Boulder, University of Colorado*.

Motz, H., & Geiseler, J. (2001). Products of steel slags an opportunity to save natural resources. *Waste Management*, *21*(3), 285–293. https://doi.org/10.1016/S0956-053X(00)00102-1

Mudd, G. M., Jowitt, S. M., & Werner, T. T. (2017). The world's by-product and critical metal resources part I: Uncertainties, current reporting practices, implications and grounds for optimism. *Ore Geology Reviews*, *86*, 924–938. https://doi.org/10.1016/j.oregeorev.2016.05.001

Murray, R. W., Miller, D. J., & Kryc, K. A. (2000). *Analysis of Major and Trace Elements in Rocks, Sediments, and Interstitial Waters by Inductively Coupled PlasmaAtomic Emission Spectrometry (ICP-AES): Vol. //*. Ocean Drilling Program. https://doi.org/10.2973/odp.tn.29.2000

Naden, J. (2013). Science and Implementation Plan. Security of Supply of Mineral Resources (SoS Minerals) Research Programme 2012–2017. *Nat. Environ. Res. Counc*, *15*.

Newbury, D. E. (2005). Misidentification of major constituents by automatic qualitative energy dispersive X-ray microanalysis: A problem that threatens the credibility of the analytical community. *Microscopy and Microanalysis*, *11*(6), 545–561.

Newbury, D. E. (2007). Mistakes encountered during automatic peak identification in low beam energy X-ray microanalysis. *Scanning: The Journal of Scanning Microscopies*, *29*(4), 137–151.

Newbury, D. E. (2009). Mistakes encountered during automatic peak identification of minor and trace constituents in electron-excited energy dispersive X-ray microanalysis. *Scanning*, *31*(3), 91–101. https://doi.org/10.1002/sca.20151

Newbury, D. E., & Ritchie, N. W. M. (2013). Is Scanning Electron Microscopy/Energy Dispersive X-ray Spectrometry (SEM/EDS) Quantitative? *Scanning*, *35*(3), 141–168. https://doi.org/10.1002/sca.21041

Newbury, D. E., & Ritchie, N. W. M. (2015). Performing elemental microanalysis with high accuracy and high precision by scanning electron microscopy/silicon drift detector energy-dispersive X-ray spectrometry (SEM/SDD-EDS). *Journal of Materials Science*, *50*(2), 493–518. https://doi.org/10.1007/s10853-014-8685-2

Pan, S.-Y., Chang, E. E., & Chiang, P.-C. (2012). CO2 Capture by Accelerated Carbonation of Alkaline Wastes: A Review on Its Principles and Applications. *Aerosol and Air Quality Research*, *12*(5), 770–791. https://doi.org/10.4209/aaqr.2012.06.0149

Pan, S.-Y., Chiang, A., Chang, E.-E., Lin, Y.-P., Kim, H., & Chiang, P.-C. (2015). An Innovative Approach to Integrated Carbon Mineralization and Waste Utilization: A Review. *Aerosol and Air Quality Research*, *15*(3), 1072–1091. https://doi.org/10.4209/aaqr.2014.10.0240

Panda, S., Biswal, A., Mishra, S., Panda, P. K., Pradhan, N., Mohapatra, U., Sukla, L. B., Mishra, B. K., & Akcil, A. (2015). Reductive dissolution by waste newspaper for enhanced meso-acidophilic bioleaching of copper from low grade chalcopyrite: A new concept of biohydrometallurgy. *Hydrometallurgy*, *153*, 98–105.

Pane, I., & Hansen, W. (2005). Investigation of blended cement hydration by isothermal calorimetry and thermal analysis. *Cement and Concrete Research*, *35*(6), 1155–1164. https://doi.org/10.1016/j.cemconres.2004.10.027

Parker, A. J., & Barnard, A. S. (2019). Selecting Appropriate Clustering Methods for Materials Science Applications of Machine Learning. *Advanced Theory and Simulations*, *2*(12), 1900145. https://doi.org/10.1002/adts.201900145

Parsons, M. B., Bird, D. K., Einaudi, M. T., & Alpers, C. N. (2001). Geochemical and mineralogical controls on trace element release from the Penn Mine base-metal slag

dump, California. *Applied Geochemistry*, *16*(14), 1567–1593. https://doi.org/10.1016/S0883-2927(01)00032-4

Peng, Z., Li, Z., Lin, X., Tang, H., Ye, L., Ma, Y., Rao, M., Zhang, Y., Li, G., & Jiang, T. (2017). Pyrometallurgical Recovery of Platinum Group Metals from Spent Catalysts. *JOM*, *69*(9), 1553–1562. https://doi.org/10.1007/s11837-017-2450-3

Piatak, N. M., & Ettler, V. (2021). *Introduction: Metallurgical Slags – Environmental Liability or Valuable Resource?* https://doi.org/10.1039/9781839164576-00001

Piatak, N. M., Ettler, V., & Hoppe, D. (2021). Geochemistry and mineralogy of slags. In *Metallurgical Slags* (pp. 59–124).

Piatak, N. M., Parsons, M. B., & Seal, R. R. (2015). Characteristics and environmental aspects of slag: A review. *Applied Geochemistry*, *57*, 236–266. https://doi.org/10.1016/j.apgeochem.2014.04.009

Piatak, N. M., Seal, R. R., & Hammarstrom, J. M. (2004). Mineralogical and geochemical controls on the release of trace elements from slag produced by base- and precious-metal smelting at abandoned mine sites. *Applied Geochemistry*, *19*(7), 1039–1064. https://doi.org/10.1016/j.apgeochem.2004.01.005

Piatak, N. M., Seal, R. R., Hoppe, D. A., Green, C. J., & Buszka, P. M. (2019). Geochemical Characterization of Iron and Steel Slag and Its Potential to Remove Phosphate and Neutralize Acid. *Minerals*, *9*(8), Article 8. https://doi.org/10.3390/min9080468

Popov, V. V., Grilli, M. L., Koptyug, A., Jaworska, L., Katz-Demyanetz, A., Klobčar, D., Balos, S., Postolnyi, B. O., & Goel, S. (2021). Powder Bed Fusion Additive Manufacturing Using Critical Raw Materials: A Review. *Materials*, *14*(4), Article 4. https://doi.org/10.3390/ma14040909

Potapov, P. (2016). Why Principal Component Analysis of STEM spectrum-images results in “abstract”, uninterpretable loadings? *Ultramicroscopy*, *160*, 197–212. https://doi.org/10.1016/j.ultramic.2015.10.020

Pranzini, E., & Williams, A. T. (2013). *Coastal erosion and protection in Europe*. Routledge London, UK.

Price, S. J., Ford, J. R., Cooper, A. H., & Neal, C. (2011). Humans as major geological and geomorphological agents in the Anthropocene: The significance of artificial ground in Great Britain. *Philosophical Transactions of the Royal Society A: Mathematical, Physical and Engineering Sciences*, *369*(1938), 1056–1084. https://doi.org/10.1098/rsta.2010.0296

Proctor, D. M., Fehling, K. A., Shay, E. C., Wittenborn, J. L., Green, J. J., Avent, C., Bigham, R. D., Connolly, M., Lee, B., Shepker, T. O., & Zak, M. A. (2000). Physical and Chemical Characteristics of Blast Furnace, Basic Oxygen Furnace, and Electric Arc Furnace Steel Industry Slags. *Environmental Science & Technology*, *34*(8), 1576–1582. https://doi.org/10.1021/es9906002

Pullin, H., Bray, A. W., Burke, I. T., Muir, D. D., Sapsford, D. J., Mayes, W. M., & Renforth, P. (2019). Atmospheric Carbon Capture Performance of Legacy Iron and Steel Waste. *Environmental Science & Technology*, *53*(16), 9502–9511. https://doi.org/10.1021/acs.est.9b01265

Qian, G. R., Sun, D. D., Tay, J. H., & Lai, Z. Y. (2002). Hydrothermal reaction and autoclave stability of Mg bearing RO phase in steel slag. *British Ceramic Transactions*, *101*(4), 159–164. https://doi.org/10.1179/096797802225003415

Qian, G., Sun, D. D., Tay, J. H., Lai, Z., & Xu, G. (2002). Autoclave properties of kirschsteinite-based steel slag. *Cement and Concrete Research*, *32*(9), 1377–1382. https://doi.org/10.1016/S0008-8846(02)00790-1

Rabe, W., Kostka, G., & Stegen, K. S. (2017). China's supply of critical raw materials: Risks for Europe's solar and wind industries? *Energy Policy*, *101*, 692–699.

Ragipani, R., Bhattacharya, S., & Suresh, A. K. (2019). Kinetics of steel slag dissolution: From experiments to modelling. *Proceedings of the Royal Society A: Mathematical,*

Physical and Engineering Sciences, *475*(2224), 20180830. https://doi.org/10.1098/rspa.2018.0830

Renforth, P. (2019). The negative emission potential of alkaline materials. *Nature Communications*, *10*(1), Article 1. https://doi.org/10.1038/s41467-019-09475-5

Renforth, P., Manning, D. A. C., & Lopez-Capel, E. (2009). Carbonate precipitation in artificial soils as a sink for atmospheric carbon dioxide. *Applied Geochemistry*, *24*(9), 1757–1764. https://doi.org/10.1016/j.apgeochem.2009.05.005

Renforth, P., Washbourne, C.-L., Taylder, J., & Manning, D. A. C. (2011). Silicate Production and Availability for Mineral Carbonation. *Environmental Science & Technology*, *45*(6), 2035–2041. https://doi.org/10.1021/es103241w

Reuter, M. A. (2016). Digitalizing the Circular Economy. *Metallurgical and Materials Transactions B*, *47*(6), 3194–3220. https://doi.org/10.1007/s11663-016-0735-5

Riden, P., & Owen, J. G. (1995). *British Blast Furnace Statistics, 1790-1980*. Merton Priory.

Riley, A. L., MacDonald, J. M., Burke, I. T., Renforth, P., Jarvis, A. P., Hudson-Edwards, K. A., McKie, J., & Mayes, W. M. (2020). Legacy iron and steel wastes in the UK: Extent, resource potential, and management futures. *Journal of Geochemical Exploration*, *219*, 106630. https://doi.org/10.1016/j.gexplo.2020.106630

Ritchie, N. W., Newbury, D. E., & Davis, J. M. (2012). EDS measurements of X-ray intensity at WDS precision and accuracy using a silicon drift detector. *Microscopy and Microanalysis*, *18*(4), 892–904.

Rizzo, A., Goel, S., Luisa Grilli, M., Iglesias, R., Jaworska, L., Lapkovskis, V., Novak, P., Postolnyi, B. O., & Valerini, D. (2020). The Critical Raw Materials in Cutting Tools for Machining Applications: A Review. *Materials*, *13*(6), Article 6. https://doi.org/10.3390/ma13061377

Rossouw, D., Burdet, P., De La Peña, F., Ducati, C., Knappett, B. R., Wheatley, A. E. H., & Midgley, P. A. (2015). Multicomponent Signal Unmixing from

Nanoheterostructures: Overcoming the Traditional Challenges of Nanoscale X-ray Analysis via Machine Learning. *Nano Letters*, *15*(4), 2716–2720. https://doi.org/10.1021/acs.nanolett.5b00449

Saghi, Z., Einsle, J., Blukis, R., Strodahs, A., Leary, R., Burdet, P., Harrison, R., & Midgley, P. (2016). Improved Data Analysis and Reconstruction Methods for STEM-EDX Tomography. *Microscopy and Microanalysis*, *22*(S3), 284–285. https://doi.org/10.1017/S1431927616002270

Saikia, N., Cornelis, G., Mertens, G., Elsen, J., Van Balen, K., Van Gerven, T., & Vandecasteele, C. (2008). Assessment of Pb-slag, MSWI bottom ash and boiler and fly ash for using as a fine aggregate in cement mortar. *Journal of Hazardous Materials*, *154*(1–3), 766–777.

Sander, J., Qin, X., Lu, Z., Niu, N., & Kovarsky, A. (2003). Automatic Extraction of Clusters from Hierarchical Clustering Representations. In K.-Y. Whang, J. Jeon, K. Shim, & J. Srivastava (Eds.), *Advances in Knowledge Discovery and Data Mining* (pp. 75–87). Springer. https://doi.org/10.1007/3-540-36175-8_8

Sanna, A., Dri, M., Hall, M. R., & Maroto-Valer, M. (2012). Waste materials for carbon capture and storage by mineralisation (CCSM) – A UK perspective. *Applied Energy*, *99*, 545–554. https://doi.org/10.1016/j.apenergy.2012.06.049

Sanna, A., Uibu, M., Caramanna, G., Kuusik, R., & Maroto-Valer, M. (2014). A review of mineral carbonation technologies to sequester CO 2. *Chemical Society Reviews*, *43*(23), 8049–8080.

Schulz, B., Sandmann, D., & Gilbricht, S. (2020). SEM-Based Automated Mineralogy and Its Application in Geo- and Material Sciences. *Minerals*, *10*(11), Article 11. https://doi.org/10.3390/min10111004

Scott, P. W., Critchley, S. R., & Wilkinson, F. C. F. (1986). The chemistry and mineralogy of some granulated and pelletized blastfurnace slags. *Mineralogical Magazine*, *50*(355), 141–147. https://doi.org/10.1180/minmag.1986.050.355.19

Sharma, S. K. (2012). *X-Ray Spectroscopy*. BoD – Books on Demand.

Shen, H., Forssberg, E., & Nordström, U. (2004). Physicochemical and mineralogical properties of stainless steel slags oriented to metal recovery. *Resources, Conservation and Recycling*, *40*(3), 245–271.

Shi, C., Wang, D., & Behnood, A. (2012). Review of Thaumasite Sulfate Attack on Cement Mortar and Concrete. *Journal of Materials in Civil Engineering*, *24*(12), 1450–1460. https://doi.org/10.1061/(ASCE)MT.1943-5533.0000530

Skelcher, G. (2014). Arnside & Silverdale Area of Outstanding Natural Beauty–Special Qualities Report. *Arnside & Silverdale AONB*.

Smaragdis, P., Fevotte, C., Mysore, G. J., Mohammadiha, N., & Hoffman, M. (2014). Static and dynamic source separation using nonnegative factorizations: A unified view. *IEEE Signal Processing Magazine*, *31*(3), 66–75.

Solisio, C., & Lodi, A. (2002). Bioleaching of zinc and aluminium from industrial waste sludges by means of Thiobacillus ferrooxidans. *Waste Management*, *22*(6), 667–675.

Spoerl, J. S. (2004). *A brief history of iron and steel production*.

Spooren, J., Binnemans, K., Björkmalm, J., Breemersch, K., Dams, Y., Folens, K., González-Moya, M., Horckmans, L., Komnitsas, K., Kurylak, W., Lopez, M., Mäkinen, J., Onisei, S., Oorts, K., Peys, A., Pietek, G., Pontikes, Y., Snellings, R., Tripiana, M., … Kinnunen, P. (2020). Near-zero-waste processing of low-grade, complex primary ores and secondary raw materials in Europe: Technology development trends. *Resources, Conservation and Recycling*, *160*, 104919. https://doi.org/10.1016/j.resconrec.2020.104919

Srichandan, H., Kim, D., Gahan, C. S., & Akcil, A. (2013). Microbial extraction metal values from spent catalyst: Mini review. *Advances in Biotechnology*, 225–239.

Stegen, K. S. (2015). Heavy rare earths, permanent magnets, and renewable energies: An imminent crisis. *Energy Policy*, *79*, 1–8.

Taylor, K. (2013). *Carnforth iron Works, Carnforth, Lancashire. Heritage Impact Assessment.*

Teng, C., & Gauvin, R. (2020). Multivariate Statistical Analysis on a SEM/EDS Phase Map of Rare Earth Minerals. *Scanning*, *2020*, e2134516. https://doi.org/10.1155/2020/2134516

Tian, B., & Cohen, M. D. (2000). Does gypsum formation during sulfate attack on concrete lead to expansion? *Cement and Concrete Research*, *30*(1), 117–123. https://doi.org/10.1016/S0008-8846(99)00211-2

Tominaga, M., Ortiz, E., Einsle, J. F., Ryoichi Vento, N. F., Schrenk, M. O., Buisman, I., Ezad, I. S., & Cardace, D. (2021). Tracking Subsurface Active Weathering Processes in Serpentinite. *Geophysical Research Letters*, *48*(6), e2020GL088472. https://doi.org/10.1029/2020GL088472

Tripathy, S. K., Dasu, J., Murthy, Y. R., Kapure, G., Pal, A. R., & Filippov, L. O. (2020). Utilisation perspective on water quenched and air-cooled blast furnace slags. *Journal of Cleaner Production*, *262*, 121354. https://doi.org/10.1016/j.jclepro.2020.121354

USGS. (2023). Iron and Steel Slag. *Mineral Commodity Summaries*.

Van Oss, H. (2013). *US Geological Survey 2010 minerals yearbook: Cement*. Technical Report, US Department of the Interior, US Geological Survey. http ….

van Oss, H. G. (2014). Minerals Yearbook: Cement. *United States Geological Survey (USGS). Available Online: Https://Www. Usgs. Gov/Centers/Nmic/Cement-Statistics-and-Information (Accessed on 2 October 2020)*.

Wang, G., Wang, Y., & Gao, Z. (2010). Use of steel slag as a granular material: Volume expansion prediction and usability criteria. *Journal of Hazardous Materials*, *184*(1), 555–560. https://doi.org/10.1016/j.jhazmat.2010.08.071

Wendling, L. A., Binet, M. T., Yuan, Z., Gissi, F., Koppel, D. J., & Adams, M. S. (2013). Geochemical and ecotoxicological assessment of iron-and steel-making slags for

potential use in environmental applications. *Environmental Toxicology and Chemistry*, *32*(11), 2602–2610.

Wendling, L., Douglas, G., Coleman, S., & Yuan, Z. (2010). *Assessment of the ability of low-cost materials to remove metals and attenuate acidity in contaminated waters*.

Wilkinson, A. J., Collins, D. M., Zayachuk, Y., Korla, R., & Vilalta-Clemente, A. (2019). Applications of multivariate statistical methods and simulation libraries to analysis of electron backscatter diffraction and transmission Kikuchi diffraction datasets. *Ultramicroscopy*, *196*, 88–98. https://doi.org/10.1016/j.ultramic.2018.09.011

Wilkinson, B. H. (2005). Humans as geologic agents: A deep-time perspective. *Geology*, *33*(3), 161. https://doi.org/10.1130/G21108.1

Wilson, S. A., Dipple, G. M., Power, I. M., Thom, J. M., Anderson, R. G., Raudsepp, M., Gabites, J. E., & Southam, G. (2009). Carbon Dioxide Fixation within Mine Wastes of Ultramafic-Hosted Ore Deposits: Examples from the Clinton Creek and Cassiar Chrysotile Deposits, Canada. *Economic Geology*, *104*(1), 95–112. https://doi.org/10.2113/gsecongeo.104.1.95

Xuequan, W., Hong, Z., Xinkai, H., & Husen, L. (1999). Study on steel slag and fly ash composite Portland cement. *Cement and Concrete Research*, *29*(7), 1103–1106.

Yi, H., Xu, G., Cheng, H., Wang, J., Wan, Y., & Chen, H. (2012). An Overview of Utilization of Steel Slag. *Procedia Environmental Sciences*, *16*, 791–801. https://doi.org/10.1016/j.proenv.2012.10.108

Yildirim, I. Z., & Prezzi, M. (2011). Chemical, Mineralogical, and Morphological Properties of Steel Slag. *Advances in Civil Engineering*, *2011*, e463638. https://doi.org/10.1155/2011/463638

Zhang, T., Yu, Q., Wei, J., Li, J., & Zhang, P. (2011a). Preparation of high performance blended cements and reclamation of iron concentrate from basic oxygen furnace steel slag. *Resources, Conservation and Recycling*, *56*(1), 48–55. https://doi.org/10.1016/j.resconrec.2011.09.003

Zhang, T., Yu, Q., Wei, J., Li, J., & Zhang, P. (2011b). Preparation of high performance blended cements and reclamation of iron concentrate from basic oxygen furnace steel slag. *Resources, Conservation and Recycling*, *56*(1), 48–55.

Zhang, X., Chen, J., Jiang, J., Li, J., Tyagi, R. D., & Surampalli, R. Y. (2020). The potential utilization of slag generated from iron- and steelmaking industries: A review. *Environmental Geochemistry and Health*, *42*(5), 1321–1334. https://doi.org/10.1007/s10653-019-00419-y